Western Australia School of Mines: Minerals, Energy and Chemical Engineering

Modelling and simulation of biomass fast pyrolysis process: Kinetics, reactor, and condenser systems

Adhirath Sanjay Wagh

This thesis is presented for the Degree of

Doctor of Philosophy

Of

Curtin University

February 2019

Declaration

To the best of my knowledge and belief, this thesis contains no material previously published by any other person except where due acknowledgement has been made.

This thesis contains no material which has been accepted for the award of any other degree or diploma in any university.

Date: 22/02/2019

To,

My Parents,

Family & Friends,

and Teachers

Acknowledgement

"Thank you" is not sufficient to express how I feel about everyone's contribution not only to this work but also towards my development.

I would first like to thank my supervisors, Head of School, Prof. Vishnu Pareek, Dr. Ranjeet Utikar, and Prof. J. B. Joshi for giving me this oppportunity to work at Curtin University. I would also like to thank Curtin Univeristy (CIPRS) to grant me a scholarship for my Ph.D. tenure.

Prof. Vishnu Pareek has been a constant source of inspiration and always motivating me throughout this journey. Apart from his help with the research his ability of working with people has helped me overcome few of my own barriers. He has been very patient with me, and I want to thank him for this specially.

I would like to express my deep gratitude towards Prof. J.B. Joshi, whose life long teaching spirit, curiosity, intellect, and humble character are a source of inspiration for me. His guidance has been very crucial for deciding my thesis structure.

Dr. Ranjeet Utikar has been a constant inspiration for me. I would especially like to thank him for motivating, in his own way, me to do better my best. I learned the most from his approach of defining a problem and finding its solution. He always motivates everyone to read and explore about innovations in different areas of science and engineering. This led me to watch documentaries about innovations and read about the work of eminent scientists. He does like things to be perfect and his persuasion helped improve my presentation skills. I got to learn about a lot of software tools which have and will help me. Thanks to him for changing and helping me develop a new approach of solving problems.

Thank you very much Manju ma'am for being very kind and empathetic towards all of us. Awesome food, kind words, and happy moments with you are the moments I will cherish for the rest of my life. And as we discussed, thank you wouldn't

put a full stop, I will definitely be in touch with a person like you.

A special thank you to Dr. Yogesh Shinde and Dr. Abhishek Sharma for their help with experiments and analysis of the work. Their inputs have been very valuable.

Thanks a ton to Dr. Sharmilee Mane. She is the reason I am here. I met her back in ICT and she suggested me to apply in Curtin University. Coming to Curtin has helped me improve by leaps and bounds; so a special thank you to Sharmilee.

Mrunmai, Sanket (Shankar), and Subhra, you guys made my journey very smooth. Special thanks to Mrunmai for bearing me and for being always there to help. Your kind words and unconditional support made me stand up to all the problems. The meals at different restaurants were really soothing. Mrunmai I really have no words for your support, it has been of utmost importance. Your suggestion of pursuing a Ph.D. was the best decision I took. Thanks a lot. I got to meet two really awesome guys, Sanket and Subhra. Thanks a lot sanket for helping me out when I came here. You made it very easy. Conversations about your school and our discussions to work in the area of education were really enlightening. I would really like to work with you on this in the future. I really hope I become as organized as you someday; and witty too. I had cool conversations with Subhra, and thanks to him that I got into photography. I really see a close friend in you Sanket and Subhra.

Thanks to the Wongies...Cathy, David, little Joshua, and cute Jesslyn. It was excellent and best experience living with them. So much fun and happy moments with all of you.

Thanks to Barani, Shambhu, Vaibhav, Himanshu, Vishal, Hari, Asha, Pankaj, Jay, Sakshi, Nimrat, Anupam, Ruturaj, and Rofia for the happy moments in Perth.

Thanks a lot to Jason, Araya, Roshanak, Ann, Andrew, Jimmy, and Melisa for constant support in the lab. Your assistance was really invaluable.

Thanks to my parents, family, and friends in India without whom I wouldn't have been here. Thanks to Perth, these years have been the golden years of my life.

Abstract

Biomass pyrolysis has not gained a lot of commercial success because of complex feedstock chemistry, bio-oil instability, poor fuel properties, and variation in oil composition with respect to feedstock chemistry and reaction conditions. Computational models can help understand various multiscale processes of biomass pyrolysis and help in efficient design and sustainable operation of large scale pyrolysis plants. Reactor and downstream unit operation modeling is challenging because of chemical composition of pyrolysis products which is significantly affected by complex interplay between reaction kinetics and intra-particle physical, morphological changes, and transport processes. In this thesis detailed reaction kinetics, a reaction engineering model of bubbling fluidized bed reactor, and simulation methodology and schemes were developed to address different multi-scale challenges associated with biomass pyrolysis.

TGA experiments were carried out to study the effect of heating rate and particle size on biomass pyrolysis rate. A multi-component distributed activation energy model was used to describe pyrolysis kinetics. The model parameters varied depending on the biomass particle size as well as on the choice of data-set obtained at different heating rates used to calculate the parameters. This could be attributed to morphological changes in biomass particles beyond a particular heating rate, which indicated dominance of devolatilization reactions over cross-linking reactions. The study systematically showcased the importance of appropriate choice of experimental data-set to accurately model fast pyrolysis kinetics. A detailed reaction model, reported in the literature, was modified by coupling it with the distributed activation energy model to extend the model's applicability to wide range of heating rates and account for effects of morphological changes on reaction rate.

To compare the prediction ability of modified kinetics with literature model, an extensible reaction engineering model of bubbling bed reactor (BBR) was developed based on the mixing cell approach. The BBR model was used to simulate biomass pyrolysis process using the detailed lumped kinetic model (solid devolatilization reactions) and a rigorous secondary reaction mechanism (Gas phase reactions with 511 species and 20,239 reactions). The reactor model coupled with reaction kinetics was validated using literature data. The reactor model predicted the composition of major components of bio-oil and pyrolysis gases.

Finally, simulations for fractional condensation of a mixture of model compounds (similar to those used in reaction kinetics) representing pyrolysis vapor were carried out. The objective of the study was to fractionally condense the model compounds in distinct chemical families to address the stability issue of bio-oil. A simulation strategy was developed to design liquid collection systems for biomass pyrolysis process. Based on the analysis a new multi-stage condensation scheme was proposed to collect bio-oil in individual chemical families.

The detailed reaction kinetics coupled with DAE approach extends the applicability of kinetic model to a wide range of heating rates and also quantifies the effect of morphological changes on reaction rate. The reactor model proposed in the present work can be used to simulate biomass pyrolysis process at plant scale. The pyrolysis reactor model predicts composition of major liquid and gas species for a wide range of feedstock chemistry and operating conditions (temperature and heating rate) at plant scale. The bio-oil composition can be further utilized to design robust downstream processes to achieve a constant throughput of chemicals and fuels for different lignocellulosic biomass. The modeling and simulation strategies developed in the present research address the scale-up challenges associated with variable feedstock chemistry, multiphase nature of pyrolysis reactions, and bio-oil instability.

Keywords: biomass, fast pyrolysis, modeling, simulation, reaction kinetics, fluidized bed, reactor engineering, bio-oil, multi-stage condensation, fractionation

Nomenclature

General symbols

a, A	cross sectional area, m^2
$\mathbf{A}_0$	frequency factor, 1/s
Ar	Archimedes number
$\mathbf{A}_s$	surface area, m^2
Bi	Biot number
$\mathbf{C}_p$	Specific heat capacity, J/kg/K
d	diameter, m
D	diffusivity, m^2/s
E	activation energy, kJ/mol
$\mathbf{E}_0$	mean activation energy, kJ/mol
$\mathbf{f}_c$	ratio of cloud phase to bubble phase volume fraction
$\mathbf{f}_w$	ratio of wake phase to bubble phase volume fraction
g	gravitational constant, m/s^2
h	heat transfer coefficient, $W/m^2/K$
$\mathbf{h}_{ce}$, $\mathbf{h}_{bc}$	heat transfer rate constant between cloud emulsion and bubble cloud phase, 1/s
H	height of bed in reactor, m

J1, J2, J3	normalized error
$\mathbf{k}_{ce}$, $\mathbf{k}_{bc}$	mass transfer rate constant between cloud emulsion and bubble cloud phase, m^3/s
$\mathbf{k}_{py}$	pyrolysis reaction rate, 1/s
L	characteristic length, m
$\dot{m}$	mass flow rate, kg/s
m	temperature exponent for frequency factor
n	mole fraction or splitting parameter to determine biomass composition
P	pressure, N/m^2
Py	Pyrolysis number
r	radius, m
$\mathbf{Re}_p$	particle Reynold's number
T	temperature, K
t	time, s
u	velocity, m/s
V	volume, m^3
$\mathbf{w}_c$	pseudo component mass fraction
x**,X,Y**	mass fraction
y	peak maximum for first derivative of TGA data
z	peak maximum for second derivative of TGA data

Greek symbols

α	conversion
β	heating rate, K/s
γ	solid distribution coefficient
δ	bubble volume fraction
ϵ	hold up
λ	thermal conductivity, W/m/K
ρ	density, kg/m^3
σ	standard deviation in probability distribution function, kJ/mol

Abbreviations

A2	Avrami-Erofeev nucleation model
ACAC	acetic acid
BFB	bubbling fluidized bed
Cell	cellulose
CellA	active cellulose
CF	chemical family
CFB	circulating fluidized bed
CPD	chemical percolation devolatilization
DAEM	distributed activation energy model
DAXP	dianhydro xylo-pyranose
DP	depolymeriation reaction model

DTG	differential thermal gravimetric data/ curve
ESP	electro-static precipitator
F1	first order reaction model
FE2MACR	sinapylaldehyde
FG-DVC	functional group, depolymerization, vaporization and cross-linking
GMSW	glucomannan soft wood
HCE1	active hemicellulose
HCE2	active hemicellulose
HMWL	high molecular weight lignin
ITANN	3,5-dihydro benzofuran
LCB	lignocellulosic biomass
LIG	intermediate solid lignin component
LIGCC	intermediate solid lignin component
LIGOH	intermediate solid lignin component
LIGC	lignin sub-component rich in carbon
LIGH	lignin sub-component rich in hydrogen
LIGO	lignin sub-component rich in oxygen
LMWC	low molecular weight components
MW	molecular weight
NBE	number of bubble to emulsion mixing cells
NCG	non-condensible gas
NRTL	non-random two-liquid model
NTH	Nothnagel

RCR	rotating cone reactor
SF	separation factor
STHE	shell and tube heat exchanger
TANN	tannins
TGA	thermal gravimetric analysis
TGL	triglycerides
UNIFAC	UNIQUAC functional-group activity coefficient model
UNIQUAC	universal quasichemical activity coefficient model
XYHW	xylan hardwood

Subscripts

b	bubble phase
B	biomass
bed	reactor dense bed
c	cloud phase
C	char
cw	cloud-wake phase
e	emulsion phase
fb	free-board region
g	gas phase
i,j	component or reaction number
M	moisture
mf	minimum fluidization

mix	mixture
p	pseudo-component
pe	effective particle properties
py	pyrolysis
$\mathbf{r}_j$	j^{th} reaction
s	solid
s,d	solid downward direction
SV	surface area to volume ratio of spherical particle with effective diameter
V	volume of spherical particle with effective diameter
α	splitting parameter between cellulose and hemicellulose
β	splitting parameter between lignin sub-component LIG-H and LIG-C
γ	splitting parameter between lignin sub-component LIG-O and LIG-C
δ	splitting parameter between lignin and triglyceride
ϵ	splitting parameter between lignin and tannin

Superscripts

$\mathbf{i}^{th}$	emulsion, bubble, cloud phase mixing cell number
pri	primary reactions
q	shape factor
sec	secondary reactions
$*$	maximum volatiles

Contents

List of Figures

List of Tables

Abbreviations

A2	Avrami-Erofeev nucleation model
ACAC	acetic acid
BFB	bubbling fluidized bed
Cell	cellulose
CellA	active cellulose
CF	chemical family
CFB	circulating fluidized bed
CPD	chemical percolation devolatilization
DAEM	distributed activation energy model
DAXP	dianhydro xylo-pyranose
DP	depolymeriation reaction model
DTG	differential thermal gravimetric data/ curve
ESP	electro-static precipitator
F1	first order reaction model
FE2MACR	sinapylaldehyde
FG-DVC	functional group, depolymerization, vaporization and cross-linking
GMSW	gluco-mannan soft wood
HCE1	active hemicellulose

HCE2	active hemicellulose
HMWL	high molecular weight lignin
ITANN	3,5-dihydro benzofuran
LCB	lignocellulosic biomass
LIG	intermediate solid lignin component
LIGCC	intermediate solid lignin component
LIGOH	intermediate solid lignin component
LIGC	lignin sub-component rich in carbon
LIGH	lignin sub-component rich in hydrogen
LIGO	lignin sub-component rich in oxygen
LMWC	low molecular weight components
MW	molecular weight
NBE	number of bubble to emulsion mixing cells
NCG	non-condensible gas
NRTL	non-random two-liquid model
NTH	Nothnagel
RCR	rotating cone reactor
SF	separation factor
STHE	shell and tube heat exchanger
TANN	tannins
TGA	thermal gravimetric analysis
TGL	triglycerides
UNIFAC	UNIQUAC functional-group activity coefficient model

UNIQUAC universal quasichemical activity coefficient model

XYHW xylan hardwood

Chapter 1

Introduction

1.1 Introduction

This study addresses challenges related to fast pyrolysis kinetic modeling, reactor modeling, and bio-oil instability. Simulation for bio-oil fractionation into distinct chemical families, a relatively unexplored topic in the literature, has been examined in this thesis. This chapter sets the background for this work and briefly outlines the work in each chapter.

1.2 Background

Lignocellulosic biomass (LCB) is an abundant, rich, and renewable source of carbon. Carbon is available in the form carbohydrate (cellulose and hemicellulose) and phenolic polymer (lignin) which can be converted to different products using biological, chemical, and thermo-chemical processes. The viability of conversion processes depends on type of biomass, feedstock location, and market demand for energy and chemicals. Pyrolysis and gasification are commonly adopted thermo-chemical routes to convert LCB to fuel and chemical precursors/ products. Pyrolysis process involves heating biomass particles in an inert atmosphere to 400-600 °C that leads to formation of gas, liquid (bio-oil), and solid (char) products. The relative yield of each product is a function of temperature, heating rate, and intra-particle and reactor vapor residence time. Under fast pyrolysis conditions where particle (<3 mm) heating rates are of the order of 1000 °C/s and vapor reactor

residence time between 2-5 s, liquid yield is high (60-75 wt.%) [29]. Bio-oil, a mixture of more than 300 compounds [30, 31], can be used for energy or as a source of chemicals. However, pyrolysis has not gained commercial success because of complex feedstock chemistry, bio-oil instability, poor fuel properties, and variation in oil composition with change of feedstock chemistry and reaction conditions. The multi-scale nature of these challenges is graphically represented in Figure 1.1. Computational models can help understand these multiscale processes and help in efficient design and continuous operation of large scale pyrolysis plants. This research focuses on modeling of fast pyrolysis process on particle and, reactor scale and presents a strategy to fractionally condense pyrolysis vapors into individual chemical families.

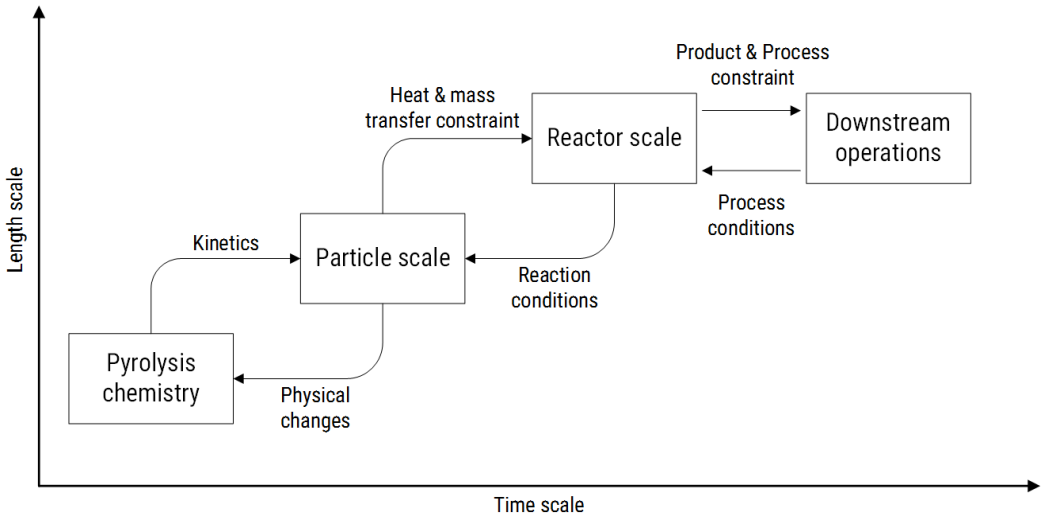

Figure 1.1: Fast pyrolysis: A multiscale problem

Reactor design requires accurate knowledge of reaction kinetics. Principal challenges towards designing a robust reactor for pyrolysis reaction are (a) variable biomass composition and (b) complex reaction chemistry. Chemical composition of biomass varies significantly with species type, soil and climatic conditions. Variability in feedstock chemistry leads to significant variation in bio-oil product composition and consequently affects manufacturing productivity. Further, pyrolysis chemistry is a complex network of numerous series and parallel reactions. The reactions can be broadly classified into depolymerization/volatilization reactions (endothermic) and cross-linking/char (exothermic) forming reactions. Under fast pyrolysis conditions, the selectivity for volatilization reactions is more

and therefore, bio-oil yield is higher as compared to char yield. It is challenging to determine the exact reaction mechanism of pyrolysis and therefore, numerous lumped kinetic models have been proposed in the literature [32]. A detailed pyrolysis reaction kinetic model has also been proposed [33], which can predict the concentration of significant bio-oil components. However, to add to the complexity of reaction processes, biomass particle undergoes significant morphological changes, like intermediate melting, and bubble formation during pyrolysis [34, 35]. This in turn affects the evolution rate of volatiles from a biomass particle and can significantly affect the bio-oil composition. Lack of modeling studies to account for the effect of morphological changes on volatile evolution rate and bio-oil product profile has motivated a significant part of this research.

Bio-oil constituents react with one another because they belong to different oxygen containing chemical families [36]. To address the undesirable reactive characteristics of bio-oil, different strategies like catalytic up-gradation [37–40], fractional and molecular distillation [16, 41, 42] and stabilizing solvent/additive addition [43–46] have been reported. Catalytic upgrading mainly involves cracking, hydro-cracking and condensation reactions that reduce the oxygen content of the bio-oil and convert the reactive species into stable compounds, improving the bio-oil shelf life. However, as any catalyst is selective to one or two chemical functionalities, the non selective components tend to degrade to gases or lead to coke formation, thus, decreasing the liquid yield [47]. Fractionation of bio-oil, condensed as a mixture from pyrolysis reactor, using distillation is constrained because the liquid will degrade under sustained heat. Addition of solvent helps improve the bio-oil stability over time but involves cost of the solvent as well as its separation before final application of bio-oil. Therefore, condensing the vapors after pyrolysis reaction into individual chemical families would address the stability issue as well as reduce the non-selective reactions during catalytic upgrading process of bio-oil. Bio-oil collection systems are reported in the literature but none are designed or operated to fractionally separate chemical families. Furthermore, there are no reports on simulations for liquid collection systems using significant number of model compounds to fairly represent phase equilibrium behavior of bio-oil. This research thus, proposes a simulation strategy for fractional condensation of

bio-oil model compounds. The work reported here connects phenomena occurring at different length scales in fast pyrolysis operation.

1.3 Motivation

Bio-oil as a whole has poor combustion properties and degrades over time [48]. Without upgradation, bio-oil fetches a low price as a fuel. Nevertheless it is a rich source of value added chemicals that belong to aldehyde, ketone, carboxylic acid, sugar and, phenol chemical families. Chemical like acetic acid is used as solvent for many industrial processes. It is also used in the manufacture of inks, dyes, plastics, pesticides, and wood glue. Phenol and its derivatives from bio-oil can be used in manufacture of resins, polymers, antiseptics, and flavors. Aldehydes and ketones can be used as precursors for specialty chemicals. Co-production of value added chemicals and fuel precursors using fast pyrolysis process is an economically attractive option. However, designing a techno-economically feasible pyrolysis process is a daunting task because of its numerous operating variables. The interdependence among significant pyrolysis process variables associated with upstream and downstream operations is summarized in Figure 1.2. A pyrolysis plant should be capable of handling different feedstock for effective continuous operation throughout the year. This implies that the reactor and bio-oil collection system should be designed to maintain, more or less, constant throughput of the desired product. However, there are several challenges associated with designing upstream and downstream unit operations.

1.3.1 Challenges

Challenges associated with reactor design and downstream processing of fast pyrolysis process are, (a) modeling reaction kinetics and inter-dependent physicochemical changes at particle scale, (b) bio-oil instability. Following are the challenges that hinder efficient pyrolysis process design:

1. Pyrolysis reaction chemistry is a combination of complex competitive reactions and the reaction selectivity is a strong function of biomass composition, particle size, temperature, and heating rate. Reactions cause signifi-

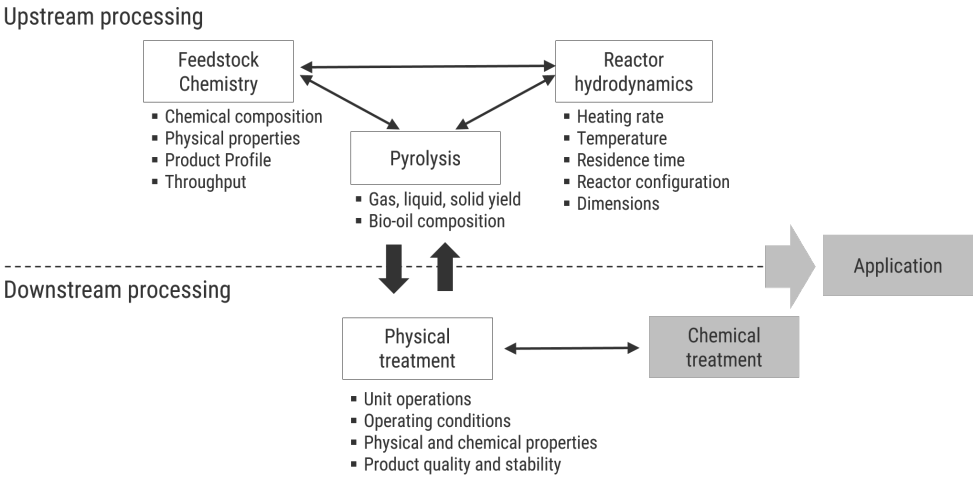

Figure 1.2: Interdependence of upstream and downstream pyrolysis process variables. The shaded area is not addressed in this work.

cant physical changes in biomass particle which in turn affect the rate of pyrolysis. Modeling the inter-dependent reaction kinetics and particle scale morphological changes (partial melting, cross-linking, and pore structure changes) is difficult.

2. Kinetic models in the literature are unable to accurately quantify the effect of these physico-chemical processes on the yield and composition of fast pyrolysis products.

3. To maintain isothermal conditions at high heating rates, pyrolysis kinetics experiments reported in the literature use biomass particle sizes which are small and do not represent the pore structure of particle sizes used in large scale pyrolysis reactors. Therefore, the effect of particle scale phenomena on reaction rates is unaccounted for. This reduces the accuracy of bio-oil yield and composition prediction.

4. Bio-oil is a mixture of different chemical families that undergo condensation reactions causing bio-oil polymerization, rendering it useless. Stabilizing bio-oil is important for its utilization as a fuel and for recovering value added chemicals from it.

Therefore, an opportunity exists to investigate and propose new kinetic model based on an experimental strategy which accounts for the interdependence of reaction chemistry and physical changes on the rate of fast pyrolysis. The research

gaps, briefly highlighted in 1.2 also reveal that a cost effective bio-oil stabilization process needs to be explored.

1.3.2 Research significance

The research work in this dissertation contributes to further understanding of, (a) multiphase and multi-scale pyrolysis kinetics and (b) bio-oil processing. A strategy for pyrolysis kinetics experiments and modeling is developed in Chapter 3. The experiments are carried out to account for the effect of operating parameters (particle size and heating rate) in large scale reactors while carefully maintaining the conditions required for reaction rate determination. Such experimental procedure will enable the researcher to possibly capture the effects of reaction chemistry on biomass particle morphology and vice-versa. The selection of kinetic model and estimation of its parameters based on such experiments could closely describe reaction scale and particle scale pyrolysis processes in large scale reactors. Further, based on the results of Chapter 3, improvements to a detailed kinetic model reported in the literature are presented in Chapter 4. The modification can increase the accuracy of predicting yield and composition of bio-oil obtained from different lignocellulosic biomass in large scale reactors. This hypothesis is tested in Chapter 5 where a reactor model is coupled with the modified kinetic model and the one in literature. The comparison of results shows that the model reported in this thesis fares better than the one in literature. Therefore, the reaction kinetics experimental strategy and the model reported in this work account for physico-chemical phenomena in fast pyrolysis and improve the prediction accuracy of yields and composition of pyrolysis products.

Simulation methodology and results of bio-oil fractional condensation in Chapter 6 can assist in designing downstream unit operations for bio-oil processing. Separation of chemical families in bio-oil can improve its shelf life and facilitate isolation of value added chemicals to make pyrolysis commercially viable.

1.4 Research Objectives

The primary aim of this work is development of a multi-scale modeling and simulation strategy for effective design and operation of pyrolysis process. Following are the objectives of the current research:

1. To model the effect of morphological changes on biomass pyrolysis kinetics.
2. To model the effect of morphological changes on the yield of significant bio-oil components by modifying detailed pyrolysis reaction kinetics.
3. To model bubbling fluidized bed reactor to predict yield and composition of pyrolysis products.
4. To present a simulation strategy to fractionally condense bio-oil into individual chemical families.

1.5 Thesis Outline

The thesis is divided into 7 chapters as follows

1. Chapter 1 gives a brief introduction to the research problem along with motivation for research.
2. Chapter 2 discusses the basic concepts and terminologies of biomass pyrolysis. An overview of type of pyrolysis processes, reactor configurations, bio-oil composition and properties, and kinetic and reactor modeling is described. The chapter is concluded with research significance and graphical abstract of the thesis.
3. Chapter 3 discusses the effect of temperature and heating rate on the mass loss profile and pore structure of biomass particles of different sizes. Distributed activation energy model (DAEM) is used to account for the effect of morphology on kinetic parameters of biomass pyrolysis.
4. Chapter 4 discusses the coupling of DAEM with detailed pyrolysis kinetics to improve the prediction ability of the primary pyrolysis products under

fast pyrolysis conditions. To quantify the effect of morphological changes on reaction rate a correction factor, dependent on heating rate, is introduced and combined with the frequency factor in rate expression. Literature based validation of the modified kinetic model is provided.

5. Chapter 5 describes the results of a continuous non-isothermal tanks-in-series model of a bubbling fluidized bed reactor for pyrolysis reactions. Modified kinetic parameters determined in chapter 4 are used to model the primary pyrolysis reactions, while the parameters for secondary gas phase reactions have been used from the literature. Literature validation of pyrolysis product profiles under different operating conditions are provided.

6. Chapter 6 presents a simulation strategy for fractional condensation of pyrolysis vapors into individual chemical families. The results establish phase equilibrium behavior of bio-oil which can be fairly represented using a set of twenty-eight model compounds. Literature based validation of the simulations is provided. A new condensation scheme is proposed to fractionally condense bio-oil into distinct chemical families.

7. Chapter 7 summaries the research work by stating important observations and findings followed by prospective areas of improvements for taking the work forward.

Chapter 2

Literature review

2.1 Introduction

Chemical industry is the backbone of modern human civilization. Discovery of crude oil caused an explosion of revolutionary materials like transportation fuels, polymers, pharmaceuticals, other commodity, and engineering products. However, following the oil crisis in the 1970's, biomass has gained traction as a renewable source for liquid fuels and chemicals. LCB is adopted as feedstock for different biomass conversion technologies. Compared to biological process, pyrolysis utilizes complete plant material and converts it to gas, liquid, and solid product within seconds just by heating in the absence of oxygen. Small residence times can facilitate decentralized pyrolysis plants to utilize biomass locally. Pyrolysis hols promise as a potential technology to commercially produce fuels, fuel pre-cursors and chemicals.

This chapter introduces LCB and its potential as a feedstock for thermo-chemical conversion of biomass. Basic principles of pyrolysis on particle, reactor and process scale are discussed. Kinetic and reactor modeling along with fractionation of bio-oil is identified to be of particular interest. Challenges in the upstream, and downstream pyrolysis processes are also briefly discussed. The chapter is concluded with significance of the research work.

2.2 LCB as a renewable carbon resource

2.2.1 Chemical structure

Biomass based fuels and chemicals synthesized using LCB as a feedstock are referred to as second generation biofuels or chemicals. LCB is plant based material made up of lignin, cellulose, hemicellulose, ash, and small proportion of lipids, proteins, extractive and other compounds. The proportion of these constituents varies with species type, soil, and climatic conditions [49]. The average composition of lignin, cellulose, and hemicellulose for different biomass types is shown in Table 2.1. The proportion of oxygen varies with the relative abundance of cellulose, hemicellulose and lignin. The O:C weight ratio for cellulose and hemicellulose is close to 1 while that for lignin is between 0.3 to 0.4. The high oxygen content reduces the calorific value of LCB, making it a poor choice for direct combustion applications.

Table 2.1: Composition of cellulose, hemicellulose and lignin for different kinds of LCB [27]

Biomass	Cellulose (wt.%)	Hemicellulose (wt.%)	Lignin (wt.%)
Hardwoods stems	40 to 55	24 to 40	18 to 25
Softwood stems	45 to 50	25 to 35	27 to 33
Nut shells	25 to 30	25 to 30	30 to 40
Corn cobs	45	35	15
Grasses	25 to 40	35 to 50	17 to 24
Wheat straw	38	25	18
Rice Straw	33	26	10 to 13
Leaves	15 to 20	80 to 85	0
Switchgrass	45	31	12

Figure 2.1 shows a representative structure of major bio-polymers of LCB. The three bio-polymers make up the secondary cell wall of the plant material. Cellulose is a linear crystalline polymer with degree of polymerization between 10000 to 15000 units. Hemicellulose in a chemically heterogeneous branched co-polymer containing pentose and hexose sugars. The mono-saccharides include pentoses (xylose, rhamnose, and arabinose), hexoses (glucose, mannose, and galactose), and uronic acids (4-O-methylglucuronic, D-glucuronic, and D-galactouronic acids) [50]. Depending on the type of biomass the relative content of these monomers

changes. Lignin is a cross-linked phenolic co-polymer that contributes to the rigidity of the plant cell wall. The three primary monomers of lignin are coniferyl alcohol, coumaryl alcohol, and sinapyl alcohol. The plant cell wall is a composite made up cellulose micro-fibers (bundles of 20 to 300 cellulose chains) wrapped in hemicellulose, which are dispersed in a web of lignin polymers[51]. The length scale of these composites is of the order of (10^{-8} to 10^{-7} m), while the size of the polymers themselves is between (10^{-10} to 10^{-9} m) [52].

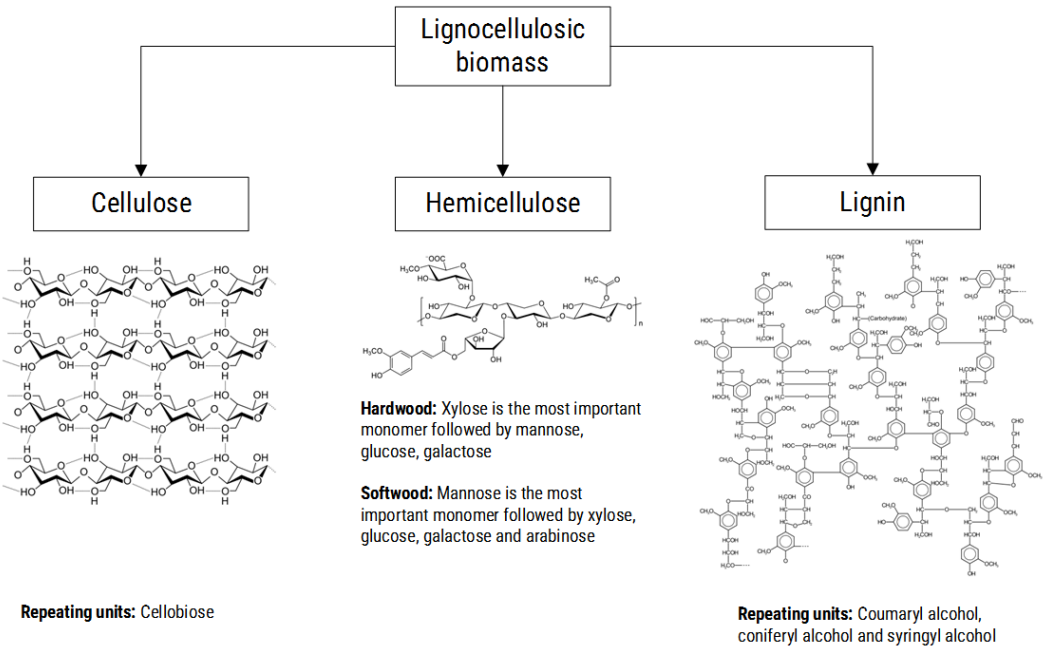

Figure 2.1: Representative chemical structure of cellulose, hemicellulose and lignin

2.2.2 Physical structure

The plant cells are arranged in a microstructure to smoothly enable various functions. For example, collection of tracheid cells form a bundle of several hollow tubes which gives rise to a porous structure having cavities (10^{-5} to 10^{-4} m) [52]. The size of the cavities varies depending on the biomass type [53]. Other such multicellular structures combine to form the macrostructure of plant. These plants/ trees are then subjected to size reduction to give particles (10^{-3} to 10^{-2} m) that are fed to biomass conversion reactors. Thus, heat and mass transport phenomena occur over a wide length scale during biomass conversion process. Different feedstock have different chemical and physical structure. Moreover, changes oc-

cur in the biomass during pyrolysis reaction. These changes pose a challenge for reaction and particle scale modeling as discussed in the later part of this chapter.

2.2.3 Biomass conversion technologies

Plant material is the only renewable source of carbon which can be converted to liquid fuels and chemicals. LCB, a non-food resource, can be converted to a spectrum of fuel, fuel pre-cursors, and platform chemicals. The conversion technologies include biological and thermo-chemical routes [54] as outlined in Figure 2.2. Microbes can digest sugars to give alcohols and other fermentation products [30]. The sugars are made available for fermentation using enzymatic or acid hydrolysis of cellulose and hemicellulose. For hydrolysis to work effectively, lignin and polysaccharides need to be separated from one another [55]. Acid hydrolysis is a harsh process which converts part of monomeric sugars to furfural derivatives which are toxic to fermentation microbes even in small concentrations. Thus, the selective enzymatic hydrolysis is preferred over acid treatment. Microbial digestion of lignin is not possible and therefore, biomass is pre-treated with acid and/or alkali to remove lignin chemically. This extra step adds to the cost of the process [56]. Moreover, time required for completion of enzymatic hydrolysis, and subsequent fermentation process is between several hours to days. This leads to use of reactors with large volumes that also require precise control over enzymatic and fermentation reaction conditions. Further higher utilization of hemicellulose derived pentose sugars is challenging as compared to glucose. Anaerobic digestion process faces similar challenges. Carbon dioxide is a major by product of anaerobic digestion. Thus, carbon efficiency of the process is low. While the methane produced during digestion can be used as an energy source, it has to be subjected to subsequent reactions for converting it to chemicals.

Small and decentralized gasification, and fast pyrolysis facilities are feasible, however, other challenges have hampered their commercialization. Gasification reaction occurs in a controlled oxygen environment to convert biomass to synthesis gas. The reaction conditions and oxygen concentration can be altered to control the CO:H_2 ratio. The synthesis gas can then be fed to Fischer Tropsch (FT) reactor to obtain FT-oil or other liquid chemicals. LCB under fast pyrolysis conditions is

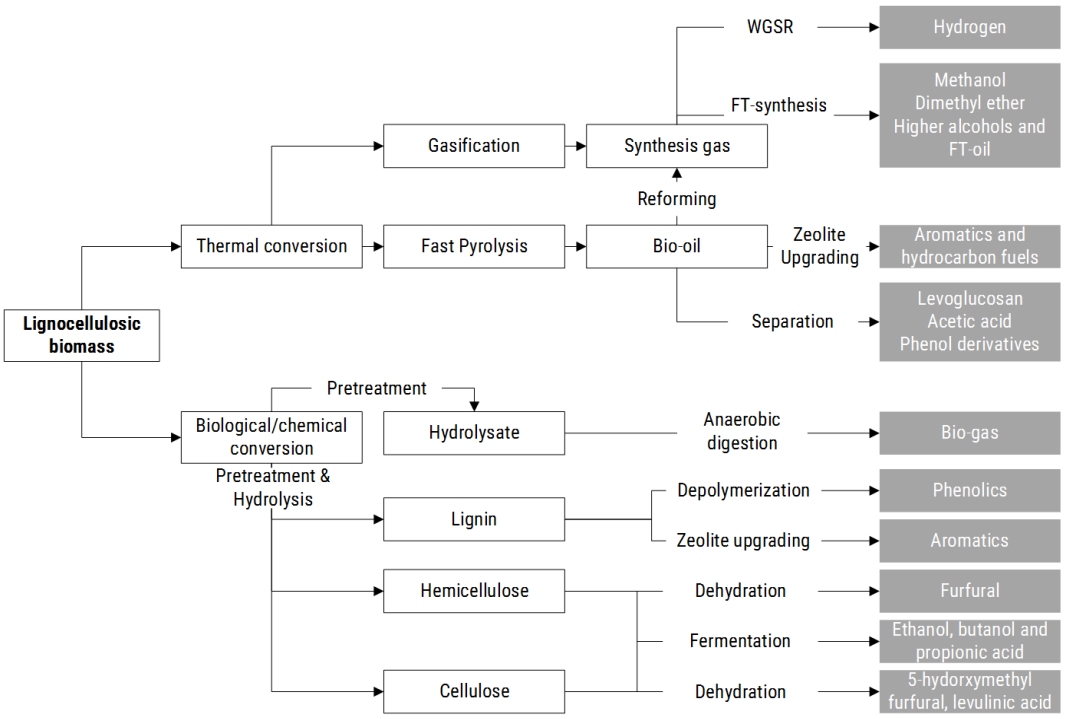

Figure 2.2: LCB conversion techniques

converted predominantly to liquid as shown in Table 2.2. The work reported here is focused on fast pyrolysis. Currently, 90% of crude oil is used for energy/transportation application while 10% of it is used for synthesis of chemicals [54]. Similarly, fast pyrolysis oil can be used a source of liquid fuel as well as a rich source of chemicals. However, scale-up, and design of fast pyrolysis process, and sustainable operation of a commercial plant is very challenging. The subsequent sections discuss various aspects of pyrolysis chemistry, kinetic and reactor modeling, and bio-oil properties. Methodology adopted to address challenges associated with each aspect are discussed followed by significance of this work.

Table 2.2: Types of pyrolysis processes

Pyrolysis Technology	Residence time	Temperature(°C)	Char	Bio-oil	Gas
Slow pyrolysis	5-30 min	400-600	<35 %	<30 %	<40 %
Fast pyrolysis	<5 sec	400-600	<25 %	<75 %	<20 %
Flash pyrolysis	<0.1 sec	650-900	<20 %	<20 %	<70 %

2.3 Fast pyrolysis of LCB

2.3.1 Multiphase and multiscale pyrolysis chemistry

Major LCB components, cellulose, hemicellulose and lignin undergo number of scission, elimination, condensation, and cross-linking reactions, with mineral matter acting as a catalyst. Hemicellulose is a branched, and amorphous co-polymer which degrades over 220-315°C; cellulose being crystalline in nature degrades between 315-400°C; and as lignin is a heterogeneous cross-linked polymer, it degrades over a wide range between 150-900°C [57]. Pyrolysis reactions can be divided into primary and secondary reactions. Chemical and physical changes that occur during fast pyrolysis are represented in Figure 2.3. LCB polymers undergo endothermic fragmentation to form low and high molecular weight oxygenates, water, and gases. Simultaneously exothermic cross-linking reactions lead to char formation [58–60]. Cellulose undergoes depolymerization to form active cellulose and low temperature charring reactions to form char and gases. Active cellulose is non-volatile and simultaneously undergoes fragmentation (formation of low molecular weight carbonyl compounds) and transglycosylation (anhydro sugars and oligosugars). These primary products undergo charring and cracking reactions while moving out of cellulose matrix [61]. Hemicellulose pyrolysis follows a similar mechanism but produces more char and fewer sugars as compared to cellulose [62]. O-acetyl groups, pentose, and hexose sugars in hemicellulose produce compounds like acetic acid, furfurals, hydroxy propanone, and water along with carbon dioxide and monoxide [63, 64]. Lignin pyrolysis is a multistage process. After an initial softening phase (160 to 190°C), dehydration (∼200°C), and cleavage of aryl-alkylether (150 to 300°C), aliphatic side chains (∼300°C), C-C linkages (370-400°C), and methoxyl groups (310 to 340°C) [65]. Families representing primary and secondary pyrolysis products of lignin are shown in Figure 2.3. Also, lignin produces more char and PAH as compared to hemicellulose and cellulose. All three polymers pass through an intermediate molten phase during pyrolysis. The extent of various primary and secondary reactions is a function of temperature, heating rate, intra-particle residence time, and mineral content. Low heat-

ing rates, long intra-particle residence time, and mineral matter promote char formation reactions of cellulose, hemicellulose, and lignin [66, 59, 67, 68]. Generally, fast pyrolysis is carried out between 400 to 600°C. Under fast pyrolysis conditions high heating rates increase selectivity for endothermic reactions, consequently increasing tar/liquid yield. The primary and secondary products shown in the figure are representative of numerous bio-oil compounds. Beyond 500 °C, where primary reactions are supposed to be completed, homogeneous tar cracking reactions start; tar and char pre-dominantly gets converted to permanent gas [69, 70]. Tar cracking can also be catalyzed by char at low temperatures, thereby increasing the gas yield. Reactions are also accompanied by physical changes that makes pyrolysis a multiphase process.

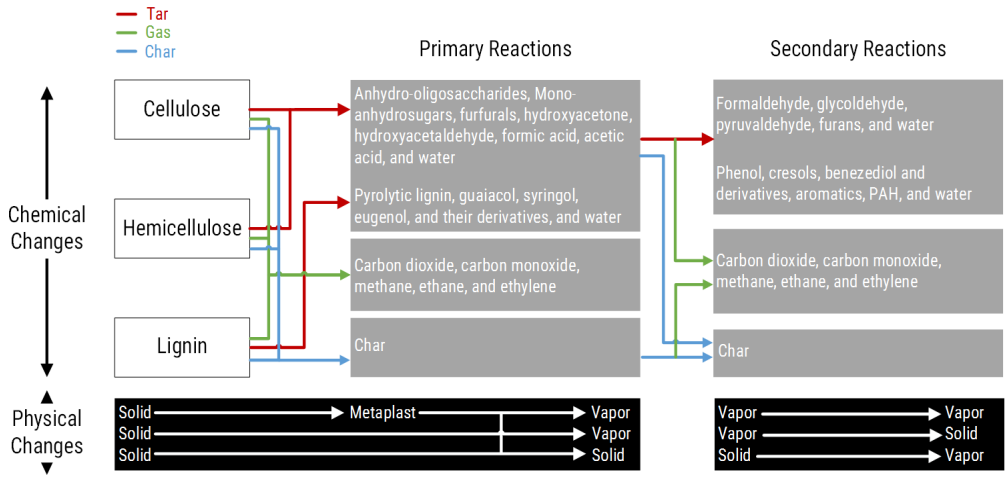

Figure 2.3: Multicomponent and multiphase nature of pyrolysis reactions.

Physical changes occurring during pyrolysis result in significant morphological changes in pore structure of biomass particle. An intermediate liquid, composed of oligomeric products, is formed inside the pores and on the biomass particle surface [71–78]. Volatile products are released from biomass cell wall as a consequence of bubble eruption [79, 35]. The vapors evolve as a consequence of reactions occurring on a scale of 10^{-10} to 10^{-9} m. Vapors accumulate to form bubble nuclei, that grow to order of 10^{-6} m [76] and rise through the intermediate liquid. The vapors generated can travel outside the needle shaped biomass particle either longitudinally or radially [80]. Pore structure of biomass particle undergoes changes during pyrolysis reaction which alters the intra-particle resistance and affects the volatile evolution profile [71, 34]. Eruption of vapor bubbles, that have

diameter of the order of cell wall thickness, lead to formation of open pore structure. Thus, there is a decrease in the resistance for vapor transport outside the reacting particle. On the other hand melting as well as tar accumulation [34] can block the pores of biomass and cause overpressure within the particle. Accumulation of vapors inside the particle hampers its volatilization rate. At the same time overpressure can cause micro-explosion of bubbles that release vapors and fine liquid droplets [74, 81]. The ejected aerosols mainly contain 'pyrolytic lignin or humins',essentially partially degraded or cross-linked oligomers from cellulose, hemicellulose, and lignin. The proportion of aerosols released decreases with increase in particle size [82, 83]. As a result, changes in morphology (Figure 2.4) of biomass can increase or decrease apparent biomass conversion rate [84] and thus, need to be accounted for while modeling biomass pyrolysis.

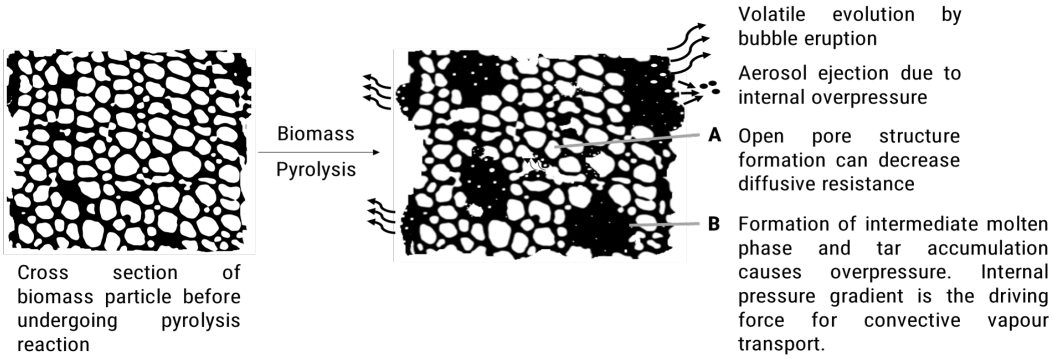

Figure 2.4: Morphological changes occurring during biomass pyrolysis.

2.3.2 Biomass pyrolysis kinetic modeling

Knowledge of reaction kinetics is essential for accurate reactor design. Kinetic model is essential to determine the yield of various pyrolysis species under different reaction conditions. Pyrolysis reactions being complex are difficult to model and therefore, several lumped kinetic models have been proposed in the literature [85–88, 2, 89, 67, 90, 5, 91, 32, 61]. Lumped models allow prediction of bio-oil, gas and char yields. Single component lumped models do not consider the variation in chemistry of LCB and kinetic parameters can not be applied to different feedstocks. To overcome this issue multi-component lumped models that treat cellulose, hemicellulose, and lignin pyrolysis independent of each other are proposed.

Biomass as a single component

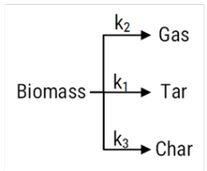

(a)

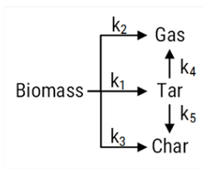

(b)

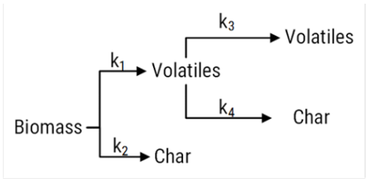

(c)

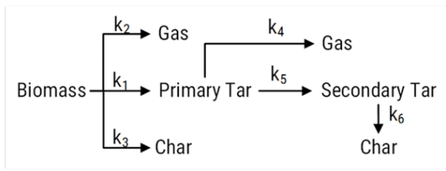

(d)

Cellulose, hemicellulose and lignin kinetics

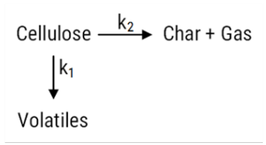

(e)

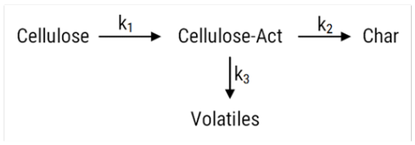

(f)

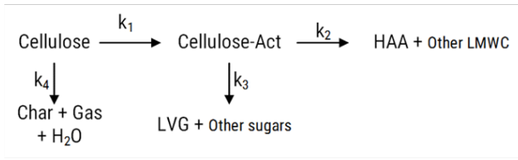

(g)

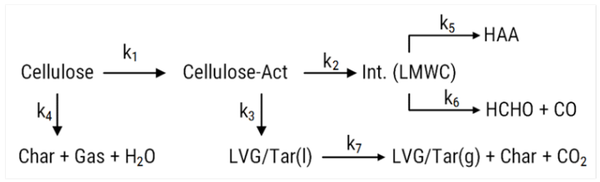

(h)

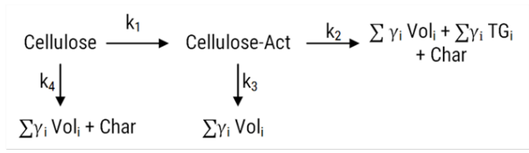

(i)

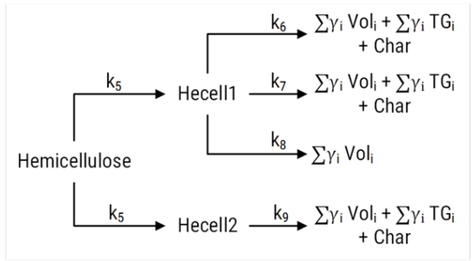

(j)

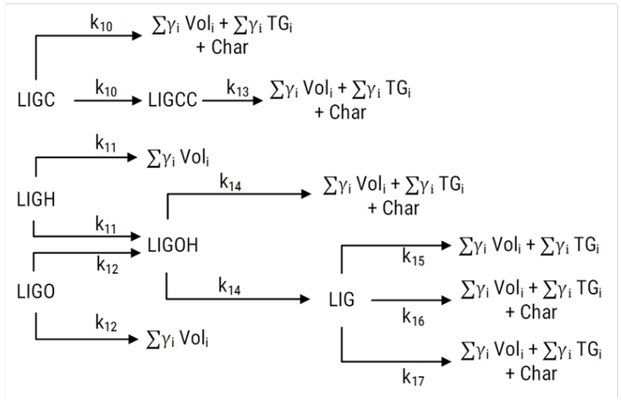

(k)

Generalized models for biomass components

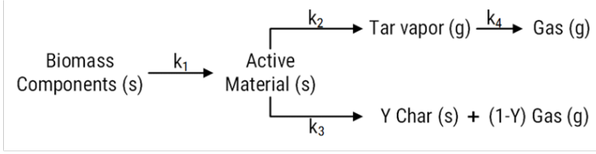

(l)

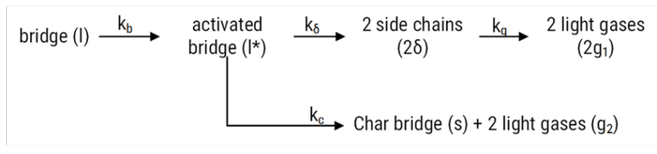

(m)

Figure 2.5: Single and multicomponent multi-reaction kinetic models for biomass pyrolysis. (a) [1, 2]; (b) [3]; (c) [4]; (d) [5]; (e) [6]; (f) [7]; (g) [8]; (h) [9]; (i),(j),(k) [10]; (l) [11]; (m) [12]. LVG: Levoglucosan; HAA: Hydroxyacetaldehyde; HCHO: Formaldehyde; LMWC: Low molecular weight compounds; Int: Intermediate; TG: trapped gases in metaplast γ: Stoichiometric coefficient; i: component id

Such models can be applied to determine pyrolysis reaction rate provided composition of these three polymers is known. However, hemicellulose and lignin structure varies based on type of LCB. Pyrolysis reactions and hence kinetic parameters can change based on the type of LCB. Recently detailed mechanistic models are formulated based on insights from molecular simulations of monomers, oligomers, and polymeric cellulose, hemicellulose and lignin [33, 92–95, 10]. Thus, over the years several issues related to qualitative and quantitative prediction of pyrolysis products have been addressed as kinetic models transformed from single component single reaction to multicomponent multi-reaction lumped models to mechanistic models.

2.3.2.1 Single component multi-reaction lumped models

Two commonly used single component pyrolysis models for biomass are shown in Figure 2.5 (a) and (b). Separate formation rates for pyrolysis gas, liquid and char are introduced in the reaction mechanism. All the reactions are assumed to follow first order reaction kinetics. Model (a) considers only primary reactions but secondary tar cracking and charring reactions have been considered in model (b) and (c). Secondary reactions do not strictly occur in the vapor phase. Biomass can depolymerize into non-volatile component like active cellulose or into high molecular weight tar which subsequently convert into volatiles and char. Thus, consideration of secondary reactions in pyrolysis kinetic mechanism is important for accurate predictions. Model (d) is based on a global kinetic scheme proposed by Diebold [96]. Thurner and Mann proposed a single step reaction model, which [97] is unable to qualitatively predict the pyrolysis product profiles with respect to temperature [67]. Coupling of particle scale models with kinetic models based on schemes (b) and (c) (Figure 2.5) [88, 2, 98] predicts quantitative trends of pyrolysis products over a wide temperature range. But inaccurate quantitative prediction of char does not allow model parameter extrapolation to fast pyrolysis reaction kinetics. CFD simulations of bubbling fluidized bed reactor [99], using model (d)

and kinetic parameters from [100, 2], fairly predict yields for gas, char and tar under fast pyrolysis conditions. But all these lumped models ((a) to (d)), make an inherent assumption that cellulose, hemicellulose and lignin undergo similar pyrolysis reactions. For cellulose and hemicellulose, the gas and char yields decrease with increase in temperature while for lignin the liquid and gas yields increase at the expense of char. Under fast pyrolysis conditions liquid and char formation is favored at low temperature while gas formation is preferred at high temperatures [67]. Such single component models are therefore, specific to a biomass, and experimental conditions employed. To overcome the variable biomass chemistry issue, kinetic models have been proposed for cellulose, hemicellulose and lignin. The effect of mineral matter on the kinetics of these three polymers is also published.

2.3.2.2 Multi-component multi reaction lumped models

Cellulose, hemicellulose and lignin polymer chemistry is significantly distinct. The mass fraction of each polymer in LCB can be quantified. Thus, LCB pyrolysis can be modeled by assuming that cellulose, hemicellulose and lignin independently undergo thermal degradation. Several cellulose pyrolysis models have been proposed in literature (Figure 2.5 (e) to (i)). Model (e) to (g) are lumped models to describe cellulose pyrolysis. Model (e) does not distinguish between char and gas and therefore can not be used to describe fast pyrolysis where gas yield increases at the expense of volatiles and char. Model (f), proposed by Shafizadeh in 1979, uses 'active cellulose' as an intermediate for the first time. However, it does not take into consideration secondary reactions and lumps liquid and gas components. Models (g) and (h) are modifications of the Shafizadeh model. The low temperature and slow char formation reaction is introduced based on experimental results reported in these articles [66, 59]. Mok and Antal [66] pointed out that the char yield was high in [6, 7] because of large sample size (100 to 250 mg) which led to significant volatile-solid secondary charring reactions. Further, Milosavljevic et.al. [59] reported that endothermic (0.54 kJ/g) tar vaporization is preferred at high heating rates over the exothermic (2 kJ/g) char formation reaction. They also observed that the rate limiting step for cellulose pyrolysis shifts from high

activation energy (218 kJ/mol) to low activation energy (140 kJ/mol) reaction beyond 320°C. The low temperature char formation is catalyzed by mineral matter. Formation of sugars and LMWC in models (g) and (h) is attributed to transglycosylation and fragmentation reaction. The selectivity for these reactions is not a strong function of temperature but of mineral content. In the presence of ash LVG yield drops significantly as comped to that of LMWC. Thus, models (g) and (h) can globally account for effect of temperature, heating rate, and mineral matter on yields of gas, char and liquid provided the kinetic parameters are optimized for sufficiently wide range of fast pyrolysis conditions.

2.3.2.3 Multi-component mechanistic reaction models

Models (i) to (k) are mechanistic models proposed by Prof. Ranzi's group to describe the pyrolysis reactions. Several modifications [101–103] have been made to the model after its initial publication [104, 105, 33] (Ranzi model). The model used in this work is the 2017 version [10], where reactions for trapped gases, extractive components, and effect of ash have been included. The primary pyrolysis reactions involve 50 species with (a) cellulose, (b)hemicellulose (xylan based for hardwood and agricultural residue, and glucomannan based for soft wood LCB), (c) oxygen (LIG-O), hydrogen (LIG-H), and carbon (LIG-C) rich lignin fractions, and (d) triglyceride and condensed tannins (extractive) as initial LCB components. All the reactions are first order Arrhenius type reactions. The other 42 species include bio-oil components (carbonyl, alcohol, furfural, phenol/phenol derivatives and small oxygenates) and permanent gases along with pseudo-components representing trapped gases. As LCB pyrolysis progresses through an intermediate liquid phase, release rate volatile/gas species can be hampered due to entrapment. Thus, out of the 29 primary pyrolysis reactions, 8 reactions describe the release of trapped gases using first order Arrhenius type reactions. The model does not account for the interactions between cellulose, hemicellulose and lignin. The lignin primary pyrolysis reaction model is a condensed version of detailed model proposed by Faravelli et.al.[92]. Secondary reactions of volatile species are modeled using 507 species and 20,239 reactions; and the files are available in the CHEMKIN format. Anca-Couce et. al. [93] proposed a modification to Ranzi's scheme by

introducing secondary charring reactions and validated the same with experimental results obtained for conventional/slow pyrolysis in fixed bed reactor [106]. Compared to original pyrolysis scheme of Ranzi et. al. [33] the modification improved the char, carbonyl and alcohol yield predictions but over predicted permanent gas yields. However, validation for fast pyrolysis, where liquid yield is maximum, has not been reported. Broadbelt et. al. [94, 95, 107] have proposed and experimentally validated a detailed mechanistic model for cellulose pyrolysis based on the results of molecular simulations for cellulose and glucose-based carbohydrates. The reaction model includes 342 primary pyrolysis reactions using 103 species that include intermediates, volatiles, permanent gases, and char. The model predictions of 11 major and minor species shows good agreement with fast pyrolysis experiments of cellulose and glucose-based carbohydrates carried out between 400 to 600°C. Similar molecular simulation studies and experimental validation is required to understand the pyrolysis of lignin and hemicellulose. Lignin is a complex heteropolymer and structural characterization of linkages and chemical functionalities is a challenge [108, 109]. To account for every lignin pyrolysis reaction knowledge of inter unit linkages and chemical group distribution is required. But, lack of such detailed structural information does not allow determination of intermediate species and therefore, some reactions and species need to be lumped. The β-O-4 (β-aryl ether) linkage commonly occurs in lignin and makes up about 60$\%$ of all the linkages in lignin. For this reason, Faravelli et. al. [92] used three model components LIG-C, LIGH, and LIG-O based on a β-O-4 skeleton to characterize the initial lignin structure. Distribution of methoxyl, aliphatic, and oxygenated side groups, in each model compound is different (for example, hardwoods contain more methoxyl groups than softwoods). Faravelli model has been verified using non-isothermal TGA data (heating rate: 20°C/min) for lignin derived form different biomass species. The model does not show a good agreement when compared with isothermal (550, 552, and 682 K) pyrolysis data for lignin. Currently, however, Ranzi model is the only model capable of predicting biomass pyrolysis oil composition.

2.3.2.4 Coal devolatilization model

Model (l) is based on model (m) (Figure 2.5) and stoichiometric coefficients are assigned to char and gases to distinguish them from one another. Model (m) is a scheme adopted by different coal devolatilization schemes, the functional group-depolymerization, vaporization, and cross-linking (FG-DVC) model [110, 111], bio-Flashchain [112], and bio chemical percolation devolatilization (CPD) [113, 12, 114, 115]. The FG model is used to describe the gas evolution and the elemental and functional group composition of tar and char. DVC model describes the evolution of tar and char through depolymerization, volatilization and cross-linking reactions [116]. The DVC model describes coal as aromatic clusters linked by weak and strong bridges. However, as coal and biomass are structurally very distinct, FG model is more relevant than DVC model. The release of CO, CO_2, H_2O, CH_4 and tar are modeled using evolution of FG, which are described with a distributed activation energy model (DAEM). Though the model provides precise time-evolution profiles of volatiles, the FG-DVC model is only applicable to the fuels the model was developed for [61]. In case of the BFC model, biomass is assumed to be composed of cellulose and lignin like structure. The term 'bridge' corresponds to monomeric units of cellulose or lignin. The bridges can undergo scission to produce smaller fragments released as tar, small condensible, and gases. Tar release is modeled using flash distillation analogy where the tar is assumed in vapor-liquid equilibrium. On the other hand, the bridges can also cross-link to form char. Like FG-DVC, the scission, condensation and char formation reactions are described using DAEM. Finally, CPD model assumes that LCB is composed cellulose, hemicellulose and lignin. LCB is assumed to be aromatic clusters connected with weak and strong bridges. The parameters that describe the structure and bridges are based on ^{13}C-NMR experiments and general structural characteristics of LCB. During pyrolysis the bridges undergo competitive scission and char formation reactions again described by DAEM. Percolation statistics describes the bridge breaking and size of fragments. Though the coal devolatilization kinetics provides good insight in the secondary charring reactions it leads to considerable ambiguity when applied to primary decomposition reactions of biomass.

2.3.2.5 Distributed activation energy model

An important feature of the coal devolatilization model is the use of DAEM to describe pyrolysis reactions. DAEM describes a rate process as a combination of probabilistic infinite parallel processes. The resistance/activation energy of each parallel process is described by an Arrhenius type equation. Activation energies are expressed using a probability distribution function. The contribution of each process, out of the infinite possibilities, to the overall rate is weighed by the associated probability of an activation energy value. Variation is activation energy of chemical reaction can be attributed to heterogeneity of molecular environment in a solid [117]. Multi-component DAEM has been employed in modeling biomass pyrolysis [118–120]. Multi-component DAEM defines the overall volatilization of biomass as a linear combination of weighted reaction rates, where the reaction of each component is described by DAEM. A detailed derivation of the DAEM equation can be found in Chapter 3. In case of LCB, the molecular chemical composition varies spatially. Therefore, activation energy for a particular reaction can vary depending on spatial location of the active site in LCB. For example, activation energy for cellulose fragmentation can be different when the active site is in vicinity of hemicellulose/lignin macromolecules when compared to an active site in vicinity of another cellulose chain. Also, presence/absence of mineral matter in LCB matrix can affect the activation of a reaction significantly. Thus, any one of the reaction described in mechanistic models can be described using DAEM to take into consideration the interaction between cellulose, hemicellulose, and lignin. Moreover, mechanistic models of lignin and hemicellulose are developed for lignin and hemicellulose extracted from LCB using acid/alkali pretreatments. These treatments lead to structural changes in lignin and hemicellulose. DAEM can thus, bridge such gaps when mechanistic models developed for cellulose, hemicellulose, and lignin are used to model pyrolysis of whole biomass. Further, the softening or melting behavior of LCB components is considerably different as demonstrated by Dufour et. al. [76, 121]. The softening/melting behavior of lignin, cellulose, and hemicellulose was reported as fraction of mobile protons present during pyrolysis using a ^{1}H-NMR in a temperature range of 150 to 450°C. Mobility of hydrogen begins in lignin (fluidity begins around 150°C and

reaches 100% between 200-225°C) and cellulose (fluidity begins around 250°C) before any mass loss while that in xylan begins after some initial degradation. The fluidity of cellulose and xylan reaches a maximum of 28% around 350°C, and 60% around 270°C respectively under a heating rate of 5 K/min. The fluidity drops after 350°C for lignin and cellulose as a result of cross-linking char forming reactions. For xylan the fluidity drops after 270°C and becomes constant at 20% thereafter. However, for the biomass- Miscanthus, the softening begins at 200°C against 150°C for isolated lignin. Moreover, the maximum fluidity achieved is 42% which is much lower than that for lignin and xylan. The high mobility for xylan and lignin is a result of reduction in molecular weight during their isolation from LCB. The low mobility in native LCB also suggests strong interaction between the three macromolecules. Presence of molten phase gives biomass viscoelastic properties which change with temperature and depend on the heating rate employed in pyrolysis. Therefore, models that describe the complex chemistry and account for the effect of morphological changes on reaction rates can accurately simulate pyrolysis process.

2.3.2.6 Experimental parameters for pyrolysis kinetics

The accuracy of a kinetic model depends on how well the model captures different processes occurring during pyrolysis; and the value of model parameters. Commonly used apparatus for determining kinetic parameters are thermo-gravimetric analyzer (TGA), TGA-FTIR, TGA-MS, wire mesh reactor, isothermal micro-pyrolyzer (Pyroprobe)/drop tube reactor coupled with GC-MS, isothermal entrained flow reactor, isothermal fixed bed reactor, and tube furnace. Sample type, sample weight, sample particle size, heating rate, and reactor temperature affect the value of kinetic parameters [67, 122, 123, 61]. The TGA data of biomass pyrolysis reported in literature uses heating rates between 2 to 150°C/min, sample size between 1 mg to 300 mg, and minimum and maximum particle sizes of 40 and 2000 μm [67, 124, 78, 91]. On the other hand the heating rate in wire mesh reactor and micro-pyrolyzer can be as high as 10000 °C/s with sample weight of the order of 0.1 mg and particle size less than 40 μm [62, 122, 123, 23]. Sample weight and particle size are chosen to avoid intra-particle heat and mass transfer limitations. To

determine if the reactions are kinetically limited, dimensionless Biot (Bi) 2.1 and pyrolysis numbers (Py) Eq.(2.2) and Eq.(2.3) are calculated. Py^I is the ratio of reaction and conduction time scales, Py^{II} is the ratio of reaction and convection time scales, and Bi is the ratio of conduction and convection time scales. Py^{III} (Eq.(2.4) ratio of conductive heat transport to reaction heat generation/consumption) and Py^{IV} (Eq.(2.5) ratio of convective heat transport to reaction heat generation/consumption) were defined in [13] to evaluate the effect of the heat of reaction on the intra particle temperature gradients.

$$Bi = \frac{hL}{\lambda} \tag{2.1}$$

$$Py^I = \frac{\lambda}{\rho C_p L^2 k_{py}} \tag{2.2}$$

$$Py^{II} = \frac{h}{\rho C_p L k_{py}} \tag{2.3}$$

$$Py^{III} = \frac{\lambda(T_\infty - T_0)}{\rho L^2 k_{py} \Delta H} \tag{2.4}$$

$$Py^{IV} = \frac{h(T_\infty - T_0)}{\rho L k_{py} \Delta H} \tag{2.5}$$

The external heat transfer coefficient, thermal conductivity, density, pyrolysis reaction rate, and heat capacity of biomass are represented by h, λ, ρ, k_{py}, and C_p, respectively; T_∞ and T_0 are the external bulk temperature of the reactor environment and initial temperature respectively. Biomass particle size in Figure 2.6 and 2.7 is Feret diameter of the particle. Feret diameter is defined as longest distance between pair of parallel lines tangent to the largest projected particle outline. Biomass particle is like a rectangular parallelepiped with smooth corners. Therefore, Feret diameter is equal to the length of the diagonal joining two edges along the length of biomass particle. Wiggins et.al. [13] used realistic biomass

particle CAD geometry to model intra-particle thermal gradients. The volume and surface area of particles with different Feret diameter are used to determine the characteristic length for calculating different dimensionless numbers. Figure 2.6 shows the reaction-transport regime map for different particle sizes under for three values of external heat transfer coefficients. Values of heat transfer coefficients used are typically achieved in TGA ($\sim$35 W/m^{2}K), fluidized bed reactor ($\sim$350 W/m^{2}K) [125], and micro-pyrolyzers ($\sim$3500 W/m^{2}K) [73]. It is important to note that values of reaction rate, heat transfer coefficient, and characteristic length can significantly affect the estimation of reaction regime. Endothermic and exothermic regions in Figure 2.7 (a) and (b) correspond the hypothetical case where pyrolysis reactions are either completely endothermic (only depolymerization reactions) or completely exothermic (only charring and cracking reactions). Assuming that the particle is at 573 K and the external temperature is 773 K, values of Py^{III} and Py^{IV} decrease with increase in particle size even for Bi < 1. This indicates that internal temperature gradients may exist within a particle as a result of heat of pyrolysis reaction. It is also important to note that biomass particle undergoes prominent expansion and shrinkage which affects the characteristic length of the particle and hence pyrolysis number. However, the regime diagram, Py^{III}, and Py^{IV} facilitate an estimate of particle size for conducting experiments in the kinetically controlled and isothermal regime. Using different apparatus experiments can be carried out over a wide range of heating rates. It is necessary to ensure that appropriate sample particle size and sample weight are chosen.

TGA and wire mesh reactor can monitor weight loss as temperature increases. The reactors can be coupled with FTIR or GC-MS to characterize the pyrolysis products. TGA apparatus is more sensitive and accurate than the current wire mesh reactors; but heating rates do not exceed 500°C/min, which is much less than heating rates employed under fast pyrolysis. Micro-pyrolyzers are operated under isothermal conditions and biomass heats up to the reactor temperature very rapidly. The products are then quantified continuously using GC-MS. However, biomass can not be heated to high temperature without passing through low temperature. Biomass starts to degrade generally around 200°C and fast pyrolysis temperature is $\sim$500°C. Therefore, the kinetic model and parameters should

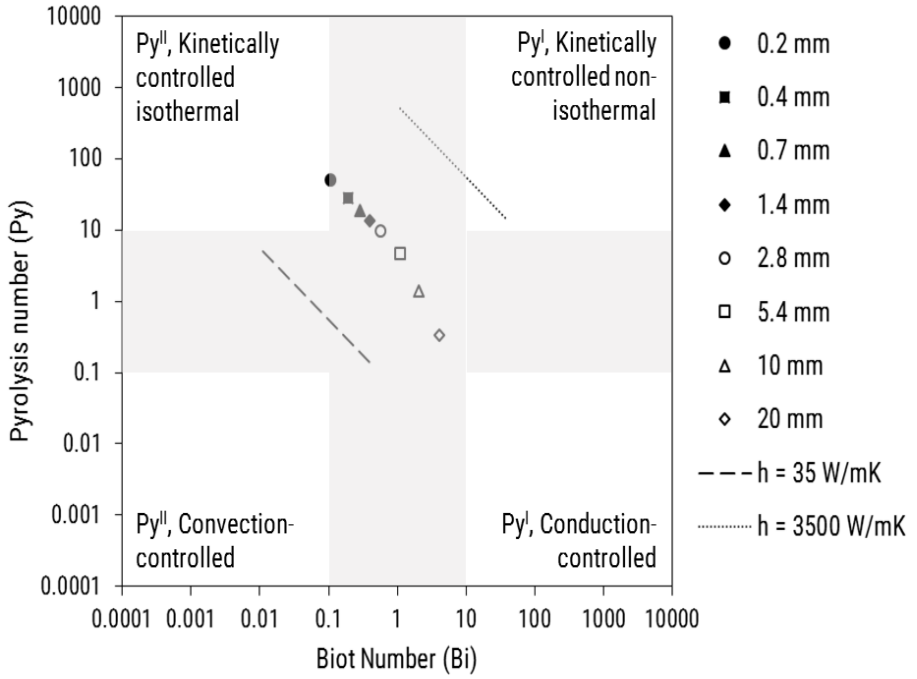

Figure 2.6: Reaction-transport process regime map calculated with h = 35, 350, and 3500 W/m^{2}K, λ = 0.16 W/mK, ρ = 720 kg/m^3, and C_p = 103.1 + 3.867T (J/kgK), k = 0.0622 s^{-1} (at T = 773 K) (figure adapted from [13]).

be capable of explaining the behavior of biomass in non-isothermal region along with final yields of pyrolysis product composition.

Pyrolysis reaction kinetics is a strong function of biomass type, heating rate and temperature. Selectivity of reactions changes with respect to heating rate. Cross-linking and depolymerization reactions happen in the intermediate liquid. At low heating rates the liquid/viscoelastic character of biomass particle may be lost due to high selectivity for charring reactions. On the other hand, at high heating rates, vapors might accumulate and form bubbles like that in a viscous boiling liquid. Though the shape of the biomass particle is maintained during pyrolysis, the pore structure may change significantly which can significantly affect volatilization rate. Thus, whether kinetics obtained at low heating rates can be applied at high heating rates is a question.

2.4 Fast pyrolysis reactors

As discussed in section 2.3.2 char formation reactions are triggered at low temperatures and char yield increases if biomass particle spends more time at low

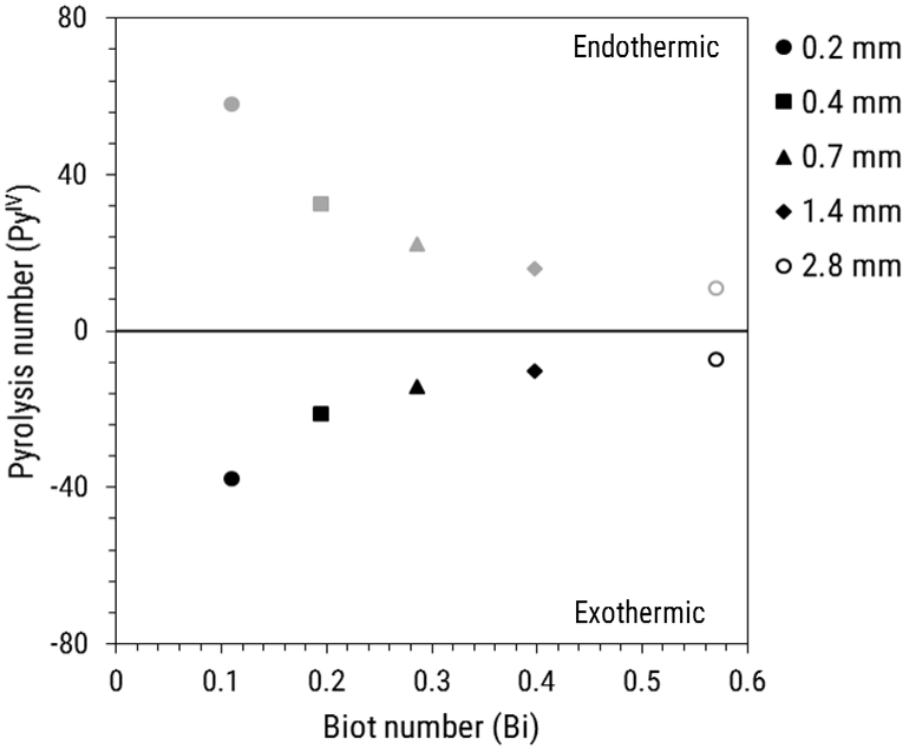

(a)

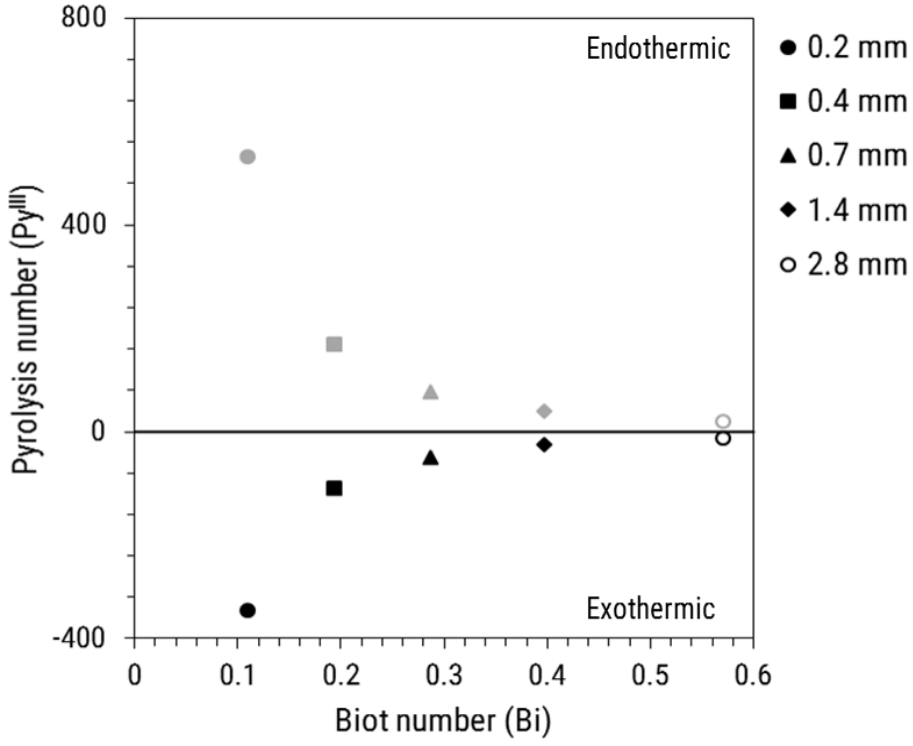

(b)

Figure 2.7: (a) and (b) Plots for Py^{III} and Py^{IV} with respect to Bi for T_∞ = 773 K, T_0 = 573 K, ΔH_{endo} = 540kJ/kg, and ΔH_{exo} = -2000kJ/kg. The particle dimension is the Ferret diameter and it has been used in [13].

temperature than at high temperature. On the other hand if the generated pyrolysis vapors spend more time at high temperature secondary charring and cracking reactions reduce the liquid yield. Therefore, a fast pyrolysis reactor should ensure (a) rapid heat transfer to biomass particle and (b) low vapor residence time, to maximize the bio-oil yield. Different reactor configurations are shown in Figure 2.8. In practice, high external medium-to-solid heat transfer rates are required (approximately >400-500 W/m^{2}K); intra-particle biomass heat transfer limitation should be avoided (requiring particles <2-3 mm to limit the heat penetration depth); and vapor phase residence times should be kept below a few seconds in order to maintain the oil yield. Other than vapor residence time, oil composition can be modified by process conditions, equipment dimensions, and the application of catalysis.

2.4.1 Rotating cone reactor

In rotating cone reactor (RCR), heat carrier particles (hot sand) and biomass particles are transported to the bottom of a conical bed Figure 2.8 (a). Centrifugal force created by the rotating cone pushes the solid particles outwards. This movement causes mixing of sand and biomass particles and brings the solids in contact with heated cone surface. Generated pyrolysis vapors travel outwards towards the condenser while the solid particles spill over top of the cone. Sand particles are heated by char combustion and also reheated before recirculating in the reactor [126]. Typical conditions of RCR are, hot sand at 500°C and cone rotation of 300 rpm with bio-oil yield of approximately 70 wt.%. The heat transfer coefficients for rotating cone reactor are found to be of the order of 500 to 1000 W/m^{2}K, which is high when compared to gas/solid contactors [127]. Biomass Technology Group- Biomass to Liquid (BTG-BTL) supplied a 2 tons/hr demonstration unit to Malaysia for converting empty fruit bunch to bio-oil in year 2004. 1000 tons of bio-oil has been produced using 5000 tons of wet biomass (70 wt.% moisture). Another BTG-BTL facility constructed by Empyro BV in 2014 converts 5 tons/hr of biomass into oil (3.2 tons/hr), process steam and electricity [128, 129].

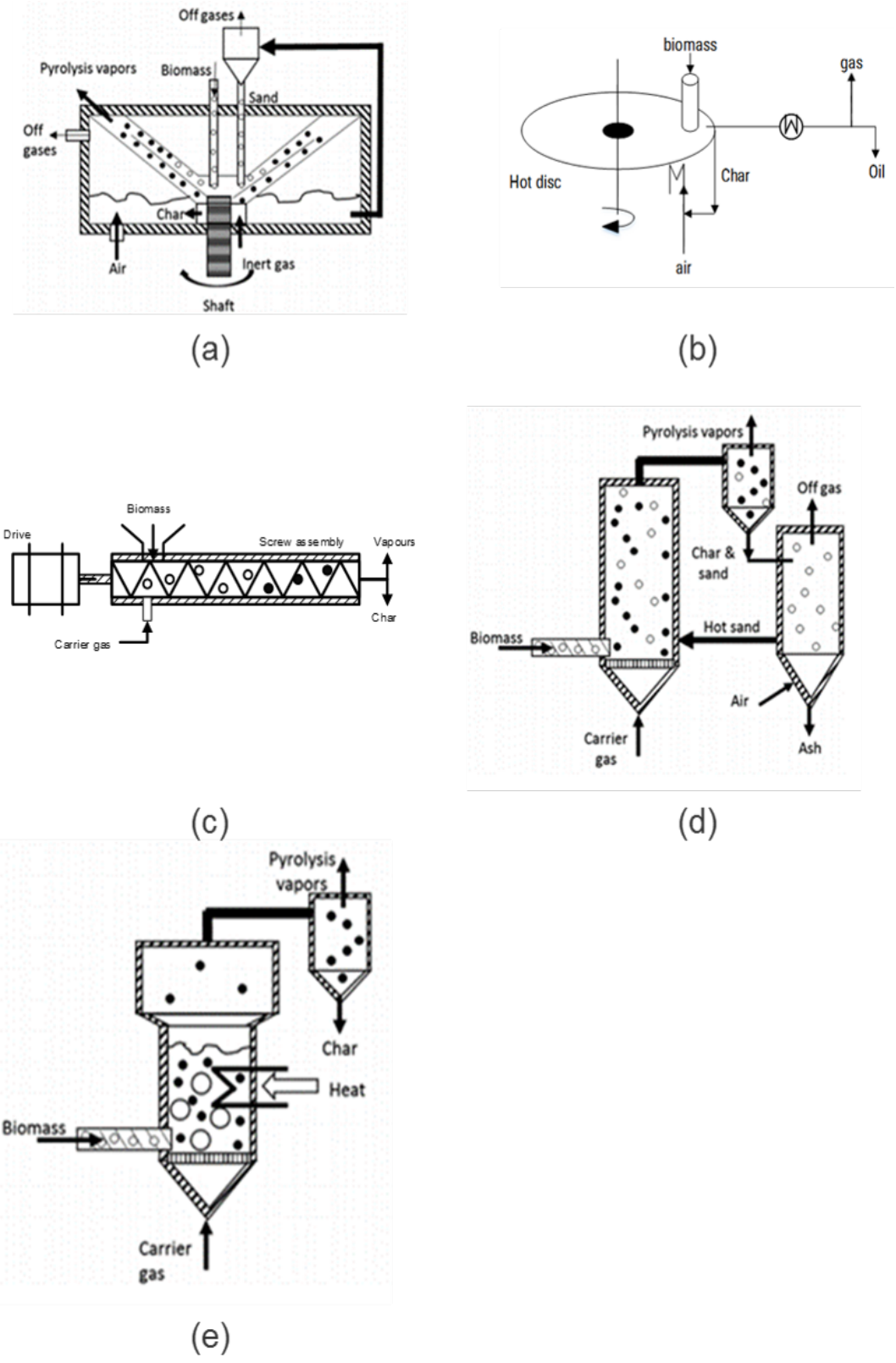

Figure 2.8: Fast pyrolysis reactor configurations (a) Rotating cone ablative reactor; (b) Ablative reactor; (c) Auger reactor; (d) Circulating fluidized bed reactor; (e) Bubbling fluidized bed reactor.

2.4.2 Ablative reactor

In ablative pyrolysis reactor biomass is heated by pressing it against a rotating hot disc. Pyrolysis of the biomass forms a oily layer on the disc which evaporates and the vapors are condensed to recover bio-oil. Char produced is combusted which heats the rotating disc [130]. Rate of reaction depends the pressure exerted on biomass in contact with hot surface and available heat transfer area [131]. An important feature of the ablative process is that biomass undergoes ablation when it is contacted with the hot surface. As biomass is pyrolyzed, new biomass surface is exposed to the heated surface. Therefore, biomass particle size does not affect the pyrolysis behavior and yield of products [132]. The limiting factor for biomass pyrolysis is rate of heat transfer to the hot surface. Though the ablative reactors can be compact, require small volume of condensers, and reduces biomass milling efforts, the following disadvantages limit the scale up of ablative reactors: (a) Heat transfer is limited because hot surface, which is roughly at 500°C, is heated indirectly by combustion gases at 800°C. Electric heating to compensate for heating requirement can limit the scale up of ablative reactors, (b) restriction on biomass particle shape to ensure its free flow since the biomass needs to be pressed against hot surface [129]. A pilot scale ablative reactor (6 tons/day, biomass particle size 60mm x 40mm x 5mm) designed by PyTec, Germany is operating and combusting produced oil to run 300 MW_e diesel engine [15].

2.4.3 Auger reactor

Biomass undergoes pyrolysis inside a heated tube and is transported through the length of the tube by a screw [133]. Carrier or inert gas is fed into the biomass hopper to avoid oxidation reaction and also provide a positive pressure to transport the vapors out of the reactor towards the condenser system. Sand can be used as a heat carrier and heat transfer to the biomass particles takes place by intimate contact with a heat carrier. The external surface of the tube can also be heated to maintain the heating required for pyrolysis. The vapor residence time inside the auger reactor is of the order of 5 to 30 s [126]. The oil yield in auger reactor is between 48-62 wt.%, which is less than fluid bed reactor. Moreover,

water formation is enhanced (30 to 55 wt.% of bio-oil) as a result of long contact time between char and pyrolysis vapors [131]. Renewable Oil International, USA and AbriTech, Canada [134] have installed auger reactors with 24 tons/day and 50 tons/day capacity respectively. However, the current status of these plants is unknown.

2.4.4 Circulating fluidized bed reactor

Bio-oil yield between 54 and 71 wt.% can be achieved using circulating fluidized bed (CFB) reactor [135, 136]. Biomass is fed into a riser or fast fluidization section, where extensive contacting between inert particles (sand) and biomass takes place. Char and sand both are entrained out of the reactor, and circulated to the regenerator where the char and coke formed on the sand is combusted. The sand is reheated as a result of char combustion. CFB technology is widely used in the petroleum industry for FCC process and the technology is well understood [137]. However, similar to fluid bed technology, large amounts of gas needed for fluidization/recirculation of the reactor should be the non-condensible part of the pyrolysis gas. Finally, to obtain a solid flux between 100 to 200 kg/m^{2}s, a gas flow rate of the order of 1000 m^3/hr (ton/hr biomass) needs to be employed [135]. Such a huge volume of non-condensible gas needs to be cooled to very low temperatures to maximize bio-oil recovery and reheated again before it is fed to the reactor. Ensyn has installed a 2 and 150 tons/day CFB in Canada, and VTT/Valment has installed a 15 (year 2009, pilot plant) and 274 (year 2013, commercial demonstration plant) tons/day CFB in Finland. Ensyn plant in Ontario has a production capacity of 11 million litre/annum of bio-oil. The bio-oil produced in the VTT/Valment commercial demonstration plant has a heating value of 13-18 MJ/kg, 20-35 wt.% water and a pH of 2-3. The oil is used in Fortum's heat and power plant in Joensuu, Finland. All these facilities are currently operational.

2.4.5 Bubbling fluidized bed reactor

Bubbling fluidized bed reactor technology is well understood and is simple in construction and operation compared to other reactors. Sand is used as a heat carrier and is fluidized using inert gases. When the gas velocity exceeds 2 to 3 times

that of the minimum fluidization velocity, gas accumulates as bubbles and travels through the fluidizing sand bed. Formation of bubbles causes solids to circulate within the bed, thus, providing mixing. Biomass particles are generally fed from the side into a heated bubbling bed [138]. The high solid density of bed material and vigorous mixing induced by bubbles ensure rapid heat transfer to biomass particles and facilitate good temperature control. Literature suggests that 2 to 3 mm of particle size is required to attain high heat transfer rates but some studies show that a particle size of approximately 0.5 mm is required to avoid retention of aerosols inside the particles and achieve high heating rates [82, 83]. Typical yield of bio-oil is between 35 to 69 wt.% for grasses or agricultural residue, 59 to 79 wt.% for softwood, and 59 to 77 wt.% for hardwood [131]. Vapor and solid residence time ($\sim$1 to 4 s) is controlled by the fluidizing gas flow rate and is higher for char than for vapors. Char acts as an effective vapor cracking catalyst at fast pyrolysis reaction temperatures, thus, rapid separation of char and pyrolysis vapor is essential to avoid bio-oil reduction. Fluidizing gas velocity is adjusted such that it can entrain char particles from the bubbling bed. However, One severe limitation of bubbling fluidized bed reactor is that rate of particle heating in the bed is usually the rate limiting step. It becomes significant for large scale reactors. Heating is generally achieved by combustion of pyrolysis gases and char and typically transferred to the bed by internal coils and externally heating the fluidizing gas. A coil with surface area of 10 to 20 m^2 is required to convert 1 ton/hr of biomass under fast pyrolysis conditions [135]. In 2000s DynaMotive installed 100 and 200 tons/day bubbling fluidized bed reactor in West Lorne and Guelph, Canada which started operating in 2005 and 2006. However, due to construction and operational issues the plants did not operate for very long [135].

Figure 2.9 (a) shows the comparison of different reactor configurations in terms of technology strength and market attractiveness, and Figure 2.9 (b) shows the current status of technology readiness for commercialization. Ensyn's RTP and BTG's RCR technologies are used currently at commercial scale. But, bio-oil obtained from commercially facilities has been primarily used for combustion or is upgraded via hydrogenation for energy applications. Recently, it is shown that fractionating bio-oil into individual chemical families can improve bio-oil stabil-

ity, facilitate efficient upgradation, and also assist in recovery value added chemicals from bio-oil. Using a fraction of bio-oil as a source of value added chemicals makes pyrolysis more attractive. However, to achieve this objective it is essential to predict pyrolysis vapor composition exiting the reactor so that downstream operations can be designed and operated as required. As a result, one part of this research focuses on coupling reactor hydrodynamics with detailed pyrolysis kinetics to predict the bio-oil composition.

2.5 Fast pyrolysis bio-oil

Fast pyrolysis vapor when rapidly quenched forms a condensate, often called bio-oil. Bio-oil is a complex mixture of several hundred compounds [29–31] formed as a result of rapid depolymerization and fragmentation of cellulose, hemicellulose, and lignin. The compounds belong to a wide spectrum of chemical functionalities namely, carboxylic acid, aldehyde, ketone, furan, carbohydrate and phenol. The molecular weight of the compounds varies between 60 to 10000 g/mol (formed as a consequence of aerosol ejection) [139], depending on heating rate, temperature, mineral content, and catalyst. Bio-oil instability is attributed to high oxygen content and presence of diverse chemical functionalities. The components undergo condensation polymerization reactions which are accelerated on exposure to heat. As a result, bio-oil viscosity increases with time and can also form separate aqueous and organic phases[140]. Unstable nature of bio-oil puts limitation on its direct applications. However, chemical and/or physical upgradation techniques can be used to produce fuel, fuel pre-cursors, intermediates, and chemicals. The choice and efficiency of upgradation technique thus, strongly relies on knowledge of bio-oil composition and characteristics.

2.5.1 Physical and chemical properties of bio-oil

Bio-oil characteristics for different biomass species are tabulated in 2.3 and compared with mineral oil properties. Substantial amount of water (biomass moisture and water of reaction) is present in bio-oil. The water content can be as high are 50 wt.% for agricultural residues [141] due to high ash content when compared to

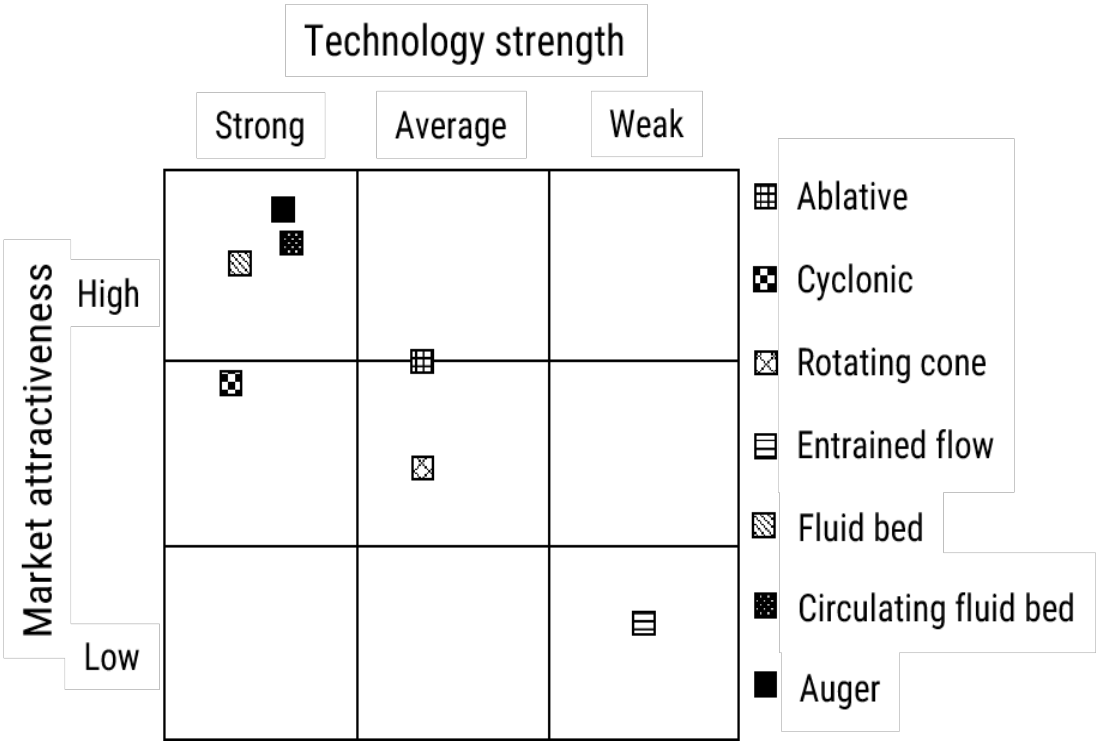

(a)

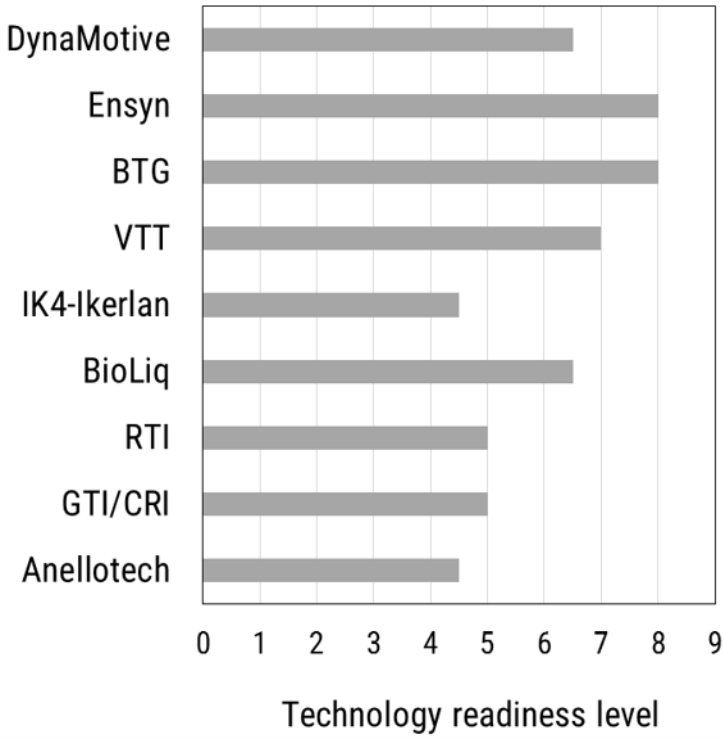

(b)

Figure 2.9: (a) Assessment of fast pyrolysis reactor technologies for commercial applications[14], (b) Technology readiness level of different pyrolysis technologies[15].

forest residues. Water content lowers the calorific value of bio-oil and delays ignition when compared to mineral oil. Acidic pH of bio-oil poses challenges for its storage and combustion applications. Bio-oil consists of polar oxygenated compounds which reduce its miscibility with hydrocarbon fuels. High oxygen ratio also lowers the heating value and causes instability in pyrolysis oil. Bio-oil undergoes aging through several reactions that occur amongst several hundred oxygenated compounds with some chemical functionalities acting as catalysts for aging reactions [142].

Table 2.3: Bio-oil characteristics as compared to mineral oil

	Pyrolysis liquid				Mineral oil
Property	Birch	Pine	Poplar	Range	
Solids (wt.%)	0.06	0.03	0.045	0.01-1	
pH	2.5	2.4	2.8	2.0-3.7	
Water (wt.%)	18.9	17.0	18.9	15-30	0.025
Density (kg/m^3)	1.25	1.24	1.2	1.1-1.3	0.89
Viscosity, cSt (50°C)	28.0	28.0	13.5	13-80	6
LHV (MJ/kg)	16.5	17.2	17.4	13-18	40.3
Ash (wt.%)	0.004	0.03	0.01	0.004-0.3	0.01
C (wt.%)	44.0	45.7	46.5	32-49	
H (wt.%)	6.9	7.0	7.2	6.9-8.6	
O (wt.%)	49.0	47.0	46.1	44-60	0
S (wt.%)	0	0.02	0.02	0-0.05	0.2
Flash point (°C)	62	95	64	50-100	60
Pour point (°C)	-24	-19		-36 to -9	-15

Bio-oil components can be broadly classified into water soluble (WS) and water insoluble (WIS) fractions. WIS fraction mainly comprises of pyrolytic lignin and lignin monomers, while WS fraction contains low molecular weight compounds like sugars, carboxylic acids, aldehydes, and ketones [143]. The proportion of these fraction changes based on the biomass feedstock and reaction conditions. Table 2.4 shows the detailed bio-oil composition of three different biomass species. WS and WIS fractions undergo different aging reactions. WIS fraction result in the formation of sticky gum like structure and cause phase separation in bio-oil [144, 145]. On the other hand the WS fraction undergoes degradation followed by polymerization reactions to form brown solids [146]. Components of WS and WIS also interact with one another to promote condensation reactions in bio-oil. Carbonyl compounds are the most reactive species present in bio-oil [147]. C-C

bond formation between lignin oligomers can be catalyzed by acids. Aldehydes like formaldehyde can condense with pyrolytic lignin in presence of carboxylic acids to form cross-linked polymers. Sugar dehydration in presence of acids results in formation of reactive furfural derivatives and levulinic acid which can self condense or react with one another to form humins [148]. Acids also trigger self polymerization and aldol condensation reactions in aldehydes to form oligomers and polymers. As a result of several polymerization reactions, molecular weight of bio-oil increases gradually with time making bio-oil useless. Thus, bio-oil as a mixture is unstable and unsuitable for many applications; and bio-oil upgradation or processing is essential.

Table 2.4: Bio-oil composition for three biomass species. Composition is represented as wt.% of organic fraction of bio-oil. Water content (wt.% dry biomass) for (a) rice straw: 22.18; eucalyptus wood: 18; pine wood: 8.32

Compounds	Rice straw [149]	Eucalyptus wood [150]	Pine wood [151]
Anhydro Sugars			
Levoglucosan	0.7	14.75	14.20
Carboxylic acids			
Acetic acid	3.16	13.02	
Propanoic acid	0.86	4.14	
2-Oxopropanoic acid	2.51		
4-Oxopentanoic acid	1.21		
propenoic acid-3(4-hydroy-3-methoxyphenyl-)		2.25	
oleic acid			0.39
3,4-dimethylbenzoic acid			0.09
Ketones			
1-hydroxy-2-Propanone*	1.21	4.91	
2-Butanone	1.3		
1,3-Cyclopentanedione	2.45		

Table 2.4 continued from previous page

Compounds	Rice straw [149]	Eucalyptus wood [150]	Pine wood [151]
2-Hydroxy-3-methyl-2-cyclopentenone	1.22		
Cyclopentanone		0.27	
3-methyl-1,2-Cyclopentanedione		0.09	1.00
methyl-2-Cyclopentene-1-one			0.29
1-(4-hydroxy-3-methoxyphenyl) Ethanone			0.16
Aldehydes			
Formaldehyde	0.42		
Hydroxy acealdehyde		8.43	
Butanedial	1.1		
Ethers			
2,2,4-Trimethyl-1,3-dioxalane	2.06		
2,2-dimethoxy propane		1.34	
Furans			
Coumaran	3.08		

Table 2.4 continued from previous page

Compounds	Rice straw [149]	Eucalyptus wood [150]	Pine wood [151]
Furfural		0.75	0.47
5- Methylfurfural			0.1
Furfuryl alcohol		0.05	
2,5-dimethoxy Tetrahydro furan		1.43	
2(5H)-Furanone		0.07	
4-Methyl-5H-furan-2-one			
5-Methyl-2(5H)-furanone		0.16	
2-(3H)-furanone,dihydro-3-hydroxy-4,4-dimethyl-		0.16	
2-furanethanol, methoxy		1.59	
5-Hydroxymethyl furfural			0.01
Phenols			
Phenol	0.99	1.30	0.77
Cresols	2.35	0.16	1.08
Dimethylphenols	3.34		0.29

Table 2.4 continued from previous page

Compounds	Rice straw [149]	Eucalyptus wood [150]	Pine wood [151]
Guaiacol	0.79	0.27	0.39
Methylguiacols	0.83	0.11	0.54
Eugenols	0.39	1.16	0.81
Benzenediol	1.28		
Methylbenzenediols	1.63		3.09
Vanillins		3.32	0.24
2,5-dimethoxy-4-ethyl benzaldehyde		0.70	
Syringaldehyde		2.64	
4-Allylsyringol		2.20	
Hydroquinone		0.20	
Aromatics			
Stilbene		0.27	
Polyaromatics			0.02
Naphthalene			0.02

Table 2.4 continued from previous page

Compounds	Rice straw [149]	Eucalyptus wood [150]	Pine wood [151]
Sulphur compounds			
diBenzothiophene		0.39	
Unidentified	**9.59**	**33.86**	**58.32**
Total Individual compounds	**35.18**	**66.14**	**41.68**

2.5.2 Catalytic upgradation of bio-oil

Pyrolysis oil can be upgraded using several chemical and physical processes like catalytic deoxygenation/ hydro-deoxygenation (HDO), cracking/ hydro-cracking, esterification, steam reforming, gasification, fractionation, and emulsification. Catalytic upgrading mainly removal of oxygen from bio-oil and converting the reactive species into stable compounds, to improve bio-oil shelf life. Zeolites and metal ion impregnated zeolites are generally used as catalysts for cracking or hydro-cracking reactions. These reactions are carried out at temperatures ranging from 300 to 600°C, and in presence/absence of hydrogen [152, 126]. The main products are oxygen devoid aromatic compounds and light hydrocarbon gases. HDO employs supported catalysts like $Pt/Al_2O_3/SiO_2$, Rh/ZrO_2, $CoMoS_2/Al_2O_3$, and $NiMoS_2/Al_2O_3$ [153, 154] under pressures of 75 to 300 bar and temperatures of 250 to 400°C. However, any catalyst is selective to one or two chemical functionalities, the non-selective components tend to degrade to gases or lead to coke formation, thus, decreasing the liquid yield and deactivating the catalyst [47]. For zeolite upgrading and HDO, coke formation is a pronounced problem. Formation of catalytic coke is attributed to accumulation, and polymerization and polycondensation of high molecular weight aromatic moieties of bio-oil on catalyst surface[152]. Compounds that have more than one oxygen atom appear to have a higher affinity for carbon formation [155]. Further, typical liquid yields after zeolite and HDO upgradation are 12-28 and 21-65 wt.% of bio-oil feed respectively. Other catalytic upgrading techniques involve ketonization, condensation, hydrogenation of carbonyl group, and hydrogenation of furanyl rings. However, these techniques are very selective and often catalyst suffer from poisoning and deactivation due to the presence of non-selective components [47]. Therefore, employing bio-oil as a mixture to upgradation leads to undesirable carbon loss.

2.5.3 Fractional condensation of pyrolysis vapors

To address bio-oil instability and storage issues, pyrolysis oil is collected in multiple condensers to concentrate bio-oil fractions having different physical and chemical properties [156, 157, 20, 26, 19, 158, 159]. Results of multi-stage conden-

sation systems are tabulated in Table 2.5. Bio-oil components have a wide range of molecular weight and boiling point. The condenser temperature, residence time of vapors and carrier gas velocity affect liquid recovery and aerosol carry-over. Series of indirect and direct contact heat exchangers and, electrostatic precipitators (ESP) are widely used for stage-wise condensation of pyrolysis vapors.

Figure 2.10 shows the composition of liquid collected in different stages of various condensation systems. Single and multi-stage molecular distillation result in 70 to 80% of water being distilled out in the first stage. Single stage distillation better separates carbonyl compounds and acids from phenol derivatives and sugars. Acids get concentrated in light fraction for single stage molecular distillation (Figure 2.10 (a)) while they are distributed approximately evenly in all fractions as shown in Figure 2.10 (b). The second strategy opted to improve bio-oil combustion and storage characteristics is fractionally condensing pyrolysis vapors in multiple condensers (Figure 2.10 (c) to (f)). The standard condensation scheme employed is a train of indirect contact heat exchangers. Factors affecting condensation of chemical families are condenser temperature, proportion of non-condensible gases, partial pressure of a component, and vapor-liquid interaction amongst different species. Use of multiple stages and low condenser temperatures does not allow separation amongst chemical families (Table 2.5, fractionation system no. 3, 6, 7, 8). Partial pressure of components can be altered to enhance the separation amongst chemical families/compounds by altering the amount of carrier/sweeping gas flow rate [160]. However, increasing the carrier gas flow rate can increase aerosols carry over. Aerosol carry over is significant when bubbling fluidized bed reactors are used for pyrolysis. Presence of sugars and pyrolytic lignin in stage 2 and 3 (Figure 2.10 (c)) is evidence of significant aerosol carry over. Therefore, ESP's are used to capture the fine droplets. Spray towers/ direct contact condensers are used to quench pyrolysis vapors to avoid secondary reactions thus, maximizing bio-oil recovery (Figure 2.10 (e)). Studies of multi-stage condensation have only focused on separating water and acids from rest of the organic components of bio-oil to improve its stability and combustion properties. Effective separation amongst chemical families is not achieved in reported condensation schemes. Westerhof et.al. [156] studied the effect of

Table 2.5: Summary of bio-oil fractionation systems

Fractionation system	Reaction conditions	Fractionation system operating conditions	Outlet vapor temperature	Outcomes	Reference
Single stage molecular distillation	Reactor: 1 kg/hr bubbling fluidized bed, 450 to 500°C	Pressure: 60 Pa, evaporator temperature: 70°C, cooling jacket: 20°C. Fraction remaining in the evaporator is heavy cut; fraction collected at 20°C is medium cut; and fraction not condensed at 20°C is the light cut		Bio-oil recovery is close to 85%. Light fraction is mostly water with high acidity and least stability.Though more than 70% of acids, aldehydes, ketones, phenols and guaiacols from whole bio-oil are present in light fraction, molecular distillation does not allow effective separation amongst chemical families in single stage.	[16]
Multi-stage molecular distillation	Reactor: 5 kg/hr bubbling fluidized bed, 500°C	Stage 1: Pressure: 1600 Pa, evaporator temperature: 80°C, cooling jacket: 20°C; this fraction is light cut. Stage 2: Pressure: 340 Pa, evaporator temperature: 80°C, cooling jacket: 20°C; distillate is medium and residue is the heavy cut.		Bio-oil recovery is close to 91%. Trace amounts of acetic and formic acid are present in residue. New compounds like 3,5-dimethoxy-4-hydroxyphenylacetic acid and benzoic acid were discovered in the bio oil. Ketones, ethers and furans show similar distillation properties as that of acids. Phenol and alkyl phenols are easily distilled present in light cut. However, cathecols and alkyl cathecols were difficult to distill even in second stage.	[17]
Two double pipe heat exchangers in series	Biomass: Wheat straw and beech wood; Reactor: 1.5 kg/hr Fluidized bed	First condenser: NR; Second condenser: NR	First condenser: Air condenser with gas outlet at 90°C; Second condenser: Cooling water with gas outlet 25^0C	Aerosols form a considerable fraction of bio-oil. Mineral matter is concentrated in the char particles. Trace amount of mineral matter in bio-oil is a consequence of aerosols.	[161]
Two-stage counter-current spray towers followed by cooler	Reactor: 20 kg/hr bubbling fluidized bed reactor	Scrubber 1: ; Scrubber 2: NR; Cooler: NR	Scrubber 1: 66°C; Scrubber 2: NR; Cooler: NR	A substantial amount of water and acids get collected in the cooler. But bio-oil in the scrubbers still has pH 3.	[20]
Two-stage counter-current spray towers followed by cooler	Reactor: 1 kg/hr bubbling fluidized bed reactor	Scrubber 1: 20 to 115°C ; Scrubber 2: 20°C; Cooler: NR	Scrubber 1: NR; Scrubber 2: NR; Cooler: 0°C	More than 90% of water and light organics are collected in stage two when scrubber 1 is operated between 70 to 90°C. Acetic acid content in stage 2 reaches 10 wt.%. However, pH of stage 1 and 2 liquid is between 2 to 3.	[156]
Three stage cyclonic condensers and ESP in series	Biomass: Birch bark; Reactor: Bubbling fluidized bed	First condenser: 80°C; ESP:30 to 70°C; Third condenser: 0°C	First condenser: 105°C; ESP:38 to 56°C; Third condenser: <15°C	Bio-oil fraction from first A substantial stage has very low water content (∼0.9wt.%) when first condenser and ESP are operated at 70°C. However, acid distribution is not reported.	[162]
Three indirect contact heat exchangers in series	Biomass: Pine wood; Recactor: Auger 8 kg/hr	First condenser: 85 to 90°C; Second condenser: 45 to 50°C; Third condenser: 10 to 15°C	First condenser: 121 to 132°C; Second condenser: 107 to 116°C; Third condenser:<25°C	Sweeping gas amount alters the dew point of the components and affects bio-oil fractionation behavior. Gas flow rates used in the study do not decrease bio-oil yield.	[160]
Sieve plate column, ESP, and jacketed cooler	Reactor : Bubbling fluidized bed	Sieve plate column: NR ; ESP: 20°C, 15kV; Glycol cooler: NR	Sieve plate column: 47 and 87°C; ESP: NR; Glycol cooler: 5 to 10 °C	High temperature in sieve plate column reduces water content.	[20]
Four selective condensers	Reactor: 0.13 kg/hr Fluidized bed	First condenser: 300°C; Second condenser: 100°C; Third condenser: 0°C; Fourth condenser: -20°C		Bio-oil obtained from first condenser has no moisture, and stage two fraction has a pH of ∼5.1. Presence of compounds like p-cresol (B.Pt. 202°C) and 4-methyl guaiacol (B.Pt.221°C) in first condenser shows affinity of such compounds to sugars and high molecular weight lignins. Effective separation achieved between aliphatic carbonyl and phenol compounds	[19]
Four selective condensers followed by ESP	Reactor: 1 to 5 kg/hr Fluidized bed	First condenser: 32 to 44°C; Second condenser: 25 to 27°C; Third condenser: 22 to 25°C; Fourth condenser: 22 to 25°C; ESP: NR		65wt.% bio-oil condensed in stage 1, while 11 and 20 wt.% is obtained from stage 4 and 5. All fractions have a pH of around 2.5 indicating poor separation of bio-oil families. Temperature conditions chosen in this study do not offer any advantage despite a five stage condneser system.	[163]
Five stage condensation system	Reactor: 8 kg/hr Fluidized bed	First condenser: 85°C; First ESP: 129°C; Second condenser: 65°C; Second ESP : 77°C; Third condesner: 18°C	First condenser: 102°C; First ESP: 129°C; Second condenser: 77°C; Second ESP : 77°C; Third condesner: 18°C	Reduced water and acid content in first three stages. Majority of bio-oil acidity is due to acetic acid which can unlikely cause hot corrosion when used in boilers. Collection of sugars and water insoluble pyrolytic lignin in first two stages suggests further separation is possible with water wash.	[18]

reactor and first spray condenser temperature on liquid composition. Antoine coefficients of pure formic acid, acetic acid, n-butric acid, p-cresol, and eugenol fairly predict yield of acids and total phenols collected in first condenser at different temperatures. However, compounds like o- and p-cresols are observed to condense at 300°C in presence of sugars [19]. Therefore, consideration of binary interaction parameters to model pyrolysis vapor condensation is essential. To summarize, fractional condensation is an economic route to concentrate similar chemical families in different stages to enable bio-oil stability and make it more suitable for selective upgradation.

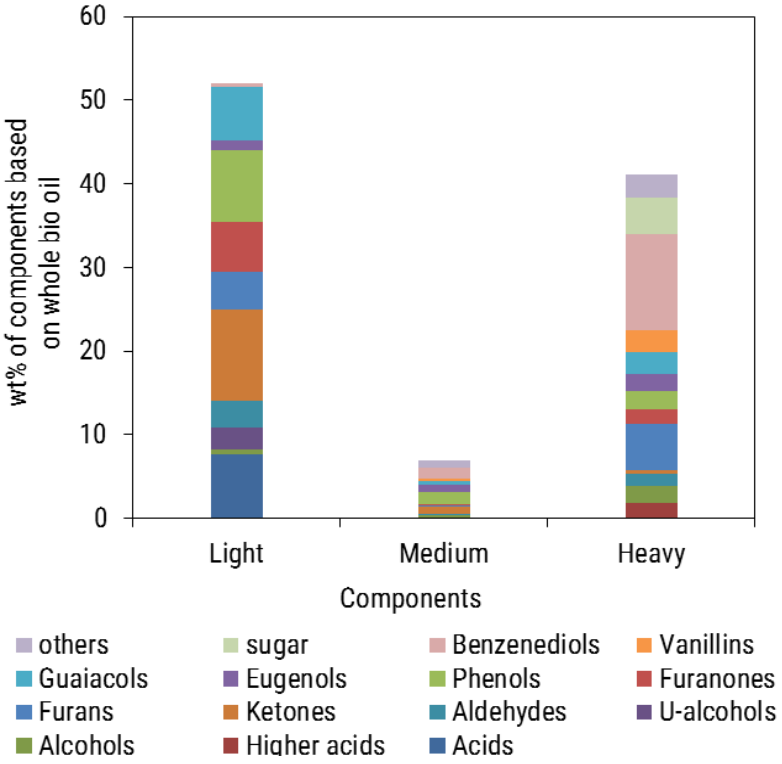

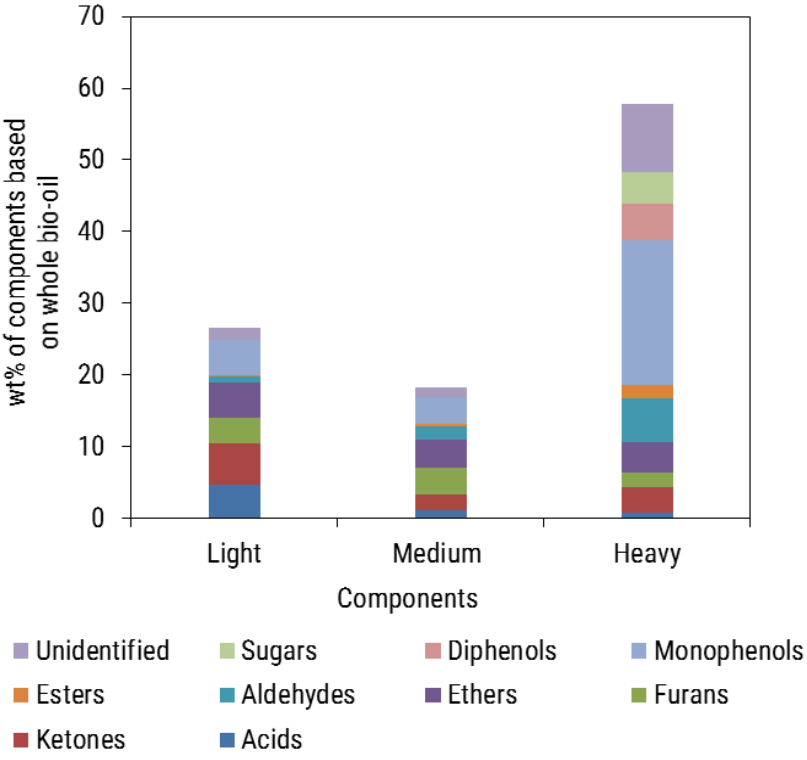

This figure is continued on the next page...

Figure 2.10

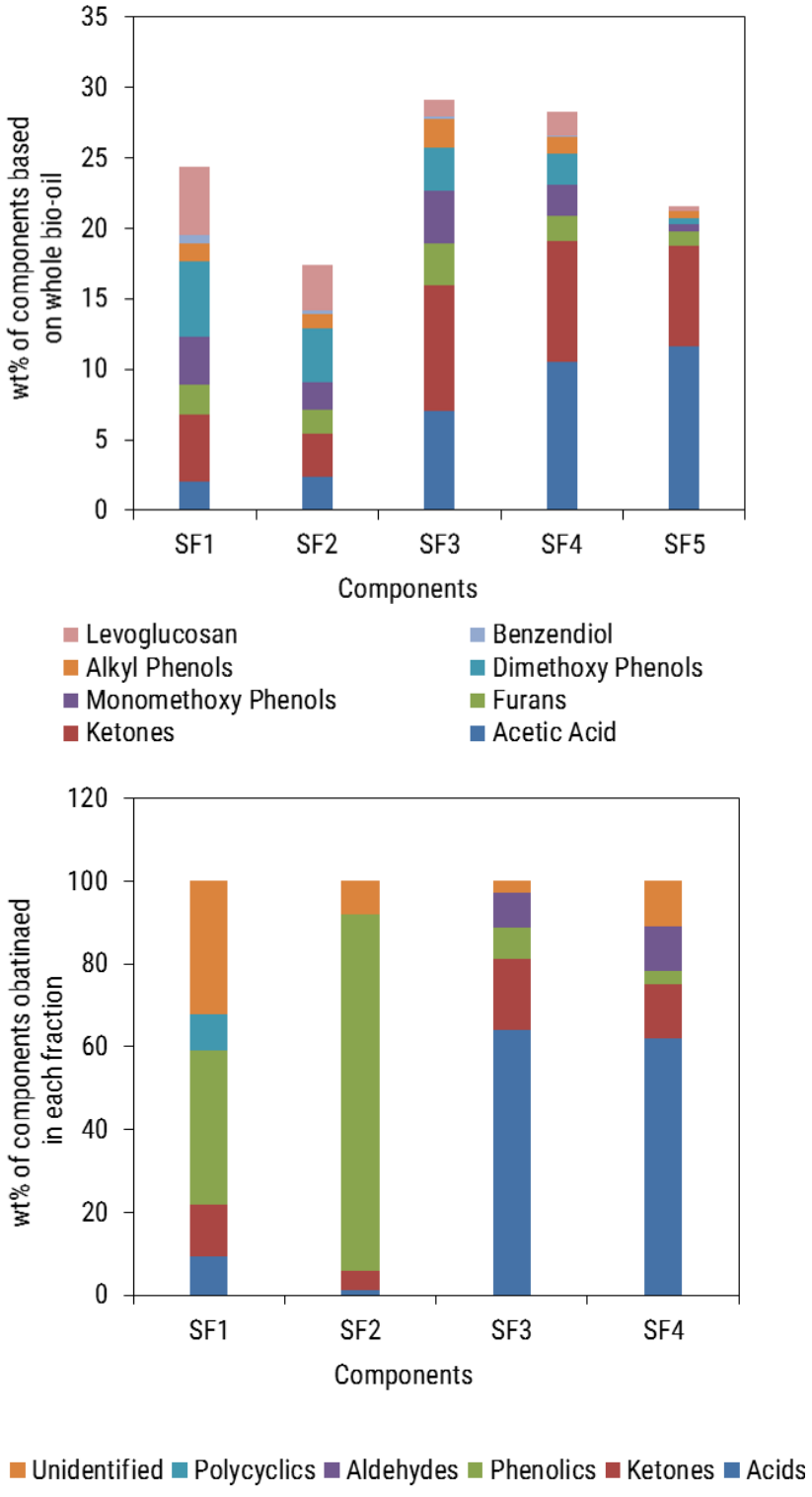

This figure is continued on the next page...

Figure 2.10

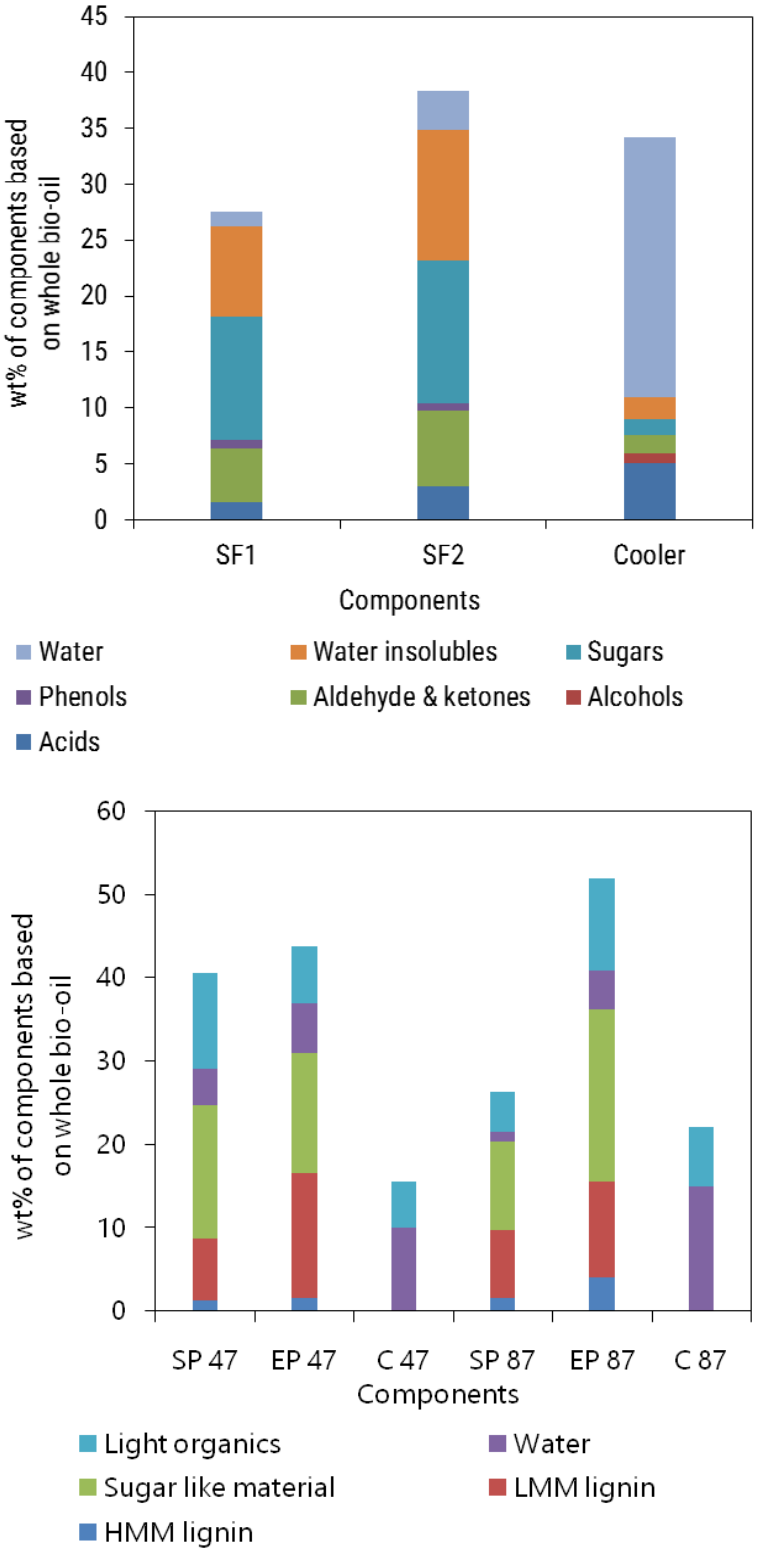

Figure 2.10: Bio-oil fractionation data from literature (a) Single stage molecular distillation [16]; (b) Multi-stage molecular distillation [17]; (c) Multi-stage condensation system with shell and tube heat exchangers and electrostatic precipitator [18]; (d) Four stage indirect contact heat exchangers [19]; (e) Two stage quenching system [20]; (f) Sieve plate column followed by EP and cooler under two gas outlet temperatures (47 and 87°C) [20]. SF: Stage fraction, SP: Sieve plate, EP: Electrostatic precipitator, C: Cooler

2.6 Significance of this research

Biomass pyrolysis process involves several series and parallel depolymerization, volatilization, and cross-linking reactions accompanied by physical changes. Increase in heating rate increases the selectivity for depolymerization and volatilization reactions over cross-linking/ char forming reactions, which is the case in fast pyrolysis. High selectivity for depolymerization reactions induces plasticity in biomass particle. The plasticity or partial melting of biomass particle not only increases molecular mobility but can also affect pore structure of biomass particle. As a result, both reaction selectivity and plasticity of biomass particle, induced beyond a particular heating rate value, will affect the kinetic model parameters. Thus, it is hypothesized here that heating rate value beyond which considerable plasticity is observed in biomass particle can be used to model kinetics of fast pyrolysis. Also, particle size plays an important role in volatile evolution rate as pore structure can change due to viscoelastic nature of biomass particle at high heating rates. Hence, biomass pyrolysis is carried out under a wide range of heating rates (5 to 250 C/min) and particle sizes - < 45 μm, 75 to 106 μm, and 300 to 425 μm (last two particle sizes have pore structure representative of those particles used in large scale fast pyrolysis reactors) in this thesis, reported in Chapter 3. Particle sizes used in this study can not be used in micropyrolyzers (popular choice for determining fast pyrolysis kinetics) because biomass will experience internal temperature gradients. Mass loss can not be recorded in micropyrolyzers when biomass undergoes temperature rise. To ensure isothermal conditions in all biomass particle sizes (Fig. 2.6), TGA apparatus is used in this study to model pyrolysis kinetics. To derive pyrolysis kinetics DAEM is used in this study due to its applicability to wide range of heating rates. It is also used to account for heterogeneity of molecular environment in biomass and quantify volatile evolution rate alterations caused due to morphological changes. Chapter 3 shows the significant effect of choice of heating rate and particle size on values of kinetic model parameters. It also reports that kinetic parameters derived using the heating rates that induce considerable plasticity can be fairly extrapolated to fast pyrolysis conditions. Thus, in order to describe reaction rates for large scale fast pyrolysis re-

actors, Chapter 3 presents that the kinetic model and its parameters should be derived under conditions which account for reaction selectivity and in-situ pore structure changes that affect the mass loss rate.

Prediction of bio-oil, char, and gas yield is not sufficient to design pyrolysis reactor and downstream operations. Knowledge of bio-oil composition is also necessary. Global kinetic model, proposed in chapter 3, does not allow detailed prediction of pyrolysis vapor composition. Though detailed kinetic models are proposed in the literature, they do not account for the effect of increase in molecular mobility caused by viscoelasticity of biomass and morphological changes that affect the product yields. Chapter 4 couples the modeling strategy developed in Chapter 3 with a detailed kinetic model (50 species and 29 reactions which occur inside biomass particle) proposed by Ranzi et.al.[10] to account for the effect of pore structure change on yield of major bio-oil components products. The model is modified by addition of certain reactions, coupling all reactions with DAEM, and introducing an empirical factor to account for changes in molecular mobility with respect to heating rate. The results also reveals the importance of considering mass loss experienced by biomass particles when it undergoes temperature rise in a reactor. Chapter 4 proposes a detailed kinetic model that not only accounts for reaction chemistry of primary pyrolysis reactions but also takes into account the effect of physical changes on the reaction rates. The model is suitable for predicting the chemical composition of pyrolysis products obtained under fast pyrolysis conditions for a wide range of biomass feedstocks.

As pyrolysis vapors exit biomass particle they spend considerable time inside the reactor at pyrolysis temperature. At these temperatures bio-oil components undergo cracking and secondary charring reactions. Based on the reactor configuration these reactions can become significant and affect the bio-oil and gas composition. Therefore, accurate description of primary and secondary pyrolysis reaction kinetics is essential. The kinetic model developed for primary pyrolysis reactions by Ranzi et. al. [10] is compared with the model developed in Chapter 4. The rate at which primary pyrolysis products are released from biomass particle is crucial because that will affect their secondary gas phase reactions. This will eventually affect the bio-oil and pyrolysis gas composition. Chapter 5 presents a engineering

model for bubbling fluidized bed reactor which accounts for 20,239 vapor phase reactions of 507 species, proposed in [10], to predict the detailed composition of pyrolysis vapors exiting the reactor. It highlights the effect of primary pyrolysis kinetic model and value of its parameters on the prediction of bio-oil, gas, and char yields over a wide range of operating temperatures. Also, the results show that the primary pyrolysis reaction kinetics model developed in this study performs better than that proposed in the literature.

Chapter 5 shows the capability of the reactor model to predict major components of pyrolysis vapors, which will be subjected to downstream condensation. However, bio-oil is a mixture of several hundred compounds which poses a challenge in designing fractional condensation system. Vapor-liquid equilibrium of bio-oil components is complex because compounds belong to different chemical families. Chapter 6 presents a strategy to design fractional condensation based on 28 compounds which are generally present in abundance in bio-oil obtained from different biomass species. Model results are validated with literature data and a new condensation system is proposed to collect bio-oil into distinct chemical families.

The kinetic modeling strategy proposed in Chapter 3 facilitated in development of a detailed kinetic model in Chapter 4, which was tested at the reactor scale in Chapter 5 and performed better than the one reported in literature. The reactor model developed in Chapter 5 and pyrolysis vapor condensation simulation strategy developed in Chapter 6 can help design upstream and downstream operations of pyrolysis plants capable of handling different biomass feedstocks.

Chapter 3

Modeling pyrolysis kinetics using DAEM

3.1 Introduction

Pyrolysis chemistry and intra-particle transport processes are very complex and interdependent [67]. All models that describe rate of transport processes use resistance and driving force as model parameters. For pyrolysis the resistances for chemical reactions and mass transport vary with the chemical composition, temperature, heating rate, internal overpressure, solid and vapor residence time, and biomass particle size [164, 165]. Heating rate controls the extent of depolymerization and recombination/crosslinking (bio-char formation) reactions [166]. Intra-particle residence time of volatile products is dependent on biomass particle size and its pore structure. Secondary cracking and char forming reactions of vapor inside the particle become dominant with increase in intra-particle residence time. To decouple each mass transfer step is a challenging task because of the difficulty in measuring internal temperature, pressure, and changes in physical properties [100, 80]. Therefore, a modeling approach which can effectively lump the complexity of pyrolysis and describe the volatilization rate is essential.

Distributed activation energy model (DAEM) describes a rate process as a combination of probabilistic infinite parallel processes. The resistance/activation energy of each parallel process is described by an Arrhenius type equation. Activation energies are expressed using a probability distribution function. The con-

tribution of each process, out of the infinite possibilities, to the overall rate is weighed by the associated probability of an activation energy value. Variation in the activation energy of chemical reaction can be attributed to heterogeneity of molecular environment in a solid [117]. Also, resistance for transport processes can vary with physical changes in the solid reactant. In case of pyrolysis, biomass particle undergo morphological changes like intermediate melting, formation of open pore structure, and shrinkage (Figure 2.4). The resistance for volatile transport outside a particle can therefore change, which affects the volatilization time of biomass particle. DAEM ilumps the variations in resistance of reactions and mass transfer in biomass volatilization process.

To explain the heat and mass transfer processes that occur during biomass pyrolysis, transport models are coupled with reaction kinetics [167, 32]. The role of transport equations becomes significant when pyrolysis occurs in the thermally thick regime ($0.2 \leq$Biot number (Bi)≤ 10). Di Blasi [166], and Babu and Chaurasia [168] have coupled primary and secondary pyrolysis reactions with transport equations which account for the effect of particle shrinkage. They both conclude that particle shrinkage affects primary as well as secondary reaction paths because it changes internal heat transfer conditions and decreases intra-particle residence time of vapors. Consideration of particle shrinkage is significant when pyrolysis occurs in the thermal wave regime ($\text{Bi} \geq 10$) [169]. Di Blasi [80] used a 2-dimensional (2D) transport model to study the anisotropic behavior of biomass. The 2D model predicted higher volatile evolution rate as compared to 1D model emphasizing the effect of heat transfer and pore structure on conversion rate. Dufour et al. [35] used multi-step kinetics combined with tar evaporation and convective transport of vapors to describe the biomass pyrolysis process. The amount of tar evaporated was modeled using ClausiusClapeyron based mathematical model. Stark et al. [170] combined a detailed multi-step reaction model of Ranzi et al.[33] with a particle scale model to predict the biomass degradation profile for particle size varying from 0.6 to 2.2 cm. They showed good prediction of pyrolysis behavior for particles bigger than 1 cm. Typically in fast pyrolysis, much smaller particles (<3 mm) are used [171]. The effect of morphological changes on biomass volatilization rate can become significant at these particle sizes. Thus,

one needs to account for the effect of changing pore structure on the physical properties of biomass particles. In such cases, the estimation of parameters required by the transport models used by the particle scale modeling approach is not always possible. The DAEM approach enables the analysis of physical changes in biomass pore structure on volatilization resistance. Therefore, DAEM is used to model the fast pyrolysis process.

The molten phase or metaplast formation, which affect the volatilization time, is reported to be dependent on the heating rate and particle size [71, 172, 173]. In this chapter heating rates and biomass particle sizes are selected such that, beyond particular value, structural changes become noteworthy to affect volatilization rate. The changes in morphology also indicate high selectivity of devolatilization reaction reactions over cross-linking reactions, which is a characteristic of fast pyrolysis. The optimized DAEM parameters thus, represent the apparent resistance for different chemical reactions and mass transfer steps that occur during biomass pyrolysis.

DAEM parameters are optimized for biomass pyrolysis carried out under heating rates varying from 5 to 250°C/min for three particle sizes $\leq$45μm, 75 to 106 and 300 to 425 μm. DAEM is coupled with three different reaction models- first order reaction, Avrami-Erofeev nucleation and random scission [174] to obtain the apparent kinetic parameters. Further, to test the predictive ability of the optimized DAEM model, biomass volatilization curves, generated under fast pyrolysis condition of 1000 °C/s by Zhang et al. [23], for four different biomass species are estimated and compared with experimental data.

3.2 Significance of experimental methodology

Biomass pyrolysis experiments were carried out under different heating rates and particle sizes to consider their effect on the reaction kinetics. Practical heating rates within the large scale bubbling fluidized bed fast pyrolysis reactors are typically of the order of 10^2 °C/s. Although micropyrolyzers are reported to achieve heating rates around 150 °C/s they are incapable of recording solid mass loss profile with respect to time or temperature. On the other hand, TGA can achieve

heating rate only within the range of 0.1 to 5 °C/s (in this case) but can produce data for mass loss profile. Literature reports derive kinetics of pyrolysis using either low heating rates (<1 °C/s in TGA) or high heating rates (10^2 °C/s in micropyrolyzers) for pyrolysis. The kinetics derived at low heating rates can not extrapolated to fast pyrolysis as cross-linking reactions are dominant at low heating rates. For high heating rates, reports assume that the biomass temperature instantly reaches reactor temperature, and model parameters are derived based on this assumption. However, for heating rates of the order of 10^2 °C/s, it would take 4.5 to 5.5 s to reach optimal fast pyrolysis temperature of 450 to 550 °C. It is important to consider the rates of competitive reactions when biomass is experiencing the temperature rise, as it may affect the ultimate composition of pyrolysis products. The TGA apparatus offers an intermediate range of heating rates which facilitates collection of sufficient data-points during the temperature rise of biomass particle for kinetic modeling. Therefore, in this study a TGA was used to model the reaction kinetics of fast pyrolysis. The heating rates chosen in this study were between 0.083 and 4.17 °C/s (5 and 250 C/min). To extrapolate the kinetics obtained at intermediate heating rates to those in fluidized bed reactors, it was essential to ensure that reaction selectivity is similar to that at high heating rates. As heating rate increases selectivity for depolymerization and volatilization reactions increase over cross-linking reactions, which induce plasticity in the biomass particle. Intermediate liquid phase and intra-particle vapor pressure causes aerosol ejection under heating rates of the order of 10^2 °C/s. Thus, plasticity or partial melting of biomass particle can be used as a qualitative indicator for increased selectivity of depolymerization and volatilization reactions over cross-linking/char forming reactions, which is a characteristic of fast pyrolysis. Extrapolation of kinetics derived at intermediate heating rates to high heating rates/fast pyrolysis conditions would be justified if considerable plasticity was induced in the bio-char obtained at different heating rates. Thus, SEM images of bio-char obtained at different heating rates were analyzed and the TGA data was accordingly used for kinetic parameters estimation.

3.3 Isoconversion Methods for Kinetic analysis

Pyrolysis chemistry is a network of competitive and parallel reactions occurring during the thermal degradation of cellulose, hemicellulose and lignin. Over the temperature range considered, if activation energies of the various reactions are about equal, the temperature effect can be described by a single Arrhenius expression. However, since hemicellulose, cellulose and lignin degrade within temperature intervals of 220-315 °C, 315-400 °C and 150-900 °C respectively [57], the activation energies involved in biomass pyrolysis vary from one another with respect to temperature and conversion. Thus, it is important to assume a dependence of activation energy on temperature and conversion [175].

Isoconversion methods can be used to deduce variation in activation energy with respect to conversion. Isoconversion principle states that at a particular value of conversion the reaction rate depends only on temperature (Eq. (3.1)). Among different isoconversion methods listed in Table 3.1, Friedman method allows model-fitting step to be eliminated by analyzing multiple heating rate experiments simultaneously. The Friedman method uses reaction rate data for calculation of activation energy.

$$\frac{dln(d\alpha/dt)_\alpha}{dT^{-1}} = \frac{-E_\alpha}{R} \tag{3.1}$$

Activation energy profile with respect to extent of conversion can be used to determine if there are changes in the rate controlling step of reaction as extent of conversion increases [176]. Moreover, the effective value of frequency factor of the reaction can also change with respect to surface area of reactant [177]. Value of the pre-exponential factor can be determined using technique reported by Flynn [178]. This work however, only considers the variation in activation energy.

Reaction model can be approximated based on values of α, $d\alpha/dt$, $d^2\alpha/dt^2$ and

Table 3.1: Isoconversion or Model Free methods for kinetic analysis of TGA curve

Model	Equation
Friedman Model	$ln\left(\beta\frac{d\alpha}{dT}\right) = ln(k_0 f(\alpha)) - \frac{E}{RT}$
KAS Model	$ln\left(\frac{\beta}{T^2}\right) = ln\left(\frac{k_0 R}{Eg(\alpha)}\right) - \frac{E}{RT}$
Miura Maki Method	$ln\left(\frac{\beta}{T^2}\right) = ln\left(\frac{k_0 R}{E}\right) + 0.6045 - \frac{E}{RT}$
FWO Method	$ln(\beta) = ln\left(\frac{k_0 R}{Eg(\alpha)}\right) - 5.331 - 1.052\frac{E}{RT}$

activation energy. Eq. (3.3) [179] can be derived from Eq. (3.2)

$$f(\alpha) = \beta\left(\frac{d\alpha}{dT}\right)_{\alpha}\left[A_\alpha exp\left(\frac{-E_\alpha}{RT_\alpha}\right)\right]^{-1} \tag{3.2}$$

$$\frac{f'(\alpha)}{f(\alpha)} = \frac{1}{\frac{d\alpha}{dt}}\left(\frac{d^2\alpha/dt^2}{d\alpha/dt} + \frac{2\beta}{T_\alpha} - \frac{\beta}{E_\alpha}\frac{dE_\alpha}{dT}\right) \tag{3.3}$$

Where, $f'(\alpha)$ is the derivative with respect to α and E_α, and T_α are activation energy and temperature values respectively at a give α. A reaction model for kinetic analysis of the data is selected by comparing the right hand side of Eq. (3.3), calculated using experimental values, with model graphs of $\frac{f'(\alpha)}{f(\alpha)}$ for different reaction models. The reaction model is used to derive the corresponding DAEM equations for α,$d\alpha/dt$,$d^2\alpha/dt^2$.

3.4 Distributed Activation Energy Model

The general rate expression, as a function of temperature (T) and conversion (α) is given as Eq. (3.4)

$$\frac{d\alpha}{dt} = f(T,\alpha) \tag{3.4}$$

The first assumption is that differential Eq. (3.4) can be expressed in variable separated form as,

$$\frac{d\alpha}{dt} = f(T)f(\alpha) \tag{3.5}$$

Solid state reaction is assumed to follow Arrhenius dependence as for the range of energies required to activate solid state reactions, Maxwell-Boltzmann equation holds good [180, 181]. Further, as biomass is composed of cellulose, hemicellulose, lignin, and mineral matter, at the molecular level local chemical composition is different. Biomass is porous in nature and the pore structure undergoes changes during pyrolysis. Hence, the energy barrier, even for a single step reaction or any heat and/or mass transfer step, can be a collection of values depending on the location of the reaction center in the solid reactant [182, 183]. Thus, representation of reaction energy barrier using a unique value is not appropriate, and DAEM [117, 184] is suitable for describing kinetics of biomass pyrolysis.

3.4.1 Assumptions

Following assumptions were made for developing the three component DAEM model,

- There are infinite $'i'$ parallel reactions occurring simultaneously during decomposition of solid, so that each point on the TGA/DTG curve is a combination of these infinite parallel reactions.
- The reactions follow the Arrhenius law.
- Activation energy of each reactions is a random variable and thus, it is safe to assume that the activation energies can be expressed by a continuous probability distribution function.
- For one pseudo-component frequency factor for every parallel reaction is assumed to be the same.
- Frequency factor is a function of temperature.

3.4.2 Mathematical model

Biomass is assumed to be made up of volatile and non-volatile matter. The volatile matter is assumed to consist of non-condensible and condensible matter formed due to the depolymerization reactions of cellulose, hemicellulose and lignin only.

Extractive compounds in the biomass are not considered amongst volatiles. During pyrolysis process, biomass undergoes multiple parallel reactions simultaneously. Formation of volatiles from the biomass due to ith reaction is expressed as Eq. (3.6)

$$\frac{d(V_i/V_i^*)}{dt} = A_i exp\left(\frac{-E_i}{RT}\right)\left(1-\frac{V_i}{V_i^*}\right)^n \tag{3.6}$$

Here, V_i is the amount reacted in the i reaction and dV_i is the amount of volatiles released in time dt. E_i is the activation energy and A_i is the frequency factor for the i reaction. It is further assumed that each i reaction can produce a maximum V_i^* volatiles. The value of V_i^* is calculated as Eq. (3.7)

$$V_i^* = M_{dry} - M_\infty \tag{3.7}$$

Where, M_{dry} and M_∞ are the initial dry weight of biomass, and final weight of residue obtained after the completion of pyrolysis reaction. The completion of biomass pyrolysis is marked by no further change in the mass loss rate. The term (V_i/V_i^*) in Eq.(3.8) is the conversion, α_i, for i reaction.

$$\alpha_i = \frac{M_{dry} - M_t}{M_{dry} - M_\infty} \tag{3.8}$$

M_t, is the amount of biomass remaining at time, t during the pyrolysis reaction. It should be noted that the formation of volatiles by the n$^t h$ order reaction is an assumption. The reaction rate can be accelerating, decelerating, or sigmoid type. Different models capable of describing such reaction rates are given in Table 3.2. Here, $g(\alpha) = \int d(\alpha)/f(\alpha)$

For the derivation of DAEM equations, the n^{th} order reaction model is chosen. The integral form of Eq. (3.6) is written as

$$\frac{V_i}{V_i^*} = 1 - \left[1-(1-n)\int_0^t A_i exp\left(\frac{-E_i}{RT}\right)dt\right]^{\frac{1}{1-n}} \qquad n \neq 1 \tag{3.9}$$

$$\frac{V_i}{V_i^*} = 1 - exp\left[-\int_0^t A_i exp\left(\frac{-E_i}{RT}\right)dt\right] \qquad n = 1 \tag{3.10}$$

Table 3.2: Kinetic models used in the solid-state kinetics

Type of Reaction	Reaction Model	Code	f(α)	g(α)
Accelerating	Power Law	P4	$4\alpha^{\frac{3}{4}}$	$\alpha^{\frac{1}{4}}$
Accelerating	Power Law	P3	$3\alpha^{\frac{2}{3}}$	$\alpha^{\frac{1}{3}}$
Accelerating	Power Law	P2	$2\alpha^{\frac{1}{2}}$	$\alpha^{\frac{1}{2}}$
Decelerating	1-D diffusion	D1	$1/2\alpha^{-1}$	α^2
Decelerating	2-D diffusion	D2	$[-ln(1-\alpha)]^{-1}$	$(1-\alpha)ln(1-\alpha)+\alpha$
Decelerating	3-D diffusion	D3	$\frac{3}{2}(1-\alpha)^{\frac{2}{3}}[1-ln(1-\alpha)^{\frac{1}{3}}]^{-1}$	$[1-(1-\alpha)^{\frac{1}{3}}]^2$
Decelerating	First Order	F1	$(1-\alpha)$	$-ln(1-\alpha)$
Decelerating	n^{th} Order	Fn	$(1-\alpha)^n$	$(n-1)^-1(1-\alpha)^{1-n}$
Sigmoid	Avrami-Erofeev	A4	$4(1-\alpha)[-ln(1-\alpha)]^{\frac{3}{4}}$	$[-ln(1-\alpha)]^{\frac{1}{4}}$
Sigmoid	Avrami-Erofeev	A3	$3(1-\alpha)[-ln(1-\alpha)]^{\frac{2}{3}}$	$[-ln(1-\alpha)]^{\frac{1}{3}}$
Sigmoid	Avrami-Erofeev	A2	$2(1-\alpha)[-ln(1-\alpha)]^{\frac{1}{2}}$	$[-ln(1-\alpha)]^{\frac{1}{2}}$
Sigmoid	Random scission	DP	$2\sqrt{\alpha}(1-\sqrt{\alpha})$	$-ln(1-\sqrt{\alpha})$

The complexity of lignocellulosic biomass is such that a continuous distribution $f(E)$ of activation energies is assumed where $\int_E^{(E+\Delta E)} f(E)dE$ describes the probability for the i reaction with the reaction having an activation energy between E and $E+\Delta E$. The mass fraction of volatile material with activation energies between E and $E+\Delta E$, dV at a given time t is given in Eq. (3.11)

$$dV = dV^* f(E)dE \tag{3.11}$$

$$dV = \sum_{i=1}^{\infty} V_i \quad \text{at time t} \tag{3.12}$$

$$V^* = \sum_{i=1}^{\infty} V_i^* \quad \text{potential volatile matter} \tag{3.13}$$

Now, V_i^* and V_i are replaced by V^* and dV, respectively. Then Eq. (3.9) and Eq. (3.10) become,

$$dV = V^*\left[1-\left[1-(1-n)\int_0^t Aexp\left(\frac{-E}{RT}\right)dt\right]^{\frac{1}{1-n}}\right]f(E)dE \qquad n \neq 1 \tag{3.14}$$

$$dV = V^*\left[1-exp\left[-\int_0^t Aexp\left(\frac{-E}{RT}\right)dt\right]\right]f(E)dE \qquad n = 1 \tag{3.15}$$

To determine the total amount of volatiles released at time t, Eq. (3.14) and Eq. (3.15) are integrated between 0 to ∞ . The limits here represent the activation energies for i reactions in the probability distribution function. The integration of Eq. (3.14) and Eq. (3.15) is

$$\alpha = 1 - \int_0^\infty \left[1 - (1-n)\int_0^t Aexp\left(\frac{-E}{RT}\right)dt\right]^{\frac{1}{1-n}} f(E)dE \quad n \neq 1 \tag{3.16}$$

$$\alpha = 1 - \int_0^\infty exp\left[-\int_0^t Aexp\left(\frac{-E}{RT}\right)dt\right] f(E)dE \qquad n = 1 \tag{3.17}$$

Where, α is the overall degree of conversion. Since, the experiments are carried out under non-isothermal conditions at temperatures linearly varying with time from a starting temperature, T_0. Under the linear heating program Eq. (3.16) and Eq. (3.17) can be rewritten as Eq. (3.18) and Eq. (3.19),

$$\alpha = 1 - \int_0^\infty \left[1 - (1-n)\int_{T_0}^T \frac{A}{\beta}exp\left(\frac{-E}{RT}\right)dT\right]^{\frac{1}{1-n}} f(E)dE \quad n \neq 1 \tag{3.18}$$

$$\alpha = 1 - \int_0^\infty exp\left[-\int_{T_0}^T \frac{A}{\beta}exp\left(\frac{-E}{RT}\right)dT\right] f(E)dE \qquad n = 1 \tag{3.19}$$

To derive the model parameters using the differential data from experiments is recommended. Thus, Eq. (3.18) and Eq. (3.19) need to be differentiated. The differential forms are expressed as Eq. (3.20) and Eq. (3.21),

$$\frac{d\alpha}{dT} = \int_0^\infty \frac{A}{\beta}exp\left(\frac{-E}{RT}\right)\left[1 - (1-n)\int_{T_0}^T \frac{A}{\beta}exp\left(\frac{-E}{RT}\right)dT\right]^{\frac{1}{1-n}} f(E)dE \qquad n \neq 1 \tag{3.20}$$

$$\frac{d\alpha}{dT} = \int_0^\infty \frac{A}{\beta}exp\left[\frac{-E}{RT} - \int_{T_0}^T \frac{A}{\beta}exp\left(\frac{-E}{RT}\right)dT\right] f(E)dE \qquad n = 1 \tag{3.21}$$

Where β is the heating rate and $\beta d\alpha/dT = d\alpha/dt$. $f(E)$ is the probability distribution function and standard continuous distribution functions can be used in the equations. Here, Gaussian distribution function, Eq. (4.6), is used,

$$f(E) = \frac{1}{\sigma\sqrt{2\pi}} exp\left(-\frac{(E-E_0)^2}{2\sigma^2}\right) \tag{3.22}$$

$$\begin{aligned} f(E) = c\left[\frac{1}{\sigma_1\sqrt{2\pi}} exp\left(-\frac{(E-E_{0,1})^2}{2\sigma_1^2}\right)\right] \\ + (1-c)\left[\frac{1}{\sigma_2\sqrt{2\pi}} exp\left(-\frac{(E-E_{0,2})^2}{2\sigma_2^2}\right)\right] \end{aligned} \tag{3.23}$$

Where, the c is the weight factor for a bimodal Gaussian distribution. The frequency factor can also be a function of temperature as in Eq. (3.24) and can be replaced in the Eq. (3.18) to Eq. (3.21).

$$A = A_0 T^m \tag{3.24}$$

To solve equations Eq. (3.18) to Eq. (3.21) an approximation for the inner temperature integral is used. The approximation is shown in Eq. (3.25),

$$\int_{T_0}^{T} T^m exp\left(\frac{-E}{RT}\right) dT = \frac{\frac{RT^{m+2}}{E} exp\left(\frac{-E}{RT}\right)(0.99954E + (0.58058 + 0.044967m)RT)}{E + (2.54 + 0.94057m)RT} \tag{3.25}$$

Eq. (3.25) is a good approximation and reduces the computation time substantially. The outer integral can be solved directly using MATLAB.

Eq. (3.18) to Eq. (3.21) are used when the decomposition rate of biomass is expressed using one pseudo-component. However, it is possible to express the decomposition or conversion rate using multiple pseudo-components. Eq. (3.26), Eq. (3.27) and Eq. (3.28) can be used for a multi-component DAEM.

$$\alpha = \sum_{c=1}^{p} w_c \alpha_c \tag{3.26}$$

$$\frac{d\alpha}{dT} = \sum_{c=1}^{p} w_c \frac{d\alpha_c}{dT} \tag{3.27}$$

$$\frac{d^2\alpha}{dT^2} = \sum_{c=1}^{p} w_c \frac{d^2\alpha_c}{dT^2} \tag{3.28}$$

Where, w_c, the pseudo-component fraction can be one of the parameters for optimization.

Eq. (3.32) is the objective function used for optimizing the DAEM parameters. The objective function is the average of square root of mean squared error for α, $d\alpha/dt$ and $d^2\alpha/dt^2$ curves.

$$J_1 = \sqrt{\sum_{j=1}^{n}\sum_{i=1}^{m} \frac{(\alpha_{expt,ij} - \alpha_{pred,ij})^2}{n}} \tag{3.29}$$

$$J_2 = \sqrt{\sum_{j=1}^{n}\sum_{i=1}^{m} \frac{((d\alpha/dt)_{expt,ij} - (d\alpha/dt)_{pred,ij})^2}{y_j^2 n}} \tag{3.30}$$

$$J_3 = \sqrt{\sum_{j=1}^{n}\sum_{i=1}^{m} \frac{((d^2\alpha/dt^2)_{expt,ij} - (d^2\alpha/dt^2)_{pred,ij})^2}{z_j^2 n}} \tag{3.31}$$

$$J = \frac{J_1 + J_2 + J_3}{3} \tag{3.32}$$

Where n is the number of heating rates used simultaneously to fit the kinetic parameters, m is the number of points on each evaluated curve, y and z are the peak maximum for each DTG and differentiated DTG curve. The use of y and z is to normalize the objective function.

3.4.3 DAEM equations used for parameter optimization

The DAEM equations for α, $d\alpha/dt$ and $d^2\alpha/dt^2$ using the three reaction models, namely, first order equation (F1, Eq. (3.34) to Eq. (3.36)), Avrami-Eroofev (A2, Eq. (3.37) to Eq. (3.39)) and random scission model (DP, Eq. (3.40) to Eq. (3.42)) have

been used for determining the apparent kinetic parameters. To avoid confusion substitution in Eq. (3.33) is used in the DAEM equations derived for all reaction models

$$I = \frac{A_0}{\beta} T^m exp\left(\frac{-E}{RT}\right) \tag{3.33}$$

DAEM equations for first order reaction model,

$$\alpha = 1 - \int_0^\infty exp\left[- \int_{T_0}^T I dT \right] f(E) dE \tag{3.34}$$

$$\frac{d\alpha}{dt} = \beta \int_0^\infty \frac{A_0}{\beta} T^m exp\left[\frac{-E}{RT} - \int_{T_0}^T I dT \right] f(E) dE \tag{3.35}$$

$$\frac{d^2\alpha}{dt^2} = \beta^2 \int_0^\infty \frac{A_0}{\beta} T^m exp\left[\frac{-E}{RT} - \int_{T_0}^T I dT \right] \left(\frac{-E}{RT^2} - I + \frac{m}{T}\right) f(E) dE \tag{3.36}$$

DAEM equations for Avrami-Erofeev reaction model,

$$\alpha = 1 - \int_0^\infty exp\left[- \left(\frac{1}{2} \int_{T_0}^T I dT \right)^2 \right] f(E) dE \tag{3.37}$$

$$\frac{d\alpha}{dt} = \beta \int_0^\infty \frac{1}{2} \frac{A_0}{\beta} T^m exp\left[- \left(\frac{1}{2} \int_{T_0}^T I dT \right)^2 - \frac{E}{RT} \right] \left[\int_{T_0}^T I dT \right] f(E) dE \tag{3.38}$$

$$\frac{d^2\alpha}{dt^2} = \beta^2 \int_0^\infty \frac{1}{2} \frac{A_0}{\beta} T^m exp\left[- \left(\frac{1}{2} \int_{T_0}^T I dT \right)^2 - \frac{E}{RT} \right] \left[I + \left(\int_{T_0}^T I dT \right) \left(\frac{m}{T} - \frac{1}{2} I \left(\int_{T_0}^T I dT \right) + \frac{E}{RT^2} \right) \right] f(E) dE \tag{3.39}$$

DAEM equations for random scission model,

$$\alpha = 1 - \int_0^\infty exp\left[- \left(\int_{T_0}^T \frac{A_0}{\beta} T^m exp\left(\frac{-E}{RT}\right) dT \right)^2 \right] f(E) dE \tag{3.40}$$

$$\frac{d\alpha}{dt} = \beta \int_0^\infty 2\left[1 - exp\left(- \int_{T_0}^{T} IdT \right)\right] exp\left(- \int_{T_0}^{T} IdT \right) I f(E) dE \tag{3.41}$$

$$\frac{d^2\alpha}{dt^2} = \beta^2 \int_0^\infty 2I exp\left(- \int_{T_0}^{T} IdT \right)\left[\left(1 - exp\left(- \int_{T_0}^{T} IdT \right)\right)\right.$$
$$\left.\left(\frac{m}{T} + \frac{E}{RT^2}\right) + I\left(2exp\left(- \int_{T_0}^{T} IdT \right) - 1\right)\right] f(E) dE \tag{3.42}$$

3.5 Materials and methods

3.5.1 Biomass Analysis

Mixture of wood and bark (mallee, species: E. polybractea) from the state of Western Australia, Australia was used for pyrolysis reactions. Biomass was sieved into different particle sizes and dried at 70°C in a vacuum oven for 12 hours. The particle size distribution of sieved biomass particles was determined using the Malvern Mastersizer 2000, LASER diffraction apparatus. An elemental analyzer (Thermo-Scientific) was used to determine the elemental composition of biomass after sieving. Further, the ash content of biomass was also evaluated for all the particle sizes considered in the study. Scanning electron microscope (Zeiss Neon 40EsB crossbeam FESEM and, TESCAN MIRA3 VP-FESEM) was used to study the biomass and the biochar surface morphology.

3.5.2 TGA Calibration

TGA used in this study (TGA-series 8000 from Perkin Elmer) was calibrated using four different Curie point temperatures. The experimental temperature range was between 150 to 700 °C, thus, alumel, nickel, perkalloy and iron were used as reference materials because their Curie point temperature are 154.2, 355.3, 596 and 770 °C respectively. Small pieces, 2-3 mm in length, of each material were used for the temperature calibration at experimental heating rates. A magnet was placed around the glass tube, surrounding the TGA furnace, which pulled the sample pan downwards. The downward pull caused an increase in weight of the pan. As each material reached its Curie point temperature, loss in magnetic property

was recorded as weight loss on the TGA curve. The onset of Curie point temperature for each material was calculated at different heating rates. As the heating rate increased, the apparent Curie point temperature also increased. A graph of apparent Curie point temperature vs. heating rate was plotted for each material. Table 3.3 shows the parameters for linear calibration equation used for different materials.

Table 3.3: TGA temperature calibration parameters valid for heating rates of 5-250 °C/min

Parameters	Alumel	Nickel	Perkalloy	Iron
slope	0.2683	0.1494	0.0867	0.0608
intercept	163.16	361.95	588.85	774.73
R^2	0.9936	0.9965	0.9957	0.9965

3.5.3 Thermogravimetric analysis of biomass

The particle sizes used in the literature for high heating rates is < 50 μm to ensure uniform temperature throughout the particle. However, pore structure of such a small particle size is not representative of biomass particles (order of 1 mm) used in large scale pyrolysis reactors. Plasticity of biomass particles during pyrolysis process can alter their pore structure and affect the volatile evolution rate. Particle sizes in the range of 0.1 to 0.4 mm are representative of biomass pore structure but may suffer from internal temperature gradients for high external heat transfer coefficients as experienced in micropyrolyzers (Fig. 2.6). This is another reason for the use of TGA apparatus and intermediate heating rates in this thesis, which ensures isothermal conditions for particle sizes between 0.1 to 0.4 mm.

TGA was equipped with a chromel-alumel thermocouple at center of the TGA-furnace (Figure 3.1). The thermocouple was at a distance of 1 to 2 mm from bottom surface of sample pan. Temperature recorded by the thermocouple was denoted as the sample temperature in the instrument. Further, the ability of the equipment to record the sample temperature and mass loss with an accuracy of 0.1 μg and at a frequency of 8 Hz facilitated numerical differentiation of the TGA data that generated the differential thermogravimetric (DTG) curve. Biomass with different particle sizes - $\leq$45μm, 75 to 106 and 300 to 425 μm was accurately weighed

in alumina pans. Typical weight of the sample taken for each experiment was a function of heating rate of the TGA program. The sample weight was varied from 0.25 to 3.5 mg for analysing the thermal lag under different heating rates. Biomass pyrolysis was carried out under a argon flow rate of 60 ml/min at different linear heating rates. Argon was used as a sweeping gas to carry the pyrolysis vapors out of the furnace as soon as they were formed to suppress secondary pyrolysis reactions. Each experiment was performed atleast three times. Table 3.4 shows the temperature program for biomass pyrolysis.

Table 3.4: Non-isothermal TGA program for biomass pyrolysis

Step No.	Initial Temperature (°C)	Final Temperature (°C)	Holding Time/Heating Rate
1	35	100	25°C/min
2	100	100	15 min
3	100	150	25°C/min
4	150	150	15 min
5	150	700	5/25/50/75/ 150/200/250 °C/min
6	700	700	20 min

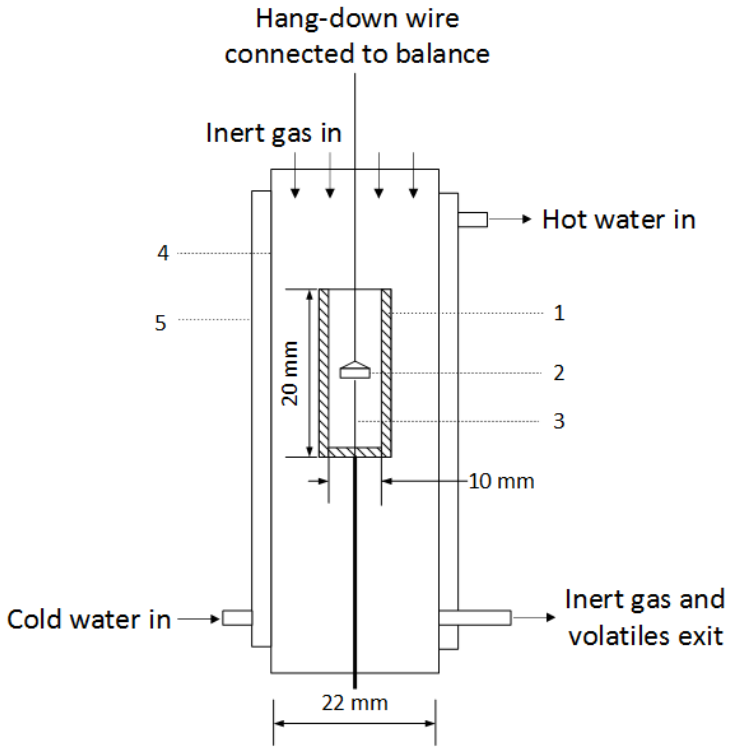

Figure 3.1: Schematic representation of TGA8000 furnace and furnace tube. 1. Furnace, 2. Alumina pan, 3. Thermocouple, 4. Furnace glass tube, 5. Cooling jacket for furnace tube. All dimensions are in mm

3.5.4 Calculation of DTG curve

The raw data from TGA was normalized to α, which represented the extent of volatiles released during biomass pyrolysis (Eq. (3.8)). The TGA data was nmerically differentiated to yield a DTG curve. To reduce the noise in the DTG curve equally spaced normalized TGA data was processed using the Soviztky-Golay digital filter (SG-filter) and filtered data was numerically differentiated, over a time step of 0.5 seconds, using extended numerical differentiation [185].

3.5.5 Optimization of DAEM parameters

As lignocellulosic biomass comprises of cellulose, hemicellulose and lignin, the biomass pyrolysis reaction was assumed to be a linear combination of degradation of the three pseudo-components. Gaussian distribution function was used to model the activation energy distribution for each component. Activation energy distribution of one of the pseudo-component was further assumed to follow a bimodal distribution, describing two distinct set of reactions [119]. Optimization of DAEM parameters was carried out using fmincon solver in MATLAB. The gradient of objective function with respect to each parameter was specified to accelerate the convergence of the solver and stabilize the solution. The square root of mean squared error for α, $d\alpha/dt$ and $d^2\alpha/dt^2$ curves was simultaneously minimized to reduce the number of solutions obtained from optimization of a 16-parameter equation.

3.6 Results and Discussion

3.6.1 Biomass Analysis

Post sieving particle size analysis of biomass is shown in Table 3.5. Biomass particles were not spherical but needle like. Volume weighted mean diameter of the particles obtained from light scattering experiment was representative of longer dimension of the biomass particle. On the other hand, shorter dimension of the biomass particle was in the range of the sieve used for size-based separation. Optical microscope images (not shown) and mean value in Table 3.5 led to the con-

clusion that for biomass particles $\leq$45 μm the aspect ratio was close to one.

Table 3.5: Particle Size Distribution of biomass. D(v,0.1), D(v,0.5) and D(v,0.9) is the particle size below which 10, 50 and 90 vol.% of the sample lies

Biomass Sieve Size Range (μm)	Volume Weighted Mean (μm)	D(v,0.1) (μm)	D(v,0.5) (μm)	D(v,0.9) (μm)	Span
$\leq$45	42.09$\pm$0.04	17.53$\pm$0.13	38.35$\pm$0.04	72.45$\pm$0.03	1.43$\pm$0.01
75 to 106	151.59$\pm$2.05	58.35$\pm$0.30	120.84$\pm$0.45	252.11$\pm$2.49	1.61$\pm$0.02
300 to 425	706.17$\pm$15.32	275.19$\pm$1.73	632.46$\pm$5.69	1284.28$\pm$13.76	1.59$\pm$0.01

Biot number for the particles was calculated using two different characteristic lengths for the three particle sizes. One characteristic length used was the volume weighted mean diameter and the other value was the longest dimension under the column D(v,0.9) from Table 3.5. For particle size, between 300 to 425 μm, Figure 3.2 shows that the Biot number exceeds one when the heat transfer coefficient in greater than or equal to 100. Biot number for other two particle sizes is below one for all values of heat transfer coefficients. The carrier gas flow rate used in the TGA program was 60 ml/min, which made the flow inside the furnace tube laminar. The magnitude of heat transfer coefficient for the annular region with characteristic length of 0.5 cm and thermally developing flow was of the order of 10 W/mK. Therefore, it was safe to assume that Biot number for all the particle sizes is less than 1. Thus, the heating rate of particle was assumed to be the same as TGA program.

3.6.1.1 Elemental and Ash content of biomass

Biomass is a heterogeneous material composed of three bio-polymers and several minerals like calcium, potassium, sodium, silica, iron, and aluminum [186]. In the current study biomass considered for the experiment was a mixture of wood and bark. Table 3.6 shows results of elemental and ash content analysis of biomass with respect to different particle sizes. The elemental composition of biomass did not vary significantly with the particle size. The variation in the ash content could be linked to the difference in the grinding characteristics of wood and bark. Bark is more brittle than wood and can be ground to finer particle size as compared to wood. The elemental and ash content of Mallee wood and bark was in the range

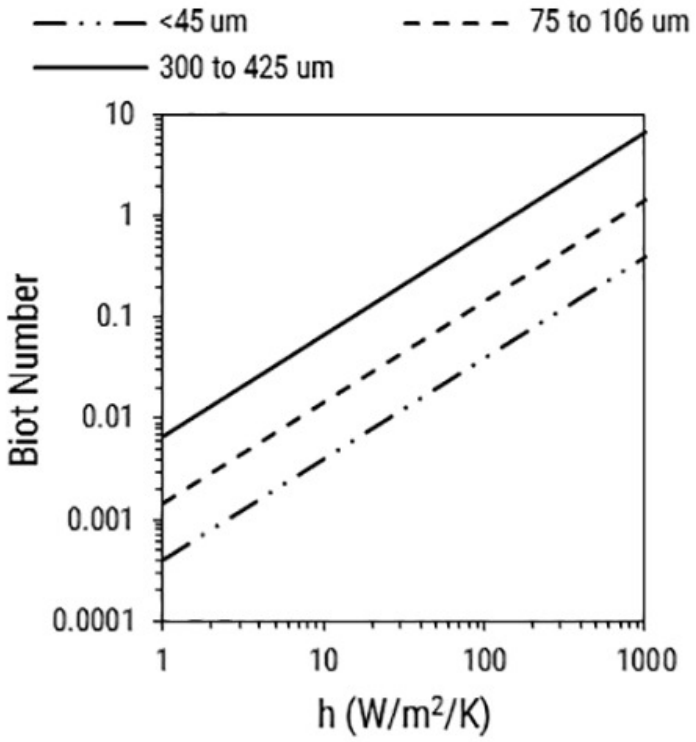

(a)

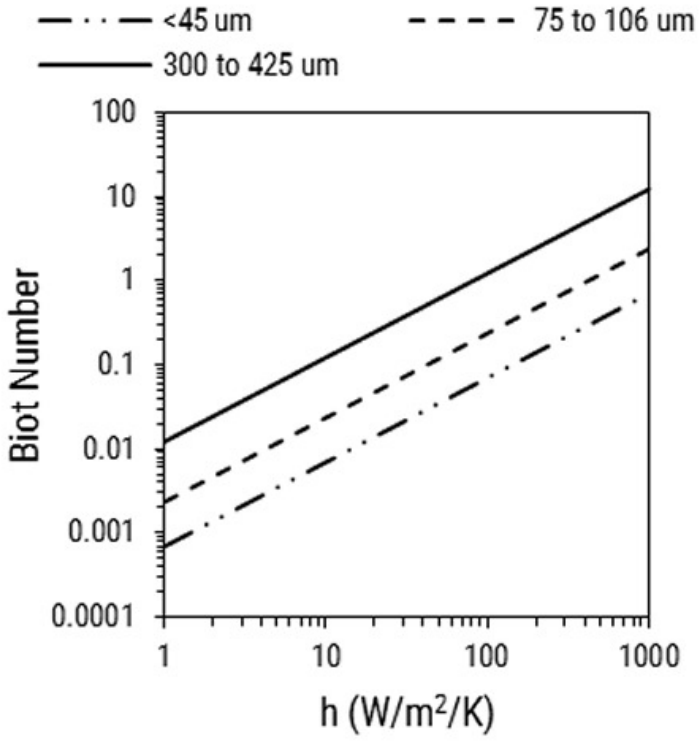

(b)

Figure 3.2: Biot number for two characteristic lengths for three particle sizes in Table 3.5 (a) 42.088, 151.588, 706.165 μm and (b) 72.449, 252.114, 1284.282 μm. The thermal conductivity of biomass is assumed to be 0.105 W/mK [21]

as reported by Abdullah et al. [187, 188]. Biomass particle size $\leq$45 μm was rich in ash, which might be indicative of higher bark content when compared to other particle sizes.

Table 3.6: Elemental analysis and ash content of biomass. *Oxygen content was calculated by difference.

Biomass Particle Size (μm)	C	H	N	O*	Ash
$\leq$45	44.67$\pm$0.15	4.99$\pm$0.53	0.21$\pm$0.01	50.13$\pm$0.50	6.24$\pm$0.30
75 to 106	46.62$\pm$0.12	5.96$\pm$0.31	0.18$\pm$0.01	47.24$\pm$0.38	1.24$\pm$0.42
300 to 425	45.82$\pm$0.14	5.83$\pm$0.46	0.13$\pm$0.01	48.22$\pm$0.43	1.37$\pm$0.25

3.6.2 Thermogravimetric analysis of biomass

3.6.2.1 Effect of initial sample weight

Large sample weight and high heating rates can lead to thermal lag in the samples due to the endothermic nature of pyrolysis reaction [78]. As the heating rate increases the effect of initial sample weight becomes prominent as shown in Figure 3.3. For heating rates upto 75°C/min, there is no shift in the TGA profile of biomass pyrolysis in terms on initial sample weight. However, for heating rate of 150°C/min and above the TGA curve shifts to high temperatures as the sample weight is reduced from 3.5 to 0.25 mg. Therefore, initial sample weight chosen for heating rates between 5 and 75°C/min and, 150 and 250 °C/min was 3.5 and 0.5 mg respectively.

3.6.2.2 Processing of TGA and DTG curve for pyrolysis kinetics

The SG-filter is a good choice for data smoothing because it does not cause the curve to shift with respect to temperature or time [185]. The processed DTG curve shows that the peak maximum, peak resolution and peak position was not altered due to smoothing (Figure 3.4).

3.6.2.3 Effect of heating rate and biomass particle size on TGA profile

The TGA and DTG profiles of biomass pyrolysis with respect to heating rate and particle size are shown in Figure 3.5. In this study, ash content of biomass varied with the particle size. Therefore, the organic content of final residue obtained at different heating rates was compared with respect to the particle size.

The total solid residue values in Table 3.7 suggest that there was no significant

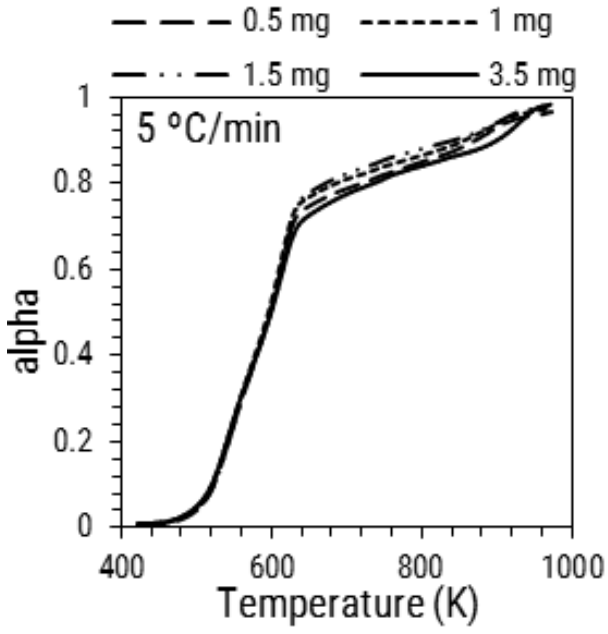

(a)

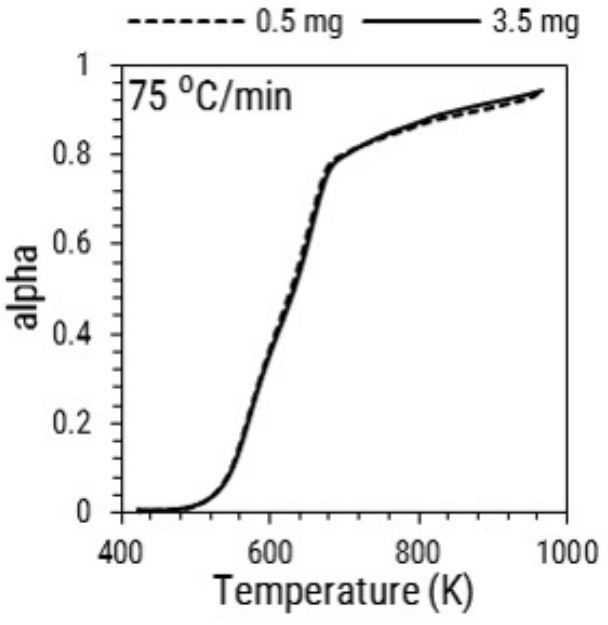

(b)

The figure is continued on the next page...

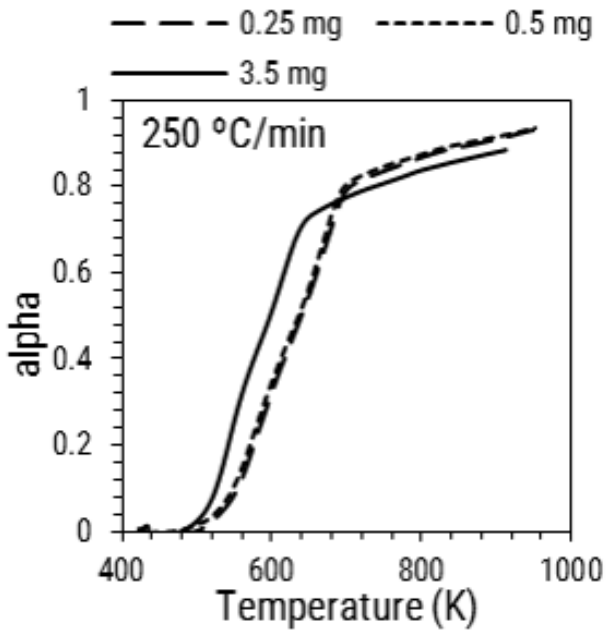

(c)

Figure 3.3: Effect of weight on the biomass pyrolysis TGA profile for heating rate (a) 5 °C/min (b) 75 °C/min (c) 250 °C/min

difference between the organic content of solid residue obtained after completion of pyrolysis for heating rates upto 75 °C/min. The TGA temperature program has an isothermal step, where the biomass was held for 20 min at 700 °C. Table 3.7 and Table 3.8 indicate that mass was also lost in the isothermal region of TGA program. Difference between organic residue for particle size $\leq$45μm and other two sizes is a consequence of char forming reactions catalyzed by higher mineral content in biomass $\leq$45μm [186]. On the other hand, a significant change in solid residue was observed for particle size 75 to 106 and 300 to 425 μm, and heating rate of 200 and 250 °C/min. Increase in heating rate increases the selectivity for depolymerization, which causes a decrease in the solid residue. Moreover, high heating rates bring about significant change in morphology of the particles leading to the formation of open pore structure which facilitates the volatiles release. On the other hand small particles, here particles with $\leq$45 μm, can sinter and lead to increased resistance for volatilization. Thus, the solid residue for particle size between 75 to 106 and 300 to 425 μm, where ash content is less and particles are spread apart from one another, have lower organic char as compared to particles with size $\leq$45 μm.

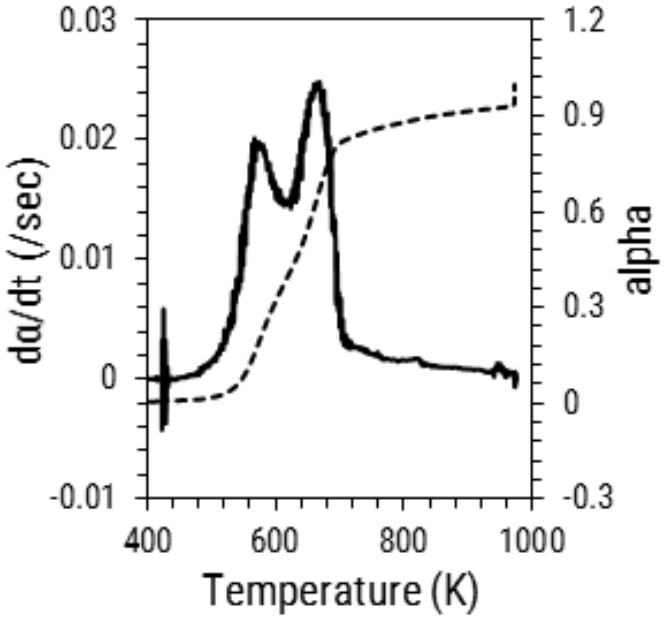

(a)

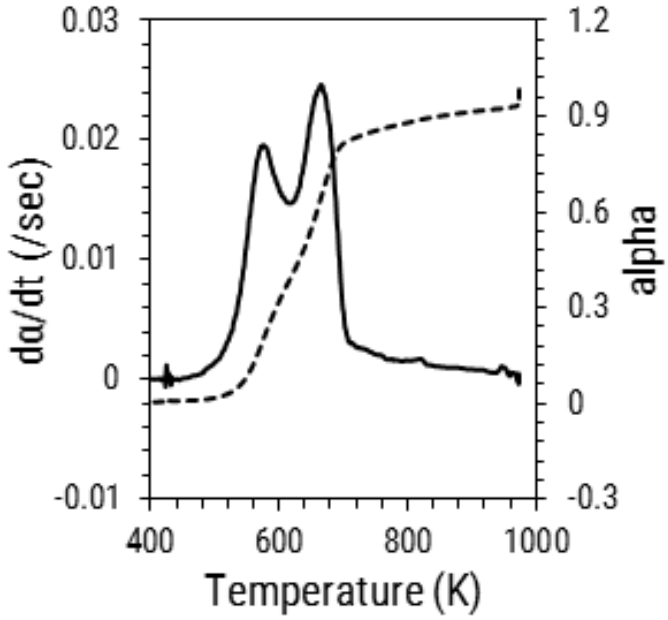

(b)

Figure 3.4: (a) Unprocessed TGA and DTG curves (b) TGA and DTG curves after applying Sovitzky-Golay filter

The percent of biomass reacted at temperatures shown in Table 3.8 represents the data recorded during pyrolysis of biomass heated at different heating rates to a final temperature of 700 ^0C. In temperature range of 400 to 600 °C, for biomass with particle size $\leq$45 μm, the amount of biomass reacted was less as compared

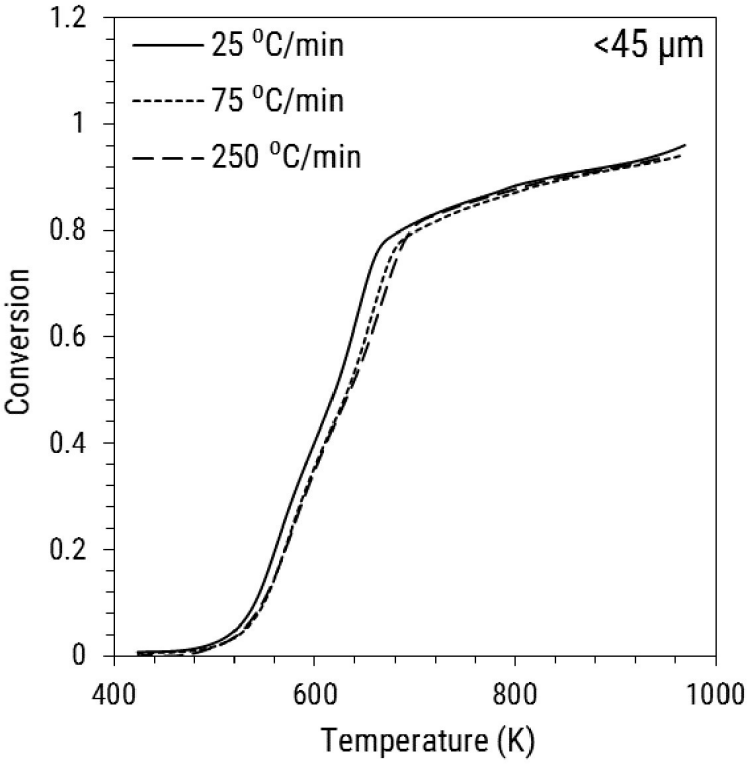

(a)

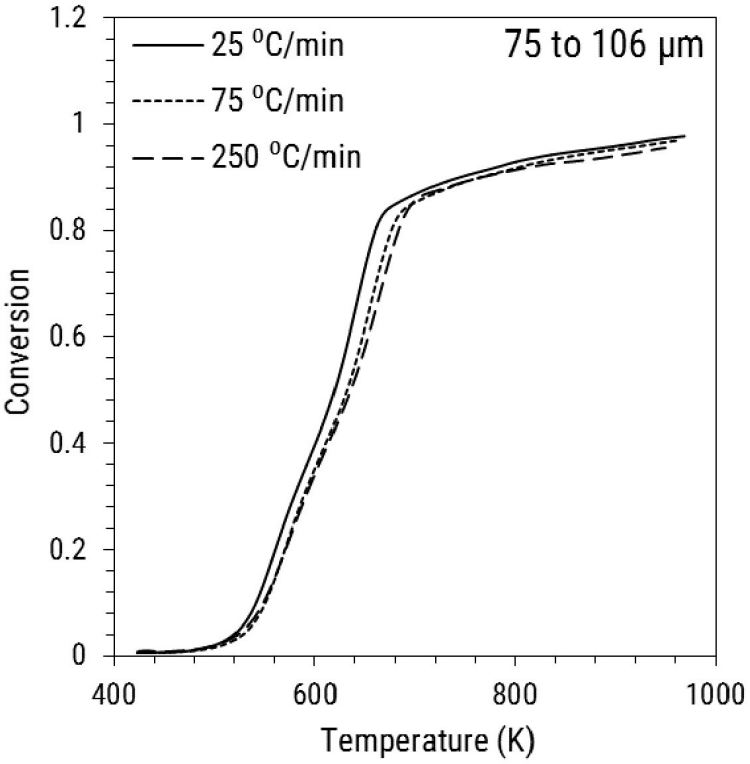

(b)

This figure is continued on the next page...

Figure 3.5

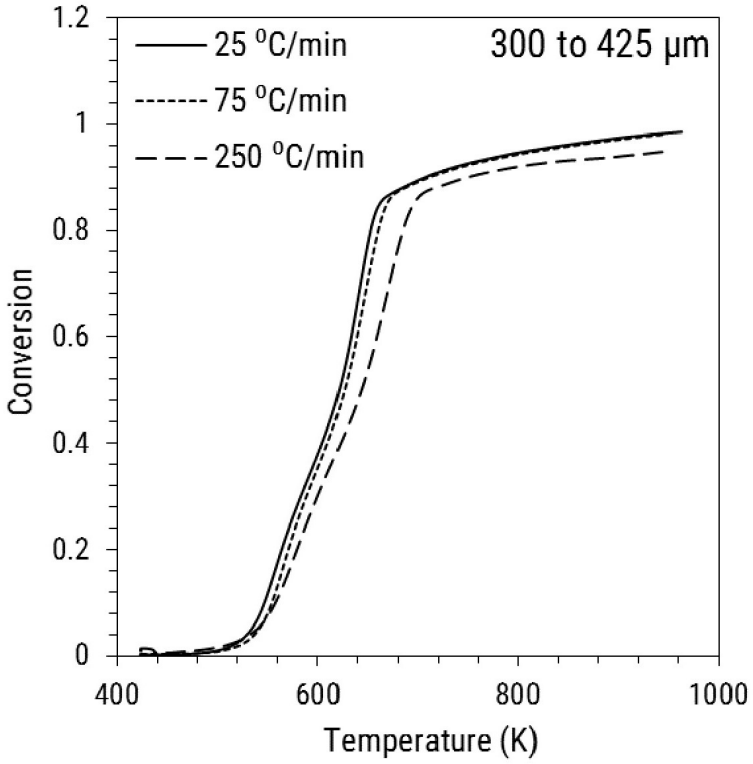

(c)

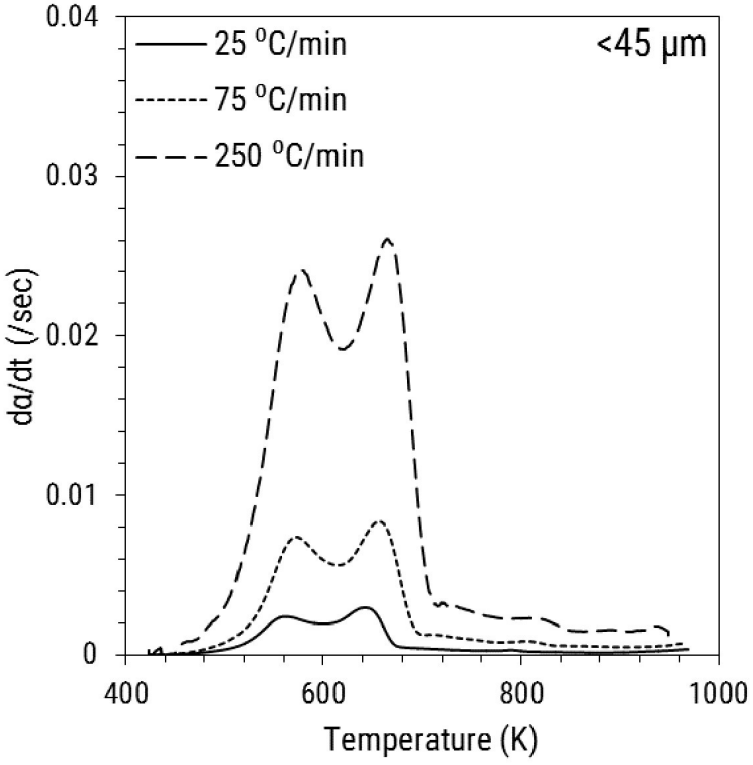

(d)

This figure is continued on the next page...

Figure 3.5

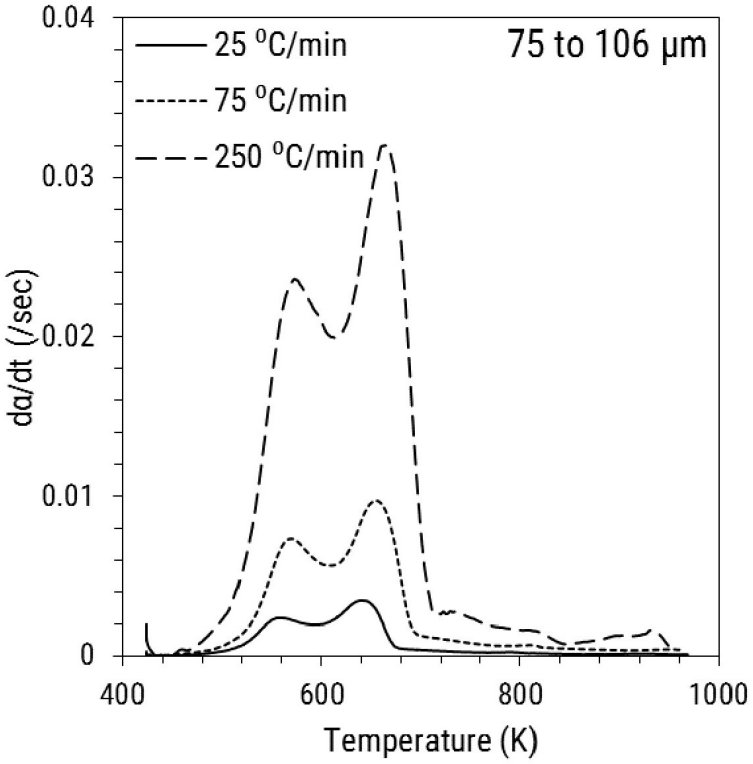

(e)

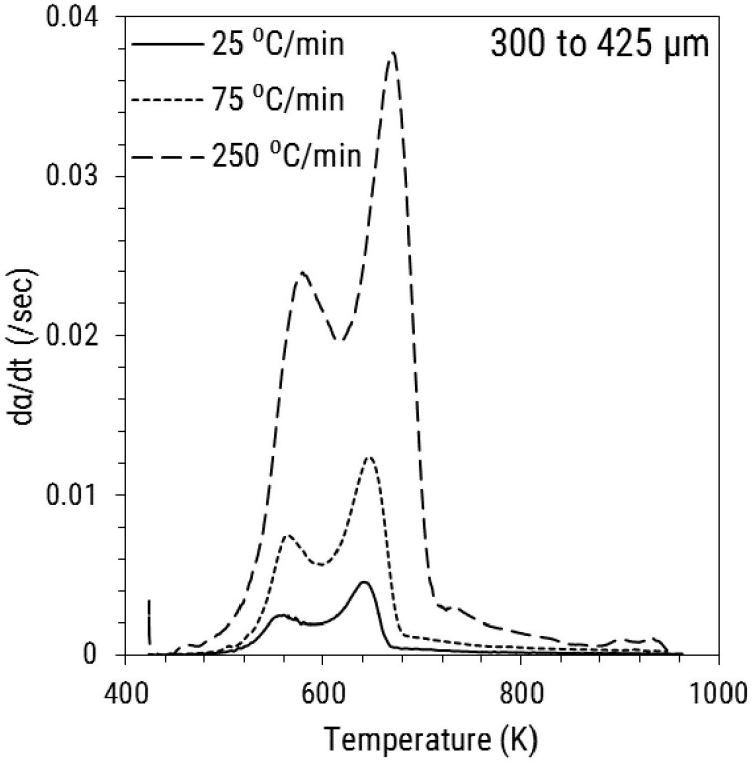

(f)

Figure 3.5: Processed (a) to (c) TGA curves and (d) to (f) DTG curves for three biomass particle sizes and heating rate varying from 5 to 250 °C/min.

Table 3.7: Solid Residue left after pyrolysis of biomass, with different particle size, under pre-defined linear heating rate programs. Values in parenthesis are obtained after subtracting the ash content from the solid residue.

Heating Rate (°C/min)	Final Solid Residue (wt.% of dry biomass)		
	<45 μm	75 to 106 μm	300 to 425 μm
5	25.04±0.20 (18.80)	20.86±0.41 (19.62)	18.29±0.03 (16.42)
25	24.99±0.19 (18.74)	20.62±0.15 (19.38)	18.80±0.39 (16.93)
50	24.67±0.06 (18.43)	20.54±0.26 (19.30)	18.86±0.03 (16.98)
75	25.11±0.06 (18.87)	19.46±1.90 (18.21)	18.21±0.54 (16.34)
150	23.26±0.78 (17.02)	20.09±0.15 (18.85)	18.42±0.28 (16.55)
200	24.65±0.05 (18.41)	12.45±0.24 (11.21)	10.23±0.97 (8.86)
250	21.65±0.68 (15.41)	12.78±1.01 (11.54)	8.82±0.16 (7.45)

to other two particle sizes. This is because the high mineral content in biomass particles $\leq$45 μm promotes char forming reactions [189, 190]. As the heating rate increases, the extent of mass reacted decreases because the time spent by the biomass particle in any small temperature interval decreases. On the other hand, between 300 and 600 °C, the percentage of biomass reacted increases beyond 150 °C/min for all particle sizes (Table 3.8). The increase in the mass loss might a consequence of increase in selectivity for devolatilization reactions that facilitates formation of porous structure, which in turn allows easy passage of volatile products out of the biomass particle. It is important to note that for 5 °C/min the percent biomass reacted up till 300 and 400 °C was much higher than any other heating rate because the reaction time was 30 min. The evolved gases were not analyzed and therefore, it was not possible to comment if the gas evolved at 300 °C under 5°C/min heating had the same chemical composition as those evolved for other heating rates.

To get a better insight into effect of pyrolysis conditions on biomass particle, optical microscope and SEM images of intermediate and final solid residue were analyzed. The pore structure of biomass used in this study was visualized using SEM

images. The lumen diameter of the biomass was between 4 to 10 μm while the diameter of the vessel cells was of the order of 20 to 40 μm. Further the vessel cells had small pores on their wall (0.5 to 1.5 μm), implying that there was some degree of open pore structure already present in biomass particle. Ciesielski et al. [53] imaged pine wood particles using confocal scanning laser microscopy and the cell wall thickness was of the order of 2 to 4 μm and the lumen diameter was of the order of 10^1 μm. Biomass particles, 300 to 425 μm, in Figure 3.6 revealed that the cell wall structure of the biomass was retained at an intermediate temperature of 300 °C and at all heating rates used in the study [34, 191].

Table 3.8: Percent Mass Reacted with respect to temperature at different heating rates for different particle sizes

	Mass Reacted (wt.% of initial dry biomass)											
	300 °C			400 °C			500 °C			600 °C		
Heating rate	<45	75to106	300 to 425	<45	75to106	300 to 425	<45	75to106	300 to 425	<45	75to106	300 to 425
°C/min	μm	μm	μm	μm	μm	μm	μm	μm	μm	μm	μm	μm
5	27.78	28.56	27.25	60.50	68.05	71.99	65.75	72.92	76.43	69.10	75.72	78.89
25	20.19	21.13	20.73	58.58	66.55	70.70	64.69	72.51	76.03	68.11	75.55	78.64
50	18.04	18.78	18.75	57.60	63.95	69.89	64.87	71.85	75.61	68.43	74.84	78.26
75	16.22	17.21	18.61	55.26	61.91	69.70	64.04	71.00	75.48	67.89	74.06	78.11
150	17.73	16.22	14.07	55.61	59.51	60.32	65.99	72.07	74.74	69.56	75.29	77.79
200	17.67	19.24	14.87	54.61	63.44	63.29	64.37	75.27	78.07	68.15	77.97	80.32
250	18.14	20.21	19.47	56.58	63.71	68.80	68.41	77.56	81.68	72.09	80.13	83.16

The preservation of the cell wall structure during pyrolysis suggested that the biomass maintains its macro-porosity even under pyrolysis conditions. This implied that the intra-particle mass transfer resistance for the pyrolysis vapors to escape from the particle was low. For a particle with a length of 700 μm and a pore size of the order of 5 to 10 μm, the characteristic time for vapor diffusion along the length of the particle was of the order of 0.50 sec, when the effective diffusion coefficient was assumed to be $10^{-6}\ m^2/s$ [100]. However, the vapor would not always travel along the length of the particle it could also travel radially as a result of formation of pores on the cell wall of biomass during pyrolysis.

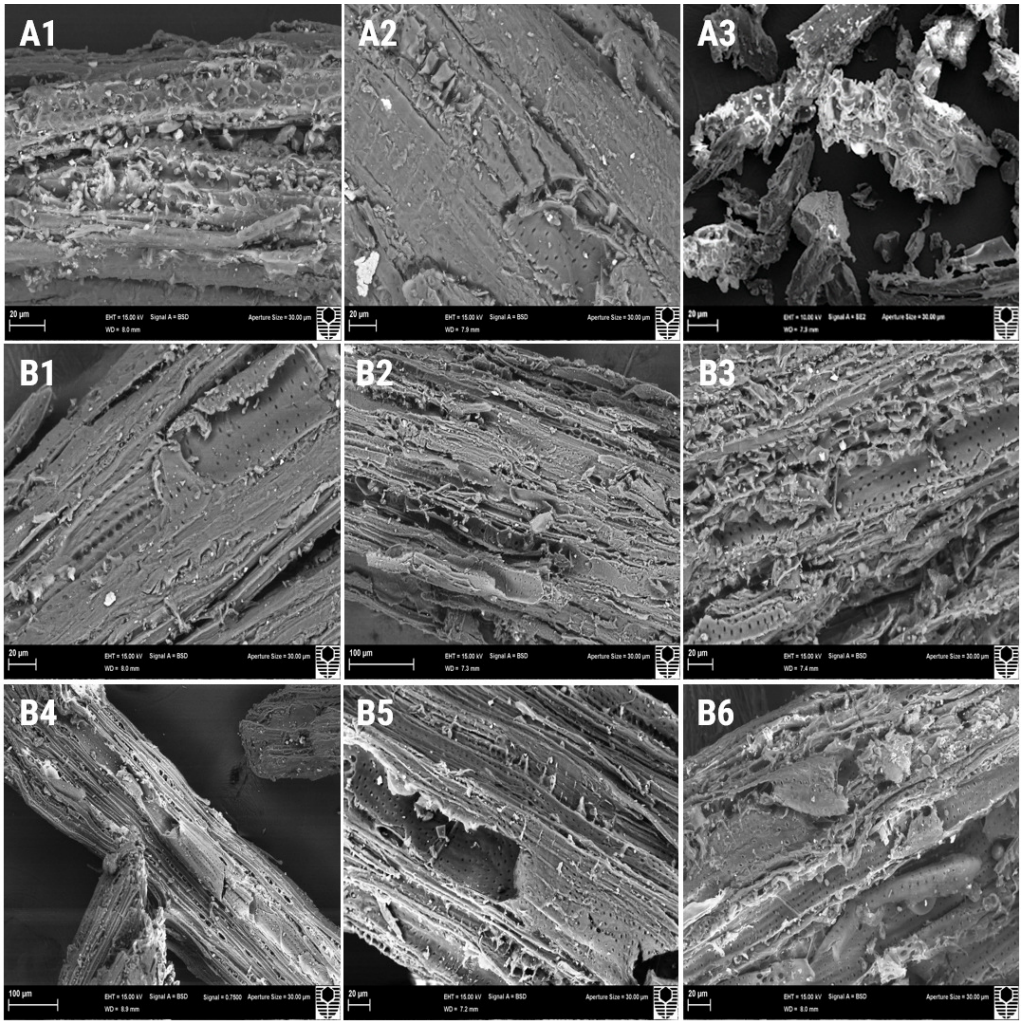

Figure 3.6: SEM images of (A1, A2) Biomass (300 to 425 μm); (A3) Biomass ($\leq$45μm); intermediate biochar obtained for biomass particle size of 300 to 425 μm at 300 °C under heating rates of (B1) 5 °C/min, (B2, B3) 25 °C/min, (B4) 75 °C/min, (B5) 150 °C/min and (B6) 250 °C/min

The pores formed on the cell wall because volatiles evolved as a consequence of bubble eruption [76, 71]. Biomass particle passed through an intermediate vis-

coelastic phase and pyrolysis vapors nucleated in the form of bubbles inside the partially molten phase. Melting could occur as a result of thermal lag [192] or partial depolymerization [78] at moderate heating rates, where the depolymerized product might condense immediately inside or on the surface of the particle. The particle sizes considered in this study do not experience considerable thermal lag ([53] and Figure 3.2). Therefore, biomass surface melting could be explained by partial depolymerization that generated non-volatile and volatile oligomers. The high resolution SEM images in Figure 3.7 (A1) to (A4), where the cell wall was in focus, showed the presence of bubbles (length scale 10^1 nm) on surface [53]. As the heating rate increased, the mean diameter of the bubble decreased while the number density of bubbles increased. This was in accordance with the nucleation phenomenon, where slow heating rates allow nuclei growth, which subsequently erupted as large bubbles to release the volatiles. The bubbles in the cell wall experience overpressure at high heating rate which caused formation of a open structured solid as compared to unreacted biomass [79]. Therefore, beyond a certain heating rate, 150 °C/min in this case, the amount of volatiles released increased at 300 and 400 °C despite decreasing reaction time (Table 3.8).

Figures 3.7 (A5) and (A7) show bubble features, with a diameter of the order of 20 to 40 μm, that formed on outer surface of the biomass particle when the heating rate of TGA program was greater than or equal to 75°C/min. This might be due to large amount of vapor accumulated inside biomass particle having a viscous liquid boundary at the surface. Formation of large bubbles could hinder the release of vapors. Optical microscope image in Figure 3.7 (A7) revealed that bubble features, marked from 1 to 4, were preserved even after holding the biochar at 700 °C for 20 min, indicative of cross-linking reactions which increased the mechanical strength of the bubble boundary. However, some bubbles might erupt at high temperatures, which could explain the increase in the height of the second peak in DTG curves for biomass particle size of 75 to 106 and 300 to 425 μm (Figure 3.5 (d) to (f)). The vapor trapped inside the bubbles might not be originating only from particle surface but might be coming from inside the particle. If this was true, the large bubbles may result in formation of open pore structure. This could serve as an alternative explanation for the data representing an increase in

biomass conversion beyond 150 °C/min presented in Table 3.8. Further, though large bubbles were not observed when the initial biomass particle size in $\leq$45 μm, the formation of loosely bound agglomerate above 150 °C/min, shown in Figure 3.7 (A8) also demonstrated presence of intermediate molten phase during pyrolysis. Shrinkage also appears to occurred from the edges of the agglomerate as a whole.

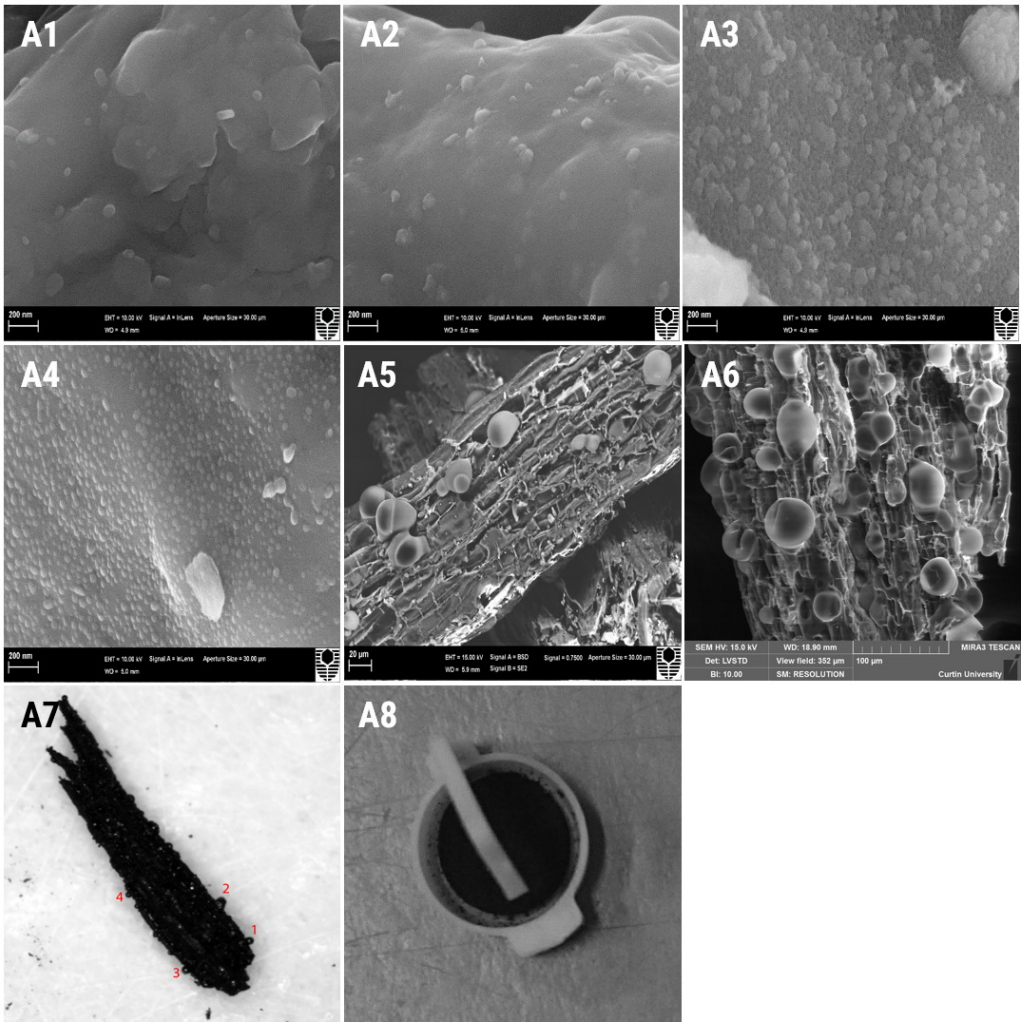

Figure 3.7: SEM images of biochar obtained at the end of TGA program with heating rate (A1) 25 °C/min, (A2) 75 °C/min, (A3) 150 °C/min, (A4) 250 °C/min; intermediate biochar obtained for biomass particle size of 300 to 425 μm at 300 °C under heating rates of (A5) 75 °C/min, (A6) 250 °C/min; optical microscope image for biochar obtained at the end of TGA program with heating rate of 150 °C/min for biomass particle size of (A7) 300 to 425 μm and (A8) $\leq$45μm

Optical microscope images (Figure 3.8) also revealed particle shrinkage along the smaller dimension of the particles. Image analysis of particles (300 to 425 μm) showed that the average external surface area (average of 82 particles) of unre-

acted biomass particles was 0.622 $\pm$ 0.236 mm^2. The average external surface of solid particles obtained under 5 °C/min and 250 °C/min was 0.364 $\pm$ 0.156 mm^2 (averaged over 48 particles) and 0.442 $\pm$ 0.136 mm^2 (averaged over 32 particles) respectively. The percent reduction in area due to shrinkage, based on initial external surface area, for particles obtained at 5 and 250 °C/min was 41.48 $\%$ and 29.01 $\%$ respectively. Despite same final conversion value, the reduction in the external surface area of 300 to 425 μm biomass particle at high heating rate was less because of possible pyrolysis product accumulation within the particle.

The foregoing discussion indicates that, morphological changes during decomposition would not lead to a constant shift in all measurement temperatures of the TGA and DTG curves with respect to the heating rate [78]. The morphological changes affect volatilization rate and hence, affect the value of DAEM parameters. Also, as large bubbles were observed beyond 300 °C, a good approach for simulating DTG curves would be considering temperature dependence of frequency factor in the kinetic expression ($A=A_0T^m$). Further, the choice of TGA data generated at different heating rates for obtaining the DAEM parameters would affect the predictability of TGA curves for heating rates outside the range considered in this study.

(a)

The figure is continued on the next page...

Figure 3.8

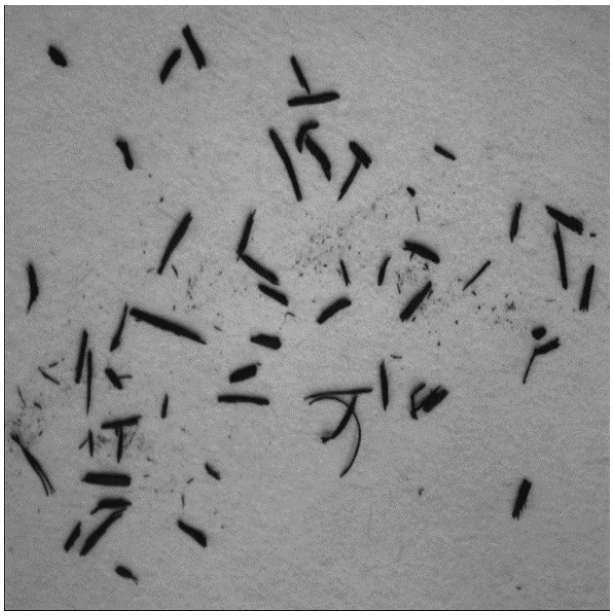

(b)

(c)

Figure 3.8: Optical microscope images of particles before and after pyrolysis (a) Biomass, 300 to 425 μm, (b) Biochar obtained at 5 °C/min, (c) Biochar obtained at 250 °C/min.

3.6.3 TGA data analysis using isoconversion method

Among different isoconversion methods, the most widely used method is Friedman method (Table 3.1). The Friedman method uses instantaneous reaction rate values for determination of activation energy, and frequency factor. The advantage of the method is that it does not require an assumption of any reaction model.

The profile of apparent activation energy (Figure 3.9) with respect to conversion offers some insight into probable mechanism of the reaction [176]. For all the particle sizes considered in this work, qualitative and quantitative profiles of activation energy with respect to extent of conversion were not significantly different.

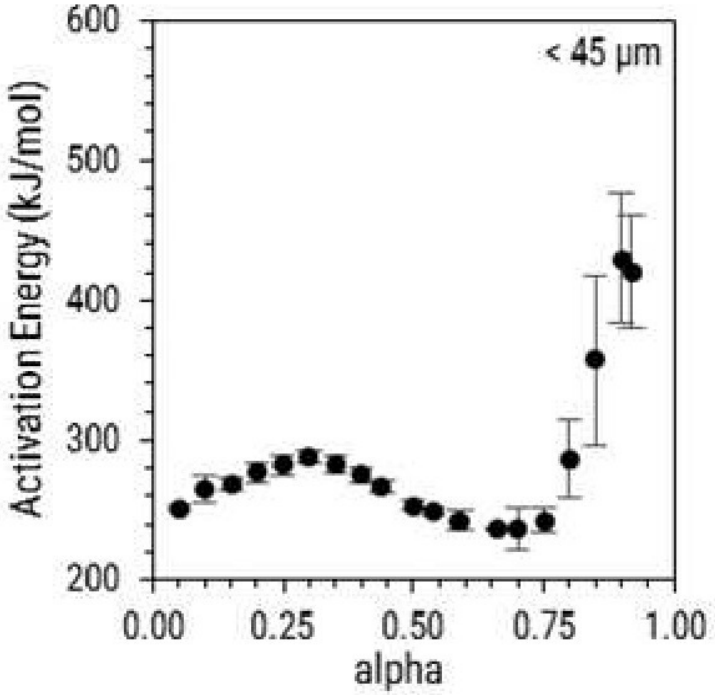

(a)

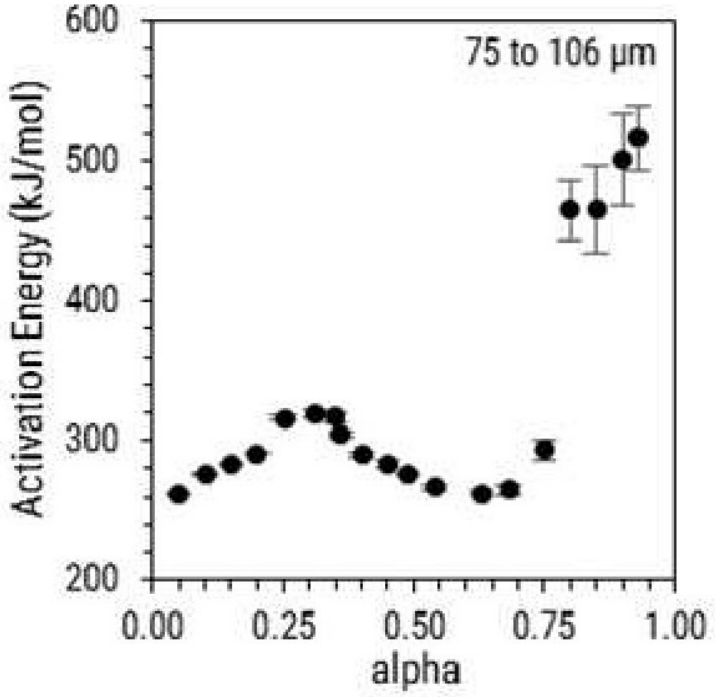

(b)

This figure is continued on the next page...

Figure 3.9

The activation energy increases linearly up to α=0.3 and then decreases in a slightly concave manner from α=0.3 up to α=0.7. Beyond α=0.7 the activation energy in-

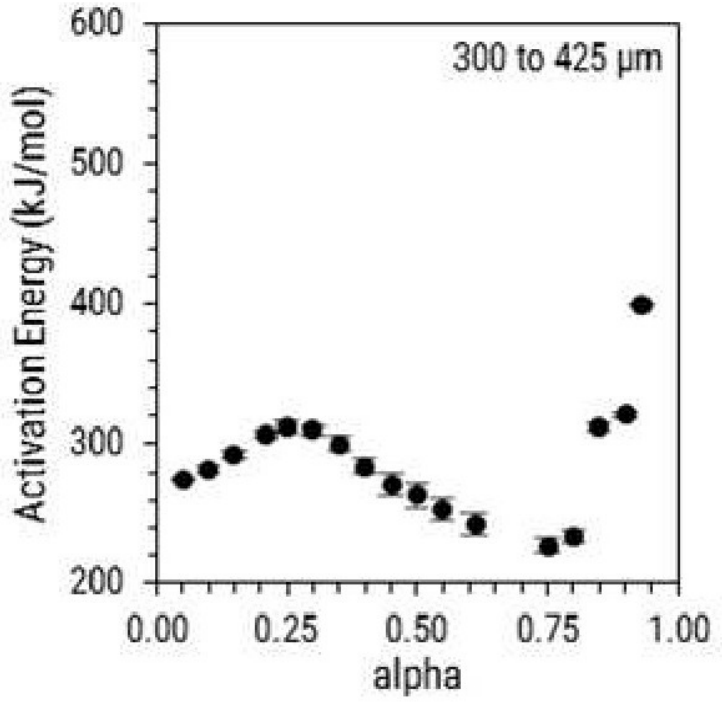

(c)

Figure 3.9: Isoconversion method plots for three particle sizes. Variation of activation energy with respect to extent of reaction.

creases again which corresponds to the presence of competitive parallel reactions [176]. After α=0.3 there is a transition or a change in the rate limiting step and the slight concave decrease of the activation energy may indicate reversible reaction [176]. On the other hand, the profile of frequency factor (Figure 3.10) versus activation energy shows kinetic compensation effect, which indicates that there must be multiple chemical changes originating from similar chemical structure or due to differences arising due to heat and mass transfer limitations [193]. As the heat transfer coefficient is of the order of 10 W/mK, Biot number of all the biomass particles was assumed to be less than 1. Therefore, the linear decrease of ln(A) from α=0.3 to α=0.7 implied that there are iso-kinetic reactions/processes occurring in these regimes. This also suggested that different reactions/processes occurred over similar time scale and were thus, difficult to decouple.

Furthermore, the obtained profile of activation energy was used to determine the reaction model using Eq. 3.3 in section 3.3. The plots for different reaction models in Table 3.2 are shown in Figure 3.11 ((d) to (f)). Experimental values of the left hand side of Eq. 3.3 compared well qualitatively with all the Avrami-Erofeev mod-

els, and the random scission model. Reaction models DP and A2 were selected for fitting the DAEM parameters to biomass pyrolysis. The random scission model used here assumes that products that have a degree of polymerization greater than two are non-volatile [174]. The assumption enables analytical integration of $f(\alpha)$, which is required to derive the DAEM equations for random scission model. Moreover, microscopic evidence of molten phase and bubble nucleation on the biomass surface justify the approximation of DP and A2 reaction models. First order reaction model is widely used for determining the kinetic parameters of biomass devolatilization. Therefore, DAEM parameters were also obtained assuming first order (F1) reaction model.

3.6.4 DAEM kinetic parameters

The DAEM parameter optimization was carried out considering different cases mentioned in Table 3.9. The effect of reaction model, and TGA, DTG, and differentiated DTG curves corresponding to different set of heating rates on DAEM parameters was considered in the study.

Table 3.9: Details for different cases used for DAEM parameter optimization.

Case no.	Heating rates used for DAEM parameter optimization (°C/min)
Reaction Model: F1	
Case 1	5 to 250
Case 1A	5 to 75
Case 1B	150 to 250
Reaction Model: DP	
Case 2	5 to 250
Case 2A	5 to 75
Case 2B	150 to 250
Reaction Model: A2	
Case 3	5 to 250
Case 3A	5 to 75
Case 3B	150 to 250

3.6.4.1 Number of pseudo-components

Presence of two peaks in the DTG curve implies at least two pseudo components be used for model fitting exercise [118, 119]. Three pseudo-components were used

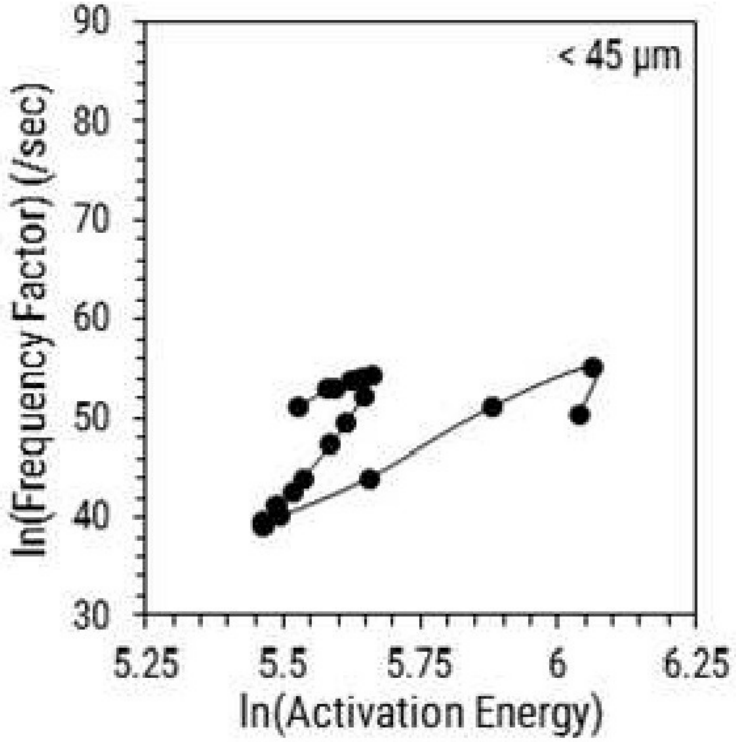

(a)

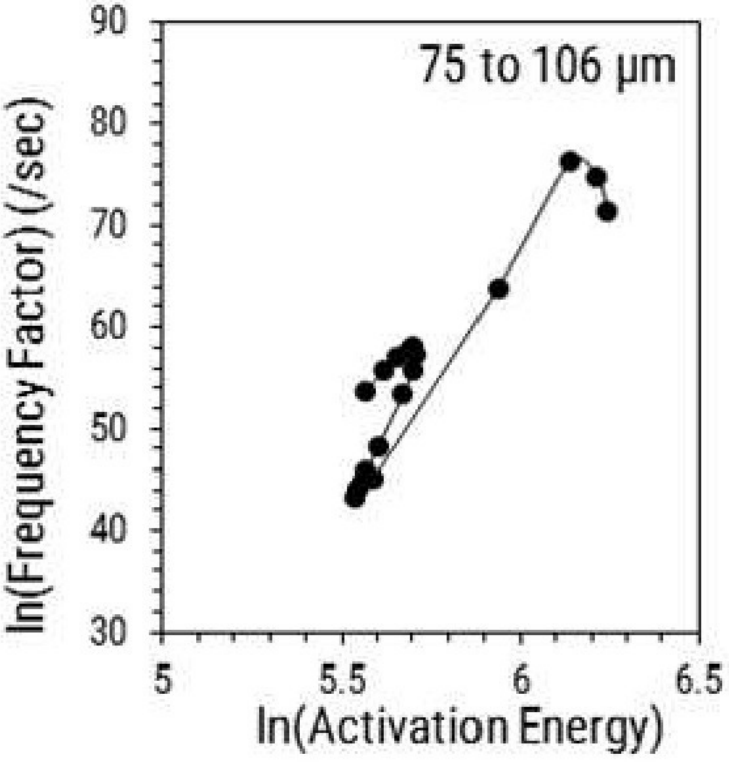

(b)

This figure is continued on the next page...

Figure 3.10

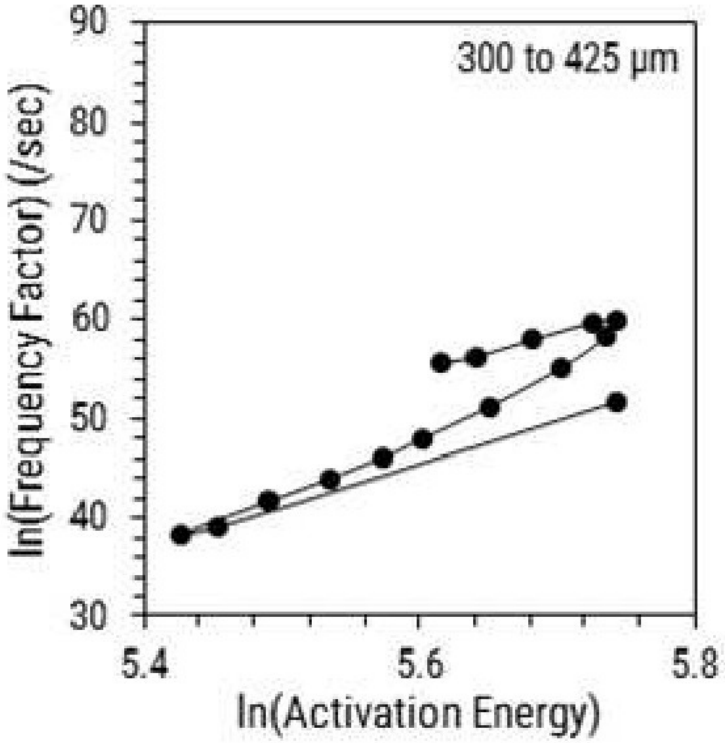

(c)

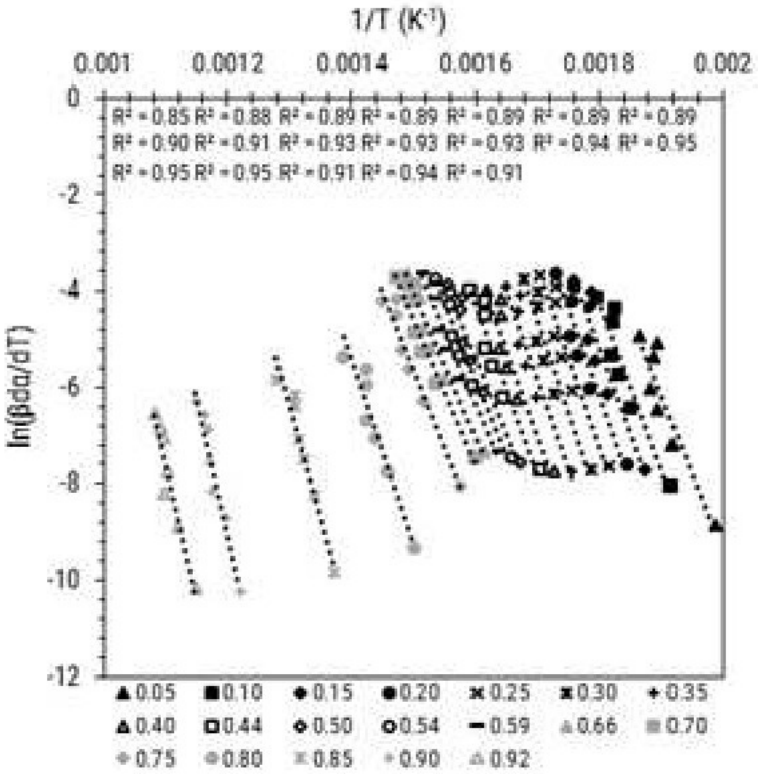

(d)

This figure is continued on the next page...

Figure 3.10

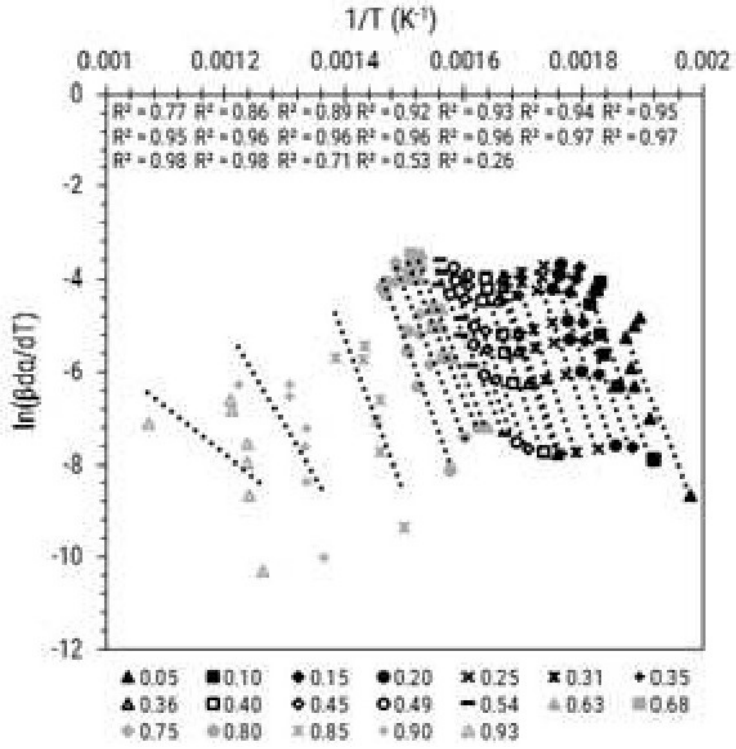

(e)

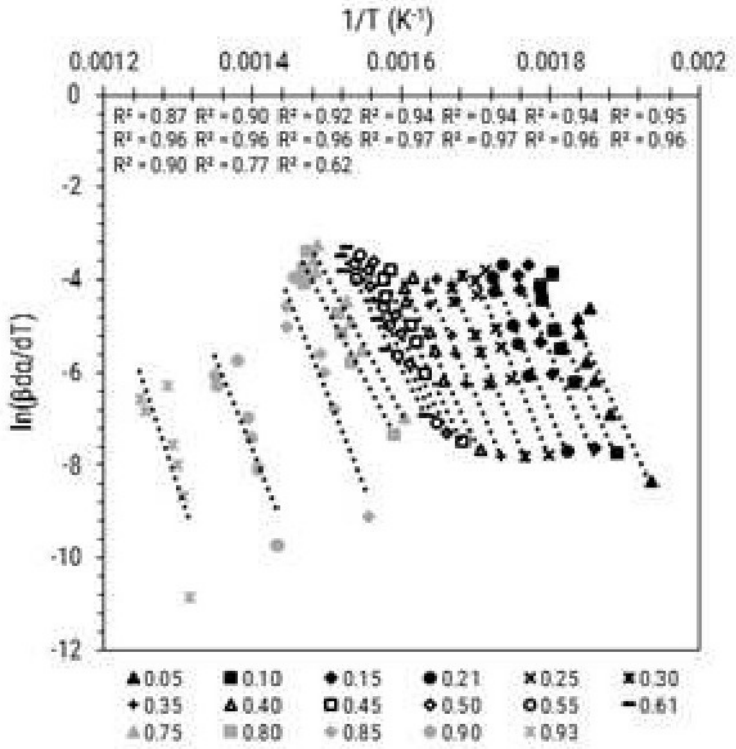

(f)

Figure 3.10: (a) to (c) Isoconversion method plots for three particle sizes. Variation of Frequency factor with respect to activation energy. (d) to (f) Isoconversion method plots for three particle sizes. Linearity plots for $ln(d(\alpha)/dt)$ vs. (1/T)

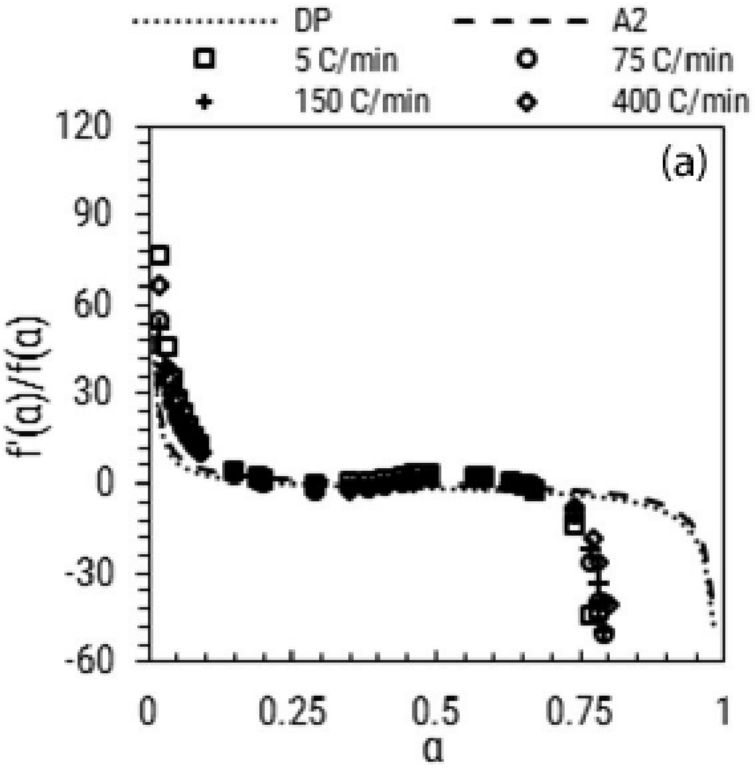

(a)

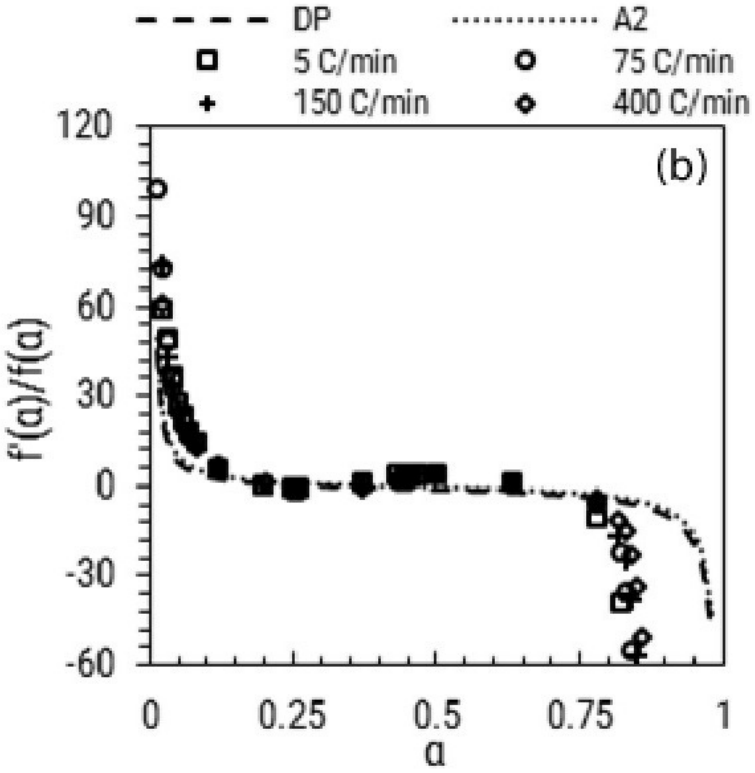

(b)

This figure is continued on the next page...

Figure 3.11

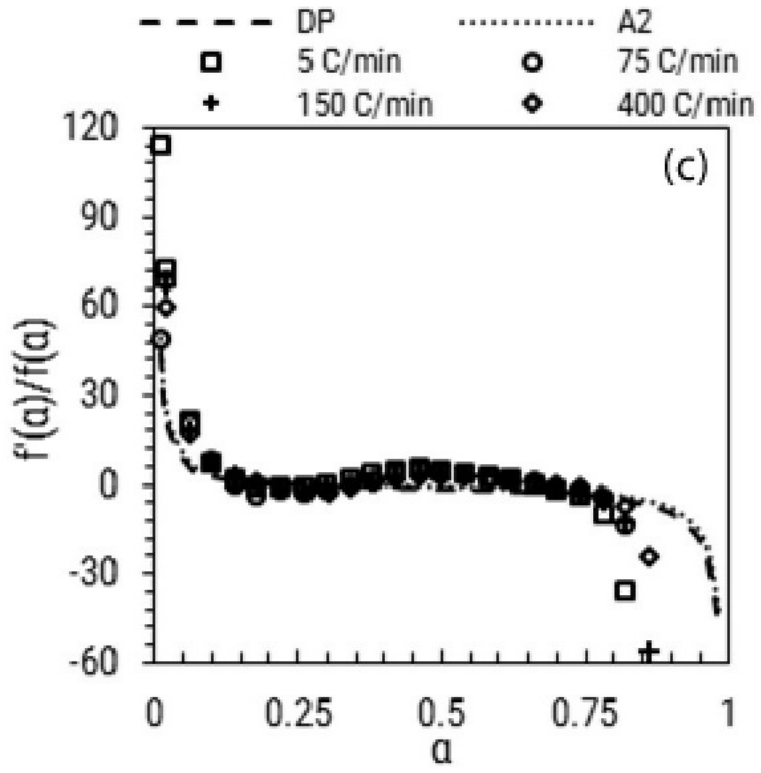

(c)

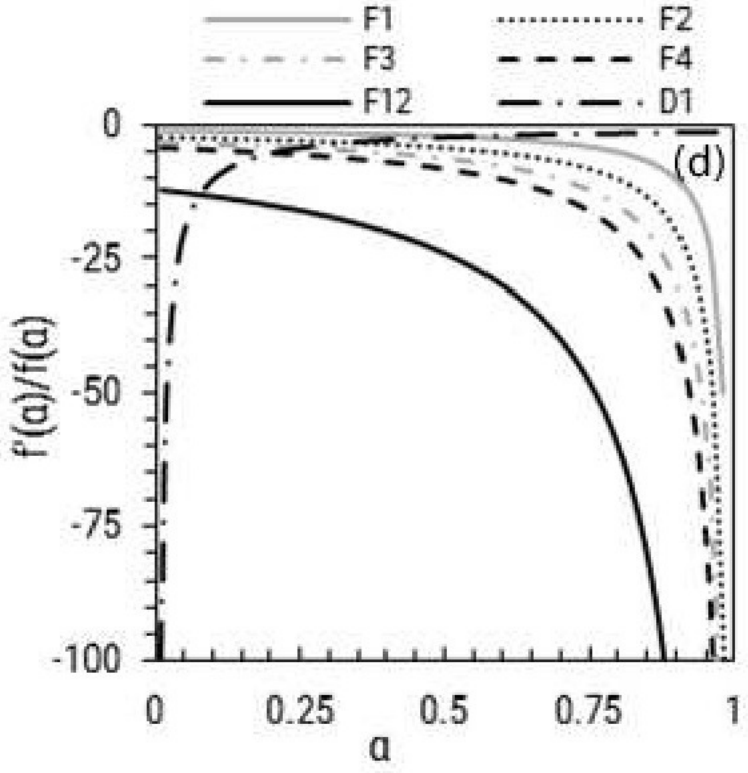

(d)

This figure is continued on the next page...

Figure 3.11

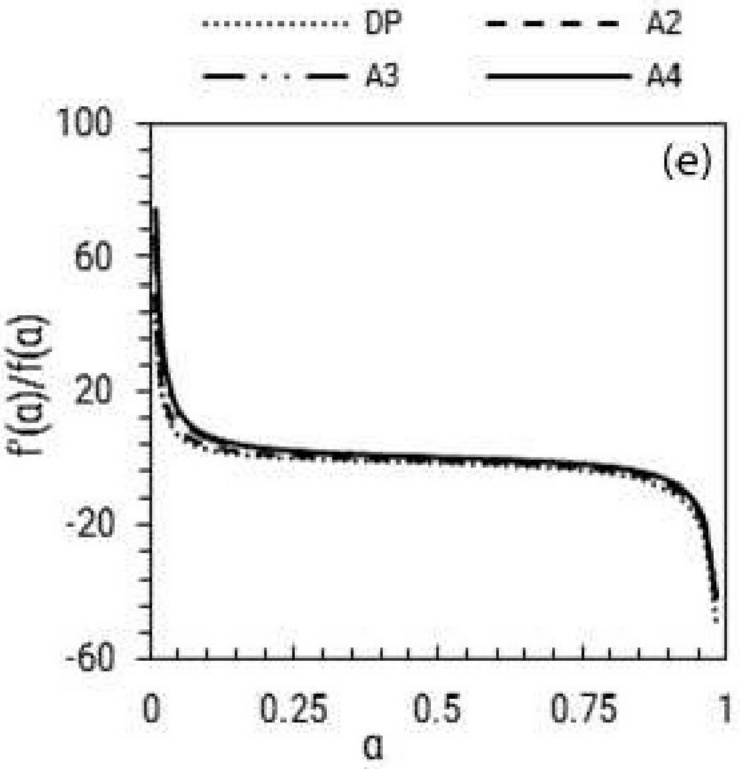

(e)

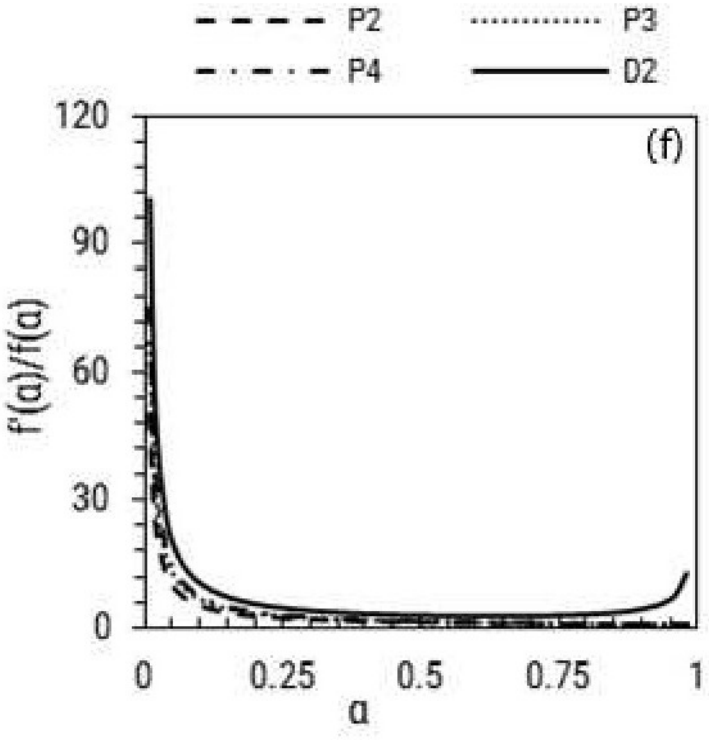

(f)

Figure 3.11: (a to c) Comparison of experimental and Model reaction plots for Eq. 3.3. (d to f) Model reaction plots for different reaction models for Eq. 3.3

to model the TGA, and DTG characteristics of the biomass under different pyrolysis conditions. The frequency factors of each pseudo-component was considered to be constant. Hemicellulose undergoes two different set of reactions [119] and hence, for the third pseudo-component single frequency factor, and a bimodal Gaussian distribution were used to represent the kinetic characteristics .

3.6.4.2 Choice of objective function

To justify the choice of objective function used in this study DAEM parameters were calculated using three different objective functions. In the first case only α values were used for evaluating DAEM parameters, that is, only J1 (Eq. (3.29)) was used as an objective function. In the second case average of J1 (Eq. (3.29)) and J2 (Eq. (3.30)) and in the third case average of J1 (Eq. (3.29)), J2 (Eq. (3.30)) and J3 (Eq. (3.31)) were used. The parameters were obtained by minimizing the objective function for all three cases using heating rates varying from 5 to 75 °C/min. Initial guess value for the parameters was kept constant for all three cases. Representative plots of experimental and predicted curves are shown in Figure 3.12. It is evident from Figure 3.12 that only using J1 as an objective function is not a good choice because the prediction for differential and double differential curves is poor as compared to second and third case. Moreover, DAEM equation in this study is a 16 parameter equation, which has multiple solutions. One way to reduce the number of solutions is to simultaneously optimize DAEM parameters for α, $d\alpha/dt$ and $d^2\alpha/dt^2$.

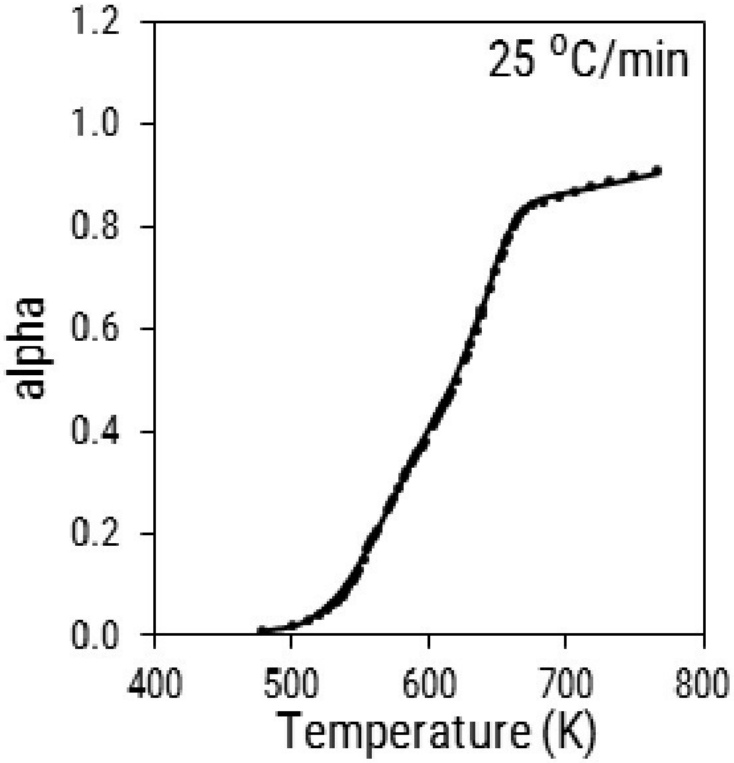

(a)

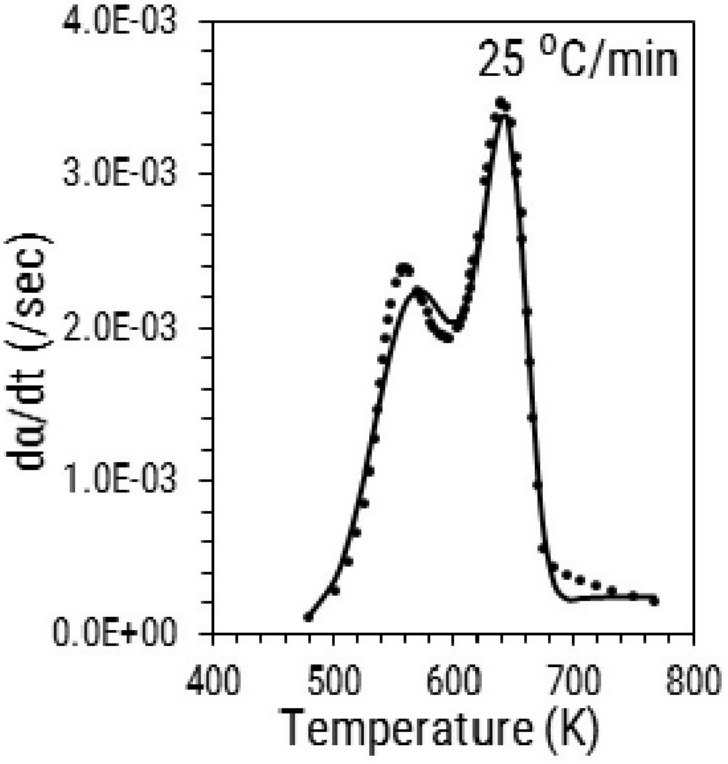

(b)

This figure is continued on the next page...

Figure 3.12

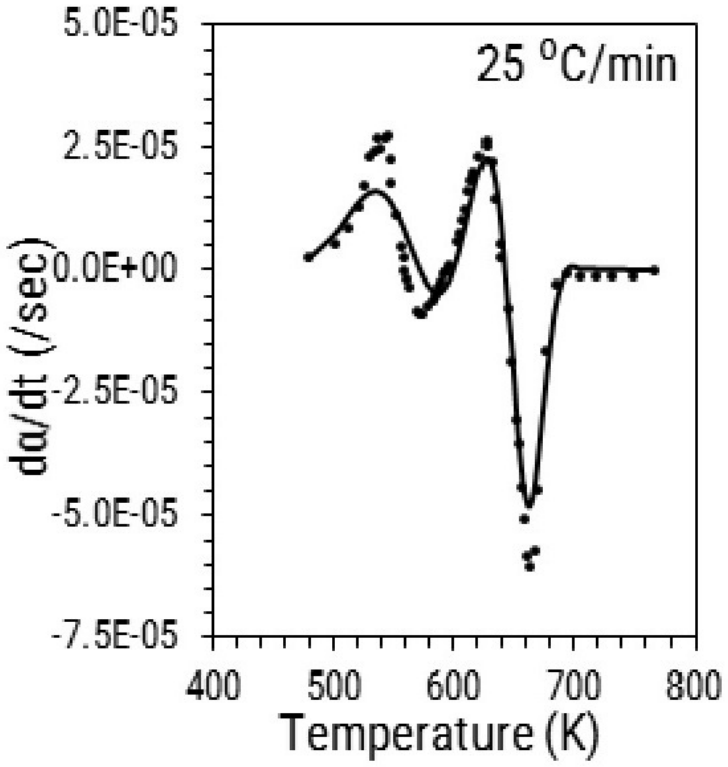

(c)

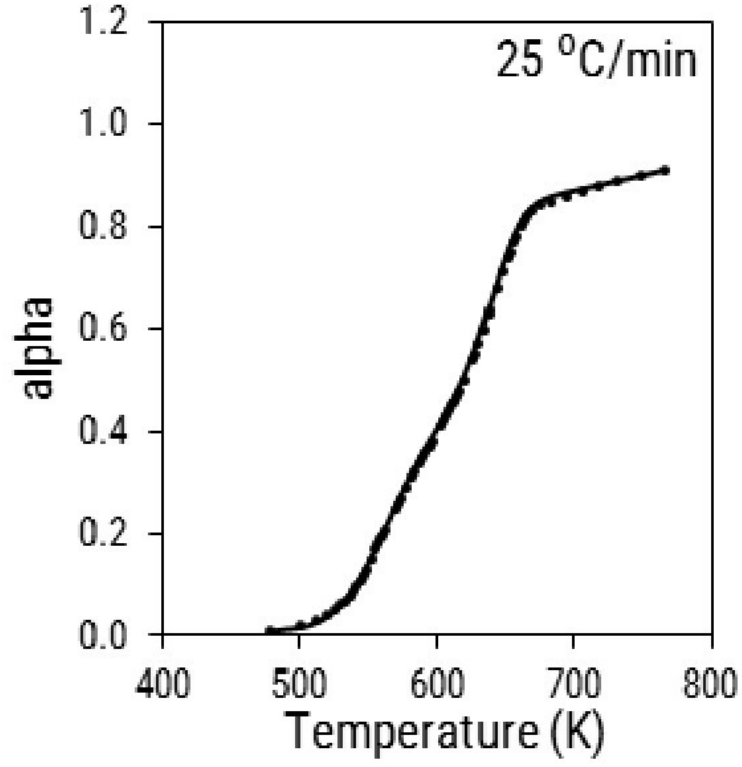

(d)

This figure is continued on the next page...

Figure 3.12

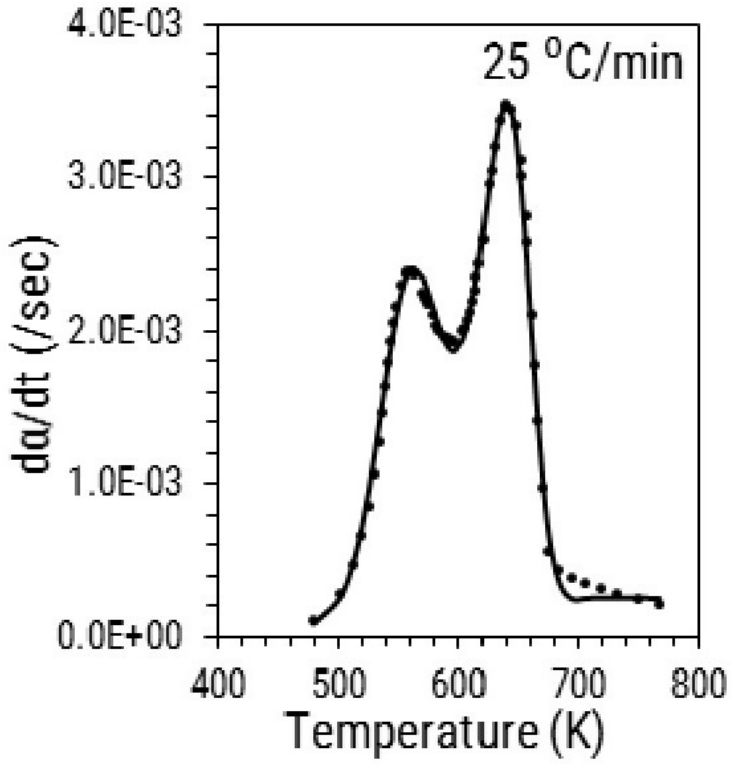

(e)

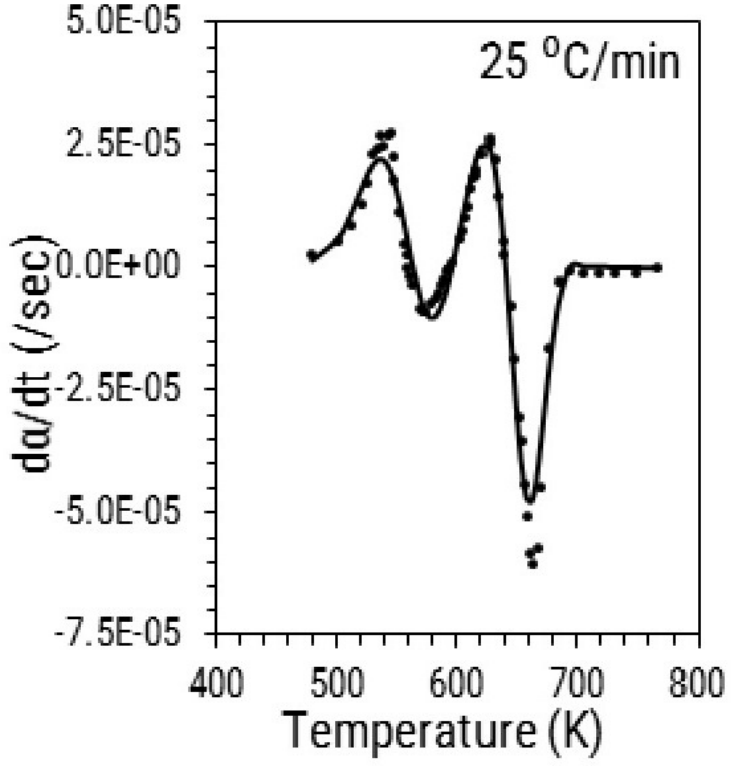

(f)

This figure is continued on the next page...

Figure 3.12

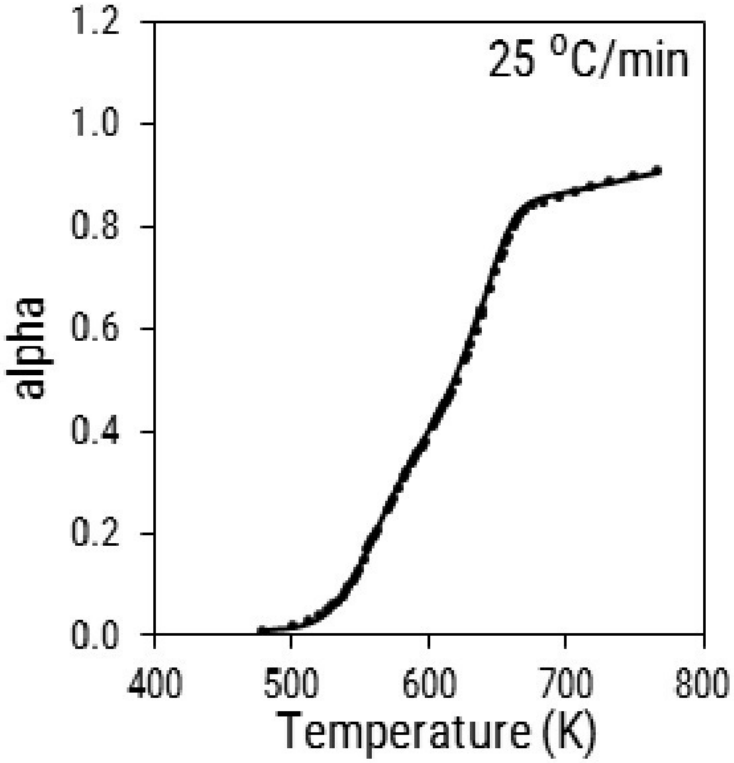

(g)

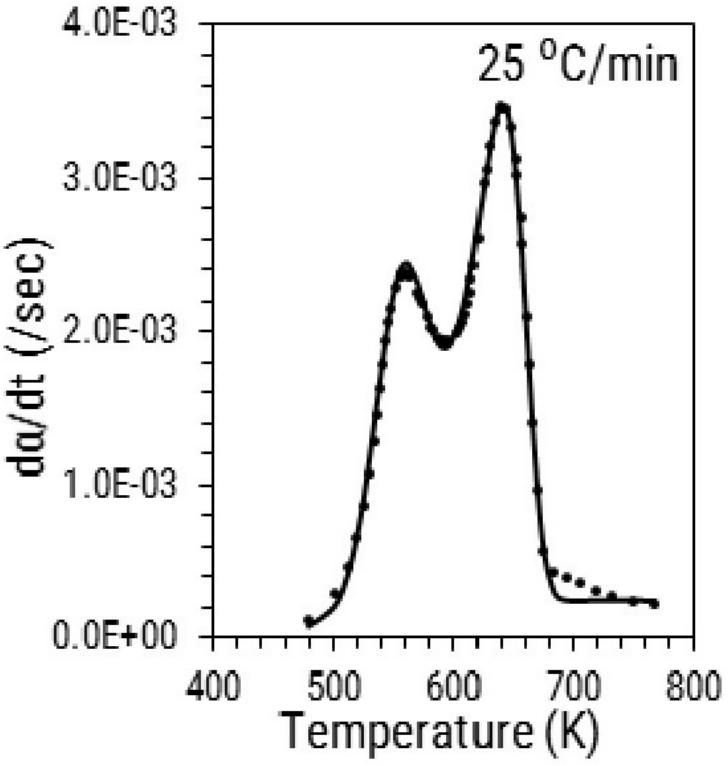

(h)

This figure is continued on the next page...

Figure 3.12

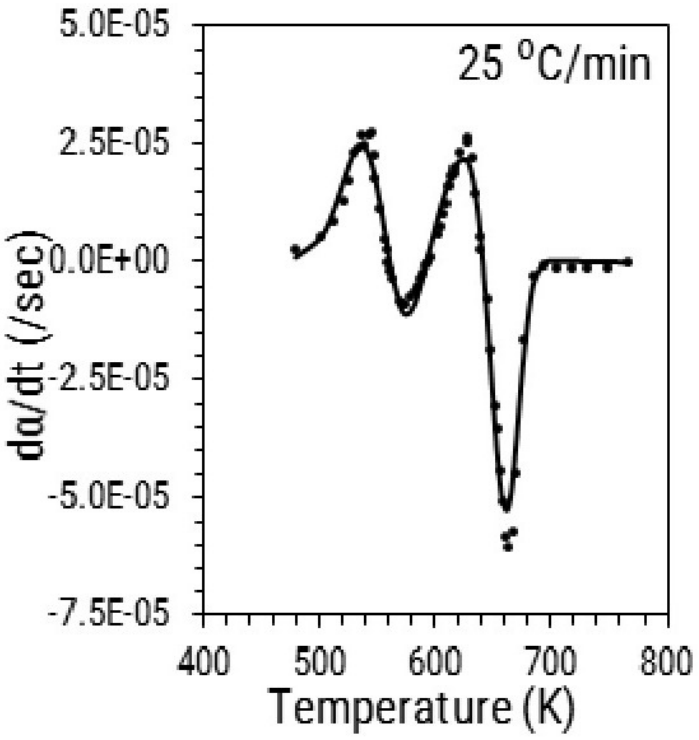

(i)

Figure 3.12: Comparison of experimental and predicted plots for α, $d\alpha/dt$ and $d^2\alpha/dt^2$ using objective function in (a) to (c) case 1, (d) to (f) case 2, and (g) to (i) case 3

There is a significant difference between the value of m between option 2 and option 3 as shown in Table 3.10. An average value of J1, J2 and J3 are used for DAEM parameter optimization.

3.6.4.3 Effect of reaction model

The infinite reactions of each pseudo-component were assumed to follow either a first order, random scission, or Avrami-Erofeev reaction model. To visualize the effect of reaction model, plots of α vs time were compared at a constant temperature of 673 K for same values of DAEM parameters (Figure 3.13). Three set of parameters were used to compare the effect of reaction model. The parameters in Table 3.11 were obtained by minimizing the objective function, J in Eq. (3.32) for heating rates varying from 5 to 250 °C/min. The parameter calculation was performed considering one reaction model at a time.

Table 3.10: Optimized DAEM parameters for a same initial guess value for Option 1: J1 is objective function, Option 2: mean of J1 and J2 is objective function, Option 3: mean of J1, J2 and J3 is objective function

Set no.	w_c	2-Gaussian model weight fractions	E_0 (kJ/mol)	σ (kJ/mol)	$\log(A_0)$ (sec^{-1})	m	obj func
initial guess	0.2262		189.229	39.883	10.511	0.2943	
	0.2383		226.236	8.216	19.283		
	0.5355	0.4473	163.038	7.110	11.857		
		0.5527	173.812	3.838			
Option 1	0.2121		190.451	39.354	6.204	1.7732	J1=0.0114
	0.4039		227.155	12.848	14.414		J2=0.0566
	0.3840	0.0214	163.588	9.292	7.935		J3=1162
		0.9786	179.569	2.178			
Option 2	0.2195		189.871	38.988	7.403	1.4532	J1=0.0144
	0.2123		226.270	8.227	15.617		J2=0.0428
	0.5682	0.3208	163.165	9.300	8.876		J3=0.0843
		0.6792	179.571	2.484			
Option 3	0.2227		189.245	39.715	10.606	0.2876	J1=0.0178
	0.2268		226.244	7.150	18.917		J2=0.0481
	0.5505	0.3443	163.057	7.429	11.718		J3=0.0753
		0.6557	174.681	0.996			

Table 3.11: DAEM parameters derived using three different reaction models for pyrolysis of biomass having particle size $\leq$45 μm. Parameters in set number, (1) derived for DP, (2) derived for F1, (3) derived for A2

Set no.	w_c	2-Gaussain model weight fractions	E_0 (kJ/mol)	σ (kJ/mol)	$\log(A_0)$ (sec^{-1})	m	obj func (J)
1	0.2768		180.139	3.582	13.062	0.0682	0.1037
	0.3418		226.840	9.758	19.776		
	0.3813	0.3317	153.219	3.075	11.643		
		0.6683	198.555	44.258			
2	0.2441		189.278	40.289	10.158	0.2103	0.1068
	0.2452		226.614	7.182	19.297		
	0.5107	0.356	164.128	5.883	12.274		
		0.644	177.291	2.970			
3	0.2105		171.258	20.200	8.736	0.1575	0.1127
	0.2766		227.505	9.300	19.877		
	0.5128	0.4784	161.544	7.445	12.333		
		0.5216	173.232	4.690			

Differences between the conversion values are prominent only in Figure 3.13 (a), while other two plots do not show considerable difference between the behavior of different reaction models. However, it was not possible to determine a priori which set of DAEM parameters would be insensitive to the reaction model used.

Therefore, all three reaction models were used to describe the volatilization behavior of biomass. The DAEM parameters calculated for reaction model, DP, were selected amongst different configurations listed in Table 3.9 and tabulated in Table 3.13.

Both random scission (DP) and Avrami-erofeev (A2) reaction models are used for description of sigmoidal reaction rates. The DP model suggests that the polymers in lignocellulosic biomass undergo homolytic scission and lead to formation of two active species which further degrade until a point where volatile species are formed. It may also involve end chain scission resulting in formation of volatile species directly. On the other hand the A2 model assumes that reactions occur at particular locations, called nuclei, in the solid. Nuclei are reactive sites in the solid and their number density depends on temperature. Thus, as the heating rate increases nuclei number density increases. These nuclei undergo different reactions and result in the formation of volatile species. Molecular modelling studies show that there is formation of active cellulose, hemicellulose, and lignin which undergo degradation to volatile species and char. These active species can either be oligomers or molecular intermediate. It is difficult to select the model based on regression coefficient because all the reaction models have physical relevance to pyrolysis reaction chemistry and have fairly close regression coefficients.

3.6.4.4 Effect of particle size and heating rate on DAEM parameters

The effect of heating rate and particle size on DAEM parameters is discussed together as the dependence on two varibales is interlinked with each other. The three different particle sizes in this study take into consideration different scales of intra-particle pore structure of biomass as discussed in section 3.6.2.3. Figure 3.14 shows the value of peak maximum increases linearly with the heating rate for all particle sizes. The slope for each line is different, which can be attributed to difference in composition of biomass particle size $\leq$45 μm and 75 to 106 and 300 to 425 μm. But, as the ash and elemental content of biomass with particle size 75 to 106 and 300 to 425 μm is quiet similar, the difference in the slope and high values of $(d\alpha/dt)_{max}$ for 300 to 425 μm can be attributed to intra-particle secondary reactions.

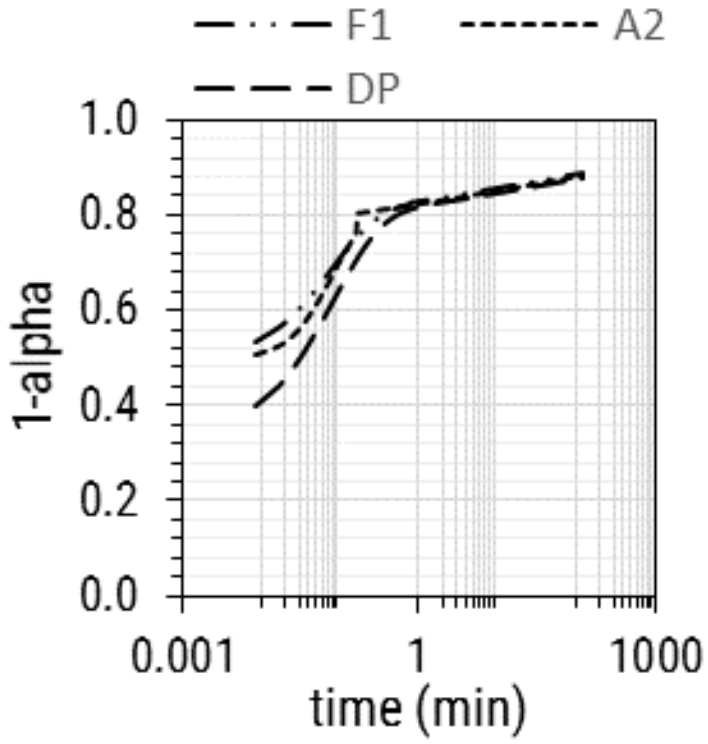

(a)

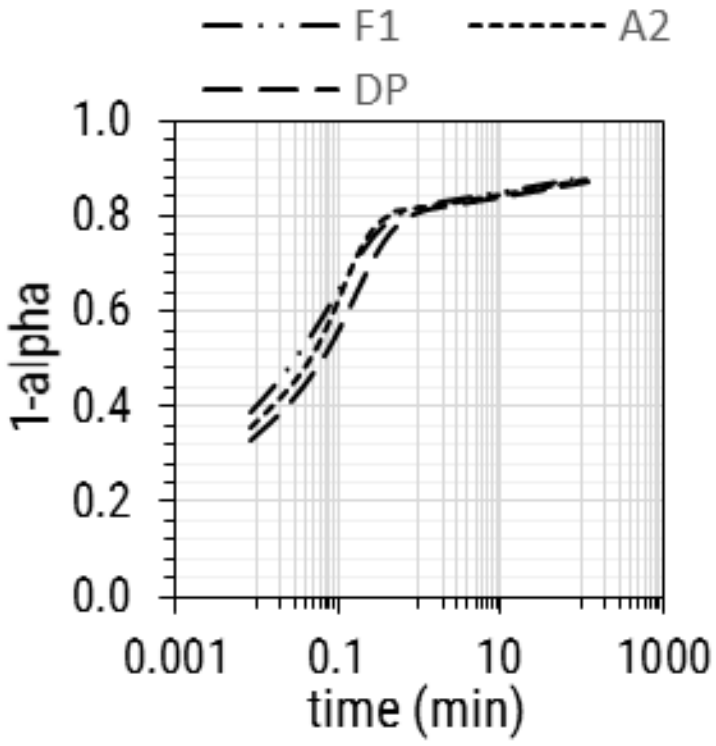

(b)

This figure is continued on the next page...

Figure 3.13

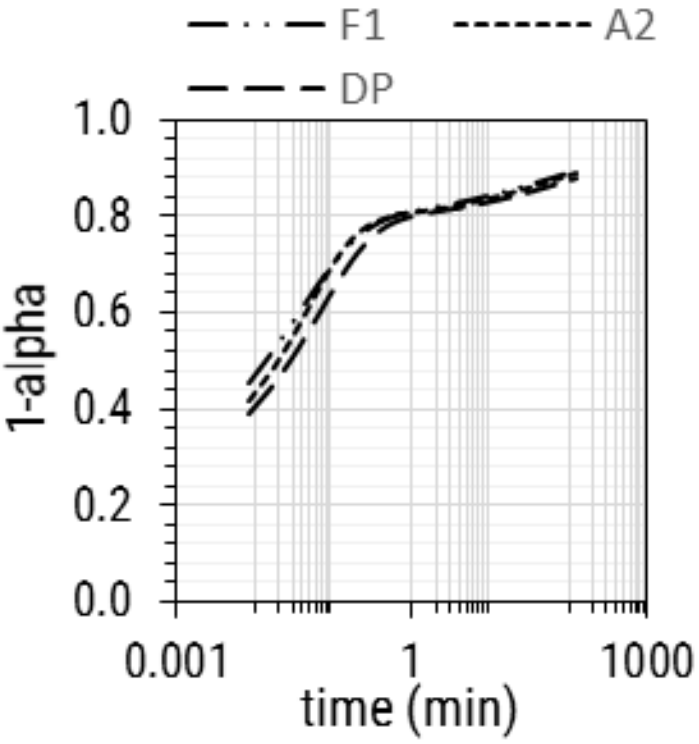

(c)

Figure 3.13: Conversion plots for three reaction models calculated using three different set of DAEM parameters in Table 3.11, (a) For set no. 1, (b) For set no. 2, (c) For set no. 3.

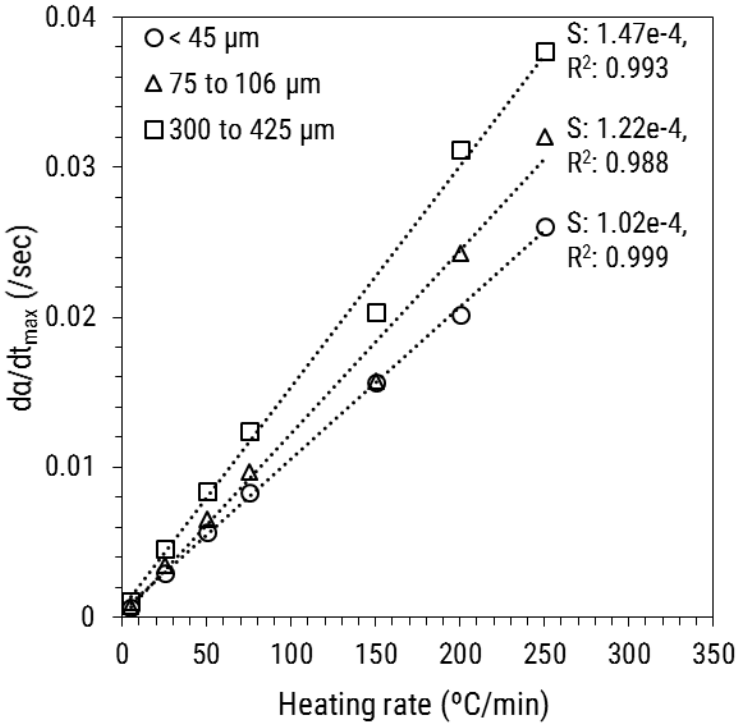

Figure 3.14: Profile of $(d\alpha/dt)_{max}$ with respect to heating rate for three particle sizes.

Table 3.12: Optimized DAEM parameters for three particle sizes for Case 1, 1A and 1B

Set no.	w_c	2-Gaussain model weight fractions	E_0 (kJ/mol)	σ(kJ/mol)	$\log(A_0)$ (sec-1)	m	obj func
Particle size $\leq$45 μm							
Case 1	0.2441		189.278	40.289	10.158	0.2103	0.1068
	0.2452		226.614	7.182	19.297		
	0.5107	0.356	164.128	5.883	12.274		
		0.644	177.291	2.970			
Case 1A	0.2704		189.200	40.318	10.131	0.1469	0.0505
	0.2682		226.188	8.728	19.195		
	0.4614	0.3316	162.347	6.881	12.092		
		0.6684	174.206	0.850			
Case 1B	0.1724		190.157	37.616	3.915	2.0853	0.0394
	0.2602		225.691	9.793	14.292		
	0.5673	0.5509	166.397	10.592	7.344		
		0.4491	179.851	2.349			
Particle size 75 to 106 μm							
Case 1	0.1744		189.209	40.283	10.203	0.2509	0.1311
	0.2539		226.323	7.737	19.298		
	0.5717	0.3554	162.517	6.278	11.950		
		0.6446	174.773	2.689			
Case 1A	0.2227		189.245	39.715	10.606	0.2876	0.0464
	0.2268		226.244	7.150	18.917		
	0.5505	0.3443	163.057	7.429	11.718		
		0.6557	174.681	0.996			
Case 1B	0.1283		189.616	39.162	6.852	0.9859	0.0402
	0.2655		226.308	8.631	17.455		
	0.6062	0.4075	162.963	7.526	10.131		
		0.5925	175.007	2.211			
Particle size 300 to 425 μm							
Case 1	0.1700		189.538	39.151	8.732	1.3973	0.1273
	0.1472		226.733	5.175	15.999		
	0.6828	0.322	163.983	11.140	9.285		
		0.678	181.712	2.622			
Case 1A	0.1309		189.660	39.508	6.520	0.7666	0.0519
	0.2193		226.114	7.873	17.252		
	0.6498	0.2204	162.343	10.008	11.020		
		0.7796	182.848	0.658			
Case 1B	0.1090		189.956	38.744	3.775	2.0387	0.0652
	0.1794		226.612	6.155	14.509		
	0.7116	0.3372	162.324	6.643	7.476		
		0.6628	179.372	2.074			

Table 3.13: Optimized DAEM parameters for three particle sizes for Case 2, 2A and 2B

Set no.	w_c	2-Gaussain model weight fractions	E_0 (kJ/mol)	σ(kJ/mol)	$\log(A_0)$ $(sec-1)$	m	obj func
Particle Size $\leq$45 μm							
Case 2	0.2369		189.484	40.473	10.240	0.3006	0.1051
	0.2952		227.277	8.929	19.318		
	0.4679	0.3013	166.075	4.723	12.391		
		0.6987	179.388	4.590			
Case 2A	0.2838		189.147	40.338	10.738	0.2288	0.0554
	0.2682		226.274	9.380	19.289		
	0.4481	0.4459	162.414	6.553	11.963		
		0.5541	173.925	2.694			
Case 2B	0.1829		189.226	40.422	9.367	0.4013	0.0254
	0.3563		225.777	10.826	19.067		
	0.4608	0.5519	163.815	7.379	11.671		
		0.4481	173.031	3.205			
Particle Size 75 to 106 μm							
Case 2	0.1812		189.224	39.893	10.590	0.3620	0.1315
	0.2685		226.250	8.839	19.236		
	0.5503	0.4847	162.904	7.114	11.733		
		0.5153	174.229	3.651			
Case 2A	0.1994		189.225	39.894	10.503	0.2774	0.0582
	0.2547		226.236	8.427	19.232		
	0.5459	0.4420	162.939	7.111	11.816		
		0.5580	173.991	2.878			
Case 2B	0.1230		189.458	38.812	8.581	0.4460	0.0498
	0.2988		226.274	9.613	19.162		
	0.5782	0.5690	164.663	7.975	11.721		
		0.4310	174.267	3.153			
Particle Size 300 to 425 μm							
Case 2	0.1773		189.261	40.022	9.960	1.2237	0.1311
	0.1693		226.614	6.019	16.779		
	0.6534	0.3796	163.067	7.952	9.514		
		0.6204	176.808	3.900			
Case 2A	0.2128		189.231	39.403	11.198	0.4679	0.0504
	0.1362		227.130	5.745	18.721		
	0.6510	0.4674	164.912	9.143	11.666		
		0.5326	179.116	1.603			
Case 2B	0.1044		189.599	39.533	6.013	1.2344	0.0301
	0.2493		226.280	7.956	16.836		
	0.6463	0.4867	164.714	7.734	9.578		
		0.5133	175.866	2.756			

Table 3.14: Optimized DAEM parameters for three particle sizes for Case 3, 3A and 3B

Set no.	w_c	2-Gaussain model weight fractions	E_0 (kJ/mol)	σ(kJ/mol)	$\log(A_0)$ (sec-1)	m	obj func
Particle size $\leq$45 μm							
Case 3	0.2869		189.199	40.255	10.748	0.3493	0.1122
	0.2727		226.139	9.414	19.191		
	0.4405	0.4324	162.846	6.811	11.871		
		0.5676	173.947	4.655			
Case 3A	0.3130		189.163	40.304	10.792	0.313	0.0600
	0.2534		226.191	9.078	19.150		
	0.4336	0.4561	162.651	6.662	11.805		
		0.5439	173.630	3.762			
Case 3B	0.1821		177.615	26.297	9.122	0.1941	0.0503
	0.3198		225.915	10.164	19.811		
	0.4980	0.5894	161.092	8.073	12.184		
		0.4106	170.884	4.235			
Particle size 75 to 106 μm							
Case 3	0.2002		189.142	40.319	10.819	0.3241	0.1349
	0.2776		226.205	9.185	19.400		
	0.5223	0.4546	162.839	6.629	11.871		
		0.5454	173.461	4.643			
Case 3A	0.2262		189.229	39.883	10.511	0.294	0.0579
	0.2383		226.236	8.216	19.283		
	0.5355	0.4473	163.038	7.110	11.857		
		0.5527	173.812	3.838			
Case 3B	0.1903		189.322	37.092	11.065	0.3882	0.0680
	0.2445		226.848	8.859	19.504		
	0.5652	0.5676	164.505	8.677	12.079		
		0.4324	175.112	4.166			
Particle size 300 to 425 μm							
Case 3	0.1670		189.327	39.556	9.284	0.7914	0.1388
	0.2007		226.415	6.642	18.045		
	0.6323	0.4390	164.158	7.711	10.611		
		0.5610	174.276	4.403			
Case 3A	0.2079		189.323	39.568	9.287	0.6150	0.0593
	0.1880		226.368	6.347	18.328		
	0.6041	0.4652	163.794	7.573	10.948		
		0.5348	174.354	2.735			
Case 3B	0.1481		189.293	39.560	8.105	0.7896	0.0718
	0.2305		226.242	7.386	18.127		
	0.6213	0.4776	163.289	7.440	10.792		
		0.5224	174.073	3.679			

As particle size increases, the amount of time spent by vapors inside the particle increases. Vapor molecules may undergo secondary cracking reactions [29] generating gases or lower molecular weight volatiles which can escape the particle without condensation. The height of the second peak is maximum for heating rate of 5 °C/min for both particle sizes as the time spent by the vapor molecules at elevated temperatures is maximum. Dufour et al. [35] used the concept of characteristic time to compare various mass transfer steps occurring during pyrolysis. As mentioned in section 3.6.2.3 and referring to Table 3.5, the time required for volatile products to come out of a particle with length of approximately 1200 μm is 1.44 sec. The time scale of vapor diffusion is comparable to the characteristic reaction times required for 90% conversion of pseudo-components 3 and 4 (Figure 3.15). Between 600 to 680K the reaction times are comparable to the vapor diffusion time scale. This is the temperature range where the second peak appears for all the heating rates and for all the particle sizes. The increased rate of conversion also explains the low solid residue left after pyrolysis of 300 to 425 μm particle as shown in Table 3.7. Further, when the ratio of $(d\alpha/dt)_{max}$ for 75 to 106 to 300 to 425 μm is calculated at any heating rate upto 200°C/min, the value is 0.766$\pm$0.020. But, the ratio increases to 0.85 for 250°C/min, where the bubble formation density on the biomass surface is highest. Thus, the increase in peak height at high heating rate can also be attributed to formation of open pore structure.

As shown in Table 3.13 the value of m for case 2B is higher as compared to 2A for all particle sizes. The increased dependence of frequency factor on temperature can be attributed to formation of large bubbles on the surface of biomass particle only after 300 °C and beyond a heating rate of 75 °C/min. Also as the particle size increases the pseudo component mass fraction for reactions corresponding to low activation energy increases which accounts for the increasing height of second peak (Figure 3.14). Different particle length scales and heating rates affect the apparent biomass conversion time during pyrolysis reactions through changes in morphology of biomass particle. Thus, the DAEM parameters, optimized for different particle sizes and heating rates account for the different resistances present in biomass pyrolysis process.

The predictive ability of DAEM changes depending on the heating rates used for

parameter optimization. Predicted curves obtained for 250 °C/min using DAEM parameters, optimized for case 2 and case 2A, showed a poor fit to the experimental data (Figure 3.16 (a) and (b)). The simulated curves for 25 and 75 °C/min in Figure 3.16 (c) did not match the experimental data as good as it did when DAEM parameters from case 2 and case 2A were used. DAEM parameters, optimized for low heating rates (5 to 75 °C/min), are unable to fairly predict the curves for high heating rates because of the uneven shift in the TGA curves with increase in heating rates.

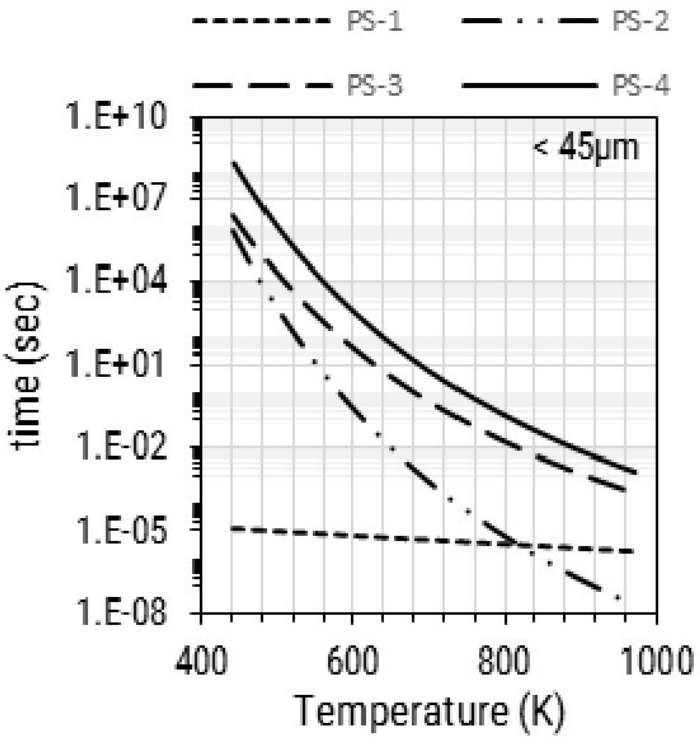

(a)

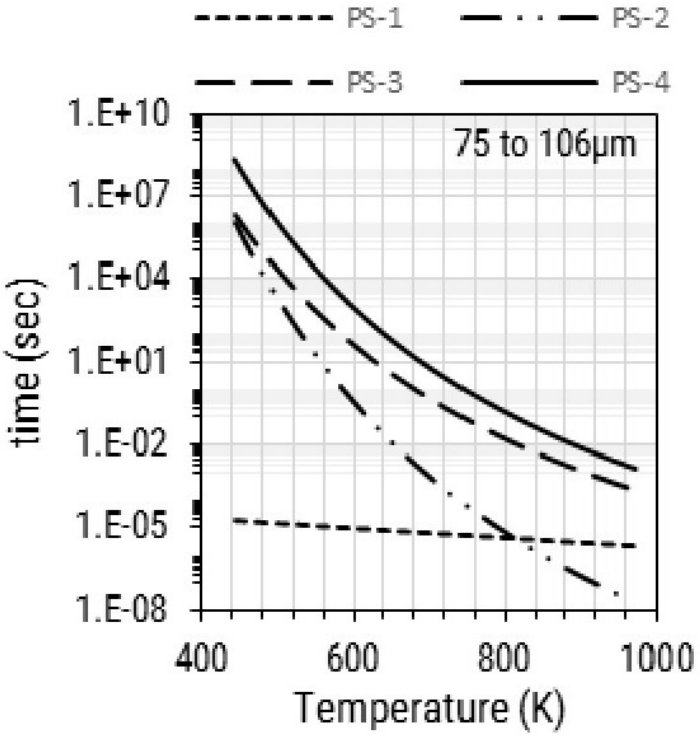

(b)

This figure is continued on the next page...

Figure 3.15

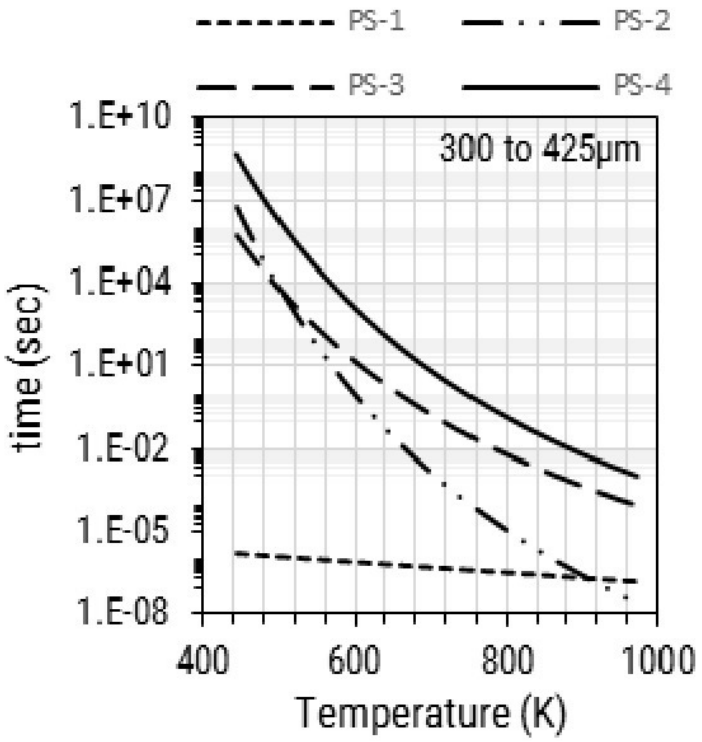

(c)

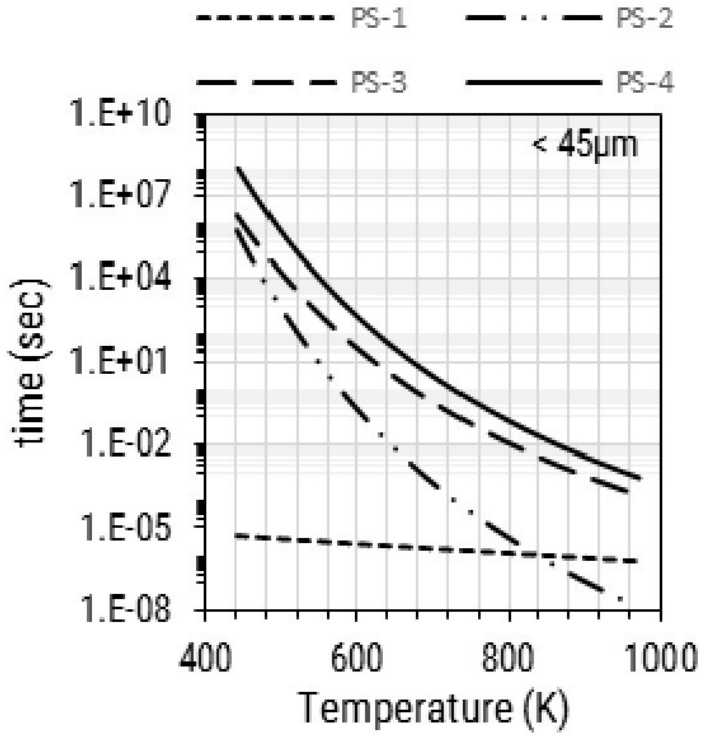

(d)

This figure is continued on the next page...

Figure 3.15

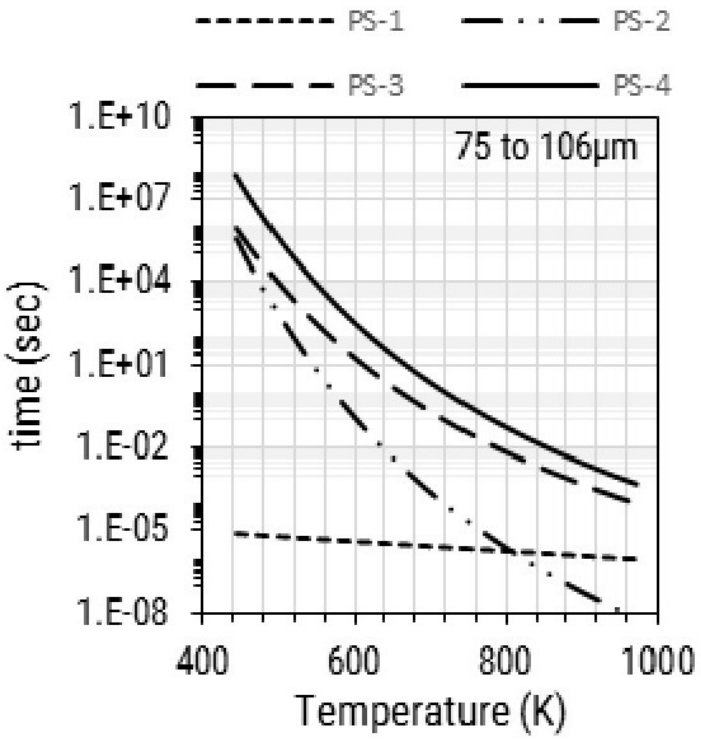

(e)

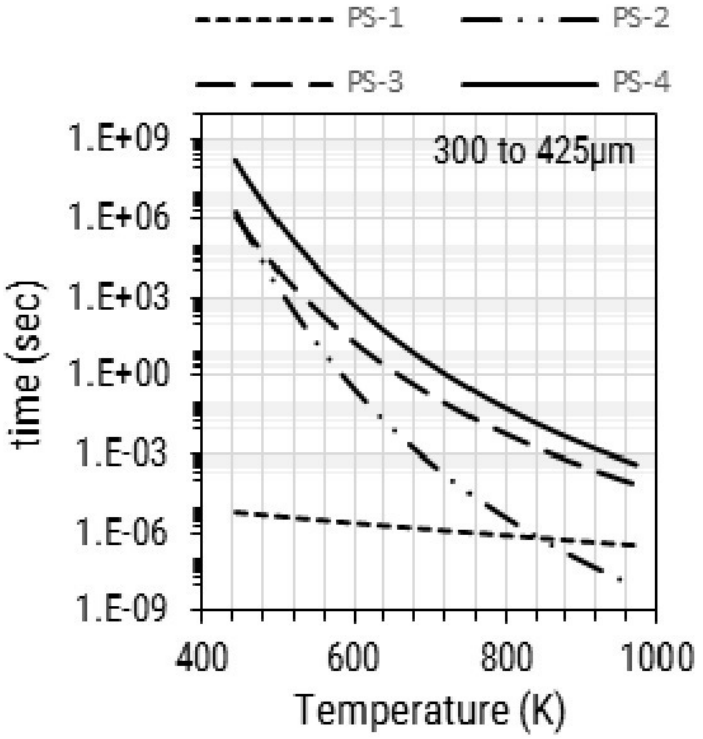

(f)

Figure 3.15: Characteristic time values corresponding to 90% conversion for three particle sizes calculated using the DAEM parameters obtained for (a) to (c) Case 2A and (d) to (f) Case 2B

The predictive ability of DAEM changes depending on the heating rates used for parameter optimization. Predicted curves obtained for 250 °C/min using DAEM parameters, optimized for case 2 and case 2A, showed a poor fit to the experimental data (Figure 3.16 (a) and (b)). The simulated curves for 25 and 75 °C/min in Figure 3.16 (c) did not match the experimental data as good as it did when DAEM parameters from case 2 and case 2A were used. DAEM parameters, optimized for low heating rates (5 to 75 °C/min), are unable to fairly predict the curves for high heating rates because of the uneven shift in the TGA curves with increase in heating rates. The uneven shift TGA curve with temperature at high heating rates (150 to 250 °C/min) was a result of significant change in morphology of the biomass particle. Formation of intermediate liquid phase, large bubbles, and subsequent formation of open pore structure alters the volatile evolution profile. Therefore, it is essential to optimize the DAEM parameters separately for heating rates beyond which there are significant morphological changes in biomass particle undergoing pyrolysis.

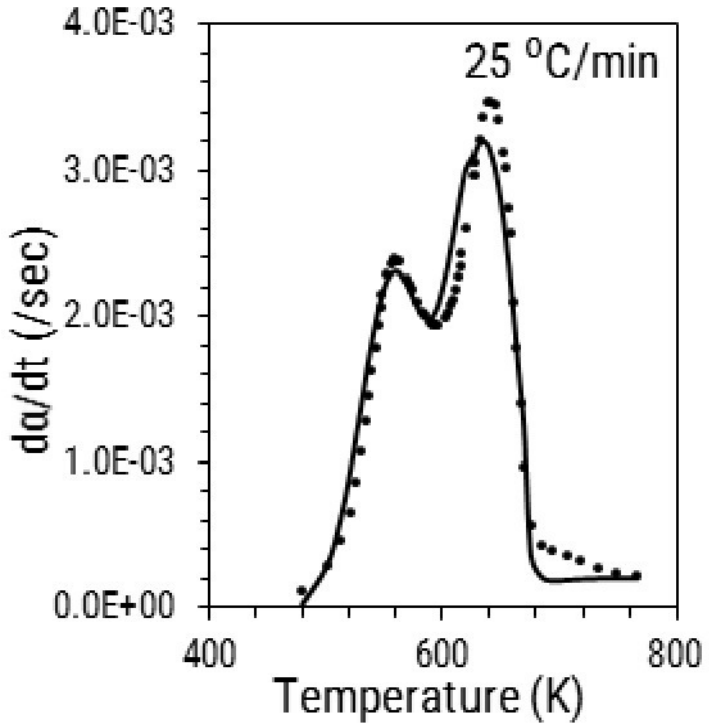

(a)

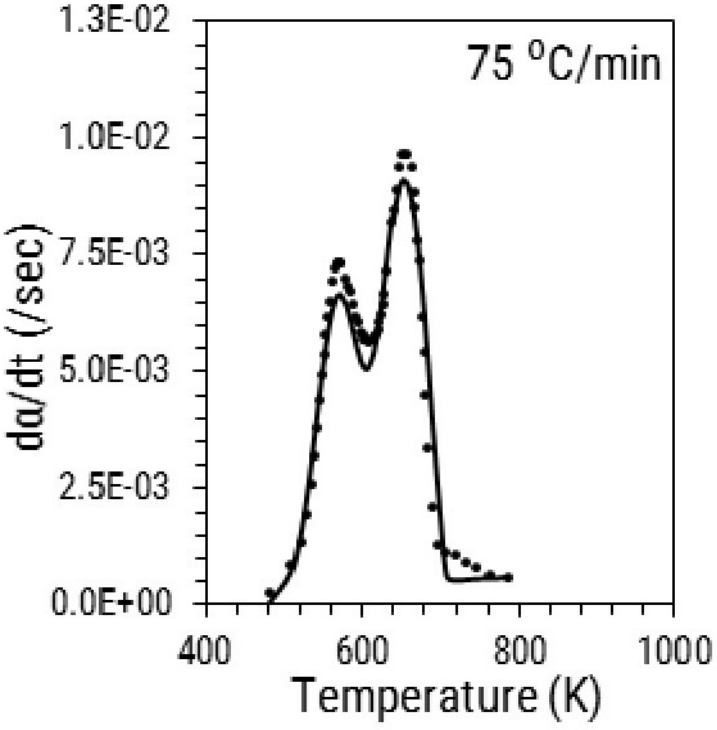

(b)

This figure is continued on the next page...

Figure 3.16

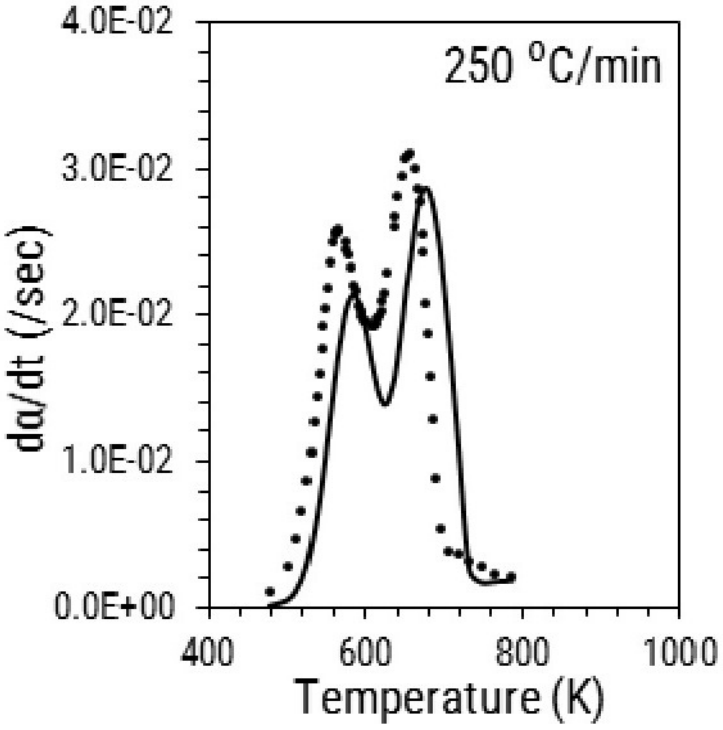

(c)

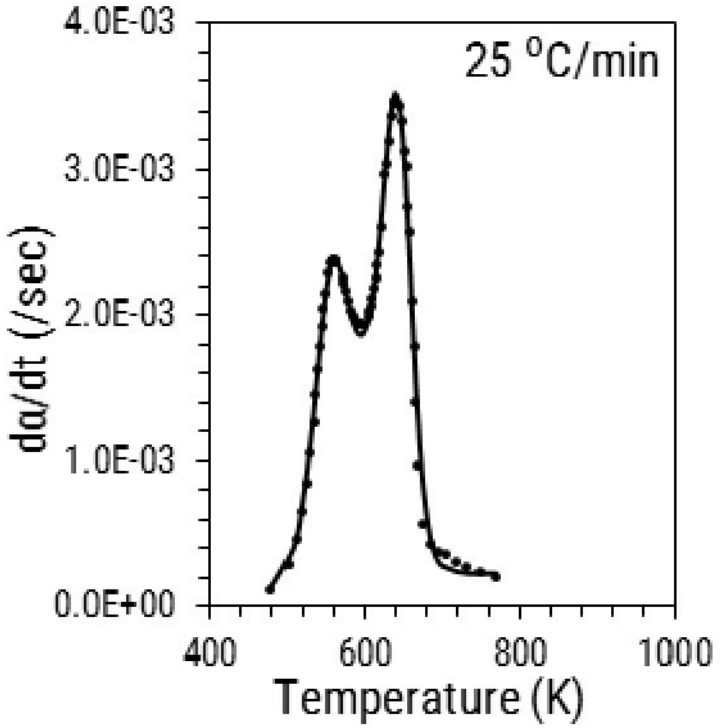

(d)

This figure is continued on the next page...

Figure 3.16

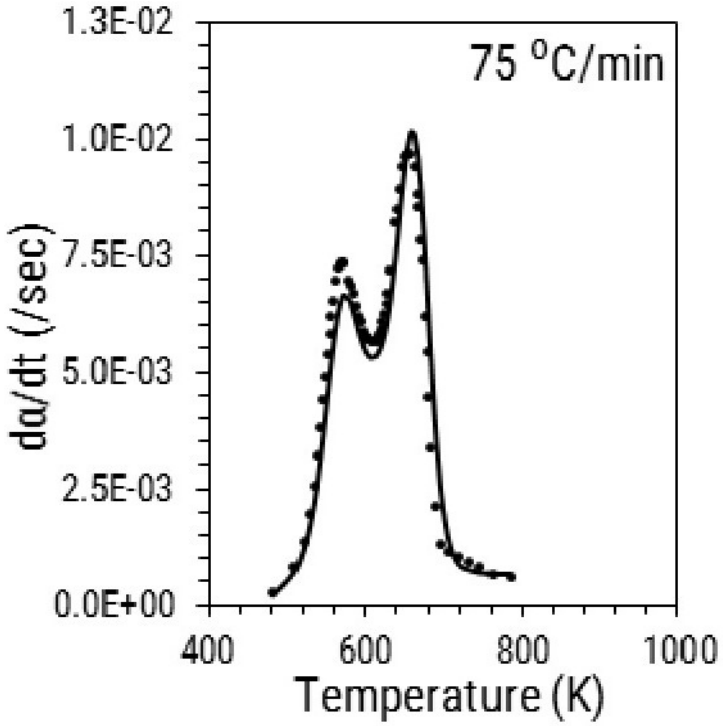

(e)

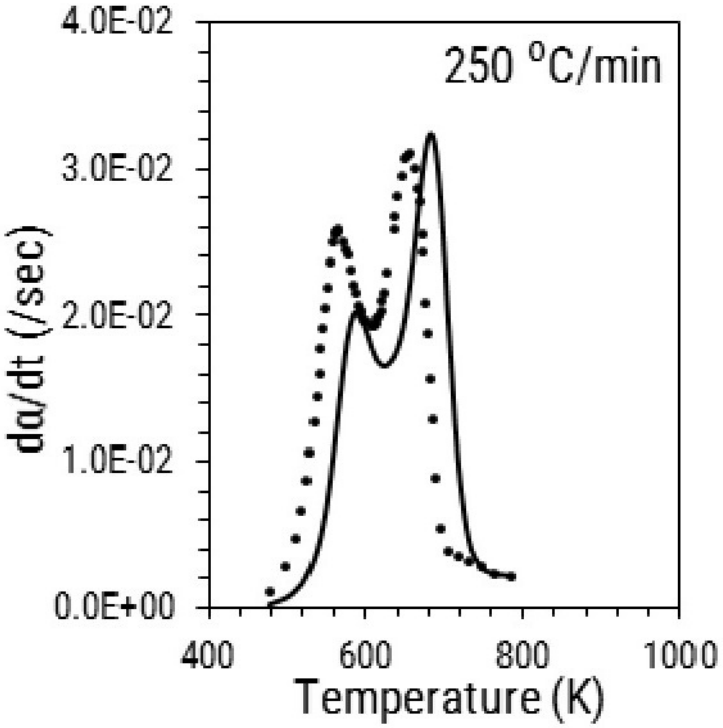

(f)

This figure is continued on the next page...

Figure 3.16

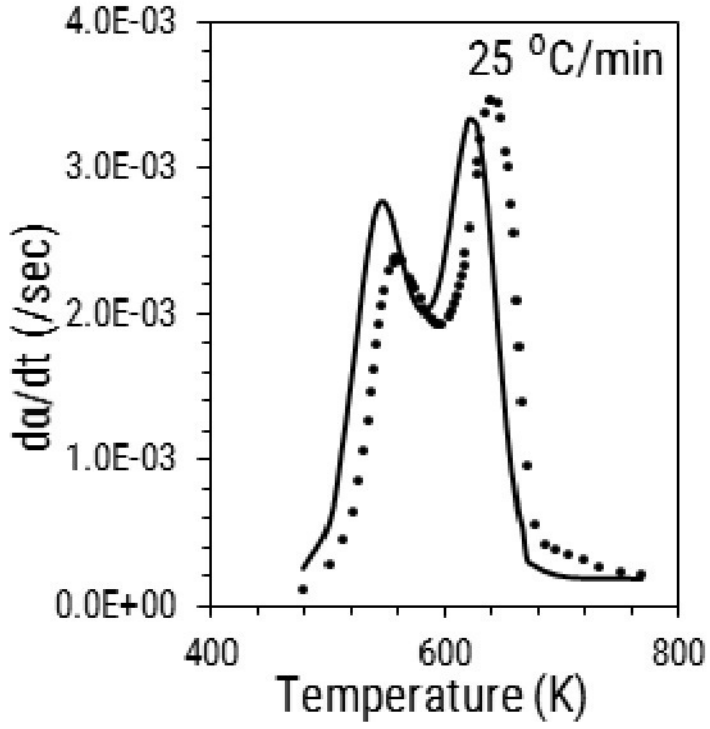

(g)

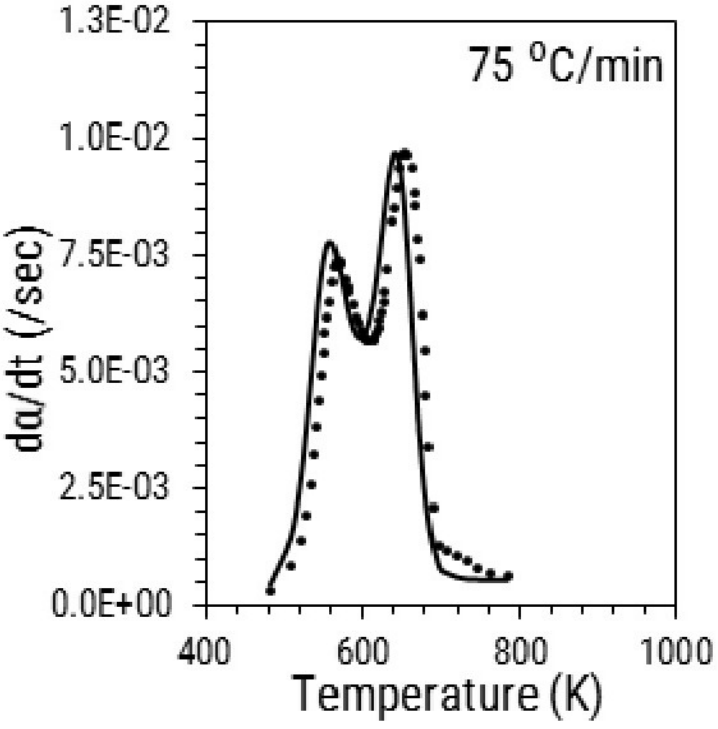

(h)

This figure is continued on the next page...

Figure 3.16

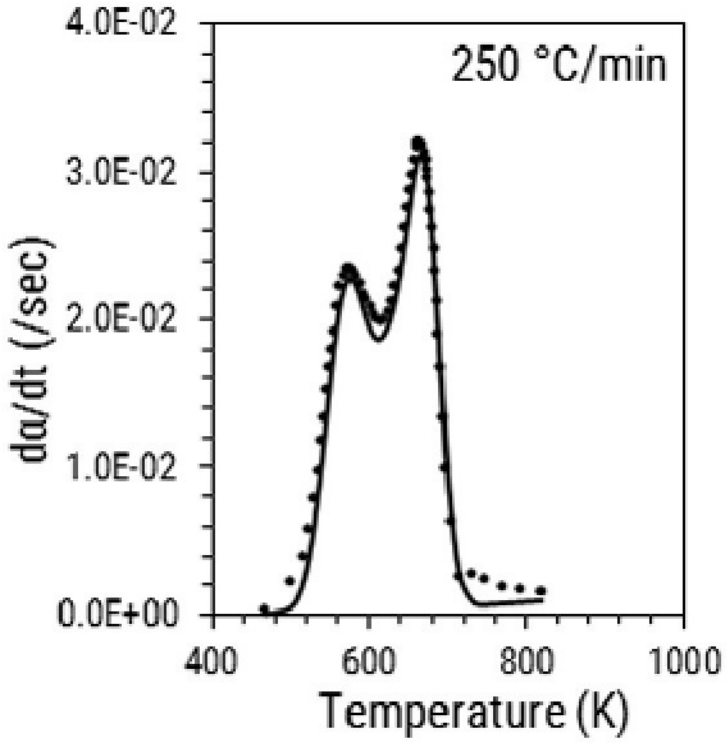

(i)

Figure 3.16: Comparison of experimental and predicted curves for different heating rates. Predicted curves are obtained by using optimized DAEM parameters for (a) Case 2 (b) Case 2A and (c) Case 2B

3.6.4.5 Prediction of TGA curve at 1000 °C/s

DAEM equations and optimized parameters obtained here describe various mass transfer processes that occur during biomass volatilization. As discussed in sections 3.6.2.3 and 3.6.4.4 heating rate has a profound effect on the morphology of biomass particle and hence affects the volatilization rate. Biomass pore structure changes at high heating rates, and thus, similar changes might occur under fast pyrolysis conditions. The DAEM parameters were optimized under conditions where morphological changes significantly affect mass loss rate. Thus, these parameters were used to predict biomass pyrolysis profile under 1000 °C/s or fast pyrolysis conditions. Three different reaction models were used to predict the volatilization curves obtained for pine, pine nut shell, rice husk, and rice straw at 1000 °C/s using a wire mesh reactor [23]. The mass loss data was converted to conversion (α) based on the final residue remaining at the end of pyrolysis. The DAEM parameters used for predicting the curves are as shown in Table 3.15. These

parameters were optimized using biomass of particle size between 75 to 106 μm and heating rates of 150 to 250 °C/min. An important observation from Figure 3.17 is that while the parameters were obtained for mallee wood, the predicted curves for pine, and pine nut shell are in fair agreement with the experimental data. One possible reason for such an agreement is similar ash content for pine, pine nut shell, and the mallee biomass used. On the other hand, the mass loss prediction for rice straw and husk is poor because the ash content for these raw materials is around 15 wt.% [23] while that for the mallee biomass is around 1.3 wt.%. This demonstrates that the DAEM parameters derived using TGA at low heating rates can predict volatile evolution profile under high heating rate conditions if the model parameters take into consideration the effect of morphological changes occurring during pyrolysis reaction.

Table 3.15: DAEM parameters optimized for three reaction models using pyrolysis curves obtained for biomass particle size between 75 to 106 μm at heating rates between 150 to 250 °C/min

Reaction Model	w_c	2-Gaussain model weight fractions	E_0 (kJ/mol)	σ (kJ/mol)	$\log(A_0)$ (sec^{-1})	m	obj func (J)
F1	0.1283		189.616	39.162	6.852	0.9859	0.0402
	0.2655		226.308	8.632	17.455		
	0.6062	0.4075	162.963	10.131	11.928		
		0.5925	175.007	2.212			
DP	0.1230		189.458	39.812	8.581	0.4460	0.0498
	0.2988		226.274	9.613	19.162		
	0.5782	0.5690	164.663	7.975	11.721		
		0.4310	174.267	3.153			
A2	0.1903		189.322	37.092	11.065	0.3883	0.0680
	0.2445		226.848	8.860	19.504		
	0.5652	0.5677	164.505	8.678	12.080		
		0.4323	175.113	4.166			

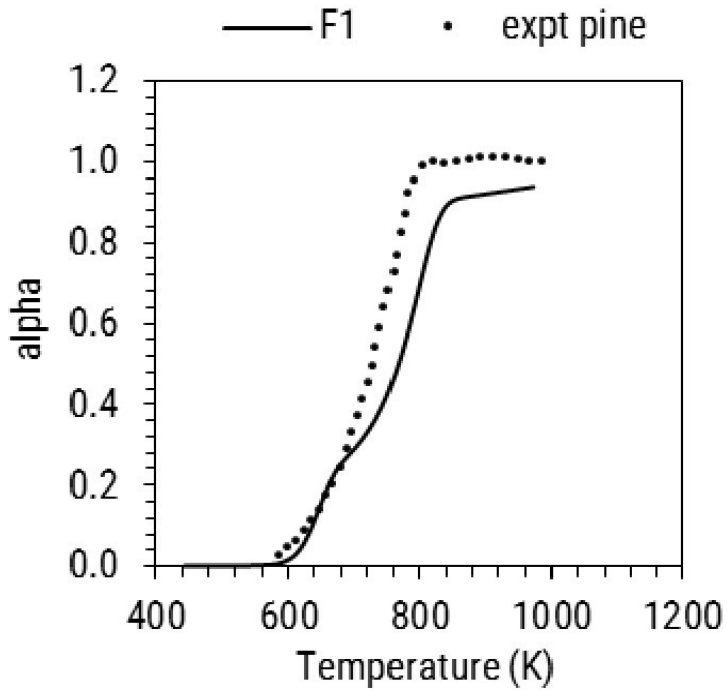

(a)

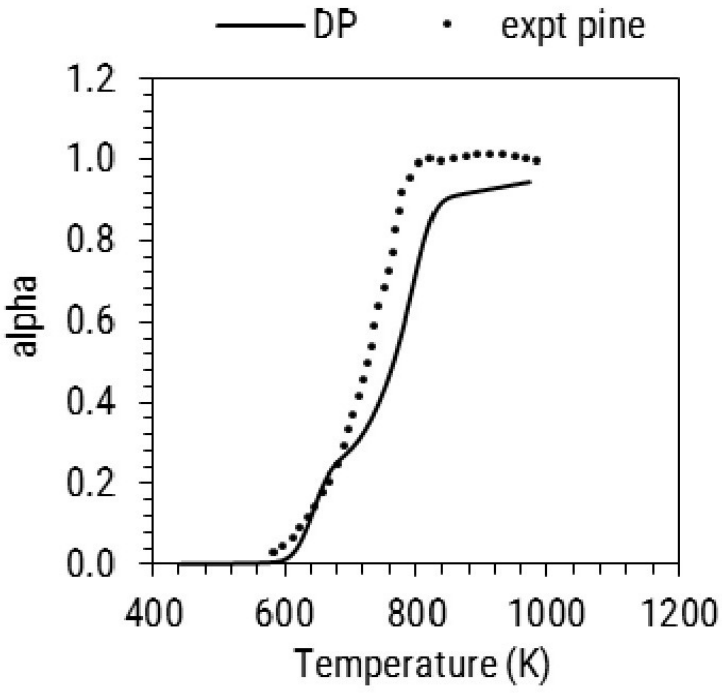

(b)

This figure is continued on the next page...

Figure 3.17

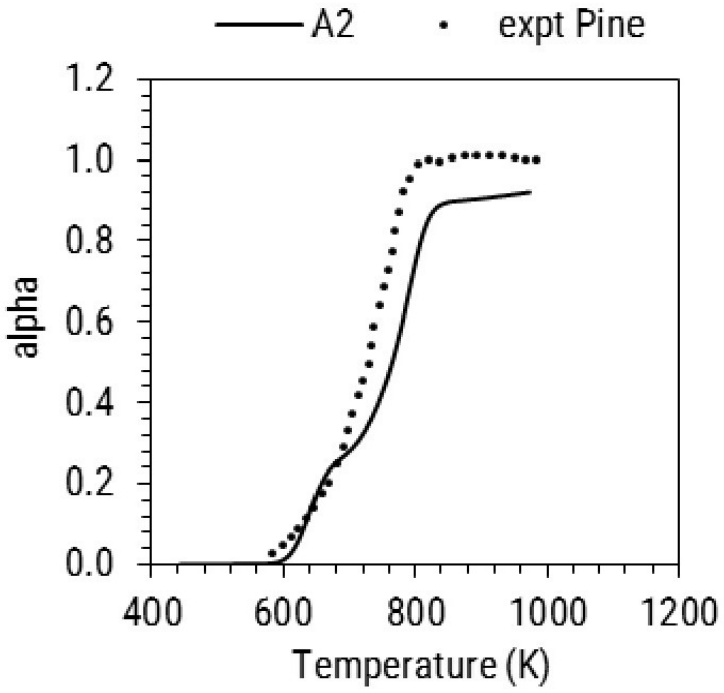

(c)

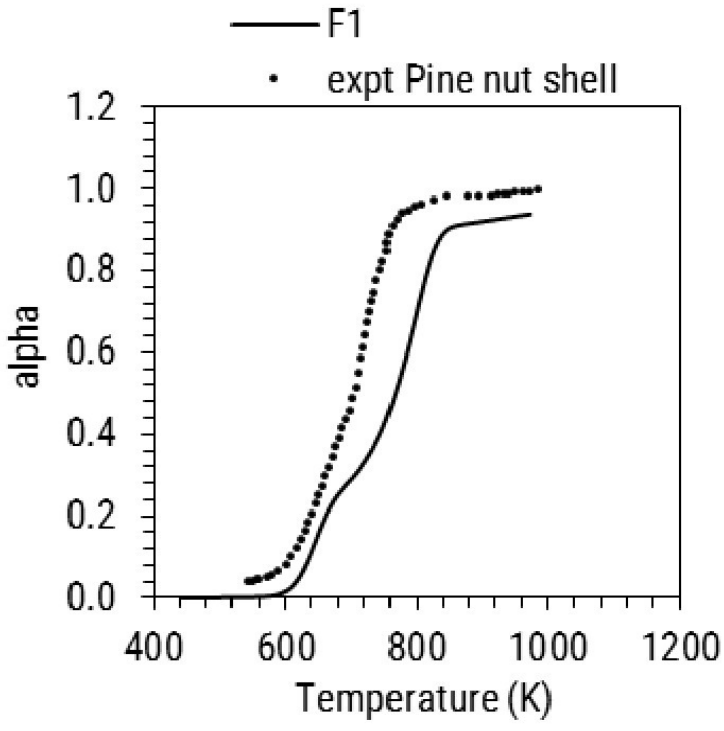

(d)

This figure is continued on the next page...

Figure 3.17

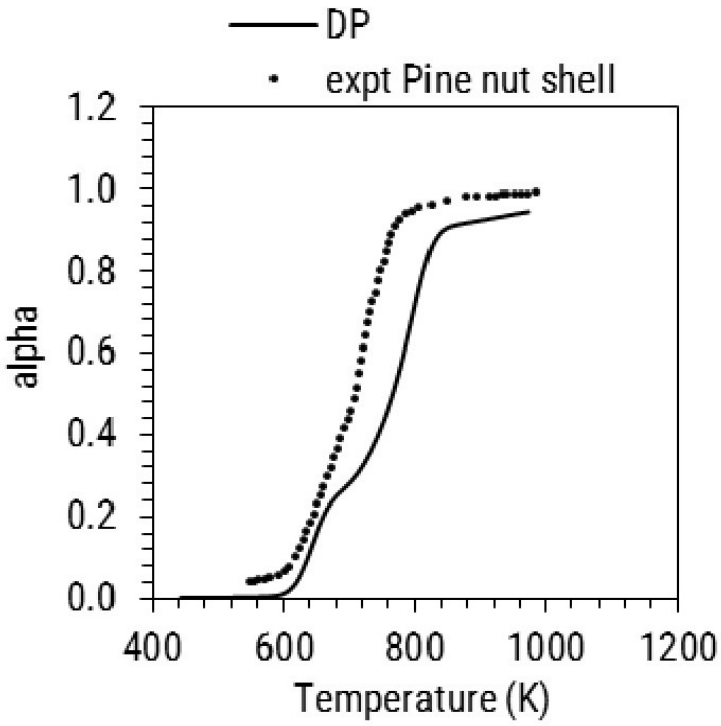

(e)

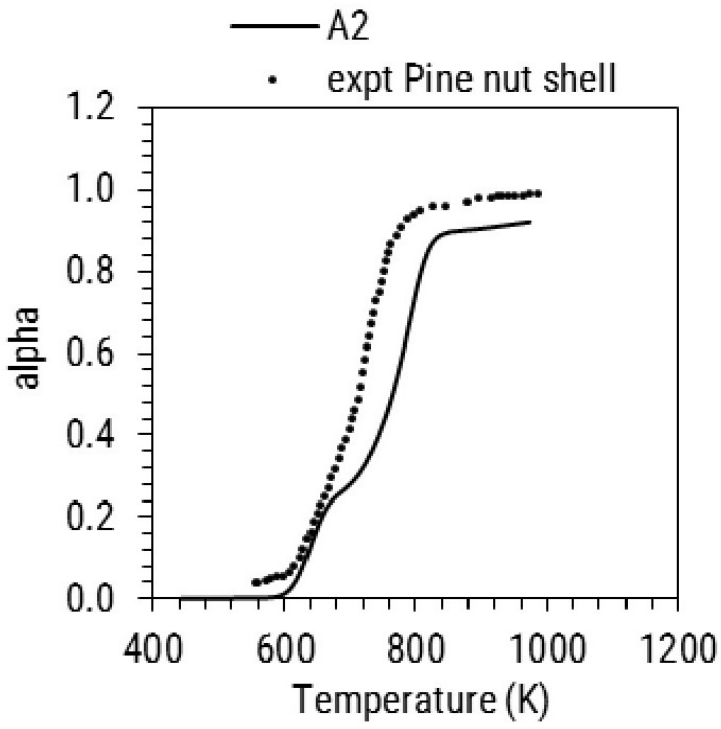

(f)

This figure is continued on the next page...

Figure 3.17

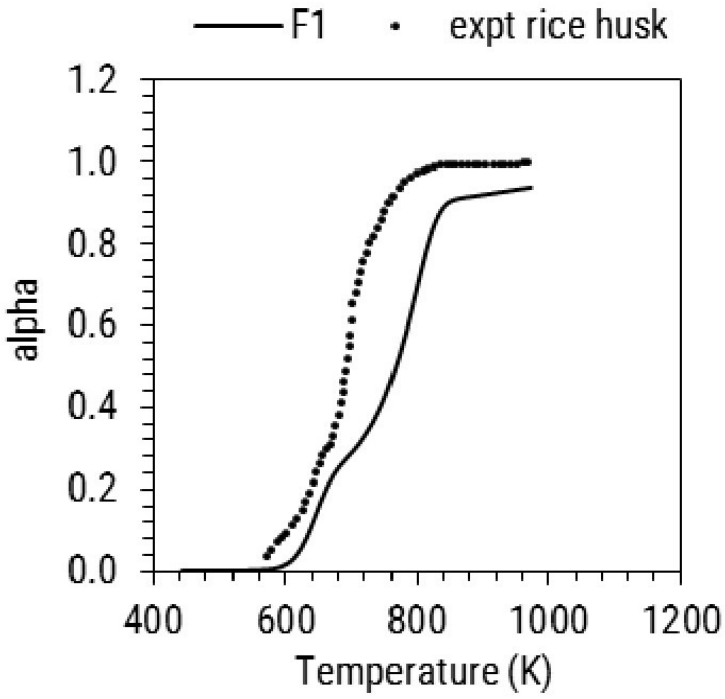

(g)

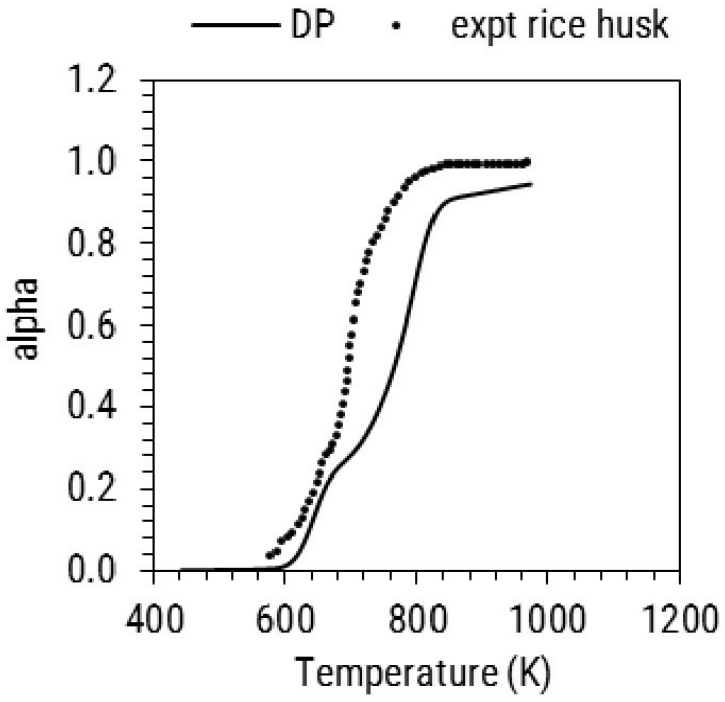

(h)

This figure is continued on the next page...

Figure 3.17

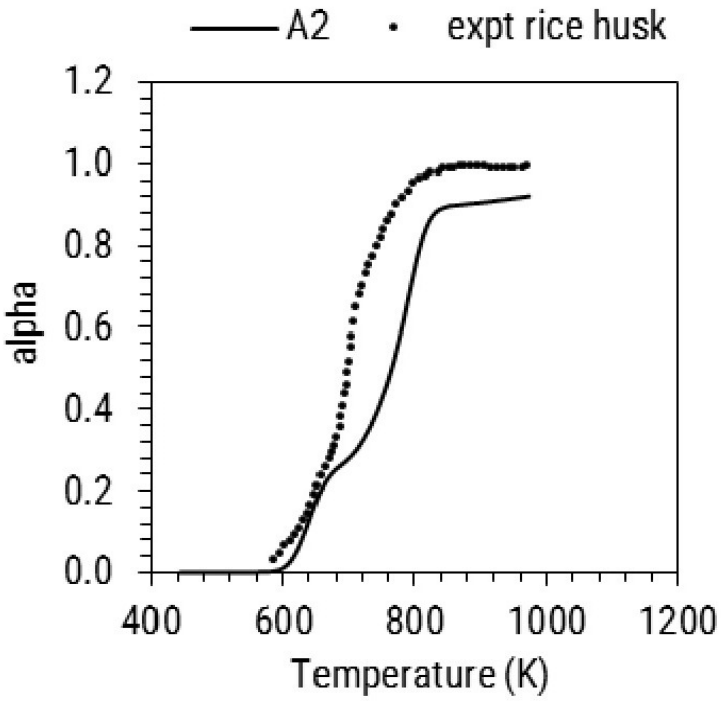

(i)

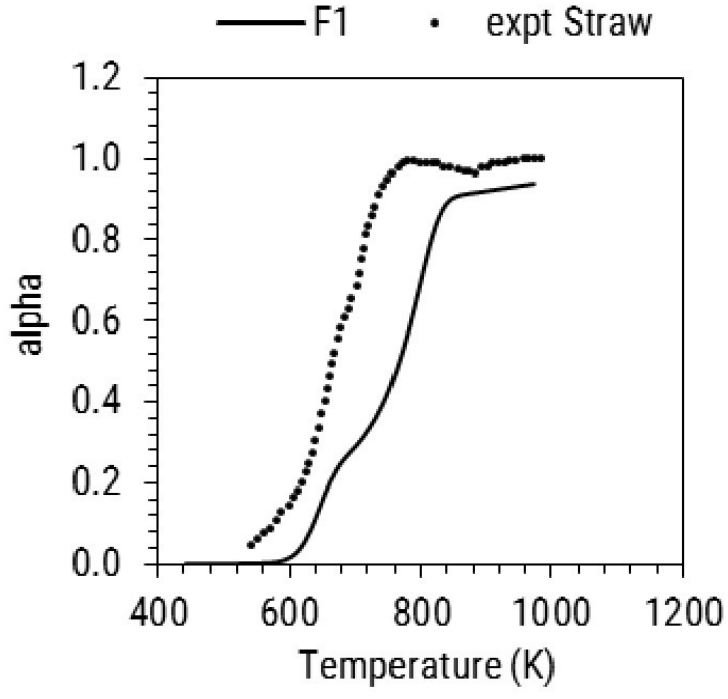

(j)

This figure is continued on the next page...

Figure 3.17

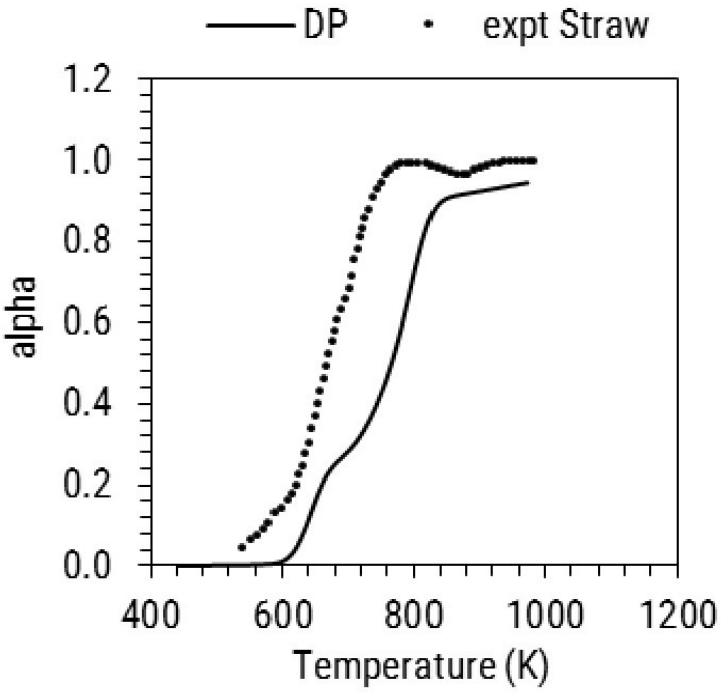

(k)

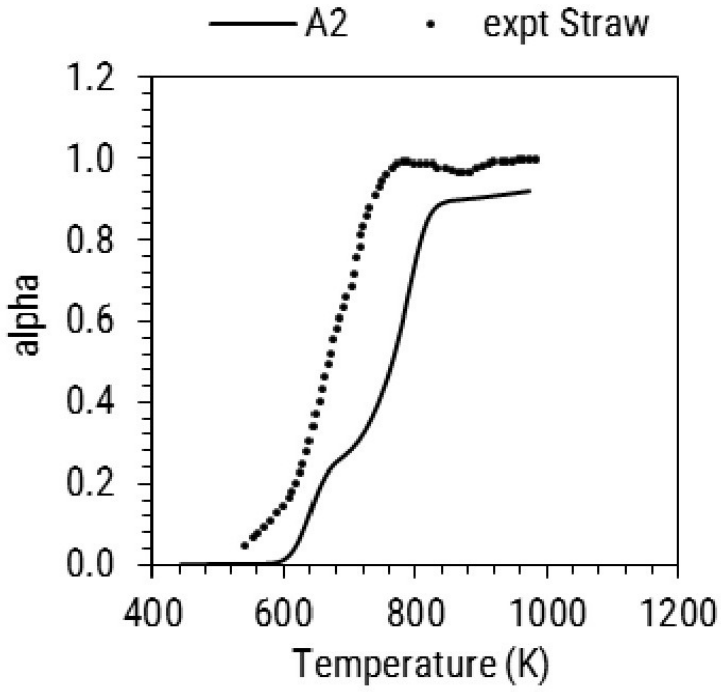

(l)

Figure 3.17: Prediction of TGA curves using F1, DP and A2 reaction models for (a) to (c) pine, (d) to (f) pine nut shell, (g) to (i) rice husk and (j) to (l) straw pyrolysis under 1000 °C/s

3.7 Summary

DAEM was used as a lumped model to describe the effect of morphological changes, which occur during pyrolysis, on apparent volatilization rate of biomass. The effect of three particle sizes ($\leq$45μm, 75 to 106 and 300 to 425 μm) and seven heating rates (5 to 250°C/min) on biomass pyrolysis profile was studied using TGA, SEM and optical microscope images. SEM images showed that heating rates chosen in this study lead to significant physical changes in structure of biomass particles which in turn affect the biomass volatilization profile. Formation of large bubbles was observed on the surface of the biomass at heating rates beyond 75 °C/min indicating presence of an intermediated molten phase. As the heating rates were increased from 5-250 °C/min, an uneven temperature shift in TGA profile was observed due to changes in pore structure of biomass. DAEM parameters - E_0, A_0, m and σ for three pseudo-components were optimized for three reaction models (first order, random scission and Avrami-Erofeev) to describe biomass pyrolysis behavior. The parameter estimation procedure showed that it was essential to separately optimize DAEM parameters to model the TGA profile at heating rates greater than 150 °C/min because of significant morphological changes in biomass. Temperature dependence of frequency factor increased beyond heating rate of 150 °C/min because changes in pore structure became prominent after 300 °C and 150 °C/min. The optimized DAEM parameters resulted in a fair prediction of biomass volatilization under 1000 °C/s. This showed that the parameters can be directly extrapolated to predict the behavior of biomass under fast pyrolysis conditions in fluidized bed reactors where biomass particle size does not exceed 1 or 2 mm. The model can be improved further to include prediction of liquid, gas and char yields is included.

Chapter 4

DAEM coupled detailed pyrolysis kinetics

4.1 Introduction

Chapter 2 describes various biomass pyrolysis lumped kinetic models to predict the gas, tar, and char yields. The distributed activation energy model was used in Chapter 3 to predict the evolution rate of total pyrolysis volatiles and predict char yield. However, to predict pyrolysis oil and gas composition, a detailed kinetic model is required. Kinetic model proposed by Ranzi et.al. [10] is capable of predicting yields of major components present in pyrolysis gas and oil for any biomass. The qualitative and quantitative predictions of any kinetic model depend on the reaction steps considered in the model and value of kinetic parameters. Variables like biomass composition, temperature, and heating rate significantly affect the nature of pyrolysis reactions. It is essential for the kinetic model equations and parameters to be valid over a wide range of these variables. This chapter therefore, compares the Ranzi model predictions for biomass pyrolysis of different biomass types under wide range of heating rates (5 to 1000°C/s). The model is modified and coupled with distributed activation energy model (DAEM) to improve predictability of gas, tar, and char yield along with the composition of major gaseous and bio-oil components for biomass pyrolysis carried out different heating rates.

Chapter 3 concludes that the morphological changes in mallee biomass become

prominent after heating rate of 150°C/min and affect the evolution profile considerably. Increase in heating rate of pyrolysis reaction reduces char yield and increases gas and liquid yields. Heating rate also affects the bubble formation and eruption during pyrolysis. At low heating rates, cross-linking reactions are dominant, hence, intermediate liquid hardens and traps volatiles within the particle. On the other hand at high heating rate the viscoelastic character of biomass particle is maintained which leads to volatile release via bubble eruption or aerosol ejection due to pressure build-up. Viscoelastic or rigid nature of biomass particle under pyrolysis conditions is dictated by the biomass type and heating rate [194]. Rigidity/elasticity of biomass particle affects the mobility of polymer chains, radical species, and other reactive intermediates which in turn affects the rate of formation of tar, gas, and char species. To incorporate the effect of morphological changes on rate of formation of different pyrolysis species, the detailed kinetic scheme is coupled with the DAEM approach in this chapter.

4.2 Mathematical model

4.2.1 Detailed lumped kinetic model: Ranzi model

Ranzi model is a detailed lumped kinetic model, which is more mechanistic than conventional lumped kinetic models. The main features of the model are (i) characterization of the biomass structure, (ii) biomass devolatilization process, which forms pyrolysis gas, liquid and char (29 reactions and 50 species), (iii) secondary gas phase reactions of evolved volatile and gas species (20,239 reactions and 507 species). To simplify the model, pyrolysis reactions of cellulose, hemicellulose, and lignin are assumed to proceed independently of one another other. Pyrolysis is assumed to be a linear combination of the three pseudo components according to their molar proportion. The reactions considered in this chapter are the primary pyrolysis reactions, where solid biomass is converted to gas, liquid, and char. Gas/vapor phase reactions occurring outside the biomass particle are not considered, because the literature data for devolatilization used here is such that secondary gas phase reactions are minimized. The secondary gas phase reactions become important in reactor modeling.

4.2.1.1 Biomass chemistry

Chapter 2 describes the different components of lignocellulosic biomass. Chemical structure and relative content of cellulose, heimcellulose, lignin, and ash differs form one another and also with biomass type. Ranzi model [10] characterizes biomass as a mixture of seven pseudo components. Structure of the pseudo-components is shown in Figure 4.1. Cellulose is the most dominant polysaccharide in plant cell wall and constitutes 15 to 50 wt% of dry plant material. It is a linear polymer made up of β-1,4 linked glucopyranose units. Degree of polymerization (DP) of cellulose is between 10 to 15 thousand glucopyranose units. Hemicellulose is a amorphous branched hetero-polysaccharide that constitutes 25-30 wt% of dry plant material. Hexose and pentose units such as xylose, arabinose, glucose, mannose, and galactose make up the hemicellulose polymer. Xylans are linear homoxylan polysaccharides have β-1,3 and β-1,4 linkages, and L-arabinose side chains are present in cell wall of cereal grains. Second class of hemicellulose comprises of mannans- galactomannan, glucomannan, and galacto-glucomannan. Glucomannan is a major component of softwood hemicellulose and less abundant in hardwood and grasses. Hemicellulose has a DP of 70-200 units, with high molecular weight in hardwoods as compared to that in softwoods. Structure of cellulose, xylan, and glucomannan repeating units is shown in Figure 4.1.

Lignin is a complex phenolic polymer with p-hydroxyphenyl (H), guaiacyl (G), and syringyl (S) propanoid units as the main building blocks. Hardwood lignin is pre-dominantly made up of guaiacyl and syringyl units with trace amount of p-hydroxyphenyl units. Softwoods are mainly composed of guaiacyl units and low amounts of p-hydroxyphenyl units. H-units content is slightly higher in grasses. Characteristic inter-unit linkages in lignin are shown in Figure 4.2. The β-O-4 linkage makes up 46 to 60% of all the linkages [195]. As discussed in section 2.3.2, LIG-H, LIG-O, and LIG-C (Figure 4.1) represent different repeating units with characteristic linkages of lignin. The proportion of each repeating moiety changes based on the type of biomass subjected to pyrolysis.

Extractives were not considered to characterize biomass in the Ranzi model. However, complete characterization of several biomass species is not possible if only cellulose, hemicellulose, and lignin are considered. Distribution of the extractives

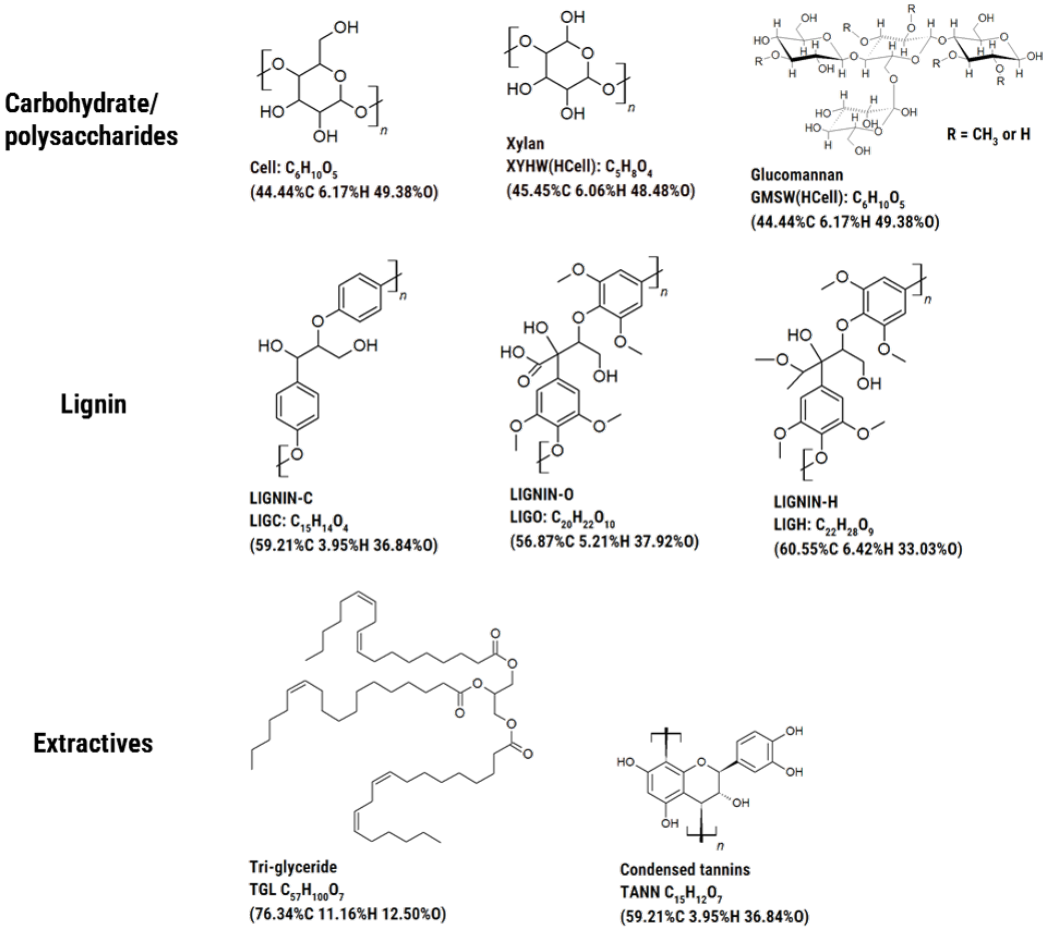

Figure 4.1: Pseudo components used to model biomass pyrolysis kinetics

in plant material is different in various plant organs, most abundant in leaves and bark. There are a wide range of extractives in plants, thus, Dibiagi et.al. [196] broadly classified them into hydrophilic and hydrophobic type. Softwood species contain upto 15 wt.% and hardwood samples contain <2 wt.% of hydrophobic extractives. The most common hydrophobic extractive in plants is triglyceride compound with high presence of linoleic acid [196]. Therefore, triglyceride (TGL: $C_{57}H_{100}O_7$) is used as a reference specie in the model. Hydrophilic extractives can be further classified into flavonoids and non-falvonoids, latter being abundant in plant material and include phenolic acids and tannins. Tannins are polyphenolic compounds and condensed tannins (TANN: $C_{15}H_{12}O_7$) is used to represent hydrophilic extractives. As shown in Figure 4.3 (a) consideration of extractives as a part of RM-2 and RM-3 mixture species allows the Ranzi model to characterize a wider range of biomass species (hardwood, softwood, and grass type) as compared to a case in which extractives are not used as pseudo-components.

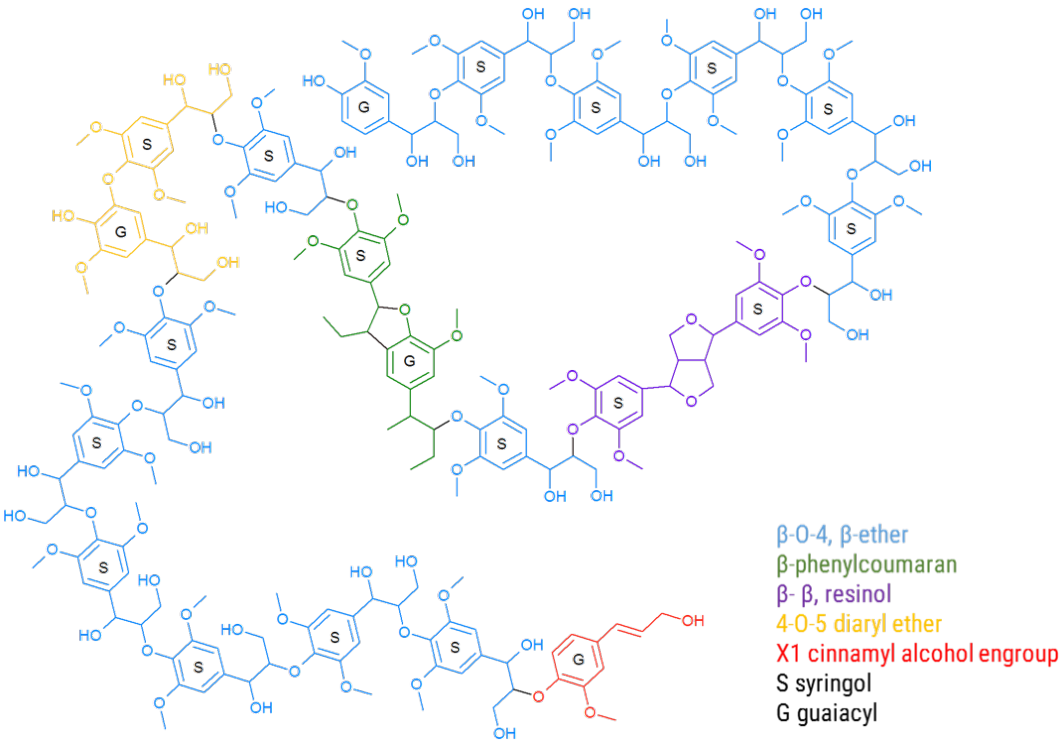

Figure 4.2: Representative chemical structure of lignin with different bond linkages [22]

The pyrolysis chemistry of cellulose, hemicellulose, lignin, and extractives is different, hence the first step in biomass pyrolysis modeling is specifying reference species which can represent different biomass components. If information on biochemical composition is unavailable, the reference specie composition can be determined using elemental analysis of biomass. H/C/O atomic balances allow to evaluate a suitable combination of three reference species (RM-1, RM-2, and RM-3). These three mixture species are further composed of Cell, Hcell, LIG-O, LIG-C, LIG-H, TGL, and TANN using mole fractions/splitting parameters n_{α}, n_{β}, n_{γ}, n_{δ}, and n_{ϵ}. RM-1 is representative of hollocellulose, whereas RM-2 and RM-3 are mixture of lignin and extractives (Figure 4.3). The value of splitting parameters are defined from experimental findings and can be modified to establish elemental balance.

Calculation of mixture species and internal composition of mixture species for different biomass samples is shown in Table 4.1. The mole fractions RM-1, RM-2, and RM-3 are estimated based on the H/C/O balance of the rice straw, rice husk, and pine nutshell reported in [23] and of pine wood reported in [122]. In this study, if the biochemical composition of a biomass specie is not reported, initial guess

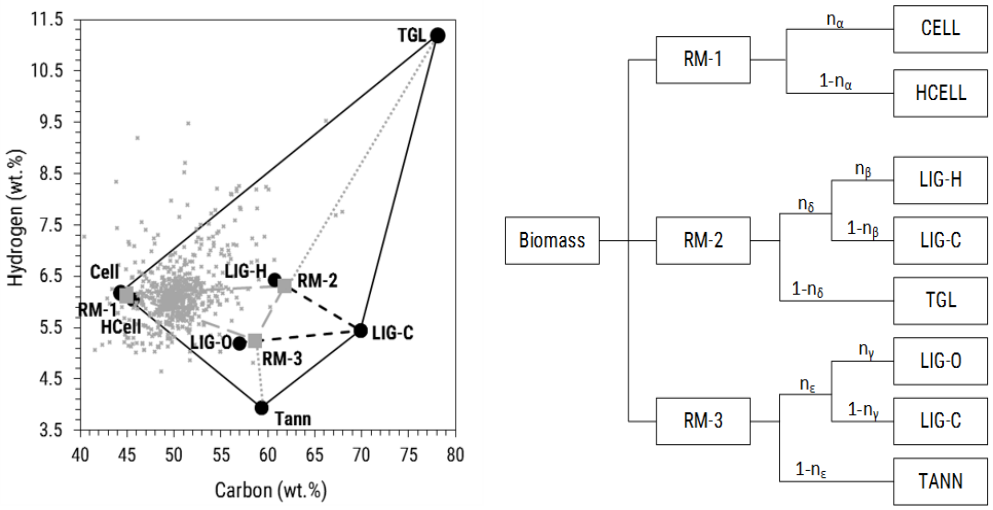

(a) (b)

Figure 4.3: Combining biomass pseudo components into three mixtures- RM-1, RM-2, and RM-3 [10]. The scatter points in figure (a) shows composition of different softwood, hardwood, and grass biomass species.

of splitting parameters is based on the database published by Debiagi et.al. [196], where biochemical, elemental, and ash analysis of more than 600 lignocellulosic biomass species is published along with estimates of splitting parameters. Using the value of splitting parameters, the H/C/O composition of mixture species RM-1, RM-2, and RM-3 is determined. The value of splitting parameters and composition of mixture species is adjusted to establish elemental balance.

Table 4.1: Estimated values of biomass pseudo-components of four biomass species using Ranzi model characterization. The pseudo-component composition is reported in mole fraction

Components	**Rice Straw [23]**	**Rice husk [23]**	**Pine nutshell [23]**	**Pine [122]**	**Spruce [24]**	**Oak [24]**	**Pine [24]**
Cell	0.4304	0.4451	0.4444	0.4462	0.5712	0.5060	0.5456
XYHW/GMSW	0.3788	0.3642	0.2945	0.3697	0.2704	0.3148	0.2871
LIGC	0.0176	0.0377	0.1029	0.0297	0.0527	0.0338	0.0220
LIGH	0.0004	0.0007	0.1122	0.0416	0.0144	0.0934	0.0220
LIGO	0.1215	0.1503	0.0313	0.0773	0.0889	0.0419	0.0869
TGL	0.0024	0.0020	0.0128	0.0016	0.0024	0.0000	0.0000
TANN	0.0487	0.0000	0.0019	0.0340	0.0000	0.0100	0.0363
RM-1	0.8092	0.7992	0.7389	0.8158	0.8417	0.8208	0.8327
RM-2	0.0029	0.0023	0.1329	0.0535	0.0172	0.1168	0.0275
RM-3	0.1879	0.1985	0.1282	0.1306	0.1411	0.0624	0.1398
alpha	0.5319	0.5500	0.6014	0.5469	0.6787	0.6165	0.6552
beta	0.9100	0.8000	0.9343	0.8000	0.9700	0.8000	0.8000
gamma	0.8736	0.8000	0.2475	0.8000	0.6300	0.8000	0.8400
delta	0.1700	0.2900	0.9038	0.9700	0.8600	1.0000	1.0000

Table 4.1 continued from previous page

Components	**Rice Straw [23]**	**Rice husk [23]**	**Pine nutshell [23]**	**Pine [122]**	**Spruce [24]**	**Oak [24]**	**Pine [24]**
epsilon	0.7405	1.0000	0.9851	0.7400	1.0000	0.8400	0.7400
				Experiment			
C (daf wt%)	0.4966	0.5050	0.5320				
H (daf wt%)	0.0583	0.0537	0.0601				
O (daf wt%)	0.4451	0.4412	0.4079				
Cellulose (dry wt%)				35	47.1±0.4	43.2±0.3	45.6±0.1
Hemicellulose (dry wt%)				29	22.3±0.4	21.9±0.7	24.0±0.7
Lignin (dry wt%)				28	29.2±0.6	35.4±0.4	26.8±0.3
Extractives (dry wt%)					1.1±0.4	35.4±0.5	26.8±0.4

Table 4.1 continued from previous page

Components	**Rice Straw [23]**	**Rice husk [23]**	**Pine nutshell [23]**	**Pine [122]**	**Spruce [24]**	**Oak [24]**	**Pine [24]**
			Prediction				
C (daf wt%)	0.5012	0.5047	0.5285				
H (daf wt%)	0.0580	0.0586	0.0639				
O (daf wt%)	0.4409	0.4367	0.4076				
Cellulose (dry wt%)				35.71	47.24	42.31	44.66
Hemicellulose (dry wt%)				29.59	22.37	21.45	23.51
Lignin (dry wt%)				28.87	29.29	34.67	26.25
Extractives (dry wt%)				5.80	1.1	1.57	5.58

4.2.1.2 Reaction chemistry

The reactions of pseudo-components are tabulated in Table 4.2. Polymeric cellulose, hemicellulose, and lignin species undergo end and mid chain depolymerization to form non-volatile oligomeric/polymeric active species along with the release of small molecules like water, and other pyrolysis gases. The active species, CellA, HCE-1, HCE-2, LIGCC, LIG, and LIGOH further depolymerize and cross-link to form gas, tar and char. Cellulose pyrolysis is assumed to follow a simple reaction path with focus on formation of typical products like levoglucosan (LVG), hydroxy acetaldehyde (HAA), and hydroxy methyl-furfural (HMFU). Active cellulose and char are formed from through two competing cellulose pyrolysis reactions. Active cellulose further evolves through two competitive pathways: end-chain scission to yield LVG and β-scission reactions inside polymer chain with subsequent dehydration, isomerization, retro Diels-Alder, and tautomerization reactions to form glyoxal, acetaldehyde, formic acid, HMFU, CO, CO_2 and other light products. The stoichiometric coefficients are based on mechanistic, experimental, and theoretical works reported in [123, 107, 197].

Table 4.2: Ranzi model for biomass pyrolysis [27]

Sr. no.	Reactant		Product	E, kJ/mol; A, s^{-1}
			Cellulose	
R1	Cell	→	CellA	1.5 x 10^{14} x exp(-196.648/RT)
R2	CellA	→	0.4 HAA + 0.05 GLYOX + 0.15 CH_3CHO + 0.25 HMFU + 0.35 ALD3 + 0.15 CH_3OH + 0.3 CH_2O + 0.61 CO + 0.36 CO_2 + 0.05 H_2 + 0.93 H_2O + 0.02 HCOOH + 0.05 $C_3H_6O_2$ + 0.05 T(CH_4)	2.5 x 10^{6} x exp(-79.914/RT)
R3	CellA	→	LVG	3.3 x T x exp(-41.840/RT)
R4	Cell	→	5 H_2O + 6 CHAR	6 x 10^{7} x exp(-129.704/RT)
			Hemicellulose	
R5	GMSW	→	0.70 HCE1 + 0.30 HCE2	1 x 10^{10} x exp(-129.704/RT)
R6	XYHW	→	0.35 HCE1 + 0.65 HCE2	1 x 10^{10} x exp(-119.244/RT)
R7	HCE1	→	0.60 XYLAN + 0.20 $C_3H_6O_2$ + 0.12 GLYOX + 0.20 FURF + 0.40 H_2O + 0.08 T(H_2) + 0.16 CO	3 x T x exp(-46.024/RT)

Table 4.2 continued from previous page

Sr. no.	Reactant		Product	E, kJ/mol; A, s^{-1}
R8	HCE1	→	0.4 H_2O + 0.79 CO_2 + 0.05 HCOOH + 0.69 CO + 0.01 T(CO) + 0.01 T(CO_2) + 0.35 T(H_2) + 0.3 CH_2O + 0.9 T(COH_2) + 0.625 T(CH_4) + 0.375 T(C_2H_4) + 0.875 CHAR	1.8 x 10^{-3} x T x exp(-12.552/RT)
R9	HCE2	→	0.2 H_2O + 0.275 CO + 0.275 CO_2 + 0.4 CH_2O + 0.1 C_2H_5OH + 0.05 HAA + 0.35 ACAC + 0.025 HCOOH + 0.25 T(CH_4) + 0.3 T(CH_3OH) + 0.225 T(C_2H_4) + 0.4 T(CO_2) + 0.725 T(COH_2)	5 x 10^{9} x exp(-131.796/RT)
			Lignin	
R10	LIGC	→	0.35 LIGCC + 0.10 COUMARYL + 0.08 PHENOL + 0.41 C_2H_4 + H_2O + 0.70 T(COH_2) + 0.30 CH_2O + 0.32 CO + 0.495 T(CH_4)	1 x 10^{11} x exp(-155.644/RT)
R11	LIGH	→	LIGOH + 0.50 ALD3 + 0.50 C_2H_4 + 0.20 HAA + 0.10 CO + 0.10 T(H_2)	6.7 x 10^{12} x exp(-156.900/RT)
R12	LIGO	→	LIGOH + CO_2	3.3 x 10^{8} x exp(-106.692/RT)
R13	LIGCC	→	0.30 COUMARYL + 0.20 PHENOL + 0.35 HAA + 0.70 H_2O + 0.65 CH_4 + 0.60 C_2H_4 + H_2 + 1.40 CO + 0.4 T(CO) + 6.75 CHAR	1 x 10^{4} x exp(-103.763/RT)

Table 4.2 continued from previous page

Sr. no.	Reactant		Product	E, kJ/mol; A, s^{-1}
R14	LIGOH	→	0.90 LIG + H_2O + 0.1 CH_4 + 0.60 CH_3OH + 0.05 T(H_2) + 0.3 T(CH_3OH) + 0.05 CO_2 + 0.65 CO + 0.6 T(CO) + 0.05 HCOOH + 0.85 T(COH_2) + 0.35T(CH_4) + 0.20 T(C_2H_4) + 4.25 CHAR	1 x 10^8 x exp(-125.520/RT)
R15	LIG	→	0.70 FE2MACR + 0.30 ANISOLE + 0.30 CO + 0.30 T(CO) + 0.30 CH_3OH	4 x T x exp(-50.208/RT)
R16	LIG	→	0.60 H_2O + 0.40 CO + 0.20 CH_4 + 0.4 CH_2O + 0.20 T(CO) + 0.40 T(CH_4) + 0.50 T(C_2H_4) + 0.40 T(CH_3OH) + 2 T(COH_2) + 6 CHAR	8.3 x 10^{-2} x T x exp(-33.472/RT)
R17	LIG	→	0.60 H_2O + 2.6 CO + 1.1 CH_4 + 0.40 CH_2O + C_2H_4 + 0.40 CH_3OH	1 x 10^7 x exp(-101.671/RT)
			Extractives	
R18	TGL	→	ACROL + 3 FFA	7 x 10^{12} x exp(-191.208/RT)
R19	TANN	→	0.85 PHENOL + 0.15 T(PHENOL) + T(CO) + H_2O + ITANN	2 x 10^1 x exp(-41.840/RT)
R20	ITANN	→	5 CHAR + 2 CO + H_2O + T(COH_2)	1 x 10^3 x exp(-104.600/RT)

Table 4.2 continued from previous page

Sr. no.	Reactant		Product	E, kJ/mol; A, s^{-1}
		Metaplast reactions		
R21	$T(CO_2)$	$\rightarrow$	CO_2	1 x 10^6 x exp(-100.416/RT)
R22	T(CO)	$\rightarrow$	CO	5 x 10^{12} x exp(-209.200/RT)
R23	$T(COH_2)$	$\rightarrow$	COH_2	1.5 x 10^{12} x exp(-297.064/RT)
R24	$T(H_2)$	$\rightarrow$	H_2	5 x 10^{11} x exp(-313.800/RT)
R25	$T(CH_4)$	$\rightarrow$	CH_4	5 x 10^{12} x exp(-299.156/RT)
R26	$T(CH_3OH\}$	$\rightarrow$	CH_3OH	2 x 10^{12} x exp(-209.200/RT)
R27	$T(C_2H_4)$	$\rightarrow$	C_2H_4	5 x 10^{12} x exp(-299.156/RT)
R28	T(PHENOL)	$\rightarrow$	PHENOL	1.5 x 10^{12} x exp(-297.064/RT)
		Moisture vaporization		
R29	ACQUA	$\rightarrow$	H_2O	1 x T x exp(-33.472/RT)

Hemicellulose is a branched polymer and has a more complicated structure than cellulose with hexose and pentose sugars as backbone with o-acetyl groups as side groups. Two different pseudo-components for hemicellulose are considered in the Ranzi model for hardwood (xylose based, XYHW) and softwood (glucomannan based, GMSW). The two intermediate species HCE-1 and HCE-2 represent different composition of hardwood and softwood hemicellulose. Hardwood hemicellulose typically yields more char as compared to softwood hemicellulose, which is considered in HCE1 decomposition. Typical hemicellulose pyrolysis products include furfural, acetol, formic acid, acetic acid, furfuryl alcohol, acetone, and permanent gases. The nature of hemicellulose pyrolysis reactions is similar to that of cellulose.

Lignin structure is more complicated than cellulose and hemicellulose. The reaction chemistry of ether (β-O-4) and C-C bond (C_α-C_β) in the syringol and guaiacyl units (Figure 4.2) plays important role during lignin pyrolysis. The multistep kinetic scheme of lignin is a simplification of detailed lignin pyrolysis scheme proposed by Faravelli et al. [92]. Beyond 200°C, lignin pyrolysis is a molten phase radical process with competing initiation, propagation, and termination reactions of different propagating radicals. LIG-O and LIG-H have methoxy groups on phenyl ring adjacent to the ether linkage which decreases the bond dissociation energy of β-O-4 in comparison to LIG-C that does not have any substituent on the phenyl ring. Therefore, the lignin constituents are differentiated from one another as they undergo reactions with different energetics during pyrolysis. Lignin pyrolysis reactions used by Faravelli et al.[92] are represented in Figure 4.4. Faravelli model uses 100 radical and molecular species and 500 elementary and lumped reactions to describe lignin pyrolysis. In the Ranzi model the reactions are further lumped to 8 reactions as shown in Table 4.2. Condensible products for lignin pyrolysis model are coumaryl alcohol, sinapyl aldehyde (FE2MACR), phenol, anisole, hydroxyacetaldehyde, formic acid, methanol, formaldehyde, and propenal.

Pyrolysis of the extractives is explained using three lumped reactions. Tannins undergo pyrolysis in two steps, first one is a volatilization reaction occurring between 125 to 300°C and the second one being a condensation/charring reaction with less release of volatile species [198–200]. Ranzi model therefore, con-

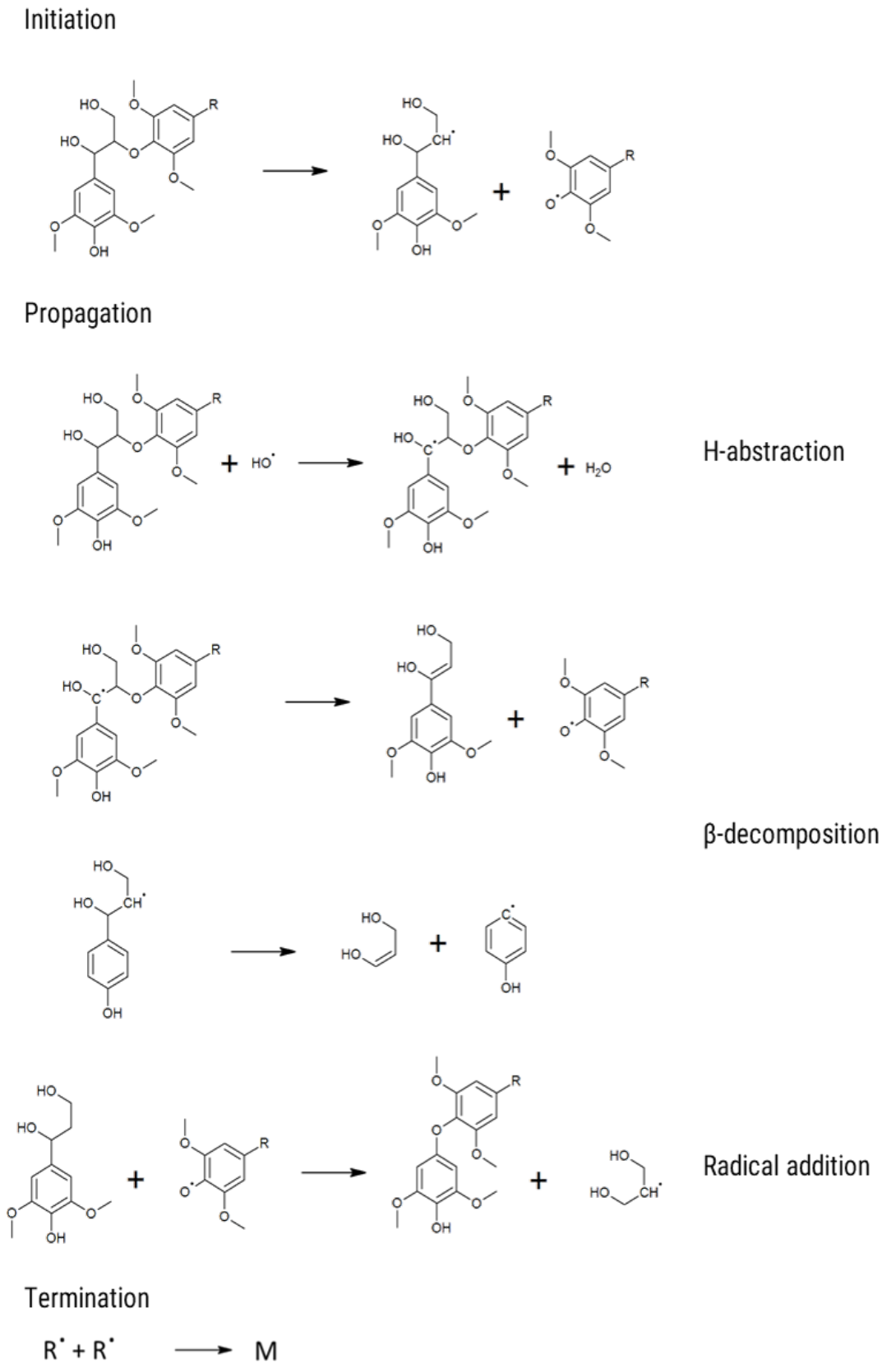

Figure 4.4: Different free radical reactions for lignin

siders a two-step decomposition of TANN, with maxmimum mass loss between 280-310°C, producing phenolic specie and an intermediate metaplast/solid specie ITANN (3,5- dihydroxy benzofuranone: $C_9H_6O_6$). ITANN then degrades to gas and predominantly char via slow decarbonylation, dehydration and charring reaction [196]. TGL pyrolysis is based on the studies of soyabean and corn oil, which when used as mixture better represent real biomass. Acrolein (C_2H_3CHO) and fatty acid (FFA, $C_{18}H_{32}O_2$) are the pyrolysis products of TGL, with negligible char [201]. Thus, the Ranzi model uses one reaction that produces acrolein and FFA at about 350°C. Ranzi model also includes reactions for the release of gases/volatiles trapped inside the intermediate liquid formed during pyrolysis. The resistance for the release of gases is expressed in the form of Arrhenius type equation. These reactions are included to account for the effect of intermediate melting on the release of volatile species formed during pyrolysis.

Ash (salt ions like K, Na, Ca, and Mg) acts as a catalyst in the pyrolysis processes and reduces the yield of organics from pyrolysis liquid with increase in water and char content [28, 202, 203]. Metal cations favour the formation of light oxygenates like aldehydes and carboxylic acids from sugars over depolymerization of polysaccharide chains [204]. Metal cations like Ca promote the formation of primary and secondary char, and light oxygenates from sugars like levoglucosan. The effect of ash on the nature of pyrolysis reactions is complete approximately beyond 5 wt.%. In other words, ash content greater than 5 wt.% (of biomass) does not have additional effect on the yield of pyrolysis char and liquid [10]. To consider the effect of ash a global dimensionless ash factor (AF, Eq.(4.1)) with values between 0 (no ash) and 1 ($\geq$5 wt.%). Ranzi model considers the effect of ash on the activation energy of R2, R4, and R8 (Table 4.2) as shown in Eq.(4.2) to Eq.(4.4). If the ash content of biomass is $\leq$1 wt.%, value of AF becomes 0.5. Thus, the activation energies tabulated in Table 4.2 are valid for ash content $\leq$1 wt.%. If the ash content exceeds 5 wt.%, value of x in the Eq.(4.2) to Eq.(4.4) is substituted as 5.

$$AF = tanh\left(\frac{ash}{2}\right) \tag{4.1}$$

$$E_2 = 19100 - 600x(AF - 0.5) \tag{4.2}$$

$$E_4 = 31000 - 1000x(AF - 0.5) \tag{4.3}$$

$$E_8 = 3000 - 1000x(AF - 0.5) \tag{4.4}$$

4.2.2 DAEM coupled modified Ranzi model

Although the Ranzi model is capable of predicting the composition of gas and major liquid species, it still has some limitations. The model does not predict the formation of cresols, guaiacol/methyl guaiacol, dimethoxy phenol, vinyl phenol, and eugenol, which are major constituents of bio-oil (Table 2.4). The model uses a relatively simple scheme for cellulose pyrolysis and considers only mid-chain cleavage of cellulose, because formation of active cellulose is not accompanied with levoglucosan formation. In the mechanistic model proposed by Zhou et. al. [107], end chain cleavage of cellulose yields both active cellulose and levoglucosan. As discussed in Chapter 3, using a unique value of activation energy may not be a good description of solid decomposition rate. Also, chemical and physical structure of biomass particle changes continuously during pyrolysis, which strongly depends on the heating rate. The next section gives a theoretical background of the modifications made to the Ranzi model (Mo-Ranzi) and the justification for coupling it with DAEM.

4.2.2.1 Model modification: Theoretical background

Heating rate affects the plasticization of biomass particle as shown in chapter 3. The plasticization is stronger at high heating rates as compared to that at low heating rates [194]. Cellulose and hemicellulose, with weak hemi-acetal bonds,

and lignin are known to undergo partial melting at high heating rates [205, 73, 112]. Heating rates affect the melting and expansion of biomass particle, which in turn affect the bond-scission, cross-linking, and intra-particle mass transfer of volatiles. Under slow heating rates, cross-linking hinders the melting of biomass particle thereby decreasing its plasticity. On the other hand at high heating rate, bond-breaking reactions dominate while cross-linking is minimized, thus, imparting fluidity to biomass particle. Extent of fluidity also depends on the oxygen and ash content of biomass. For example, herbaceous biomass have high oxygen content, which can lead to low temperature cross-linking reactions and reduce the fluidity at high heating rates when compared to woody biomass. Minerals like K and Ca can also promote polymerization reactions thereby generating char and reducing plasticity [194].

Plasticity of particle imparts additional mobility to polymer chains, intermediate radicals, and small non-volatile molecules formed during pyrolysis. The increased mobility can increase the collision frequency of reacting molecules with one another, thus, increasing the probability of conversion. Electron spin resonance spectroscopy analysis results of char obtained under same pyrolysis conditions show presence of free radicals in solidified char of wheat straw and rice husk, but there are no free radicals remaining in wood and ash leached wheat straw chars [194]. Since the wood and ash leached wheat straw are deprived of ash, biomass particle have sufficient fluidity to allow recombination of radicals and formation of polyaromatic structure. On the other hand presence of ash in wheat straw and rice husk increases cross-linking reactions and hinders the mobility of free radicals to recombine to form char or propagate to form tar molecules and intermediates. Effect of such a phenomenon on biomass conversion rate can be accounted for by modifying the frequency factor of a reaction by adding a correction factor (Table 4.3) that depends on heating rate of pyrolysis reaction. Change in the correction factor with respect to heating rate is shown in Figure 4.5. Effect of biomass fluidity on conversion would reach a limit because biomass particle does not melt completely. Different coefficients are assigned to cellulose, hemicellulose, and lignin. Char yield decreases in the order: lignin > hemicellulose > cellulose. Lignin pyrolysis proceeds through radical formation which further de-

compose to tar molecule or recombine to form char. Therefore, in most of the reactions describing lignin pyrolysis char and tar are co-produced. Hemicellulose is amorphous and more reactive than cellulose. Further effect of ash on hemicellulose pyrolysis is more profound because inorganic species are associated with glucuronic acid units [206]. Hence, different coefficients are assigned to char forming and volatilization reactions.

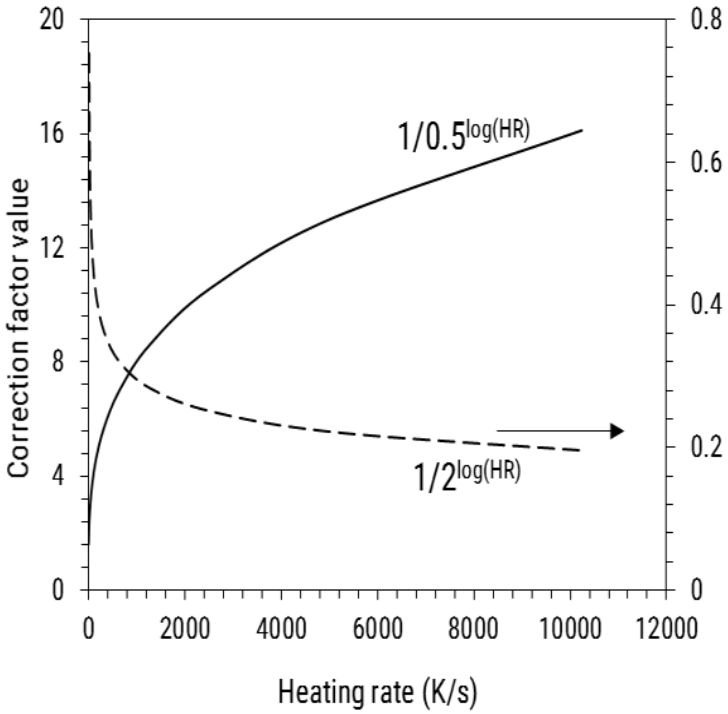

Figure 4.5: Correction factor profile with respect to heating rate

Activation energy of each reaction in Table 4.3 is assumed to follow Gaussian probability distribution. The model assumes that biomass pyrolysis is a linear combination of pseudo-components described in section 4.2.1. The composition of biomass particle at molecular level also changes spatially. So, change in molecular environment leads to change in the activation energy of a given reaction. Further, lignin pyrolysis models have been formulated based on lignin extracted from biomass. The degree of polymerization and structure of extracted lignin is different than native lignin. Also, as described in Chapter 3, DAEM can be used to describe the effect of morphological changes on the resistance of biomass volatilization process. Although Ranzi model considers separate reactions for release of trapped gases, but evolution of other tar/liquid species can also be affected by

physical changes in pore structure of biomass. Therefore, DAEM coupling with each reaction accounts for the effect of changing morphology and molecular environment of biomass particle during pyrolysis.

Finally, reactions MR5, MR13, and MR17 are added to the original Ranzi model. Reaction MR5 accounts for end chain cleavage of cellulose polymer based on mechanistic model proposed by Zhou et.al.[107]. Also, furfural is added as one of the product in reaction MR2, because furfural forms through triple dehydration of fructose, where the latter is an isomerization product of glucose. The activation energy and frequency factor of MR1 and MR5 is also adopted from the cellulose mechanistic model. Experimental data show that along with dianhydro xylopyranose (DAXP), xylose is also one of the pyrolysis products of hemicellulose [62]. Therefore, along with DAXP, (considered int he Ranzi model) xylose is also incorporated as one of the hemicellulose pyrolysis products in MR8. MR13 and MR17 are added based on the detailed lignin model proposed by Faravelli et.al.[92] to incorporate major monomeric pyrolysis products of lignin (High molecular weight lignin, KETM2, methyl guaiacol, sinapyl alcohol, propionic acid). A list of species used in the Ranzi and modified Ranzi model are reported in Table 4.4.

Table 4.3: Modified Ranzi model coupled with DAEM for biomass pyrolysis

Sr. no.	Reactant		Product	E, kJ/mol; A, s^{-1}	σ	Correction Factor
			Cellulose			
MR1	Cell	$\rightarrow$	CellA	1.5 x 10^{14} x exp(-223.844/RT)	σ_{MR1}	$1/(v_{Cell}^{log(HR)})$
MR2	CellA	$\rightarrow$	0.4 HAA + 0.05 GLYOX + 0.15 CH_3CHO + 0.25 HMFU + 0.35 ALD3 + 0.0805 FURF + 0.15 CH_3OH + 0.3 CH_2O + 0.61 CO + 0.36 CO_2 + 0.05 H_2 + 0.93 H_2O + 0.02 HCOOH + 0.05 $C_3H_6O_2$ + 0.05 T(CH_4)	2.5 x 10^6 x exp(-79.914/RT)	σ_{MR2}	$1/(v_{Cell}^{log(HR)})$
MR3	CellA	$\rightarrow$	LVG	3.3 x T x exp(-41.840/RT)	σ_{MR3}	$1/(v_{Cell}^{log(HR)})$
MR4	Cell	$\rightarrow$	5 H_2O + 6 CHAR	6 x 10^7 x exp(-129.704/RT)	σ_{MR4}	$1/(c_{Cell}^{log(HR)})$
MR5	Cell	$\rightarrow$	0.5 CellA + 0.5 LVG	3 x 10^{15} x exp(-215.476/RT)	σ_{MR5}	$1/(v_{Cell}^{log(HR)})$
			Hemicellulose			
MR6	GMSW	$\rightarrow$	0.70 HCE1 + 0.30 HCE2	1 x 10^{10} x exp(-129.704/RT)	σ_{MR6}	$1/(v_{HCell}^{log(HR)})$
MR7	XYHW	$\rightarrow$	0.35 HCE1 + 0.65 HCE2	1 x 10^{10} x exp(-119.244/RT)	σ_{MR7}	$1/(v_{HCell}^{log(HR)})$
MR8	HCE1	$\rightarrow$	0.30 XYLAN + 0.347 DAXP + 0.20 $C_3H_6O_2$ + 0.12 GLYOX + 0.20 FURF + 0.40 H_2O + 0.08 T(H_2) + 0.16 CO	3 x T x exp(-46.024/RT)	σ_{MR8}	$1/(v_{HCell}^{log(HR)})$

Table 4.3 continued from previous page

Sr. no.	Reactant		Product	E, kJ/mol; A, s^{-1}	σ	Correction Factor
MR9	HCE1	$\rightarrow$	0.4 H_2O + 0.79 CO_2 + 0.05 HCOOH + 0.69 CO + 0.01 T(CO) + 0.01 T(CO_2) + 0.35 T(H_2) + 0.3 CH_2O + 0.9 T(COH_2) + 0.625 T(CH_4) + 0.375 T(C_2H_4) + 0.875 CHAR	1.8 x 10^{-3} x T x exp(-12.552/RT)	σ_{MR9}	$1/(c_{HCell}^{log(HR)})$
MR10	HCE2	$\rightarrow$	0.2 H_2O + 0.275 CO + 0.275 CO_2 + 0.4 CH_2O + 0.1 C_2H_5OH + 0.05 HAA + 0.35 ACAC + 0.025 HCOOH + 0.25 T(CH_4) + 0.3 T(CH_3OH) + 0.225 T(C_2H_4) + 0.4 T(CO_2) + 0.725 T(COH_2) + 0.6336 CHAR	5 x 10^9 x exp(-131.796/RT)	σ_{MR10}	$1/(c_{HCell}^{log(HR)})$
			Lignin			
MR11	LIGC	$\rightarrow$	0.35 LIGCC + 0.201 COUMARYL + 0.16 PHENOL + 0.41 C_2H_4 + H_2O + 0.70 T(COH_2) + 0.30 CH_2O + 0.32 CO + 0.496 T(CH_4) + 3.844 CHAR	1 x 10^{11} x exp(-155.644/RT)	σ_{MR11}	$1/(v_{Lignin}^{log(HR)})$
MR12	LIGH	$\rightarrow$	LIGOH + 0.50 ALD3 + 0.50 C_2H_4 + 0.20 HAA + 0.10 CO + 0.10 T(H_2)	6.7 x 10^{12} x exp(-156.900/RT)	σ_{MR12}	$1/(v_{Lignin}^{log(HR)})$

Table 4.3 continued from previous page

Sr. no.	Reactant		Product	E, kJ/mol; A, s^{-1}	σ	Correction Factor
MR13	LIGH	$\rightarrow$	0.24 HMWL + 0.28 KETM2 + 0.39 MGUAIA + 0.35 PHENOL + 1.2 H_2O + 0.4 CO_2 + 0.25 CO + 0.2 CH_2O + 0.3 CH_3OH + 0.5 ALD3 + 0.306 HAA + 0.2 T(CH_3OH) + 0.2 T(CO) + 0.1 T(CO_2) + 5.251 CHAR	1 x 10^9 x T x exp(-166.73/RT)	σ_{MR13}	$1/(v_{Lignin}^{log(HR)})$
MR14	LIGO	$\rightarrow$	LIGOH + CO_2	3.3 x 10^8 x exp(-106.692/RT)	σ_{MR14}	$1/(v_{Lignin}^{log(HR)})$
MR15	LIGCC	$\rightarrow$	0.30 COUMARYL + 0.20 PHENOL + 0.35 HAA + 0.70 H_2O + 0.65 CH_4 + 0.60 C_2H_4 + H_2 + 1.40 CO + 0.4 T(CO) + 6.75 CHAR	1 x 10^4 x exp(-103.763/RT)	σ_{MR15}	$1/(v_{Lignin}^{log(HR)})$
MR16	LIGOH	$\rightarrow$	0.796 LIG + H_2O + 0.1 CH_4 + 0.60 CH_3OH + 0.05 T(H_2) + 0.3 T(CH_3OH) + 0.05 CO_2 + 0.55 CO + 0.6 T(CO) + 0.054 HCOOH + 0.85 T(COH_2) + 0.35T(CH_4) + 0.20 T(C_2H_4) + 4.15 CHAR	1 x 10^8 x exp(-125.520/RT)	σ_{MR16}	$1/(c_{Lignin}^{log(HR)})$
MR17	LIGOH	$\rightarrow$	0.45 SINAPYLALC + 0.55 MGUAIA + 0.3 PROPAC + 0.978 CH_3OH + 0.444 H_2 + 0.4 CO + 11.1 CHAR	1 x 10^9 x T x exp(-163.176/RT)	σ_{MR17}	$1/(c_{Lignin}^{log(HR)})$
MR18	LIG	$\rightarrow$	0.60 FE2MACR + 0.20 ANISOLE + 0.28 MGUAIA + 0.1 CRESOL + 0.135 DIMEPHENOL + 0.582 CO + 0.30 T(CO) + 0.30 CH_3CHO	4 x T x exp(-50.208/RT)	σ_{MR18}	$1/(v_{Lignin}^{log(HR)})$

Table 4.3 continued from previous page

Sr. no.	Reactant		Product	E, kJ/mol; A, s^{-1}	σ	Correction Factor
MR19	LIG	$\rightarrow$	0.701 H2O + 0.467 CO + 0.234 CH4 + 0.467 CH_2O + 0.234 T(CO) + 0.467 T(CH_4) +0.584 T(C_2H_4) + 0.467 T(CH_3OH) + 2.336 T(COH_2) + 7.009 CHAR + 0.234 ALD3 + 0.054 HCOOH	8.3 x 10^{-2} x T x exp(-33.472/RT)	σ_{MR19}	$1/(c_{Lignin}^{log(HR)})$
MR20	LIG	$\rightarrow$	0.876 H2O + 3.795 CO + 1.606 CH4 + 0.584 CH_2O + 1.46 C2H4 + 0.584 CH_3OH + 2.853 CHAR	1 x 10^{7} x exp(-101.671/RT)	σ_{MR20}	$1/(c_{Lignin}^{log(HR)})$
			Extractives			
MR21	TGL	$\rightarrow$	ACROL + 3 FFA	7 x 10^{12} x exp(-191.208/RT)	σ_{MR21}	$1/(v_{extractive}^{log(HR)})$
MR22	TANN	$\rightarrow$	0.85 PHENOL + 0.15 T(PHENOL) + T(CO) + H_2O + ITANN	2 x 10^{1} x exp(-41.840/RT)	σ_{MR22}	$1/(v_{extractive}^{log(HR)})$
MR23	ITANN	$\rightarrow$	5 CHAR + 2 CO + H_2O + T(COH_2)	1 x 10^{3} x exp(-104.600/RT)	σ_{MR23}	$1/(c_{extractive}^{log(HR)})$
			Metaplast reactions			
MR24	T(CO_2)	$\rightarrow$	CO_2	1 x 10^{6} x exp(-100.416/RT)	σ_{MR24}	$1/(v_{trap}^{log(HR)})$
MR25	T(CO)	$\rightarrow$	CO	5 x 10^{12} x exp(-209.200/RT)	σ_{MR25}	$1/(v_{trap}^{log(HR)})$
MR26	T(COH_2)	$\rightarrow$	CO + H_2	1.5 x 10^{12} x exp(-297.064/RT)	σ_{MR26}	$1/(v_{trap}^{log(HR)})$
MR27	T(H_2)	$\rightarrow$	H_2	5 x 10^{11} x exp(-313.800/RT)	σ_{MR27}	$1/(v_{trap}^{log(HR)})$

Table 4.3 continued from previous page

Sr. no.	Reactant		Product	E, kJ/mol; A, s^{-1}	σ	Correction Factor
MR28	T(CH_4)	$\rightarrow$	CH_4	5 x 10^{12} x exp(-299.156/RT)	σ_{MR28}	$1/(v_{trap}^{log(HR)})$
MR29	T(CH_3OH)	$\rightarrow$	CH_3OH	2 x 10^{12} x exp(-209.200/RT)	σ_{MR29}	$1/(v_{trap}^{log(HR)})$
MR30	T(C_2H_4)	$\rightarrow$	C_2H_4	5 x 10^{12} x exp(-299.156/RT)	σ_{MR30}	$1/(v_{trap}^{log(HR)})$
MR31	T(PHENOL)	$\rightarrow$	PHENOL	1.5 x 10^{12} x exp(-297.064/RT)	σ_{MR31}	$1/(v_{trap}^{log(HR)})$
			Moisture evaporation			
MR32	ACQUA	$\rightarrow$	H_2O	1 x T x exp(-33.472/RT)	σ_{MR32}	$1/(v_{trap}^{log(HR)})$

Table 4.4: List of species used in the Ranzi and modified Ranzi model.

Chemical name		$\Delta \mathbf{H}_f^0$
Formaldehyde	CH_2O	-25.96
Methanol	CH_4O	-48.11
Formic acid	CH_2O_2	-86.66
Glyoxal	$C_2H_2O_2$	-50.60
Acetaldehyde	C_2H_4O	-39.50
Acetic acid (ACAC)	$C_2H_4O_2$	-103.90
Hydroxyacetaldehyde (HAA)	$C_2H_4O_2$	-73.50
Ethanol	C_2H_6O	-55.93
Acrolein (ACROL)	C_3H_4O	-20.30
Propanal (ALD3)	C_3H_6O	-45.30
Acetol	$C_3H_6O_2$	-87.40
Propionic acid (PROPAC)	$C_3H_6O_2$	-108.94
Furfural (FURF)	$C_5H_4O_2$	-36.10
Xylose	$C_5H_{10}O_5$	-248.57
dianhydro Xylopyranose (DAXP)	$C_5H_4O_2$	-151.60
Phenol	C_6H_6O	-23.00
5-hydroxymethyl furfural (HMFU)	$C_6H_6O_3$	-79.80
Levoglucosan	$C_6H_{10}O_5$	-200.90
Cresol	C_7H_8O	-29.95
Anisole	C_7H_8O	-17.10
methylGuaiacol (MGUAIA)	$C_8H_{10}O_2$	-69.77
Dimethoxy phenol	$C_8H_{10}O_3$	-101.61
Coumaryl alcohol	$C_9H_{10}O_2$	-49.20
Sinapyl alcohol	$C_{11}H_{14}O_4$	
Sinapylaldehyde (FE2MACR)	$C_{11}H_{12}O_4$	-70.30
KETM2	$C_{11}H_{12}O_5$	
High molecular weight lignin (HMWL)	$C_{24}H_{28}O_4$	40.00

4.2.2.2 Model equations

All the reactions are assumed to follow first order reaction kinetics. Each equation is coupled with DAEM as shown below, The model equations for the coupling of DAEM and Ranzi model are as

$$\frac{dx_i}{dt} = \sum_{j=1}^{rxn} \int_0^{\infty} \frac{1}{CF_{comp}^{log(HR)}} A_{0,j} T^{m_j} exp\left(\frac{-E_j}{RT}\right) f(E) dE \prod_{i=1}^{spc} Y_{i,j} x^{\nu_{i,j}} \tag{4.5}$$

$$f(E) = \frac{1}{\sigma_j \sqrt{2\pi}} exp\left(-\frac{(E_j - E_{0,j})^2}{2\sigma_j^2}\right) \tag{4.6}$$

Where, i and j specie and reaction number while rxn and spc are total number of reactions and species; CF stands for correction factor (either v or c as given in Table 4.3) $comp$ signifies cellulose, hemicellulose, lignin, extractives, or trapped species. x_i is the mass fraction of any species i. $Y_{i,j}$ is the coefficient for any specie i and reaction j, and ν is the species order in any j reaction. $f(E)$ is the Gaussian function describing the probablistic distribution of activation energy for each reaction mentioned in Table 4.3. The values of frequency factor ($A_{0,j}$), mean activation energy ($E_{0,j}$), and temperature exponent (m_j) are used as input parameters (Table 4.3). The values of σ_j, v_{comp}, and c_{comp} are optimized using fmicon function in MATLAB and the set of differential equations are solved using ode45 solver of MATLAB.

4.3 Optimization of DAEM parameters and correction factor

Values of mean activation energy of each reaction assumed are stated in Table 4.3. The activation energy of reactions R2, R4, and R9 were calculated based on the ash content of biomass. The variance of Gaussian distribution and coefficients for correction factors, totaling 40 parameters, were optimized using pattern search algorithm (MATLAB2016). As the number of parameters was large, pattern search algorithm was chosen because it is faster than gradient specified fmincon (used in

Chapter 3). The literature data of rice straw, rice husk, and pine nutshell weight loss under pyrolysis conditions with heating rates of 5 and 1000°C/s [23] was used for optimization. The optimized parameters are reported in Table 4.5. The parameters were optimized by minimizing the error between predicted and experimental values simultaneously for 5 and 1000°C/s. As, the number of variables for optimization was large, the parameters were tested and adjusted so as to accurately predict the oil, gas, and char yield of other biomass samples (spruce, oak, and pine [24]) at different temperatures.

Table 4.5: Optimized DAEM parameters and correction factor coefficients

DAEM parameters			**Correction factor**		
σ	**ash≤1 wt.%**	**ash≥5 wt.%**	**Coefficients**	**ash≤1 wt.%**	**ash≥5 wt.%**
σ_{MR1}	10.10	10.10	v_{cell}	0.5	0.20
σ_{MR2}	6.09	6.09	c_{cell}	2.8	1.10
σ_{MR3}	2.19	2.19	v_{hcell}	0.3	0.30
σ_{MR4}	4.12	4.12	c_{hcell}	1.8	0.60
σ_{MR5}	8.97	8.97	v_{lignin}	0.15	0.15
σ_{MR6}	6.42	6.42	c_{lignin}	0.1	0.15
σ_{MR7}	7.35	7.35	$v_{extractive}$	0.4	0.2
σ_{MR8}	2.35	2.35	$c_{extractive}$	0.3	2.3
σ_{MR9}	0.59	0.59	v_{trap}	0.5	1.8
σ_{MR10}	6.58	6.58			
σ_{MR11}	6.29	6.29			
σ_{MR12}	6.98	6.98			
σ_{MR13}	8.41	8.41			
σ_{MR14}	5.22	5.22			
σ_{MR15}	4.61	4.61			
σ_{MR16}	4.79	4.79			
σ_{MR17}	3.00	3.00			
σ_{MR18}	1.53	1.53			
σ_{MR19}	1.25	1.25			
σ_{MR20}	5.03	5.03			
σ_{MR21}	9.57	9.57			
σ_{MR22}	0.93	0.93			
σ_{MR23}	4.87	4.87			
σ_{MR24}	29.03	29.03			
σ_{MR25}	46.64	21.64			
σ_{MR26}	36.79	20.79			
σ_{MR27}	37.97	21.97			
σ_{MR28}	4.94	20.94			
σ_{MR29}	62.64	62.64			
σ_{MR30}	4.94	20.94			
σ_{MR31}	20.79	28.79			

4.4 Results and discussion

Along with the Ranzi model and modified-Ranzi-DAEM coupled-correction factor included (Model 1, M1) model, two more cases of model variations were considered to test the model applicability over a wide range of heating rates. In one instance correction factor is ignored modified-Ranzi-DAEM shall be denoted by Model 2 (M2); and in another, correction factor and DAEM approach were ignored i.e. only modified Ranzi model- Model 3 (M3). Total volatile evolution profile, global yields for oil, gas, and char, and yields of major oil and gas species were compared for these four cases.

4.4.1 Model comparison: Total volatile evolution profile

The parameters were optimized using total volatile evolution profiles of rice straw (ash: 14.64 wt.%), rice husk (ash: 15.15 wt.%), and pine nutshell (ash: 1.74 wt.%). Zhang et. al. [23] employed a wire mesh reactor for biomass pyrolysis. Figure 4.6 shows the comparison of different model systems. Ranzi and M3 model systems predict the volatile release at higher temperature as compared to experimental data obtained at 5°C/s; while M2 and M1 show close predictions. The difference in the prediction of different model systems becomes evident for the experimental data acquired at 1000°C/s. The effect of correction factor becomes significant at high heating rates, which may indicate the effect of plasticity on the conversion rate of biomass to volatiles.

Conversion of intermediate species is not complete for Ranzi, M3, and M2 model systems under a heating rate of 1000°C/s (Figure 4.7). However, Krumm et.al. [207] have reported that yield of furans from cellulose flattens out in 500 ms at 500°C. Furans are triple dehydration products of mono-sugars, which are intermediate products of cellulose pyrolysis. Thus, cellulose conversion time at 500°C is less than 500 ms. The time required to heat the biomass to 700°C from room temperature is 675 ms and the particle spends 200 ms as the temperature rises from 500 to 700°C. Both Ranzi and M1 model systems correctly predict the complete conversion of cellulose, hemicellulose, and lignin but the conversion of intermediates is not complete for the Ranzi model. On the other hand, under heating rate

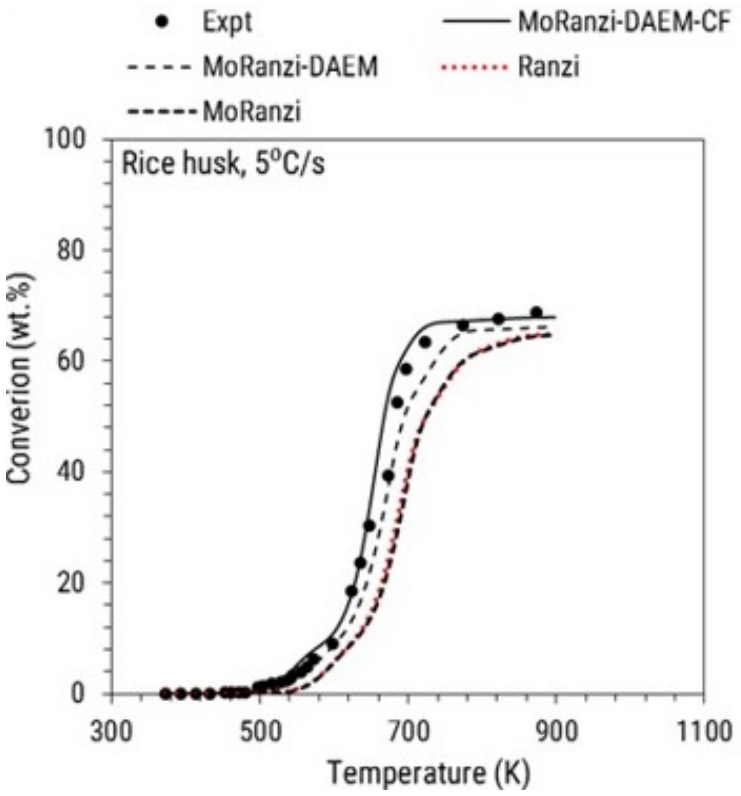

(a)

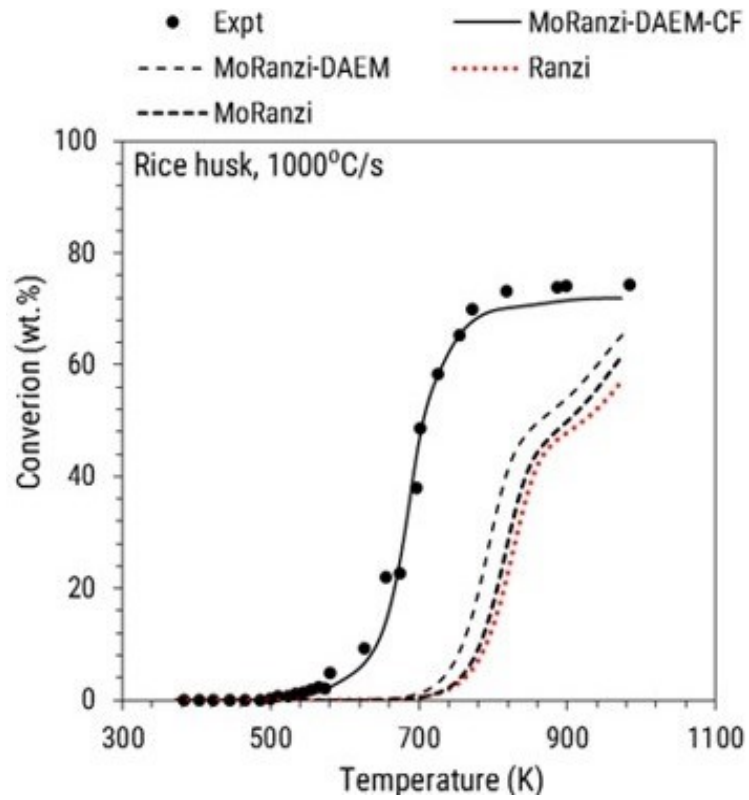

(b)

This figure is continued on the next page...

Figure 4.6

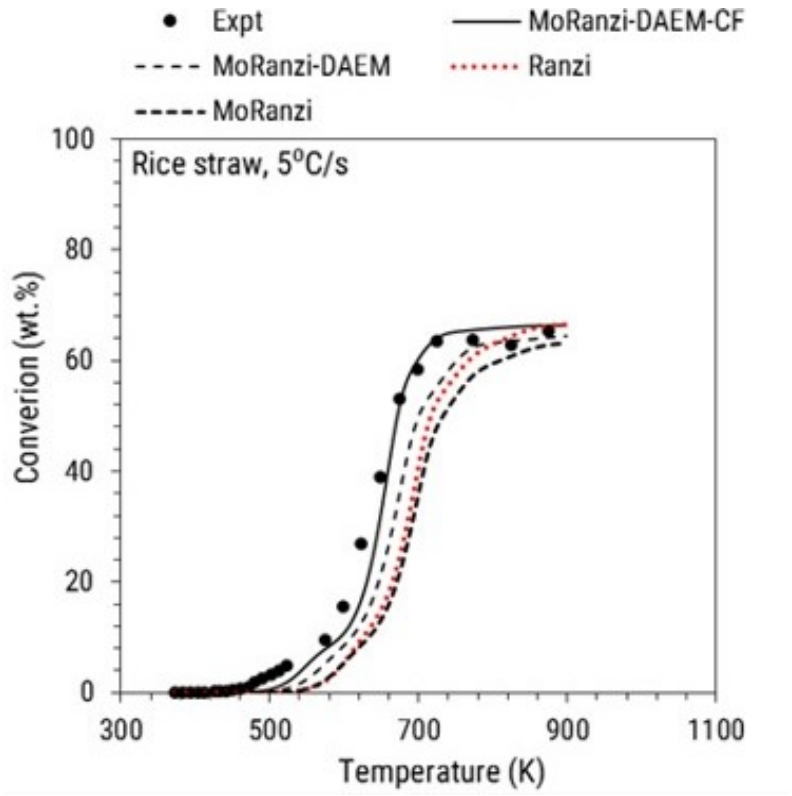

(a)

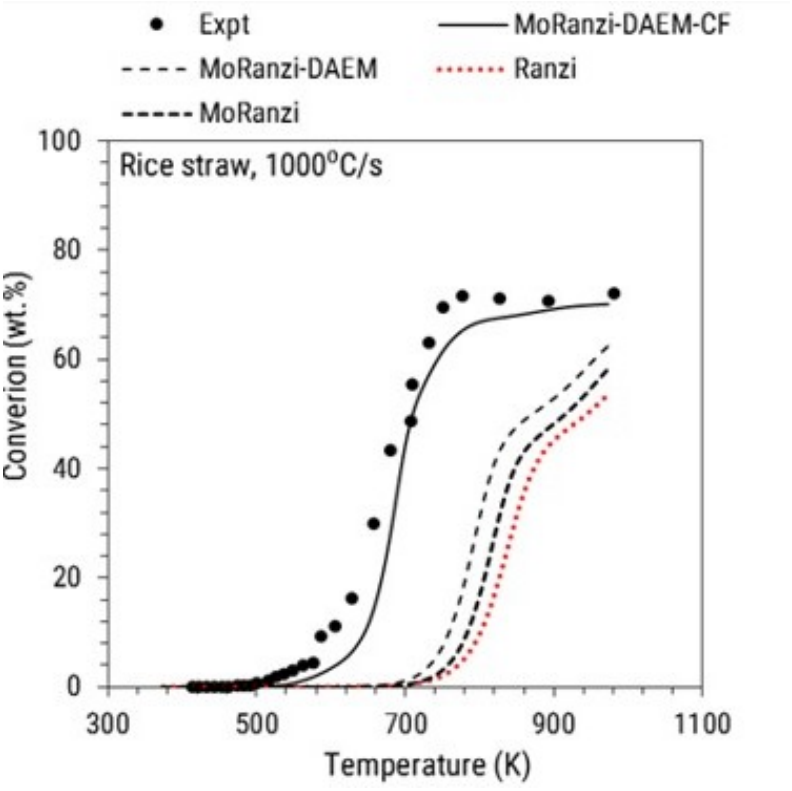

(b)

This figure is continued on the next page...

Figure 4.6

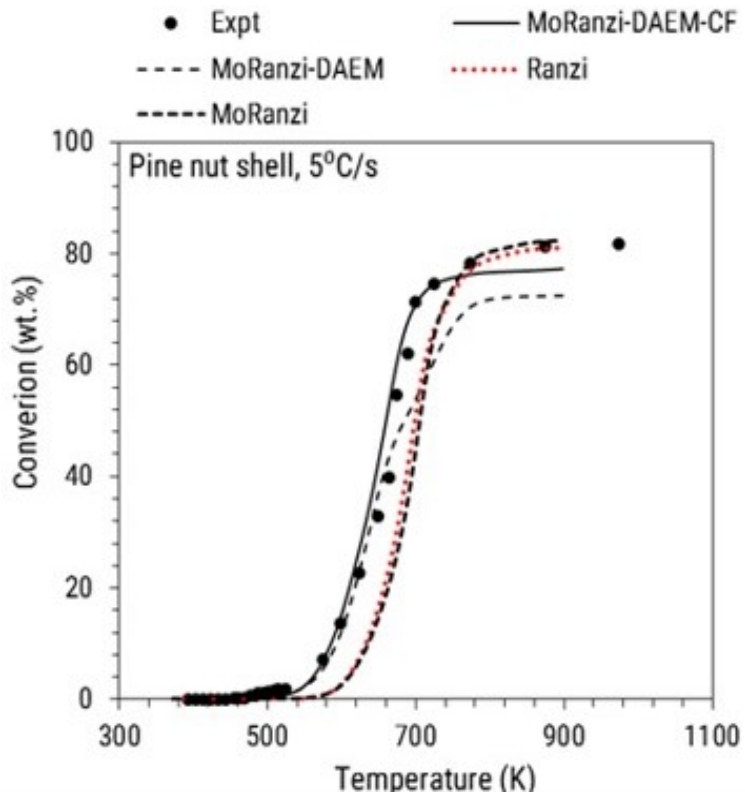

(c)

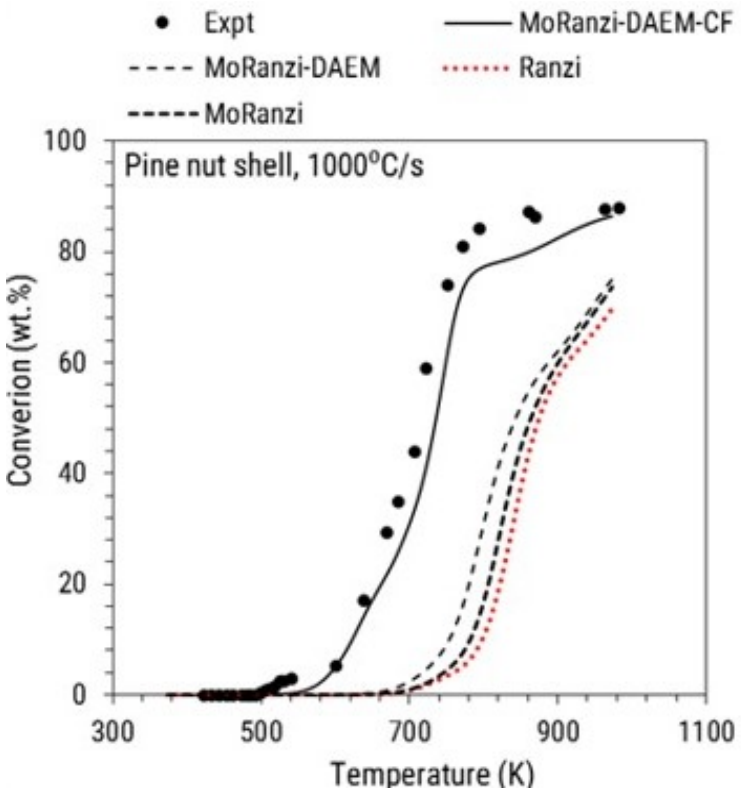

(d)

Figure 4.6: Comparison of experimental [23] and predicted values of total volatile evolution profile of rice straw, rice husk, and pine nutshell for four model systems

of 5°C/s Ranzi model shows good predictions, because the time spent by the particle at any given temperature is long enough to allow the reaction to proceed to completion. Therefore, it is necessary to compare the steady-state yield of oil, gas, and char at 1000°C/s for different model systems.

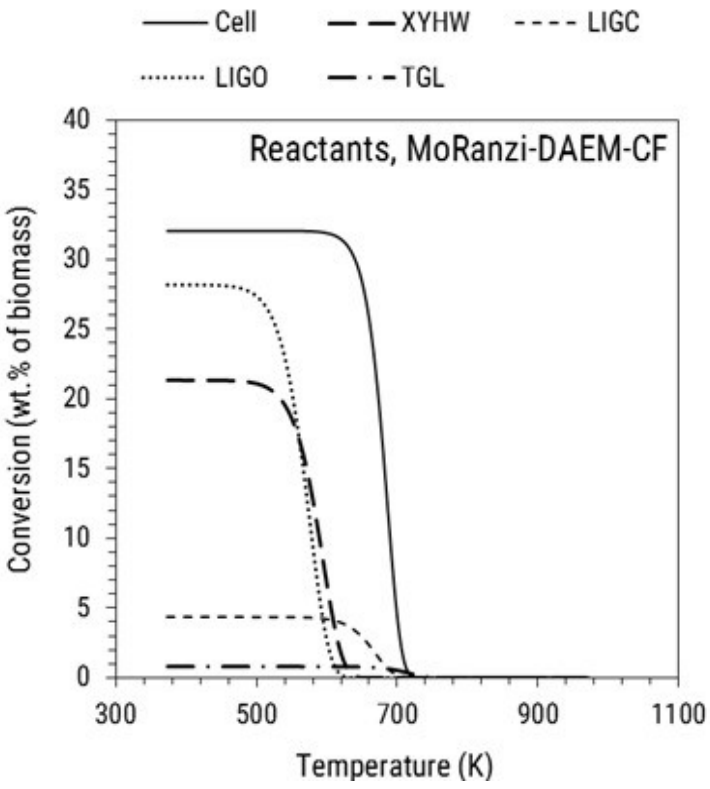

(e)

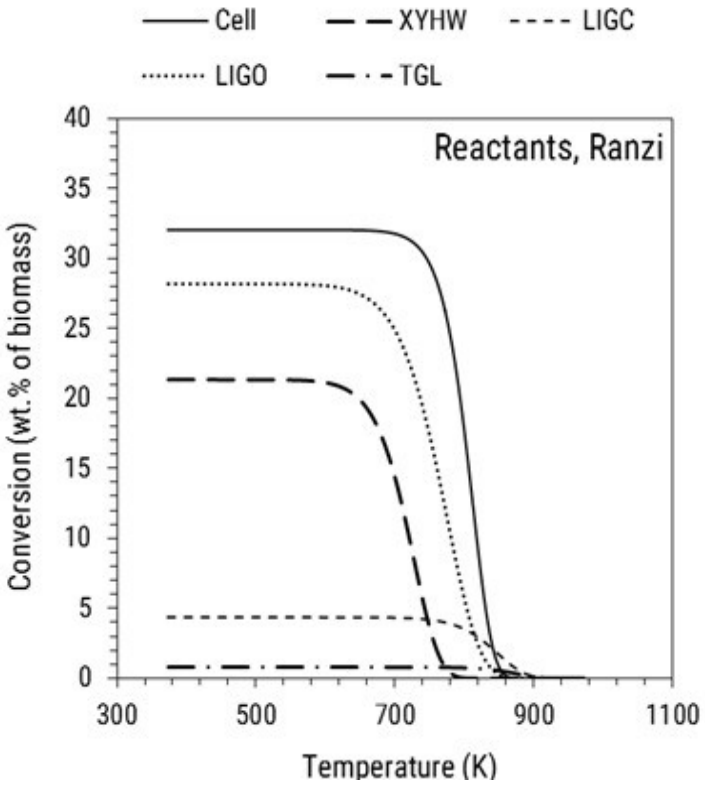

(f)

This figure is continued on the next page...

Figure 4.7

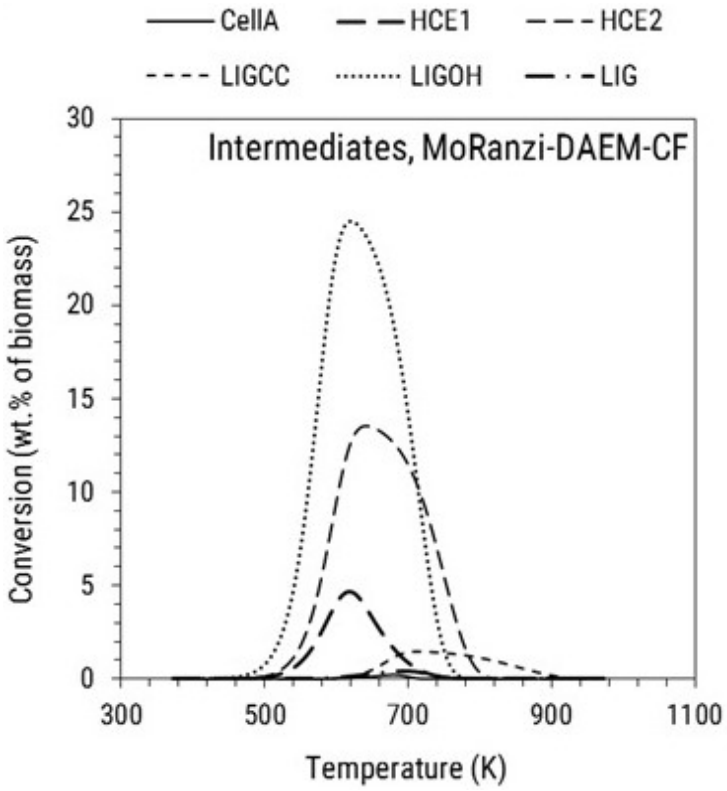

(a)

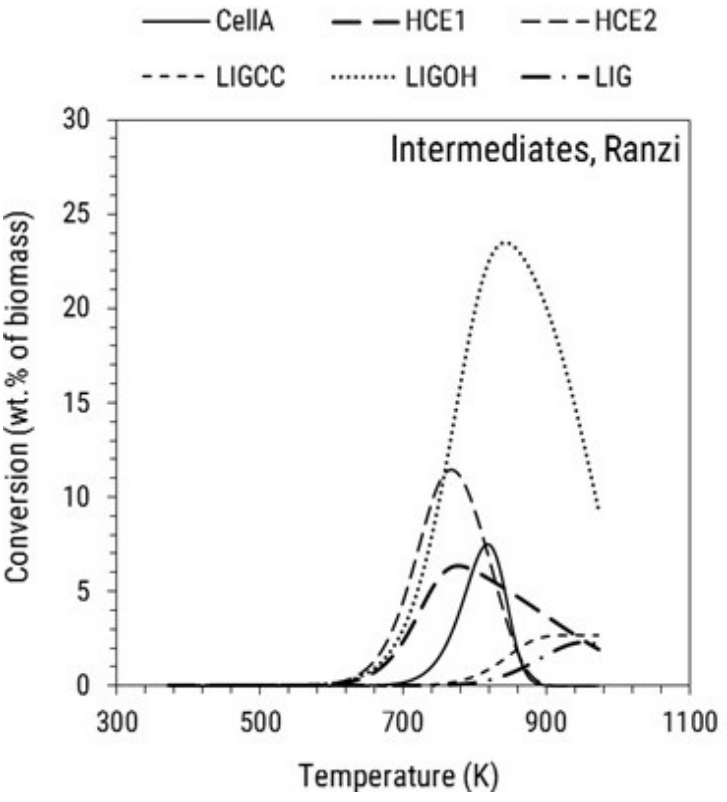

(b)

Figure 4.7: Predicted profiles of reactants and intermediates for Ranzi and M1 model systems for rice husk

4.4.2 Model comparison: Global oil, gas, and char yield

Figure 4.8 shows the comparison of four model systems predictions for oil, gas, and char yield of three biomass samples. The pyrolysis data generated under 1000°C/s for spruce, oak, and pine is adopted from [24]. The pyrolysis is carried out at 325, 450, and 525°C using a wire mesh reactor, with 15 s as holding time. There is no significant difference between the predictions of steady state oil, gas, and char yield for all model systems and for all biomass samples. However, the reaction times vary for the different model systems (Figure 4.9).

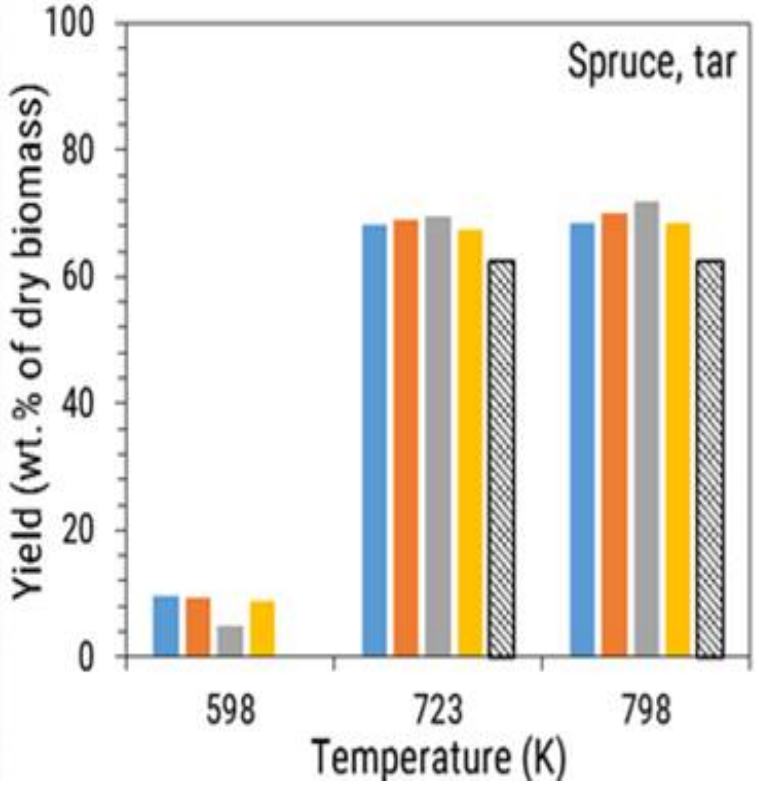

(a)

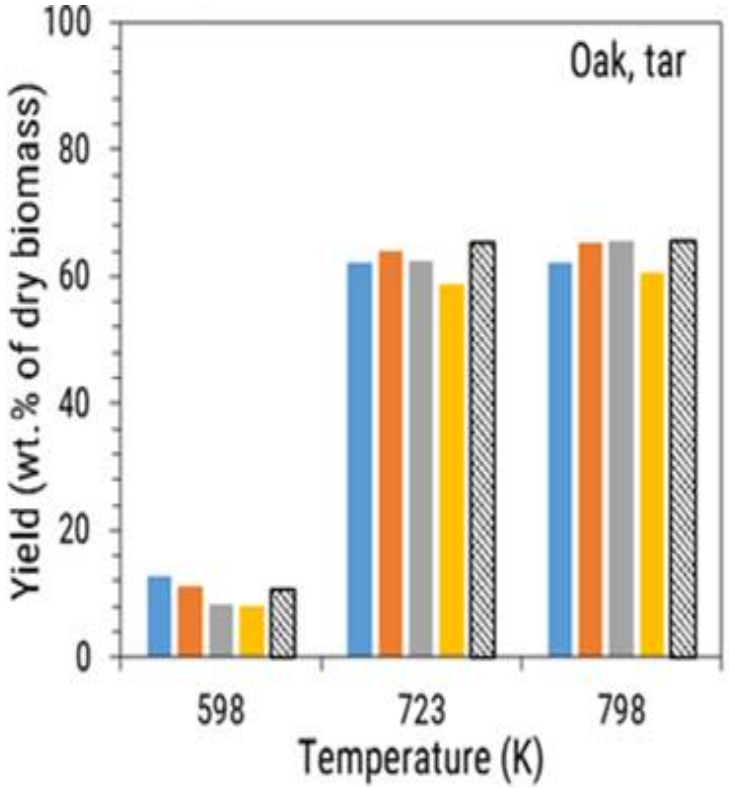

(b)

This figure is continued on the next page...

Figure 4.8

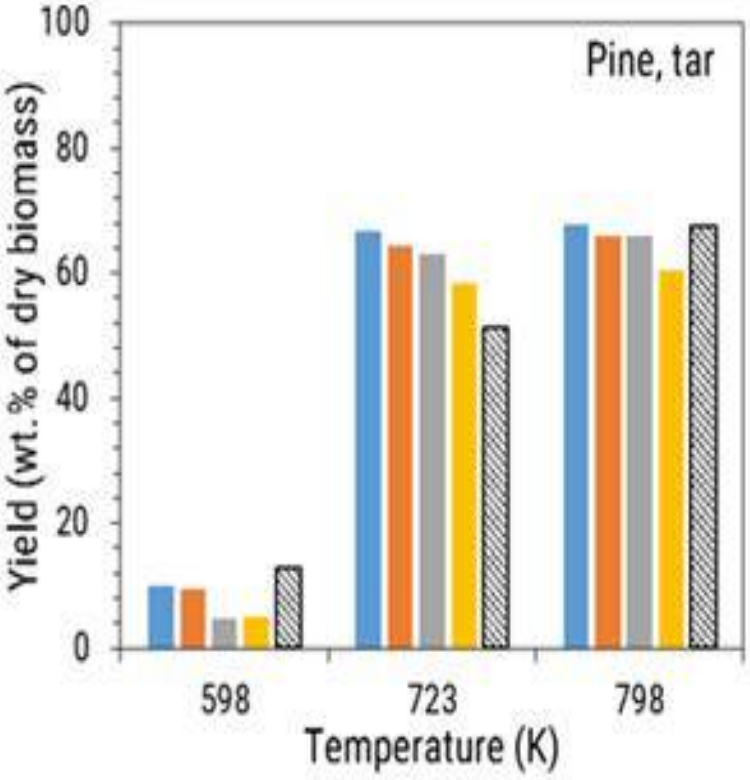

(c)

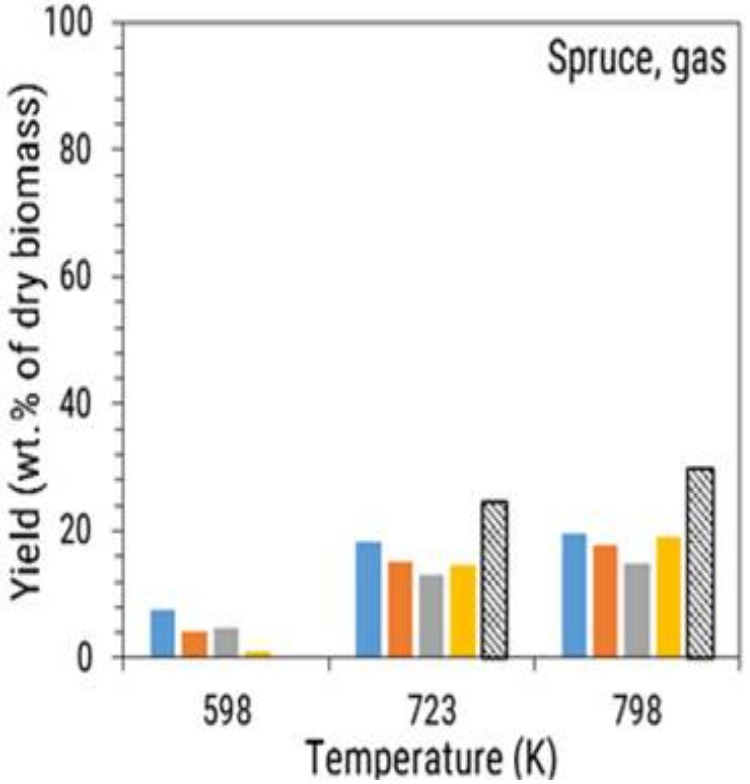

(d)

This figure is continued on the next page...

Figure 4.8

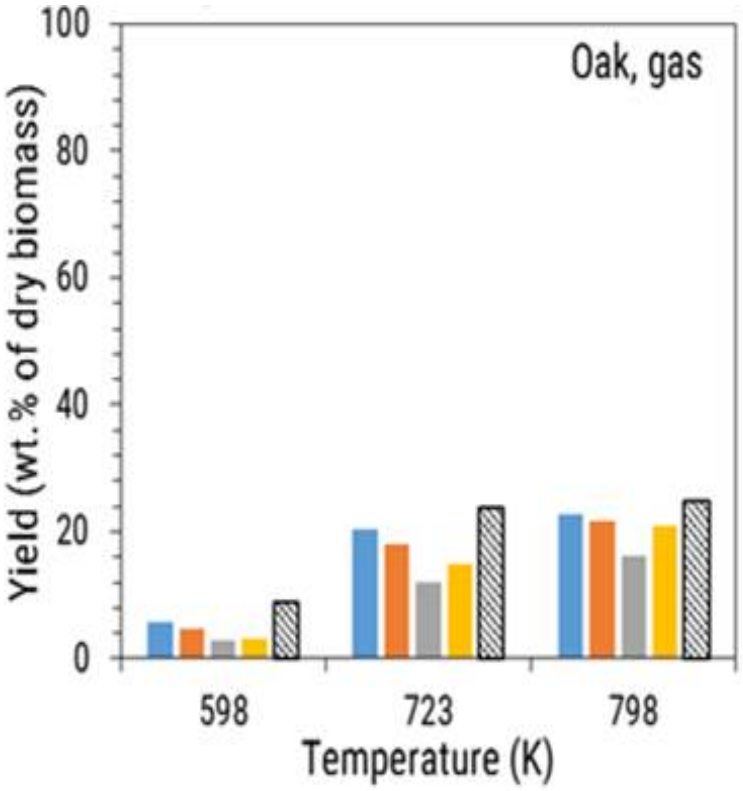

(e)

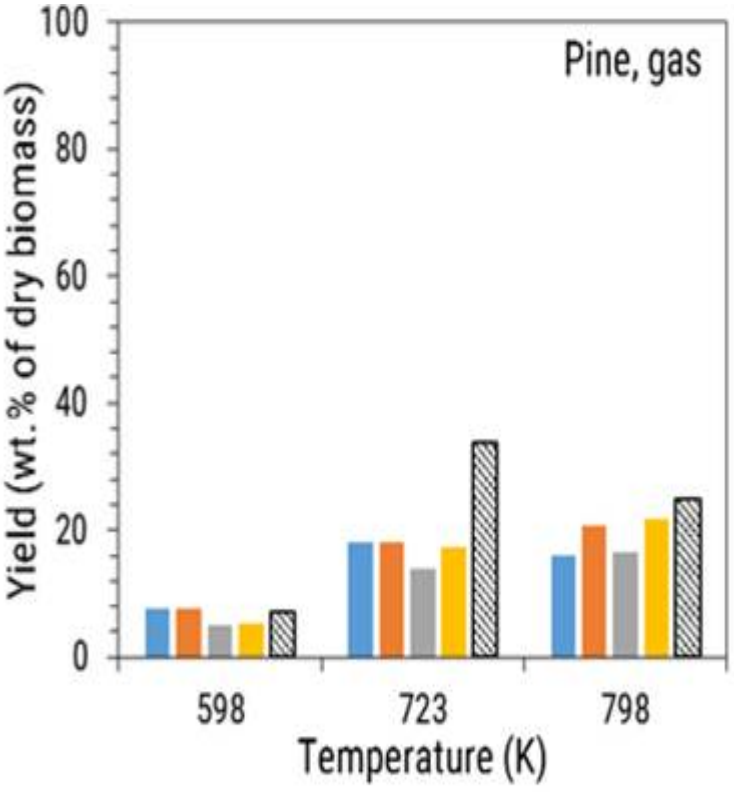

(f)

This figure is continued on the next page...

Figure 4.8

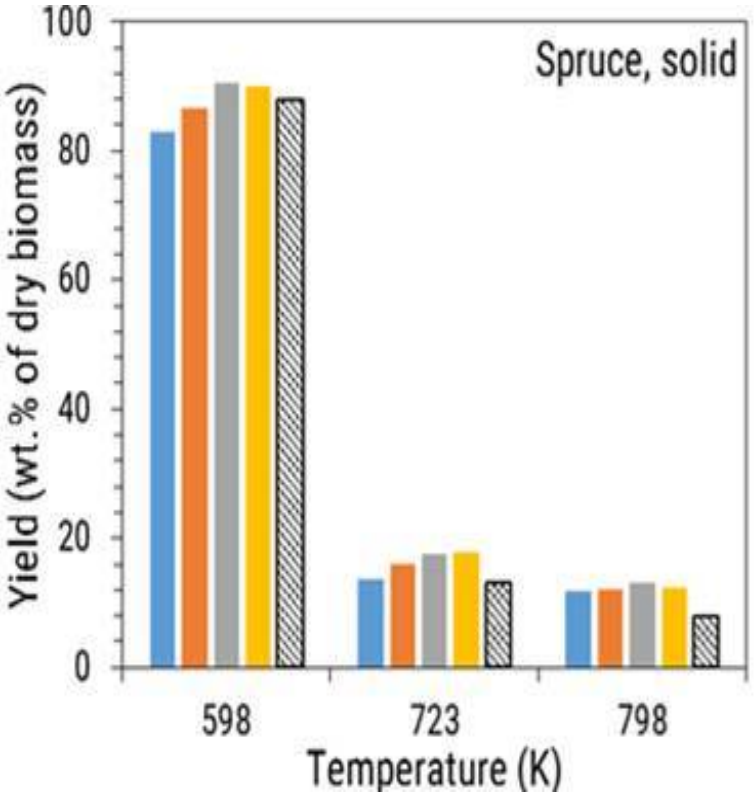

(g)

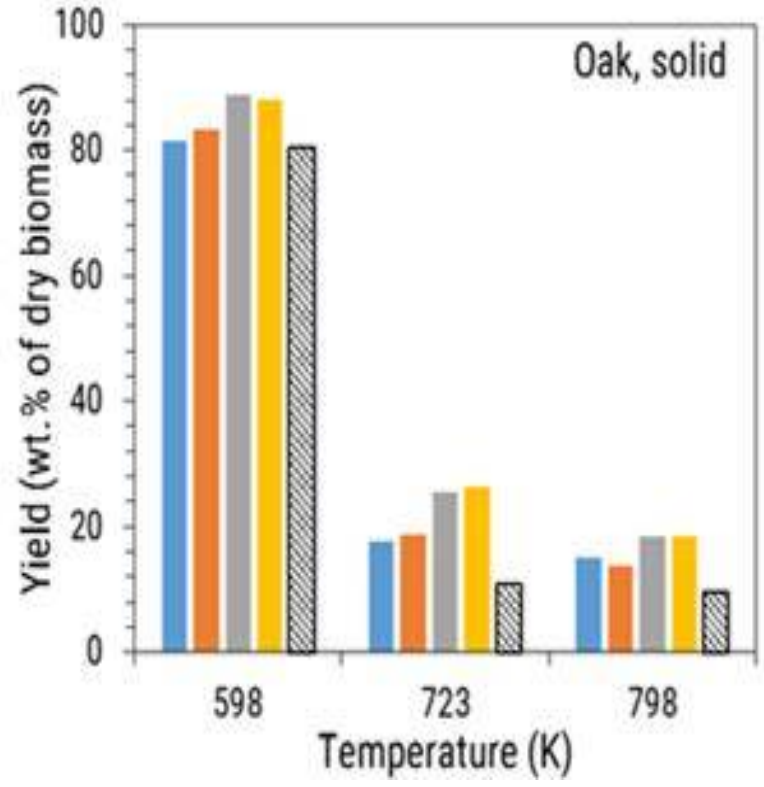

(h)

This figure is continued on the next page...

Figure 4.8

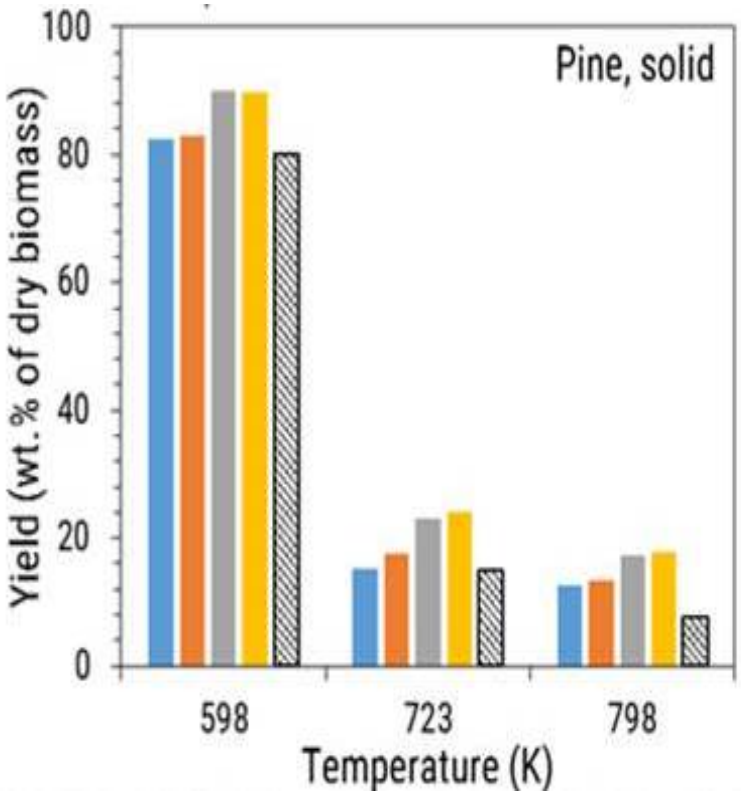

(i)

Figure 4.8: Comparison of experimental [24] and predicted values of tar, gas, and solid yield for spruce, oak and pine under 1000°C/s and 598, 723, and 798 K. The ash content of all biomass samples is $\leq$1

Accurate rate measurements for different biomass pyrolysis products [208] show that yields of the products becomes stable between 1000 to 1500 ms at 450°C. The predicted value of total volatiles does not reach a constant value until 3000 ms for Ranzi and M3 model systems; while that for M1 reaches a steady state value at 1600 ms. The final predicted values of oil, gas, and tar yield are in agreement to the experimental values, because secondary gas phase reactions were eliminated by the experimental apparatus used in [24]. However, in case of industrial/pilot scale reactors, the secondary gas phase reactions become important and the final yield of pyrolysis liquid/organics depends on the vapor residence time. It is therefore, important to accurately predict the rate of product formation. At the same time, the pyrolysis behavior in the non- isothermal region can become significant even for heating rates of 1000°C/s [207]. The heating rates in bubbling fluidized bed reactors vary between an order of 10^2 to 10^3C/s depending on the temperature difference between biomass particle and reactor. Thus, the extent of

cross-linking and depolymerization reactions that occur in the non- isothermal region, which govern the plasticity of biomass particle, can play a significant role in decomposition of biomass particle at steady state reactor temperature. Therefore, reaction kinetics should be valid over a wide range of heating rates.

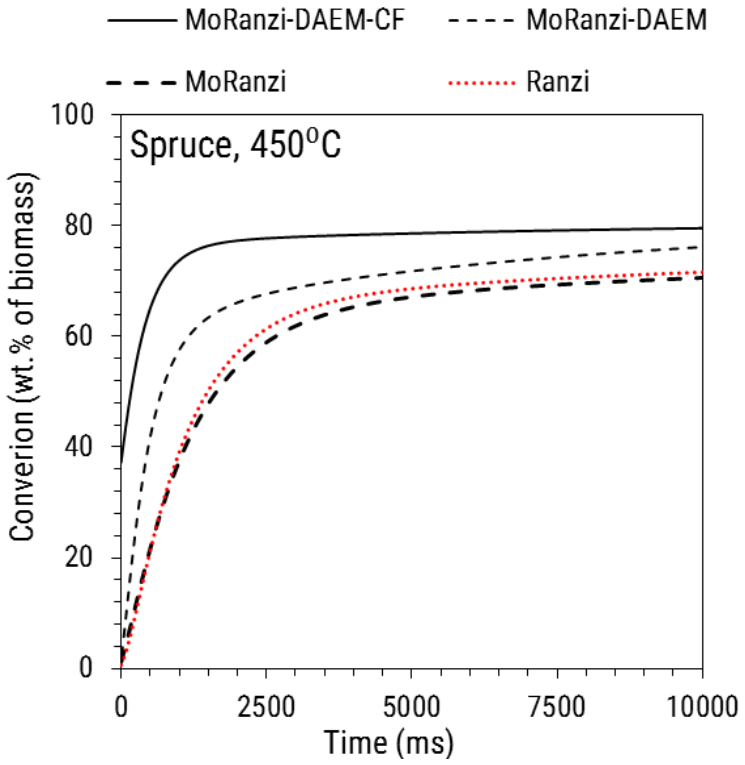

Figure 4.9: Comparison of conversion time for M1, M2, M3, and Ranzi model systems for spruce at 450°C

The DAEM parameters and correction factor coefficients (Table 4.4) for non- isothermal (section 4.4.1) and isothermal (section 4.4.2) pyrolysis data are thus validated for different heating rates, temperatures and biomass samples. For bio-mass having ash content close to 1 wt.% and ≥5 wt.% the DAEM parameters for metaplast reactions and correction factors are different. Cellulose does not form significant char in the absence of mineral content. With increase in ash content, char yield increases but the yield of levoglucosan decreases at the expense of formic acid, glyoxal, and glycoldehyde yields [28]. The value of $v_{cell,ash\leq 1} > v_{cell,ash\geq}$ but also, $c_{cell,ash\leq 1} > c_{cell,ash\geq 5}$, therefore, char yield increases at the expense of volatile content with increase in ash content for cellulose for M1 model. The effect on char formation and morphology is profound for hemicellulose as it is closely associated with mineral matter through side units like glucuronic acid [206]. However, as

compared to cellulose, hemicellulose pyrolysis in the presence of ash significantly increases the char yield but the yield of volatiles (except furfural) decreases with increase in ash content [28]. As the value of $v_{hcell,ash\leq1} = v_{hcell,ash\geq5}$ and $c_{hcell,ash\leq1} > c_{hcell,ash\geq5}$, the yield of char increases at the expense of volatiles. Finally, the correction factors for lignin do not change significantly with ash content signifying that char and volatile yield from lignin is not affected by presence of ash. A similar observation is reported in [28]. Lignin pyrolysis proceeds through free radical formation. As the biomass particle undergoes plasticization during pyrolysis, the free radicals can recombine to char or can equally like form volatile compounds and vaporize [194]. For extractives, the values of correction factors show that an increase inash content increases the rate of volatilization reaction and decreases the char formation. However, experimental evidence for this observation is not available and the observation is only a speculation. The release of trapped gases is hindered with increase in the ash content of biomass, because ash promotes formation of char and reduces the plasticity of biomass particle during pyrolysis. Thus, the liquid film on the surface of the bubble can undergo cross-linking reaction, hardening the bubble wall and trapping volatiles within biomass particle. Therefore, not only is $v_{trap,ash\leq1} < c_{trap,ash\geq5}$, but value of $\sigma_{trap,ash\leq1} >> \sigma_{trap,ash\geq5}$ (except σ_{28} to σ_{31}). The same value of DAEM parameters (σ_1 to σ_{23}) give good results for both cases of ash content, because the effect of ash is already considered by altering the activation energies as stated in section 4.2.1.2.

4.4.3 Model comparison: Gas and liquid product profile

Product profiles for pyrolysis of cellulose, hemicellulose, and lignin under heating rate of 162°C/s [209] at 500°C using micropyrolyzer are reported by Patwardhan [28]. The samples were held for 10 s at 500°C. Yield of products are expressed as wt% of initial sample weight. Thus, predictions of M1, M2, M3, and Ranzi models were compared with the experimental results of Patwardhan for ash-free and 5 wt% switchgrass ash induced cellulose, hemicellulose, and lignin.

Table 4.6 shows the comparison of product profile for ash-free cellulose pyrolysis for M1, M2, M3, and Ranzi models. Levoglucosan is significantly under predicted by Ranzi model as compared to the experimental data. M1, M2, and M3 closely

predict the levoglucosan yield. Except formic acid and char, all the models over-predict the yield of acetol, furfural, and 5-hydroxymethyl furfural. Ranzi model does not consider furfural as a cellulose product which is not true according to the experimental data. Formic acid and char is substantially under-predicted by all the models. Thus, the models require re-evaluation in terms of reaction chemistry or kinetic parameters to accurately account for the yield predictions of char and formic acid from cellulose pyrolysis. Table 4.7 tabulates the product profile for cellulose with 5 wt% switchgrass ash. Levoglucosan yield drastically decreases in the presence of ash, while that of formic acid and acetol increases. The M1 and Ranzi model overall poorly predict the product profile in presence of ash. Experimental data shows that in the presence of ash, yield of smaller oxygenates, [28] especially acetol and formic acid at the expense of levoglucosan. Cellulose in the presence of Ca^{+2} ions undergoes homolytic fission and is converted to lighter oxygenates like formic acid, acetol, and furfurals [28]. This competitive reaction needs to be considered to account for effect of ash on cellulose pyrolysis.

Table 4.6: Comparison of experimental [28] and predicted values of ash-free cellulose pyrolysis products for M1, M2, M3, and Ranzi models

Cellulose					
Compound	**Expt yield (wt%)**	**M1**	**M2**	**M3**	**Ranzi**
Formic Acid	6.6±0.23	0.20	0.22	0.20	0.39
Furan/Acetone	0.7±0.01				
Glycolaldehyde	6.7±0.72				
Acetic acid	0±0				
2-Methyl furan	0.4±0.01				
Acetol	0.3±0.02	0.81	0.88	0.81	1.59
2-Furaldehyde	1.3±0.05	1.69	1.84	1.68	0.00
2-Furan methanol	0.5±0.03				
3-Furan methanol	0.3±0				
5-Methyl furfural	0.2±0.02				
2-Hydroxy-3-methyl cyclopenten-1-one	0.2±0.01				
Levoglucosenone	0.4±0.03				
5-Hydroxymethyl furfural	2.8±0.18	6.87	7.51	6.86	13.50
Anhydro xylopyranose	3±0.66				
Levoglucosan pyranose	58.8±0.27	62.62	60.20	62.84	28.66
Levoglucosan furanose	4.1±0.09				
Other Anhydro Sugars	1.4±0.04				
Char	5.4±1.21	1.08	0.72	1.02	1.18

Table 4.7: Comparison of experimental [28] and predicted values of cellulose (with 5 wt% switchgrass ash) pyrolysis products for M1, M2, M3, and Ranzi models. *Char yield is for 1 wt% switchgrass ash

Cellulose			
Compound	**Expt yield (wt%)**	**M1**	**Ranzi**
Formic Acid	19.31	0.25	0.44
Acetol	5.28	0.99	1.78
2-Furaldehyde	0.92	2.07	0.00
5-Hydroxymethyl furfural	2.3	8.44	15.16
Levoglucosan pyranose	8.73	55.92	12.27
Char*	14.33	0.51	4.73

Table 4.8 shows the comparison of product profile for ash-free hemicellulose pyrolysis for M1, M2, M3, and Ranzi models.

M1 accurately predicts the char yield for hemicellulose, on the other hand Ranzi model substantially under predicts char. Ranzi model does not consider the formation of DAXP, but M1, M2, and

M3 over predicts the sugar yield. As models considers hemicellulose of softwood and hardwood origins, acetic acid prediction is dominant over formic acid. Since, Patwardhan extracted hemicellulose from switchgrass, xylose is a major repeating unit. The extraction of hemicellulose generally leads to loss of acetylated side chains. These acetylated side chains are responsible for the producing acetic acid during hemicellulose pyrolysis. However, it is important to understand the origin formic acid from hemicellulose. Ranzi model closely predicts the yield of carbon dioxide and carbon monoxide against M1. In presence of 5 wt% switchgrass ash, M1 better predicts the char yield as compared to Ranzi model (Table 4.9). Sugar yield decreases in the presence of ash for both the models. It is vital to note that ash profoundly affects the char yield of hemicellulose pyrolysis but does not affect the product profile of light volatiles substantially [28]. Similar trend is observed for both Ranzi and M1 models.

Table 4.8: Comparison of experimental [28] and predicted values of ash-free hemicellulose pyrolysis products for M1, M2, M3, and Ranzi models. *Water content was not determined experimentally but is a theoretical prediction [28]

Hemicellulose					
Compound	**Expt yield (wt%)**	**M1**	**M2**	**M3**	**Ranzi**
CO	2.8±0.1	13.18	14.27	5.47	5.47
CO2	18.8±0.2	14.64	15.79	14.10	14.10
Acetaldehyde	0.7±0.1	0.00	0.00	0.00	0.00
Formic Acid	11±0.3	0.57	0.64	0.64	0.64
2-methyl furan	1.5±0.1				
Acetic acid	1.1±0.1	10.34	10.34	10.34	10.34
Acetol	3±0.1	3.91	3.43	3.44	3.44
2-furaldehyde	2.2±0.1	5.08	4.45	4.46	4.46
DAXP 1	1.6±0.1				
DAXP 2	7±0.1	10.47	9.18	9.20	
Other DAXP	0.6±0.1				
AXP	2±0.1				
Other AXP	1.4±0.2	0.00	0.00	0.00	0.00
Xylose	4.9±1.1	10.47	9.18	9.20	23.50
Water*	15.1	3.68	3.68	3.68	18.41
Char	10.7±0.5	10.83	12.10	27.24	3.68

Table 4.9: Comparison of experimental [28] and predicted values of hemicellulose (with 5 wt% switchgrass ash) pyrolysis products for M1, M2, M3, and Ranzi models. *Water content was not determined experimentally but is a theoretical prediction [28]

Hemicellulose			
Compound	**Expt yield (wt%)**	**M1**	**Ranzi**
CO	3.1	6.80	6.83
CO_2	20.4	18.86	17.32
Acetaldehyde	0.7	0.00	0.00
Formic Acid	11.3	0.84	0.85
Acetic acid	1.5	10.34	10.34
Acetol	3.3	2.14	2.08
2-furaldehyde	1.5	2.77	2.70
DAXP 2	4.5	5.72	
Xylose	3	5.72	11.15
Char	21.1	26.65	33.96

Table 4.10 and Table 4.11 show the comparison of product profile for ash-free and 5 wt% ash induced lignin pyrolysis for M1, M2, M3, and Ranzi models respectively. In absence of ash, M1 accurately predicts yield of sinapyl alcohol, 2-methoxy-4-methyl phenol (methyl guaiacol) which are modification made to Ranzi model's lignin pyrolysis scheme. M1 also accurately predicts the char yield as compared to that of other models. Gas composition and yield both are inaccurately predicted by all the model systems. Except for carbon monoxide, carbon dioxide, and methyl guaiacol predictions, M1 performs better than Ranzi model for ash induced lignin. Overall, the predictions of M1 are better than other model cases for both ash-free and ash induced samples.

Table 4.10: Comparison of experimental [28] and predicted values of ash-free lignin pyrolysis products for M1, M2, M3, and Ranzi models. *Water content was not determined experimentally but is a theoretical prediction [28]

	Lignin				
Compound	**Expt yield (wt%)**	**M1**	**M2**	**M3**	**Ranzi**
CO	1.8±0.1	24.44	19.49	11.48	11.53
CO2	15.2±0.37	0.91	0.86	0.85	0.91
Acetaldehyde	0.9±0	0.04	0.62	0.68	0.91
Formic acid	0.7±0.03	0.69	0.43	0.41	0.42
2-methyl furan	0.1±0.03				
Acetic acid	11.5±0.87				
2-furaldehyde	0.2±0.01				
Phenol	1.9±0.08	1.25	1.06	1.06	0.53
2-methoxy phenol	0.9±0.02				
2-methyl phenol	0.1±0				
4-methyl phenol	0.6±0.04	0.04	0.51	0.55	
2-methoxy-4-methyl phenol	0.7±0.02	0.74	4.46	5.01	
3,5-dimethyl phenol	0.1±0				
3-ethy phenol	0.6±0.03				
4-ethyl-2-methoxy phenol	0.4±0.02				
4-vinyl phenol	3.5±0.15				
2-methoxy-4-vinyl phenol	1.8±0.03				
Unidentified (Mol. Wt. 114)	1.4±0.32				
2,6-dimethoxy phenol	1±0.05	0.07	0.97	1.07	
2-methoxy-4-(1-propenyl)-phenol (Euginol)	0.2±0				
4-methyl-2,6-dimethoxyphenol	0.8±0.03				
3,5-dimethoxy-4-hydroxy benzaldehyde	0.4±0.02				
3,4-dimethoxy acetophenone	0.8±0.03				
4-allyl-2,6-dimethoxyphenol	0.2±0				
4-allyl-2,5-dimethoxyphenol2	0.3±0				
3,5-dimethoxy-4-hydroxy acetophenone	0.3±0.01				
Sinapyl alcohol	0.7±0.03	0.66	2.72	3.12	
Unidentified (Mol. Wt. 280)	0.4±0				
Water*		6.57	5.32	5.05	5.55
Char	37±0.22	36.94	34.04	43.41	44.10

Table 4.11: Comparison of experimental [28] and predicted values of lignin (with 5 wt% switchgrass ash) pyrolysis products for M1, M2, M3, and Ranzi models. *Water content was not determined experimentally but is a theoretical prediction [28]

Lignin			
Compound	**Expt yield (wt%)**	**M1**	**Ranzi**
CO	1.8±0.1	13.94	11.53
CO2	15.2±0.37	0.89	0.91
Acetaldehyde	0.9±0	0.88	0.91
Formic acid	0.7±0.03	0.49	0.42
Phenol	1.9±0.08	1.07	0.53
4-methyl phenol	0.6±0.04	0.72	
2-methoxy-4-methyl phenol	0.7±0.02	4.11	
2,6-dimethoxy phenol	1±0.05	1.39	
Sinapyl alcohol	0.7±0.03	1.38	
Water*		5.44	5.55
Char	37±0.22	39.24	44.10

4.5 Summary

Reactions in the Ranzi model for biomass pyrolysis were first modified by adding three reactions and eight species to account for the formation of seven different lignin monomers and dianhydro xylopyranose. Modified detailed lumped Ranzi model was coupled with DAE modeling approach and a correction factor with logarithmic dependence on heating rate was added. Necessity of DAEM coupling and correction factor were attributed to the effect of plasticization and morphological changes on rate of biomass conversion under pyrolysis conditions. The DAEM parameters and coefficient for correction factors were optimized using non- isothermal pyrolysis data of rice husk, rice straw, and pine nut shell from literature. The modified model (M1) substantially improved the prediction of biomass pyrolysis behavior under non- isothermal conditions for heating rate of 1000°C/s. Two more variation, M2 (no correction factor) and M3 (no DAEM and correction factor) were also tested to justify the use of DAEM and correction factor for close prediction of non- isothermal biomass pyrolysis behavior. Fairly accurate predictions of biomass pyrolysis reaction times as compared to Ranzi model, further justified the use of DAEM coupling and heating rate dependent correction factor. However, M1, M2, M3 and Ranzi model accurately predicted the steady state global yields of oil, gas, and char for spruce, oak, and pine biomass for pyrolysis carried out at 325, 450, and 525°C under a heating rate of 1000°C/s and negligible gas phase secondary reactions. This observation suggests that DAEM coupling and correction factor incorporation would play important role when secondary gas phase reactions are significant; which is the case in industrial/pilot scale reactors. The predictability of the models was also tested for liquid and gas composition of ash-free and ash induced cellulose, hemicellulose and lignin pyrolysis. M1 fairly accurately predicts the liquid composition of ash-free cellulose, hemicellulose and lignin (except carboxylic acid yields) when compared to the Ranzi model. However, additional reactions and kinetic constants are required to account for the effect of ash on biomass pyrolysis.

Chapter 5

Biomass fast pyrolysis: Bubbling fluidized bed reactor modeling

5.1 Introduction

Hydrodynamic characteristics of the reactor affect the physico-chemical processes of pyrolysis. The gas, liquid, and solid yields, and rate of primary pyrolysis reactions (biomass devolatilization) are affected by biomass composition, particle heating rate, temperature, and solid residence time. Secondary gas/vapor phase reactions that occur outside biomass particle are affected by gas temperature, vapor concentration, and gas residence time. Vigorous mixing in BFB promotes rapid heat transfer to biomass particle thus, increasing the selectivity for primary volatilization reactions over charring reactions. Under fast pyrolysis temperatures (400 to 600°C), vapors released from biomass immediately undergo secondary gas phase reactions and significantly reduce the liquid yield of organics if the vapor residence time is of the order of 2 to 5 s. It is therefore essential to accurately model the primary devolatilization reaction time, because time spent by primary pyrolysis vapors governs the extent of secondary gas phase reactions. Chapter 4 shows that Ranzi model underpredicts primary pyrolysis reaction rate, which can affect the extent of secondary pyrolysis reaction inside the reactor and in turn over predict the oil yield [210]. The DAEM coupled Ranzi model proposed in chapter 4 improves the prediction of pyrolysis reaction rates. The objective of this chapter is to develop an engineering model for BFB to simulate fast pyrolysis

process and compare the performance of DAEM coupled Ranzi model and Ranzi model. The extent of secondary gas phase reactions for these two reaction kinetic schemes is also studied.

The objective of the present work is to test the effect of primary reaction chemistry on yield and composition of liquid, gas, and solid products, while maintaining the same secondary gas phase reaction chemistry.

5.2 Mathematical model

Figure 5.1 shows schematic of fast pyrolysis BFB modeling framework developed in the present study. The framework consists of three interconnected modules, (a) pyrolysis reaction kinetics, (b) reaction engineering model, and (c) hydrodynamics. The kinetics module defines primary and secondary pyrolysis reaction chemistry. Two cases are considered for defining the primary pyrolysis reaction chemistry, Ranzi model [10] and DAEM coupled modified Ranzi model with incorporation of correction factor (Chapter 4). The gas phase secondary reaction chemistry is adopted from Ranzi model [10]. A total of 507 vapor/gaseous species undergo 20,239 secondary reactions in the gas phase. The particle size and properties specific hydrodynamic correlations are provided through the hydrodynamics module. The reaction engineering model defines the transient mass and energy balance equations for the gas and solid phases.

5.3 Pyrolysis kinetics

Pyrolysis chemistry is classified in two categories- primary and secondary reactions (Chapter 2 Figure 2.3). The primary reactions are described using Ranzi model and DAEM coupled modified Ranzi model as tabulated in Chapter 4 Table 4.2 and 4.3. The application of primary pyrolysis reaction chemistry is divided into two cases, Case 1: Ranzi model and Case 2: DAEM coupled Ranzi model with considering correction factor. Secondary reactions comprise of homogeneous gas phase reactions as well as char devolatilization reactions. However, the char devolatilization reactions are not considered in this study. The gas phase reactions used in this study are reported in [10, 210]. The total number of reactant, inter-

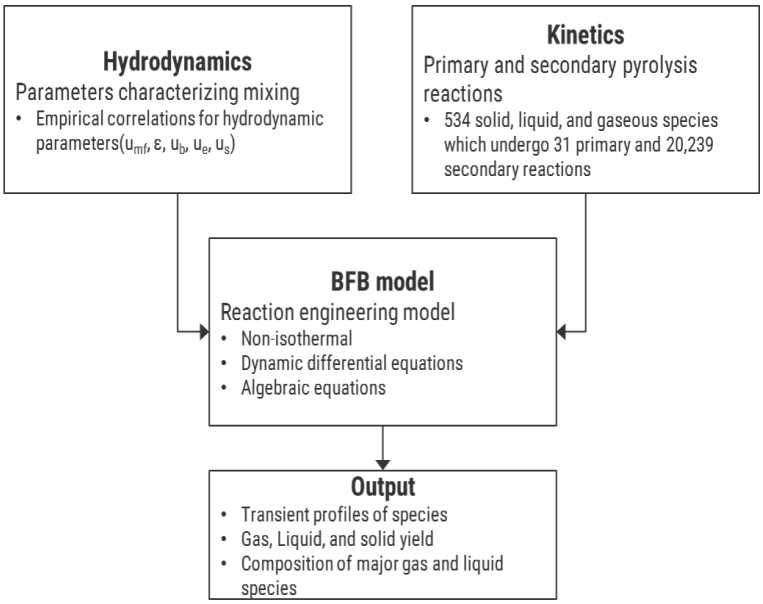

Figure 5.1: Schematic of Pyrolysis BFB Model

mediate, and product species is 534, of which 507 gaseous species undergo 20,239 reactions.

5.4 Fluidized bed reaction engineering model

A fluidized bed reactor can be assumed to be in the bubbling regime under gas velocities 3 to 8 times u_{mf} [211]. Models of varying complexity, describing the mixing behavior of bubbling fluidized bed reactors (BFB) are reported in the literature [212]. The hydrodynamics of the BFB is usually represented using two phases namely bubble and emulsion phase [213, 211]. An additional third phase, referred as cloud phase can also be included depending on the operating gas velocity[214]. The gas velocity in the cloud phase is significantly high as compared to that in the emulsion phase [212]. If the cloud fraction is significant, the overall gas residence time in the reactor decreases.

Mixing in BFB is complex, especially for the case of binary solids [170, 215]. In the literature, all the phases (emulsion, cloud, and bubble) are modeled either as a perfectly mixed or plug flow. The actual behavior of the bed is between these two ideal cases. Representing each phase as a series of perfectly mixed tanks provides flexibility to vary the degree of mixing in each phase [214]. Thus, a mixing cell framework is used in this study to model the hydrodynamics of a BFB. The resi-

dence time of gas and solid phases can be easily adjusted by changing the number of tanks. The effect of biomass feed location on the overall yield of products can also be easily evaluated using the mixing cell model.

The emulsion, bubble, and cloud phases are modeled as interacting sets of mixing cells. Solid circulation and inter-phase heat and mass transfer connect the three phases. The number of mixing cells can be adjusted for the emulsion, bubble, cloud phase such that the bubble and cloud phase have the same number of tanks and the ratio of bubble/cloud tanks to emulsion tanks is an integer. Figure 5.3 (a) shows the flow patterns in a BFB [212], and Figure 5.1 (b) shows a mixing cell modeling framework of BFB developed in the present study.

For initially estimating the hydrodynamic parameters of reactor model, density and viscosity of nitrogen are used. The bubble and cloud cells are assumed to be in plug flow, while the emulsion cell is assumed to be perfectly mixed [212, 215]. Additionally, the following assumptions are made in developing equations for fluidized bed reaction engineering model.

1. Bubble phase and free-board region do not contain any solids. Thus, primary pyrolysis reactions occur only in the emulsion and cloud phase.

2. Biomass is fed at the bottom most emulsion and cloud cells.

3. Intra-particle heat and mass transfer for biomass particle is negligible [53, 13].

4. Solids are not elutriated from the bed but recirculate within the emulsion and cloud phases.

5. Solids move upward in the cloud phase in the form of wake, while those in the emulsion phase move downwards.

6. Biomass particle size remains same, hence volume fraction in a give tank remains same. The density decreases with increase in char fraction.

7. Circulation velocities for sand and biomass particles are same. Thus, biomass and sand phase do not segregate.

8. Emulsion and cloud phase are assumed to be under minimum fluidization state.

9. Excess gas in addition to that required for the fluidization of solid particles passes through the bed in the form of bubbles and thus represent the bubble phase.

10. The number of bubble and cloud phase cells is the same.

11. The ratio of number to bubble or cloud phase cells to number of emulsion cells is an integer.

Using the above assumptions transient mass and energy conservation equations for the emulsion, bubble, and cloud phase are written.

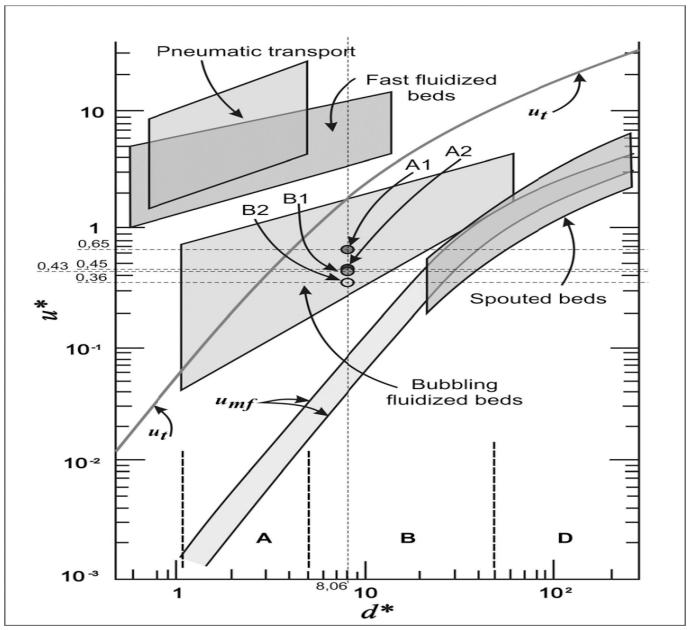

Figure 5.2: Flow regime diagram for gas-solid contacting

5.4.1 Emulsion phase balance

The emulsion cells contains both solid and gas species. Species and heat transport between the emulsion and corresponding cloud cells is also included in the conservation equations. Mass conservation of i^{th} emulsion cell for all biomass, sand, and gas species and overall enthalpy balance for the emulsion cell is written as follows.

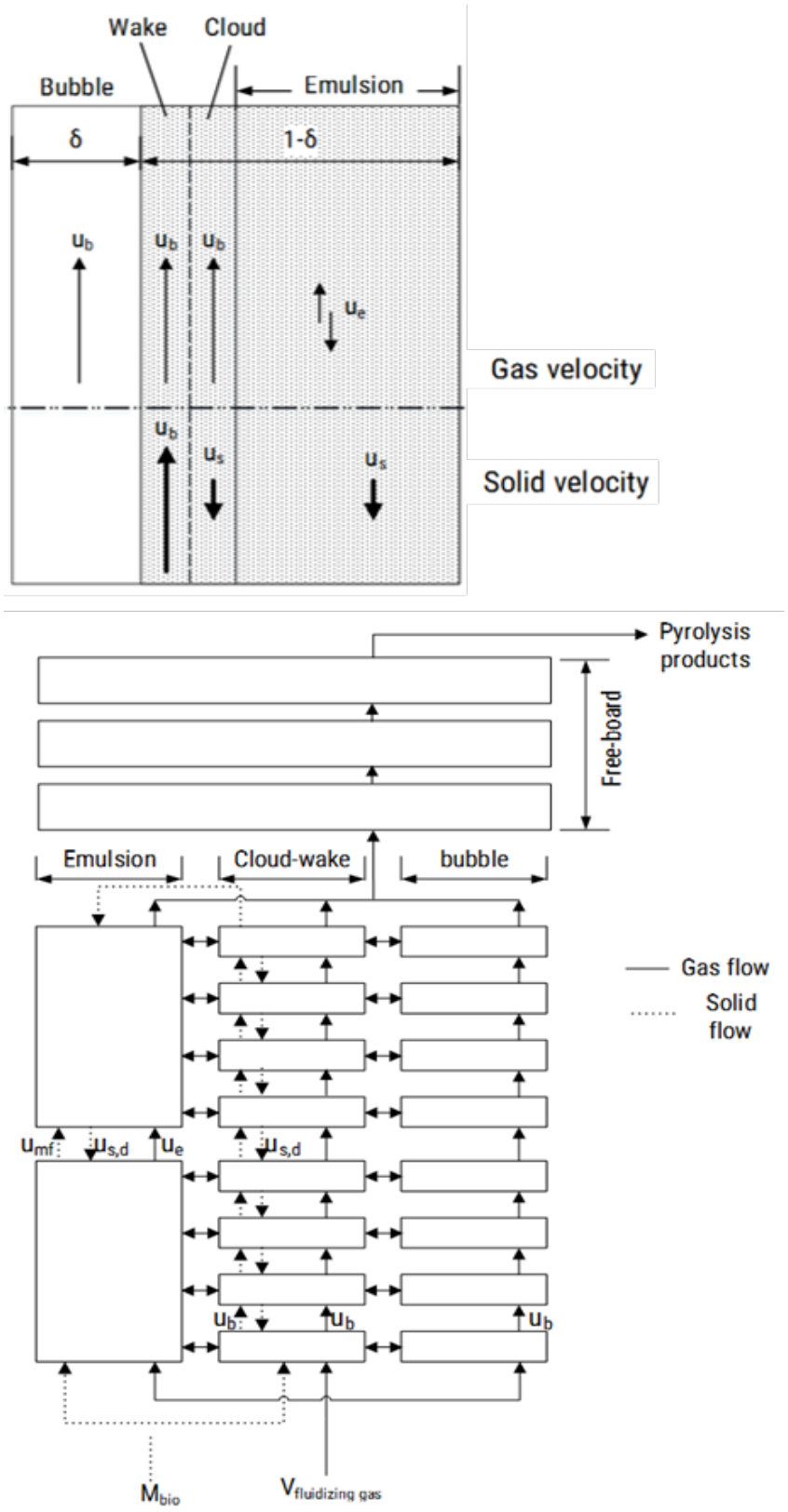

Figure 5.3: (a) Flow patterns in bubbling fluidized bed reactor, (b) Tank is series engineering model for bubbling fluidized bed reactor

5.4.1.1 Emulsion phase mass balance

Mass balance for solid species j in biomass involved in primary devolatilization reactions,

$$\frac{d}{dt}\left(\rho^i_{mix,e}X^i_B Y^i_{B,j}\right) = \frac{1}{V^i_e(1-\epsilon_{mf})}\Bigg(u_{s,d}a^{i+1}_e(1-\epsilon_{mf})\rho^{i+1}_{mix,e}X^{i+1}_B Y^{i+1}_{B,j} + u_{mf}a^{i-1}_e(1-\epsilon_{mf})\rho^{i-1}_{mix,e}X^{i-1}_B Y^{i-1}_{B,j} - (u_{s,d}+u_{mf})a^i_e(1-\epsilon_{mf})\rho^i_{mix,e}X^i_B Y^i_{B,j} + R^i_{Y_{B,j}}\Bigg) \tag{5.1}$$

$$\rho^i_{mix,e} = X^i_B\rho_B + X^i_B Y^i_{B,C}\rho_C + (1-X^i_B)\rho_{sand} \tag{5.2}$$

Overall mass balance for biomass in emulsion cell,

$$\frac{d}{dt}\left(\rho^i_{mix,e}X^i_B\right) = \frac{1}{V^i_e(1-\epsilon_{mf})}\Bigg(u_{s,d}a^{i+1}_e(1-\epsilon_{mf})\rho^{i+1}_{mix,e}X^{i+1}_B + u_{mf}a^{i-1}_e(1-\epsilon_{mf})\rho^{i-1}_{mix,e}X^{i-1}_B - (u_{s,d}+u_{mf})a^i_e(1-\epsilon_{mf})\rho^i_{mix,e}X^i_B + \sum_{j=1}^{n_{B,s}} R^i_{Y_{B,j}}\Bigg) \tag{5.3}$$

Overall mass balance for sand in emulsion cell,

$$\frac{d}{dt}\left(\rho^i_{mix,e}(1-X^i_B)\right) = \frac{1}{V^i_e(1-\epsilon_{mf})}\Bigg(u_{s,d}a^{i+1}_e(1-\epsilon_{mf})\rho^{i+1}_{mix,e}(1-X^{i+1}_B) + u_{mf}a^{i-1}_e(1-\epsilon_{mf})\rho^{i-1}_{mix,e}(1-X^{i-1}_B) - (u_{s,d}+u_{mf})a^i_e(1-\epsilon_{mf})\rho^i_{mix,e}(1-X^i_B)\Bigg) \tag{5.4}$$

The upward velocity of solids in the emulsion cell (u_{mf}) is set to zero, so that solids move in the downward direction only. For the top most emulsion cell, solids come in from the top most cloud cell, while solids leaving the bottom most emulsion cell recirculate to the bottom most cloud cell. The primary pyrolysis reaction rate is based on the mass fraction of reactant species.

Mass balance for vapor/gas phase species released from primary devolatilization

reactions,

$$\frac{d}{dt}\left(Y_{G,j}^{i}\right) = \frac{RT_e^i}{PV_e^i \epsilon_{mf} MW_{G,avg}^i}\left(\frac{PMW_{G,avg}^{i-1}}{RT_e^{i-1}} u_e a_e^{i-1} \epsilon_{mf} Y_{G,j}^{i-1} - \frac{PMW_{G,avg}^{i}}{RT_e^{i}} u_e a_e^{i} \epsilon_{mf} Y_{G,j}^{i} + R_{C_{G,j}}^i + V_e^i \epsilon_{mf} R_{Y_{G,j}}^i + \sum_{i=1}^{N_{ceR}} k_{ce} V_{cw}^i \left[\frac{PMW_{G,avg}^i}{RT_{cw}^i}\frac{Y_{G,j}^{cw,i}}{MW_{G,j}} - \frac{PMW_{G,avg}^i}{RT_e^i}\frac{Y_{G,j}^{e,i}}{MW_{G,j}}\right]\right) \tag{5.5}$$

Gas velocity (u_e) in the emulsion cell is relative velocity between upward moving gas and downward moving solids. The gas moves only in the upward direction because Geldart B type particles are considered in this study. For Geldart A and AB type particles, the gas velocity through the emulsion phase can be in the downward direction [212].

5.4.1.2 Emulsion phase energy balance

Energy balance equation for emulsion cell,

$$\begin{aligned}\frac{dT_e^i}{dt} = &\left(\frac{RT_e^i}{RT_e^i(Cp_{B,mix}^i X_B^i + Cp_S(1-X_B^i))V_e^i(1-\epsilon_{mf})\rho_{mix,e}^i + PV_e^i MW_{G,avg}^i \epsilon_{mf} \sum_{j=1}^{n_G} Y_{G,j}^i Cp_{G,j}}\right) \\ &\Bigg[u_{s,d} a_e^{i+1}(1-\epsilon_{mf})\rho_{mix,e}^{i+1}(X_B^{i+1} Cp_{B,mix}^{i+1} + (1-X_B^{i+1})Cp_S)(T_e^{i+1} - T_{ref}) \\ &+ u_{mf} a_e^{i-1}(1-\epsilon_{mf})\rho_{mix,e}^{i-1}(X_B^{i+1} Cp_{B,mix}^{i-1} + (1-X_B^{i-1})Cp_S)(T_e^{i-1} - T_{ref}) \\ &- (u_{s,d} + u_{mf}) a_e^{i}(1-\epsilon_{mf})\rho_{mix,e}^{i}(X_B^{i} Cp_{B,mix}^{i} + (1-X_B^{i})Cp_S)(T_e^{i} - T_{ref}) \\ &+ u_e a_e^{i-1}\epsilon_{mf}\frac{PMW_{G,avg}^{i-1}}{RT_e^{i-1}}\sum_{j=1}^{n_G} Y_{G,j}^{i-1} Cp_{G,j}(T_e^{i-1} - T_{ref}) \\ &- u_e a_e^{i}\epsilon_{mf}\frac{PMW_{G,avg}^{i}}{RT_e^{i}}\sum_{j=1}^{n_G} Y_{G,j}^{i} Cp_{G,j} Cp_{G,j}(T_e^{i} - T_{ref}) \\ &+ \left\{\sum_{j=1}^{n_{B,s}} R_{Y_{B,j}}^i \Delta H_{r_j}\right)\Bigg\} \\ &+ V_e^i \epsilon_{mf} R_{Y_{G,j}}^i \Delta H_{r,j} - \sum_{m=1}^{N_{ceR}} h_{ce} V_{cw}^m (T_e^i - T_{cw}^m)\Bigg]\end{aligned} \tag{5.6}$$

$$Cp^i_{B,mix} = \sum_{j=1}^{N_{B,s}} C^i_{B,j} Cp_B MW_j + C^i_{G,C} Cp_C MW_C + C^i_{G,M} Cp_M MW_M \tag{5.7}$$

5.4.2 Cloud phase balance

5.4.2.1 Cloud phase mass balance

The present model implements integral number of cloud cells corresponding to each emulsion cell. The volume fraction of cloud phase is related to the bubble volume fraction. Bubble diameter changes along the length of the reactor and so does its volume fraction. The present model assumes that the bubble size remains the same along the length of the reactor. Thus, the volume of a bubble cell is simply the total volume fraction of bubble phase in the fluidized bed divided by the total number of bubble cells. The number of bubble and cloud cells is assumed to be the same in the present model. As a result, the volume of each cloud cell is calculated using the bubble cell volume.

Mass balance for solid species in biomass involved in primary devolatilization reactions,

$$\begin{aligned}\frac{d}{dt}\left(\rho^i_{mix,cw} X^i_B Y^i_{B,j}\right) = \frac{1}{V^i_{cw}(1-\epsilon_{mf})}\Big(& u_{s,d} a_c^{i+1}(1-\epsilon_{mf})\rho^{i+1}_{mix,cw} X_B^{i+1} Y^{i+1}_{B,j} \\ & + u_b a_w^{i-1}(1-\epsilon_{mf})\rho^{i-1}_{mix,cw} X_B^{i-1} Y^{i-1}_{B,j} \\ & - (u_{s,d} a^i_c + u_b a^i_w)(1-\epsilon_{mf})\rho^i_{mix,cw} X^i_B Y^i_{B,j} + R^i_{Y_{B,j}}\Big)\end{aligned} \tag{5.8}$$

The volume of each cloud cell is calculated as:

$$V_{cw} = \frac{a_{bed} H_{bed} \delta^i_b (f_c + f_w)}{NBE_{ratio}} \tag{5.9}$$

Where f_c and f_w are the ratios of cloud and wake volume to bubble volume respec-

tively. Overall mass balance for biomass in cloud cell,

$$\frac{d}{dt}\left(\rho^i_{mix,cw}X^i_B\right) = \frac{1}{V^i_{cw}(1-\epsilon_{mf})}\Bigg(u_{s,d}a^{i+1}_c(1-\epsilon_{mf})\rho^{i+1}_{mix,cw}X^{i+1}_B + u_b a^{i-1}_w(1-\epsilon_{mf})\rho^{i-1}_{mix,cw}X^{i-1}_B - (u_{s,d}a^i_c + u_b a^i_w)(1-\epsilon_{mf})\rho^i_{mix,cw}X^i_B + \sum_{j=1}^{n_{B,s}} R^i_{Y_{B,j}}\Bigg) \tag{5.10}$$

Overall mass balance for sand in cloud cell,

$$\frac{d}{dt}\left(\rho^i_{mix,cw}(1-X^i_B)\right) = \frac{1}{V^i_{cw}(1-\epsilon_{mf})}\Bigg(u_{s,d}a^{i+1}_c(1-\epsilon_{mf})\rho^{i+1}_{mix,cw}(1-X^{i+1}_B) + u_b a^{i-1}_w(1-\epsilon_{mf})\rho^{i-1}_{mix,cw}(1-X^{i-1}_B) - (u_{s,d}a^i_c + u_b a^i_w)(1-\epsilon_{mf})\rho^i_{mix,cw}(1-X^i_B)\Bigg) \tag{5.11}$$

The downward flow of solids described by velocity, $u_{s,d}$, is set to zero. Mass balance for vapor/gas phase species released from primary devolatilization reactions,

$$\frac{d}{dt}\left(Y^i_{G,j}\right) = \frac{RT^i_{cw}}{PV^i_{cw}\epsilon_{mf}MW^i_{G,avg}}\Bigg(\frac{PMW^{i-1}_{G,avg}}{RT^{i-1}_{cw}}u_b a^{i-1}_{cw}\epsilon_{mf}Y^{i-1}_{G,j} - \frac{PMW^i_{G,avg}}{RT^i_{cw}}u_b a^i_{cw}\epsilon_{mf}Y^i_{G,j} + R^i_{C_{G,j}} + V^i_{cw}\epsilon_{mf}R^i_{Y_{G,j}} - V^i_{cw}k_{ce}\left[\frac{PMW^{cw,i}_{G,avg}}{RT^i_{cw}}\frac{Y^{cw,i}_{G,j}}{MW_{G,j}} - \frac{PMW^{e,i}_{G,avg}}{RT^i_e}\frac{Y^{e,i}_{G,j}}{MW_{G,j}}\right] + V^i_b k_{bc}\left[\frac{PMW^{b,i}_{G,avg}}{RT^i_b}\frac{Y^{b,i}_{G,j}}{MW_{G,j}} - \frac{PMW^{cw,i}_{G,avg}}{RT^i_{cw}}\frac{Y^{cw,i}_{G,j}}{MW_{G,j}}\right]\Bigg) \tag{5.12}$$

The gas moves only in the upward direction with a velocity equal to the bubble rise velocity, u_b.

5.4.2.2 Cloud phase energy balance

Energy balance equation for cloud cell,

$$\frac{dT^i_{cw}}{dt} = \left(\frac{RT^i_{cw}}{RT^i_{cw}(Cp^i_{B,mix}X^i_B + Cp_S(1-X^i_B))V^i_{cw}(1-\epsilon_{mf})\rho^i_{mix,cw} + PV^i_{cw}MW^i_{G,avg}\epsilon_{mf}\sum_{j=1}^{n_G} Y^i_{G,j}Cp_{G,j}} \right)$$
$$\Bigg[u_{s,d}a^{i+1}_c(1-\epsilon_{mf})\rho^{i+1}_{mix,cw}(X^{i+1}_B Cp^{i+1}_{B,mix} + (1-X^{i+1}_B)Cp_S)(T^{i+1}_{cw} - T_{ref})$$
$$+ u_b a^{i-1}_w(1-\epsilon_{mf})\rho^{i-1}_{mix,cw}(X^{i+1}_B Cp^{i-1}_{B,mix} + (1-X^{i-1}_B)Cp_S)(T^{i-1}_{cw} - T_{ref})$$
$$- (u_{s,d}a^i_c + u_b a^i_w)(1-\epsilon_{mf})\rho^i_{mix,cw}(X^i_B Cp^i_{B,mix} + (1-X^i_B)Cp_S)(T^i_{cw} - T_{ref})$$
$$+ u_b a^{i-1}_{cw}\epsilon_{mf}\frac{PMW^{i-1}_{G,avg}}{RT^{i-1}_{cw}}\sum_{j=1}^{n_G} Y^{i-1}_{G,j}Cp_{G,j}(T^{i-1}_{cw} - T_{ref})$$
$$- u_b a^i_{cw}\epsilon_{mf}\frac{PMW^i_{G,avg}}{RT^i_{cw}}\sum_{j=1}^{n_G} Y^i_{G,j}Cp_{G,j}(T^i_{cw} - T_{ref})$$
$$+ \left\{ \sum_{j=1}^{n_{B,s}} R^i_{Y_{B,j}}\Delta H_{r_j} \right) \Bigg\}$$
$$+ V^i_{cw}\epsilon_{mf}R^i_{Y_{G,j}}\Delta H_{r,j} + h_{ce}V^i_{cw}(T^i_e - T^i_{cw}) + h_{bc}V^i_b(T^i_b - T^i_{cw}) \Bigg] \tag{5.13}$$

5.4.3 Bubble phase balance

Bubble cells do not contain any solid and the gas flows only in the upward direction. Therefore, only secondary gas phase reactions occur in the bubble phase.

5.4.3.1 Bubble phase mass balance

Mass balance for vapor/gas phase species released from primary devolatilization reactions,

$$\frac{d}{dt}\left(Y^i_{G,j}\right) = \frac{RT^i_b}{PV^i_b MW^i_{G,avg}}\Bigg(\frac{PMW^{i-1}_{G,avg}}{RT^{i-1}_b}u_b a^{i-1}_b Y^{i-1}_{G,j}$$
$$- \frac{PMW^i_{G,avg}}{RT^i_b}u_b a^i_b Y^i_{G,j} + V^i_b R^i_{Y_{G,j}}$$
$$- V^i_b k_{bc}\left[\frac{PMW^{b,i}_{G,avg}}{RT^i_b}\frac{Y^{b,i}_{G,j}}{MW_{G,j}} - \frac{PMW^{cw,i}_{G,avg}}{RT^i_{cw}}\frac{Y^{cw,i}_{G,j}}{MW_{G,j}} \right] \Bigg) \tag{5.14}$$

5.4.3.2 Bubble phase energy balance

Energy balance equation for bubble cell,

$$\frac{dT_b^i}{dt} = \left(\frac{RT_b^i}{PV_b^i MW_{G,avg}^i \sum_{j=1}^{n_G} Y_{G,j}^i Cp_{G,j}}\right) \left[u_b a_b^{i-1} \frac{PMW_{G,avg}^{i-1}}{RT_b^{i-1}} \sum_{j=1}^{n_G} Y_{G,j}^{i-1} Cp_{G,j}(T_b^{i-1} - T_{ref}) - u_b a_b^i \frac{PMW_{G,avg}^i}{RT_b^i} \sum_{j=1}^{n_G} Y_{G,j}^i Cp_{G,j}(T_b^i - T_{ref}) + V_b^i R_{Y_{G,j}}^i \Delta H_{r,j} - h_{bc}^i V_b^i (T_b^i - T_{cw}^i)\right] \tag{5.15}$$

5.4.4 Free board region balance

The volume of the reactor above the fluidized bed is referred to as the free-board region. The mixing behavior of this region is close to plug flow. Like the bubble cells, free-board region does not have solid fraction and therefore, only gas phase reactions occur in this region as well.

5.4.4.1 Free-board mass balance

Mass balance for vapor/gas phase species released from primary devolatilization reactions,

$$\frac{d}{dt}\left(Y_{G,j}^i\right) = \frac{RT_{fb}^i}{PV_{fb}^i MW_{G,avg}^i}\left(\frac{PMW_{G,avg}^{i-1}}{RT_{fb}^{i-1}} u_{fb} A_c Y_{G,j}^{i-1} - \frac{PMW_{G,avg}^i}{RT_{fb}^i} u_{fb} A_c Y_{G,j}^i + V_{fb}^i R_{Y_{G,j}}^i\right) \tag{5.16}$$

5.4.4.2 Free-board region energy balance

Energy balance equation for gas phase in free board cell,

$$\frac{dT_{fb}^{i}}{dt} = \left(\frac{RT_{fb}^{i}}{PV_{fb}^{i}MW_{G,avg}^{i}\sum_{j=1}^{n_G}Y_{G,j}^{i}Cp_{G,j}}\right) \left[u_{fb}A_c\frac{PMW_{G,avg}^{i-1}}{RT_{fb}^{i-1}}\sum_{j=1}^{n_G}Y_{G,j}^{i-1}Cp_{G,j}(T_{fb}^{i-1}-T_{ref}) - u_{fb}A_c\frac{PMW_{G,avg}^{i}}{RT_{fb}^{i}}\sum_{j=1}^{n_G}Y_{G,j}^{i}Cp_{G,j}(T_{fb}^{i}-T_{ref}) + V_{fb}^{i}R_{Y_{G,j}}^{i}\Delta H_{r,j} + \dot{Q}^{i}\right] \tag{5.17}$$

5.4.5 Estimation of hydrodynamic parameters

The mixing behavior of a bubbling bed can be characterized using hydrodynamic parameters like minimum fluidization velocity, bubble volume fraction, bubble size, bubble rise velocity, solid rise and circulation velocity, inter phase mass and heat transfer coefficients. These parameters have been correlated to the design and operating parameters using several empirical correlations. Accurate estimation of the hydrodynamic parameters is essential because they govern the residence time of each phase in the reactor. The present model uses well known correlations as stated here.

Minimum fluidization voidage (ϵ_{mf}) and velocity (u_{mf}) for effective diameter (d_{pe}) and density (ρ_{pe}) of sand and biomass, with mass fractions x_b and x_s respectively,

$$\frac{1}{\rho_{pe}} = \frac{x_b}{\rho_b} + \frac{x_s}{\rho_s} \tag{5.18}$$

$$d_{pe} = d_b d_s\left(\frac{x_b\rho_s + x_s\rho_b}{x_b\rho_s d_s + x_s\rho_b d_b}\right) \tag{5.19}$$

$$Ar = \frac{d_{pe}\rho_g(\rho_{pe}-\rho_g)g}{\mu^2} \tag{5.20}$$

$$Re_{mf} = \sqrt{30.28^2 + [0.046(1-x_b) + 0.108\sqrt{x_b}]Ar} \tag{5.21}$$

$$u_{mf} = \frac{Re_{mf}\mu_g}{\rho_g d_{pe}} \tag{5.22}$$

$$\epsilon_{mf} = 0.586(\phi)^{-0.72}\left(\frac{\mu^2}{\rho_g(\rho_{pe}-\rho_g)d_{pe}^3}\right)^{0.029}\left(\frac{\rho_g}{\rho_{pe}}\right)^{0.021} \tag{5.23}$$

Bubble diameter (d_b) and bubble velocity (u_b),

$$d_{b0} = 0.00376(u_g - u_{mf})^2 \tag{5.24}$$

$$d_{b,max} = 0.652[A_{bed}(u_g - u_{mf})]^{0.4} \tag{5.25}$$

$$d_b = d_{b,max} - \left[(d_{b,max} - d_{b0}) \exp\left(\frac{-0.15H}{D_r}\right)\right] \tag{5.26}$$

$$u_b = u_g - u_{mf} + 0.711\sqrt{gd_b} \tag{5.27}$$

Bubble volume fraction (δ_b) in bed,

$$\delta_b = \frac{u_g - u_{mf}}{u_b + u_{mf}} \qquad u_b \simeq u_{mf}/\epsilon_{mf} \tag{5.28}$$

$$\delta_b = \frac{u_g - u_{mf}}{u_b} \qquad u_b \simeq 5u_{mf}/\epsilon_{mf} \tag{5.29}$$

Cloud and wake volume to bubble volume (f_c, f_w), and emulsion fraction (f_e) in bed,

$$f_b = \frac{3}{0.711\sqrt{gd_b}\frac{\epsilon_{mf}}{u_{mf}} - 1} \tag{5.30}$$

$$f_w = 0.24 \tag{5.31}$$

$$f_e = 1 - \delta_b - f_w\delta_b \tag{5.32}$$

Ratio of volume of solid in b, c, w, and e phase to volume of bubble,

$$\gamma_e = \frac{(1 - \epsilon_{mf})(1 - \delta_b)}{\delta_b} - \gamma_b - \gamma_c \tag{5.33}$$

$$\gamma_b = 0 \tag{5.34}$$

$$\gamma_c = (1 - \epsilon_{mf})f_c \tag{5.35}$$

$$\gamma_w = (1 - \epsilon_{mf})f_w \tag{5.36}$$

Emulsion solid velocity ($u_{s,d}$) and emulsion gas rise velocity (u_e),

$$u_{s,d} = \frac{f_w\delta_b u_b}{1 - \delta_b - f_w\delta_b} \tag{5.37}$$

$$u_e = \frac{u_{mf}}{\epsilon_{mf}} - u_{s,d} \tag{5.38}$$

Bubble-emulsion mass transfer coeffcients (k_{be}),

$$k_{bc} = 4.5\frac{u_{mf}}{d_b} + 5.85\frac{\sqrt{D_g}g^{1/4}}{d_b^{5/4}} \tag{5.39}$$

$$k_{ce} = 6.78\sqrt{\left(\frac{\epsilon_{mf}D_g u_b}{d_b^3}\right)} \tag{5.40}$$

$$\frac{1}{k_{be}} = \frac{1}{k_{bc}} + \frac{1}{k_{ce}} \tag{5.41}$$

Bubble-emulsion heat transfer coeffcients (h_{be}),

$$h_{bc} = 4.5\frac{u_{mf}\rho_g C_{P_g}}{d_b} + 5.85\frac{\lambda_g\rho_g\sqrt{C_{P_g}}g^{1/4}}{d_b^{5/4}} \tag{5.42}$$

$$h_{ce} = 6.78\sqrt{\left(\frac{\epsilon_{mf}u_b\lambda_g\rho_g C_{P_g}}{d_b^3}\right)} \tag{5.43}$$

$$\frac{1}{h_{be}} = \frac{1}{h_{bc}} + \frac{1}{h_{ce}} \tag{5.44}$$

Biomass volume fraction in bed,

$$\epsilon_{bio} = \frac{\dot{m}_{bio}}{rho_{bio}A_{bed}u_{mf}} \tag{5.45}$$

5.5 1-D single particle heat conduction

To solve the BFB reaction engineering model for case 2, heating rate of biomass particle is required for calculating correction factor of the DAEM coupled modified Ranzi model. The heating rate depends on heat transfer coefficient in fluidized bed, which in turn governs time required for biomass particle to reach the reactor temperature. The heat transfer coefficient is a function of particle Reynold's number (Re_p). Volume and surface area of the biomass particle is calculated from realistic 3-D biomass particle geometry reported in [53, 13]. The value of Re_p is calculated using effective diameter (D_{SV}) (calculated using Eq. (5.46)) [13]. Prandtl number for the presetn study is calculated assuming nitrogen as the fluidizing medium. The heat transfer coefficient is estimated using the Ranz-Marshall correlation [216]. To estimate the time required for the biomass particle to reach the reactor temperature a generalized 1-D form of heat conduction equation (Eq.

(5.49)), applied to spheres, slabs, and cylinder [217], is used in the present study. Numerical solution of Eq. (5.49) gives transient values of volume averaged temperatures for a reactor temperature.

$$D_{SV} = \frac{D_V^3}{D_S^2} \tag{5.46}$$

$$D_S = \left(\frac{S}{\pi}\right)^{0.5} \tag{5.47}$$

$$D_V = \left(\frac{6V}{\pi}\right)^{(1/3)} \tag{5.48}$$

D_{SV} is the sphere diameter with the same external surface area to volume ratio as that of the particle.

$$\frac{1}{r^q}\frac{\partial}{\partial r}\left(\lambda r^q \frac{\partial T}{\partial r}\right) = \rho C_p \frac{\partial T}{\partial t} \tag{5.49}$$

where r is the spatial co-ordinate, q is the shape factor (0 for slab, 1 for cylinder, and 2 for sphere), T is the temperature (K), λ is the thermal conductivity (W/m/K), ρ is the solid density (kg/m^3), C_p is the solid specific heat capacity (J/kg/K), and t is time (s). The diameter of the particle is assumed to be constant for simulations. Boundary conditions used for solving the conduction equation are as follows,

$$\frac{\partial T}{\partial r} = 0 \qquad at \quad r = 0 \tag{5.50}$$

$$\lambda\frac{\partial T}{\partial r} = h(T_\infty - T_R) \qquad at \quad r = R \tag{5.51}$$

The boundary conditions define the symmetry condition at the center of the particle and convective heat transfer the the outer surface of the particle. The 1-D heat conduction equation is solved in MATLAB 2017b using the pdepe solver.

5.6 Solution methodology

The reactor code was written in MATLAB 2017b and the differential equations were solved using CVODES solver from Sundials. Cantera's MATALB toolbox [218] was used to determine the physical properties of the mixture gases and heat of

reaction for secondary gas phase reactions. The heat of reaction for primary pyrolysis reactions was evaluated using heat of formation of species tabulated in Chapter 4 Table 4.4. The solution methodology of the BFB reaction engineering

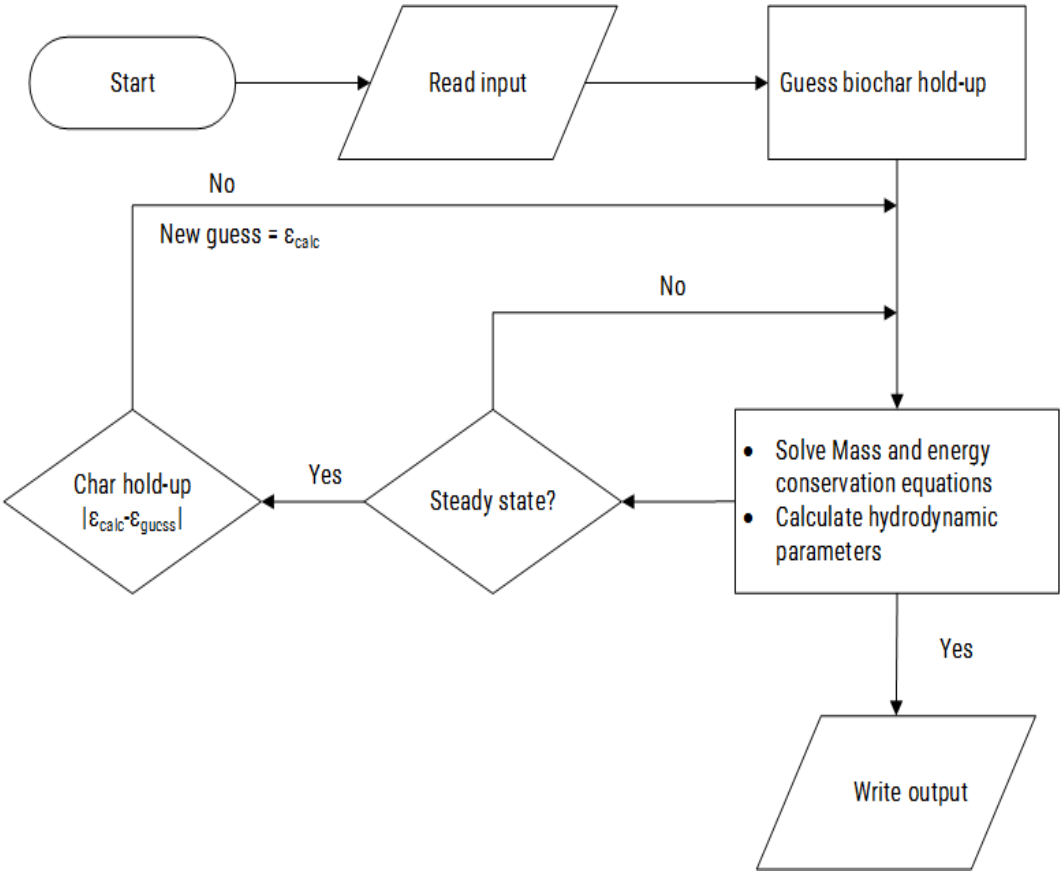

Figure 5.4: Solution methodology for BFB reaction engineering model

model is given in Figure 5.4. Initially input is read from the input module. Hydrodynamic parameters are calculated based on the gas velocity, guess of bio-char hold-up, and physical properties of sand and bio-char. The mass and energy balance equations are solved simultaneously for the given input. Output is written for every time step to analyze the dynamic behavior of the system. When the bio-char hold up is within the error limits, steady is reached. The reaction engineering model gives the mass fractions of all 511 gaseous and 23 solid species. The mass fractions are used to calculate the overall yield of gas, liquid, and solid products. The engineering model also provides composition of major liquid and gaseous pyrolysis species.

5.7 Results and discussion

The present BFB reaction engineering model is used to simulate biomass pyrolysis reaction to evaluate the performance of primary pyrolysis reaction models (a)detailed lumped kinetic model proposed by Ranzi [10] (Case 1) and (b) DAEM coupled modified Ranzi model proposed in present work (Chapter 4) (Case 2). The secondary gas phase reaction chemistry is the same for both cases. The input parameters used for evaluating the primary pyrolysis reaction models are stated in Table 5.1. The density and viscosity of gas phase are calculated using mixture property of Cantera. The number of emulsion cells chosen in the present study is one [170] and bubble and cloud phase are modeled using three cells each. The performance of the reactor remained same for three and five bubble and cloud cells. The free-board region is divided into five cells to emulate plug flow. Preliminary numerical simulations were carried out to finalize the tolerances and adjustable model parameters. A relative tolerance of 10^{-9} was chosen for the CVODES solver and a error tolerance of 0.001% was set to as the steady state criteria. Depending on the operating temperature a reactor simulation of 100 s required 12 to 28 real time hours on a Intel Xenon 3.7 GHz processor computer. The run time for operating temperature between 598 to 773 K is between 12 to 14 hours, while that for 798 to 873 K is between 24 to 28 hours. The rate of secondary reactions becomes significant at high temperatures and more iterations are required at each time step to achieve convergence.

Table 5.1: Simulation parameters for model validation. Nitrogen is used as fluidizing gas for all the simulations. The reactor geometry and operating conditions used in the present study are adopted form [25]

Reactor parameters	Physical parameters	Biomass Composition
D (m): 0.1	Cp_{sand} (J/kg/K) : 830	Cellulose (wt.%): 35
H_{bed} (m) : 0.25	Cp_{bio} (J/kg/K) : 1500 + T	Hemi-Cellulose (wt.%): 29
$H_{recator}$ (m): 0.42	Cp_{char}(J/kg/K): 420 + 2.09T + 6.85^{-4}T^2	Lignin (wt.%): 28
m_{sand} (kg): 2.1	ρ_{sand} (kg/m^3): 2560	LIGC/LIGH/LIGO : 0.133/0.0049/0.143
$\dot{m}_{bio,in}$ (kg/hr): 1	ρ_{bio} (kg/m^3) : 500	Ash (wt.%): 0.26
$T_{reactor}$ (K) : 598 to 873	ρ_{char} (kg/m^3) : 350	Extractives (wt.%): 7.74 (calc.)
$T_{bio,in}$ (K) : 298	$d_{p,sand}$ (μm): 250	TGL/TANN: 0.0083/0.0691
u_g (m/s): 0.14	$d_{p,bio}$ (μm): 1000	

5.7.1 Model Validation

The BFB reaction engineering model is used in the present study to analyze the effect of primary pyrolysis reaction models. Numerical simulations were carried out at eight initial reactor temperatures 598, 623, 673, 723, 773, 798, 848, and 873 K for both case 1 and case 2. Heating rate values required for case 2 are estimated by numerically solving the 1-D heat conduction equation. Steady state gas, liquid, and solid yields for all the reactor temperatures are compared with literature data [25].

5.7.2 Heating rate estimation for biomass particle

To calculate the correction factor for case 2 heating rate of biomass particle is required. The Re_p value is of the order of 0.5 for biomass particle for D_{SV} = 3.37 x 10^{-4} (particle size = 1 mm, particle volume = 5.276 x 10^{-11}, particle surface area = 9.388 x 10^{-7}), moving with velocity equal to the $u_{s,d}$ velocity, for temperatures between 598 to 873 K. The convective heat transfer coefficient is between 676 to 653 for reactor temperature between 598 to 873 K. Figure 5.5 Transient values of volume averaged temperature of biomass particle under different operating temperatures. The heating rate (K/s) values estimated from 1-D simulations are 170

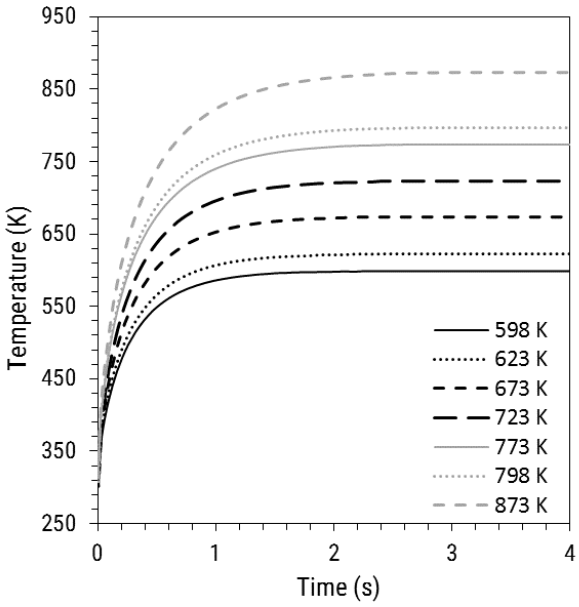

Figure 5.5: Volume averaged temperature profile of biomass particle for eight different reactor temperatures. Physical properties for pine wood used for the simulations are, density (ρ): 500 kg/m^3; thermal conductivity (k): 0.134 W/m/K

and 205 K/s for reactor temperature between 598 to 723K and 773 to 873 K respectively. The estimated heating rate values for pine wood are fairly close to the values predicted in [13, 219] where the authors have used realistic biomass morphology to estimate internal temperature profiles of biomass particle.

5.7.3 Estimation of pyrolysis product yields

Performance of the BFB reaction engineering model for Case 1 and Case 2 is evaluated by comparing overall gas, liquid, and solid yields reported in [25]. Steady state mass fraction values of gas and solid species are used to evaluate the flow rate of species, which are in turn used to estimate the overall product yields. Figure 5.6

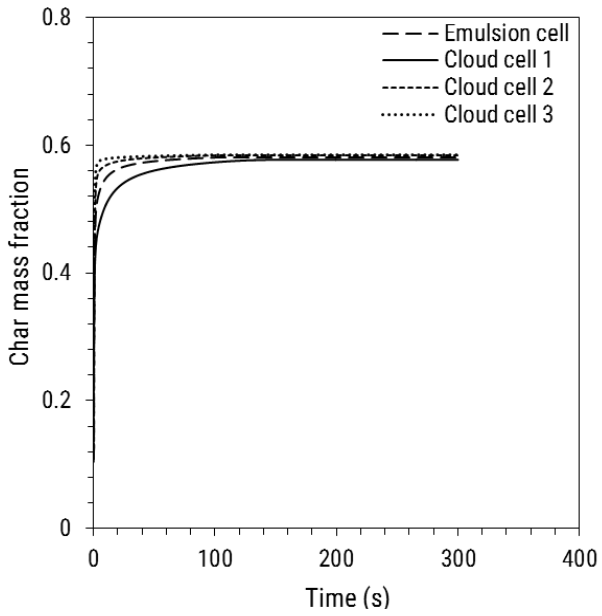

Figure 5.6: Dynamic response of BFB reaction engineering model for bio-char mass fraction in emulsion and cloud cells.

shows the dynamic response of the char mass fraction within biomass particle for a temperature of 774 K. The char fraction is stabilized for the bottom most cloud cell at 155 to 160 s. Biomass is fed in the bottom most cell and thus, more time is required for the cell to reach a steady state. Product yields are computed using 60 to 90 s of data after reaching steady.

Figure 5.7 shows the comparison between overall gas, liquid, and solid yield of pine wood pyrolysis process for experimental data, case 1, and case 2. The material balance of the experimental data is between 90 to 101 %. The error in estimation of water content is maximum. Therefore, it is difficult ascertain a qualitative

trend water produced during pyrolysis reaction. For Case 1 and Case 2 the discrepancy for yield of organic and solid components at low reactor temperatures is significant. However, for Case 2 the predictions are better than Case 1. Better prediction ability in Case 2 is a consequence of using distributed activation energy (DAE) approach, which activates the reaction at lower temperature. Solid product of the pyrolysis process is assumed to comprise unreacted biomass, intermediate solids (or non-volatile solids), char, and trapped species. Figure 5.8 shows that there is a significant difference in the reactivity of intermediate solids for Case 1 and Case 2. The difference is attributed to the incorporation of the DAE approach as well as the correction factor which accounts for the effect of heating rate on pyrolysis reaction rate. At heating rates of the order of 100 K/s, biomass particles attain plasticity, which enhances the chances of collisions and therefore, reaction rate increases (Chapter 4, section 4.2.2.1). Thus, prediction of gas, liquid, and solid yield at low temperatures is better for Case 2 than Case 1. At temperatures greater than 623 K, Case 1 significantly over predicts the solid yield, mainly due to unreacted intermediates solids (especially LIGCC) and trapped species (mainly T[COH_2]). On the other hand, for Case 2, with increase in temperature from 673 to 873 K, reaction of intermediate solids is almost complete. Solid and gas yield predictions for Case 2 are is close agreement with the experimental results for temperatures beyond 673 K. This shows that not only DAE approach but also incorporation of the correction factor is significant to accurately predict the pyrolysis product yields over a wide range of operating temperatures. Case 2 over predicts the organics yield and marginally under predicts the gas yield. This issue can be over come by adjusting the stoichiometric coefficients in the primary pyrolysis reactions. For Case 1, the organics yield is in close agreement with the experiments. But if unreacted intermediate solid is allowed to react completely then Case 1 would also over-predict the organics yield.

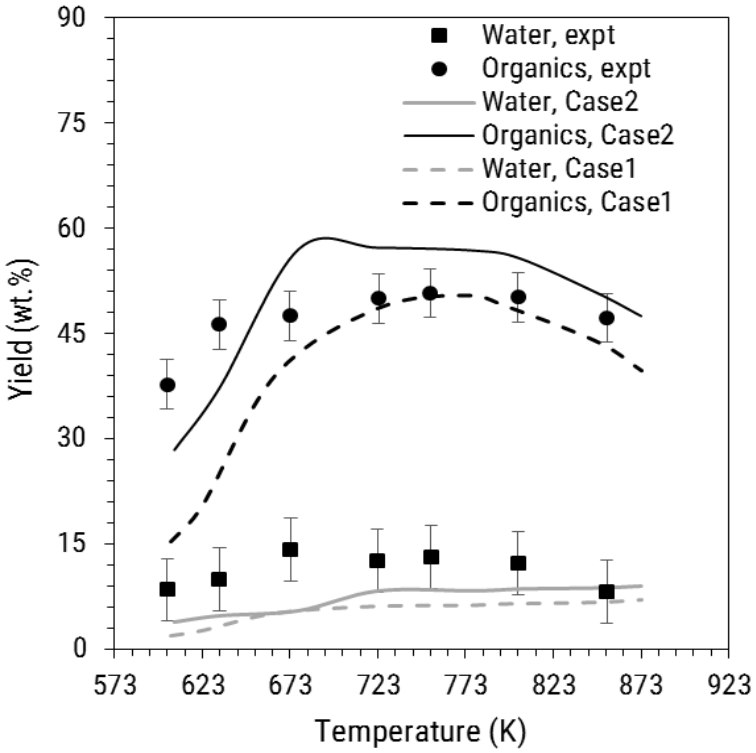

(a)

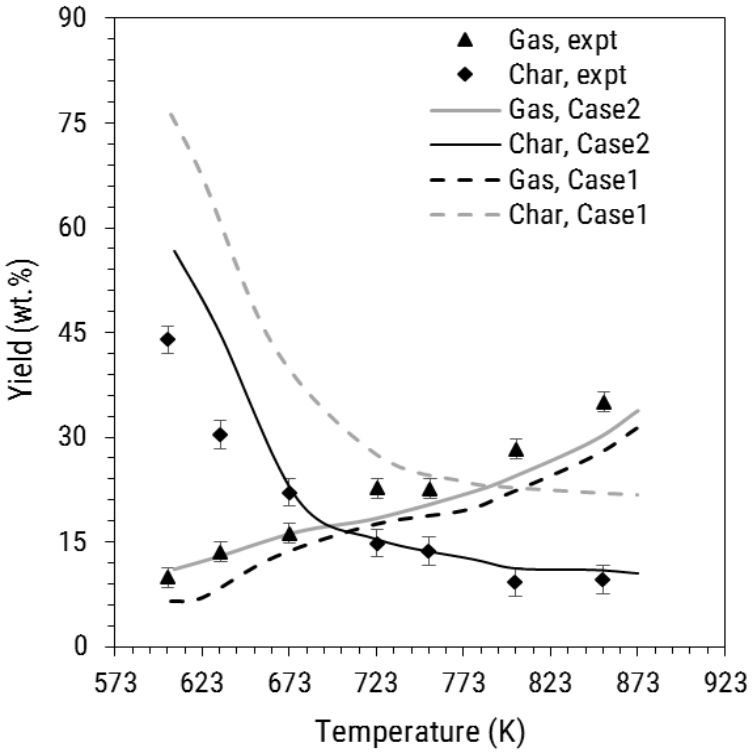

(b)

Figure 5.7: Comparison between experimental and BFB reaction engineering model results for (a) Organics and water, (b) Gas and char products. The experimental data is taken from [25].

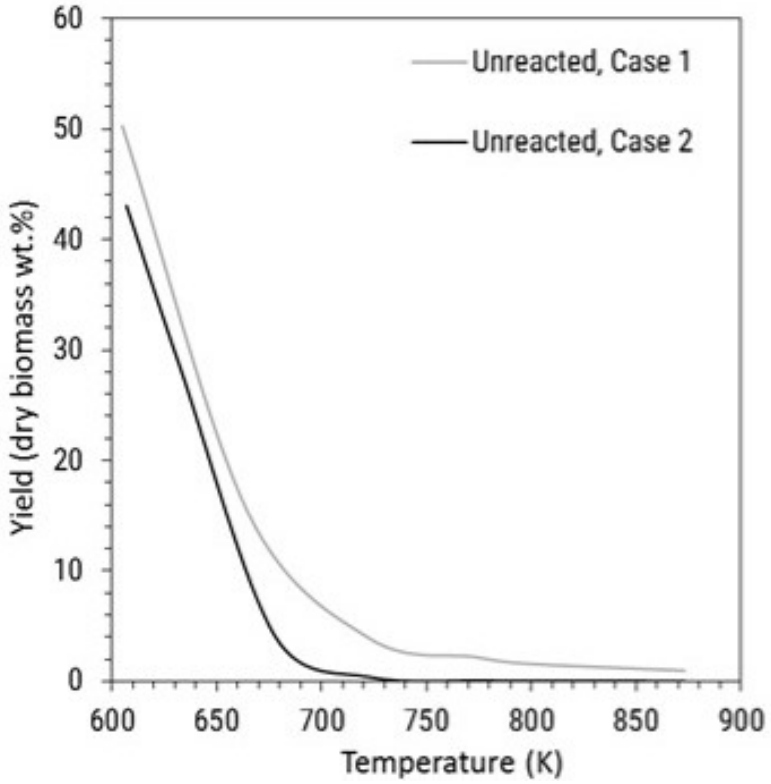

(a)

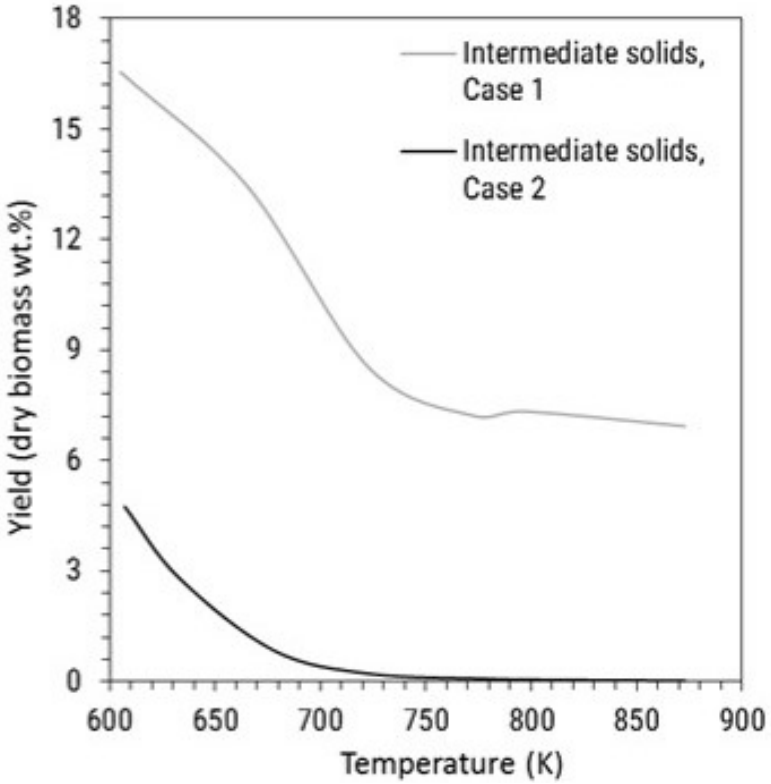

(b)

This figure is continued on the next page...

Figure 5.8

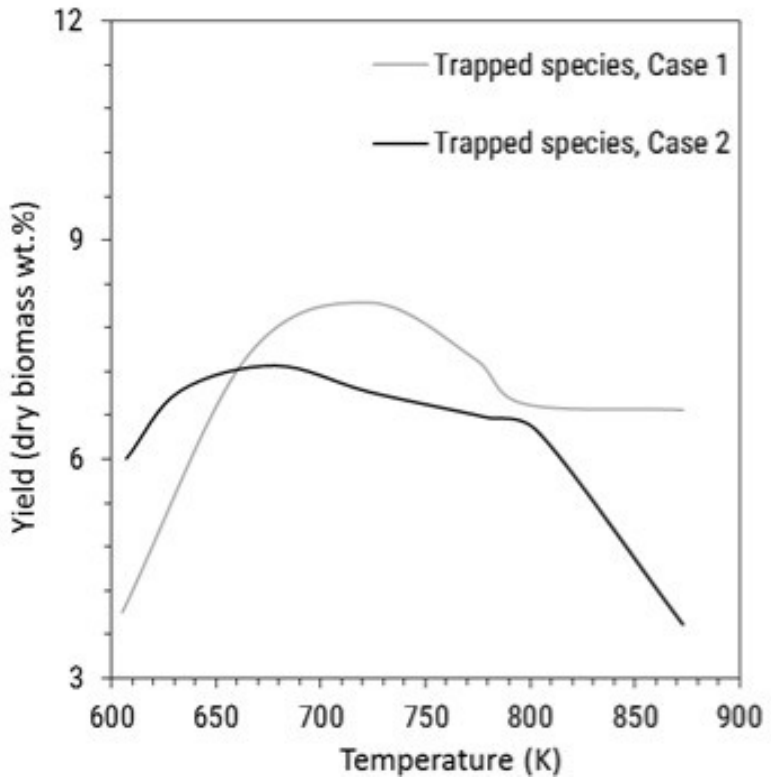

(c)

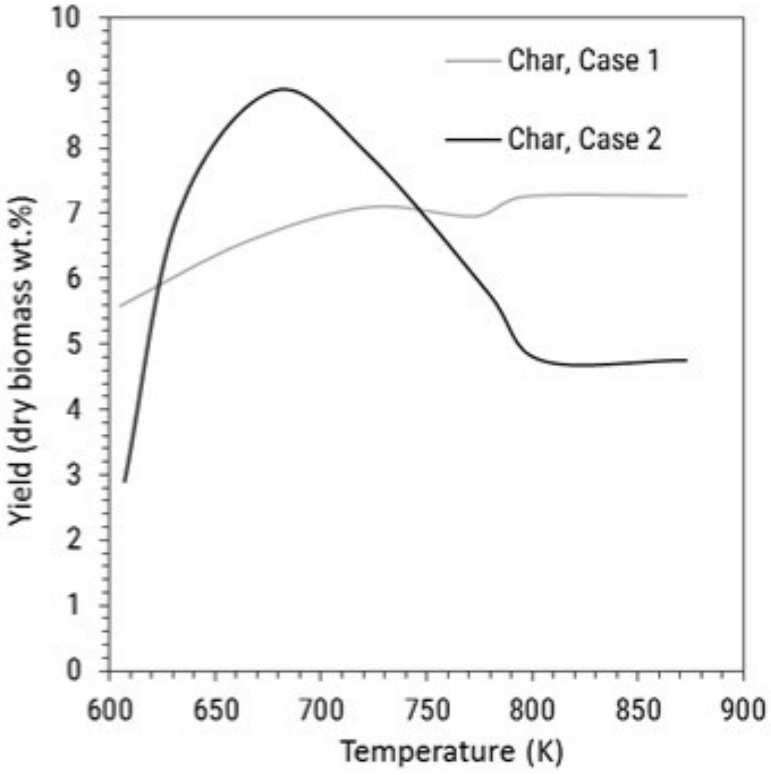

(d)

Figure 5.8: Comparison between yields of different solid product for Case 1 and Case 2.

Case 1 and Case 2 both qualitatively agree with the profiles of gas, organics, and solid yield. However, just adjusting the activation energy of few reactions in Case 1 may not suffice, and a DAE approach might be essential. In the present study the heating rate of biomass particle does not change significantly because it is a function of gas flow rate and reactor geometry. As the numerical simulations are carried out at a single gas flow rate, the effect of correction factor on the reaction kinetics can not be explored further.

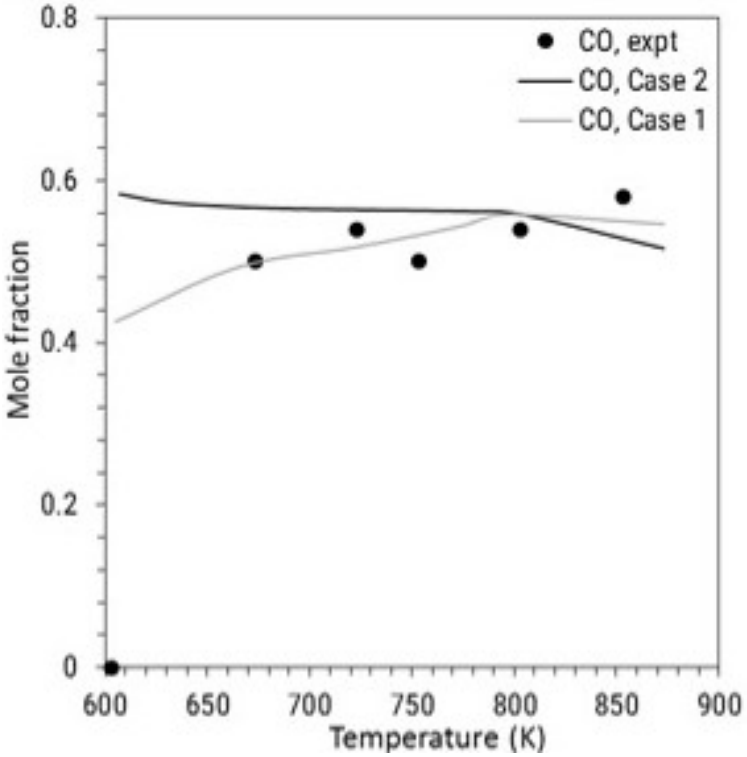

(a)

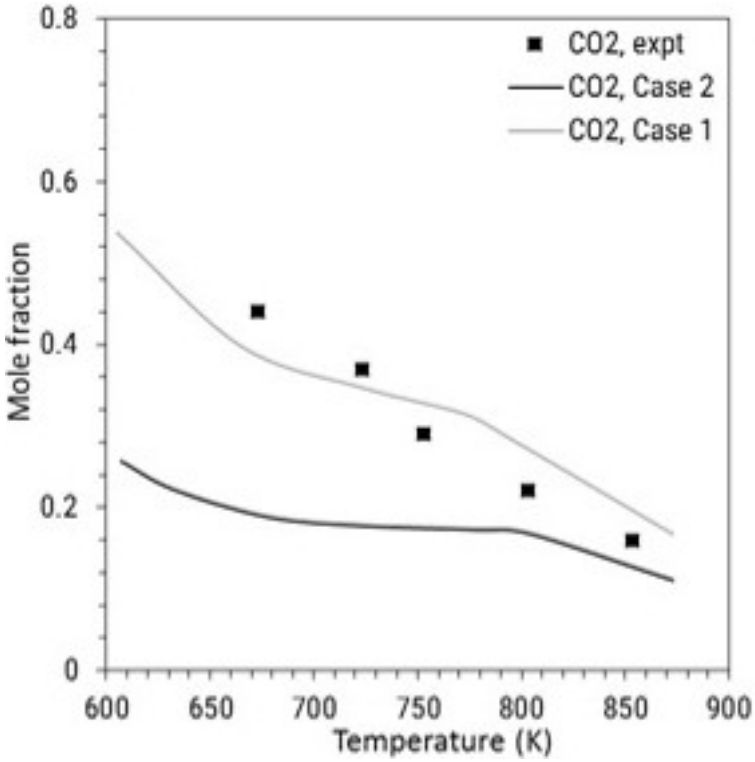

(b)

This figure is continued on the next page...

Figure 5.9

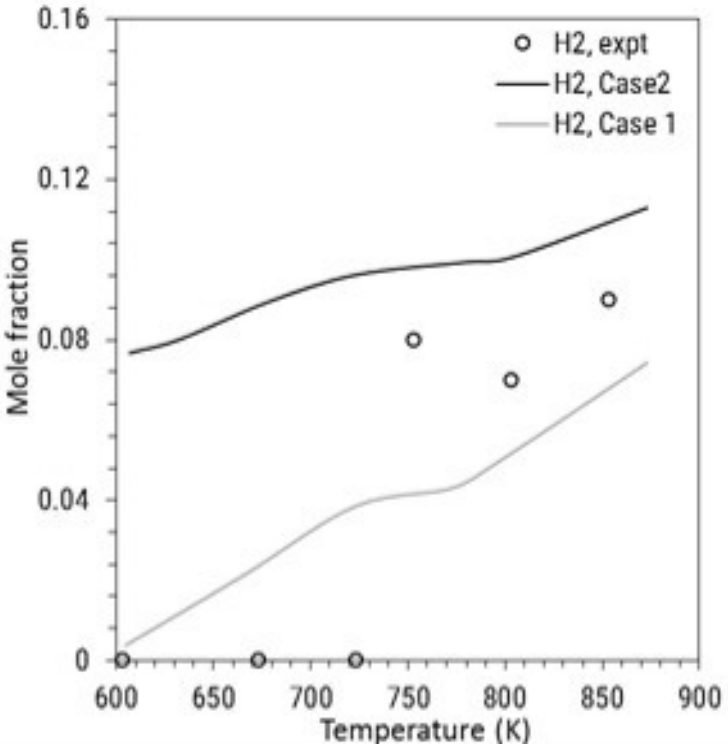

(c)

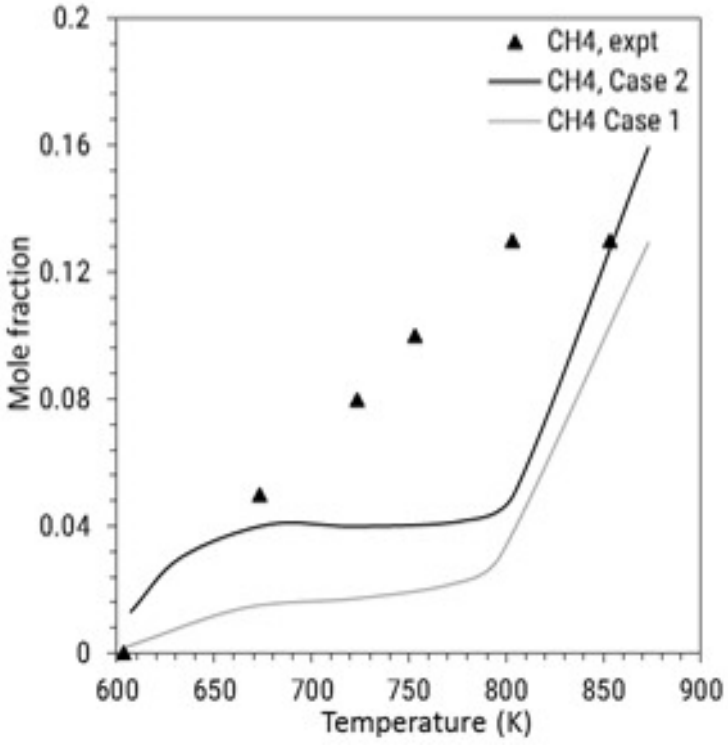

(d)

This figure is continued on the next page...

Figure 5.9

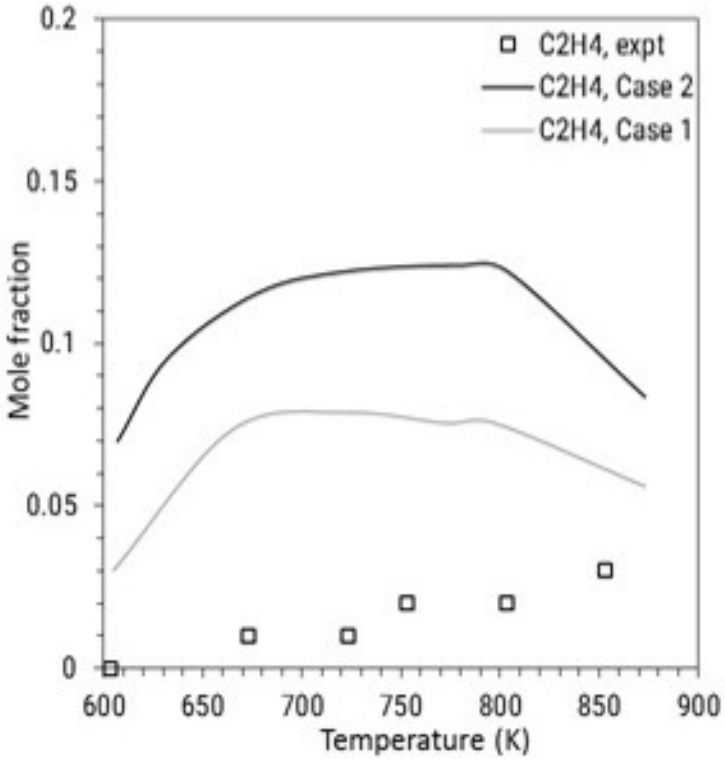

(e)

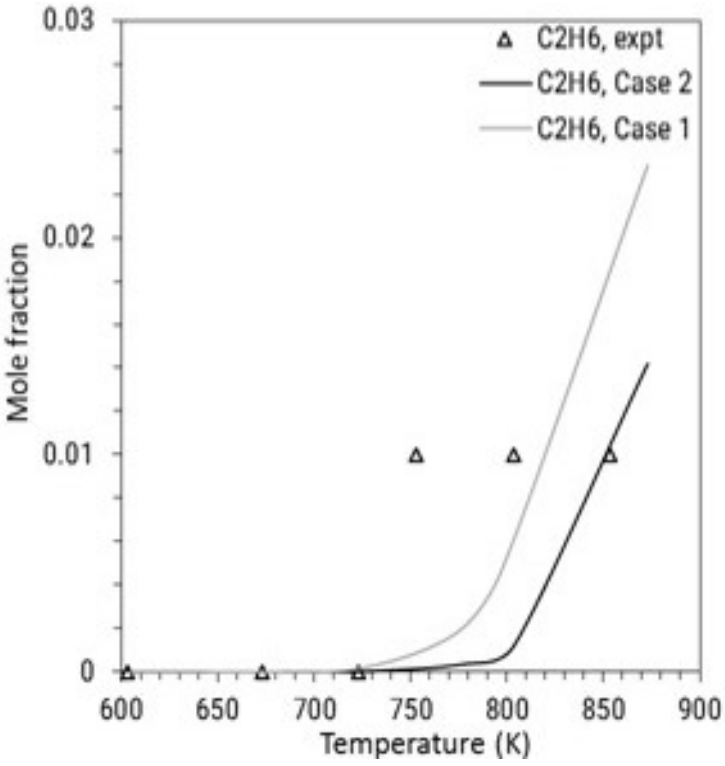

(f)

Figure 5.9: Comparison between mole fractions of different pyrolysis gaseous species for experiment, Case 1 and Case 2.

Mole fraction of gas species for Case 1 and Case 2 are compared with the experimental data in Figure 5.9. Predictions for CO for both Cases is fairly close to the experimental data. However, Case 1 performs better both qualitatively as well as quantitatively than Case 2 for CO_2 predictions. Stoichiometric coefficients of primary reactions for Case 2 need further adjustment to address this discrepancy. For other gaseous species, qualitative and quantitative predictions for Case 1 and Case 2 are in poor agreement with experiments. Case 1 under predicts the mole fraction again because of the unreacted intermediate species. At higher temperatures (> 750 K), where secondary gas phase reactions become prominent, light gases are produced. Thus, few modifications to the secondary gas phase reactions might be essential to account for the formation of methane and hydrogen.

The predictions of different liquid components for Case 1 and Case 2 is reported in Table 5.2. In the literature the liquid composition of a pilot scale facility is usually reported on the basis of GC-MS area %, the data can not be used to compare with the simulations. However, to estimate if the reaction model require further modifications, lumped component yields can be compared with literature data. Figure 5.10 shows the lumped yields of sugars, phenolics and C1-C3 oxygenates (aldehydes, ketones, acids, and other oxygenates). The yields of sugars, phenolics and C1-C3 oxygenates for pine wood reported in [141] are 38, 18, and 24 wt.% of moisture free bio-oil respectively. The reactor used is a solid circulating reactor with a gas residence time of approximately 1 s which is similar to that used in the present study. The reactor temperature is 700 K. Sugar yield for Case 2 is substantially over predicted as compared to Case 1. This suggests that additional sugar degradation reactions might have to be included as suggested in [94]. Yield of C1-C3 oxygenates so good agreement at 700 K with the experimental data. This may suggest that secondary reactions for C1-C3 oxygenates are triggered at low temperature for Case 2. As the primary reaction rates are high for Case 2, the concentration of C1-C3 oxygenates in the gas phase is high as compared to Case 1. Thus, secondary reactions become dominant even in low temperatures. Both Case 1 and Case 2 under predict phenolics because the models are a condensed version of a detailed lignin pyrolysis mechanism (Chapter 4).

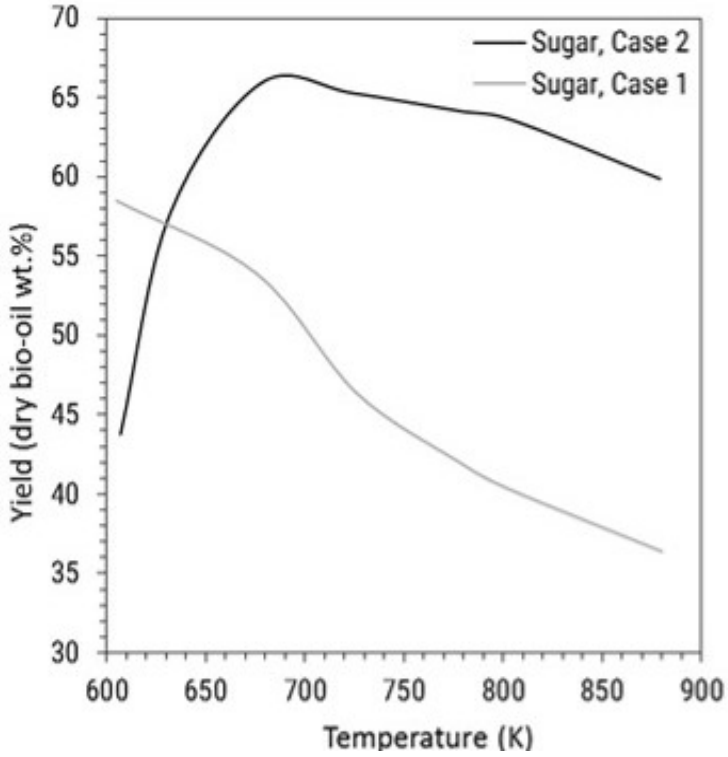

(a)

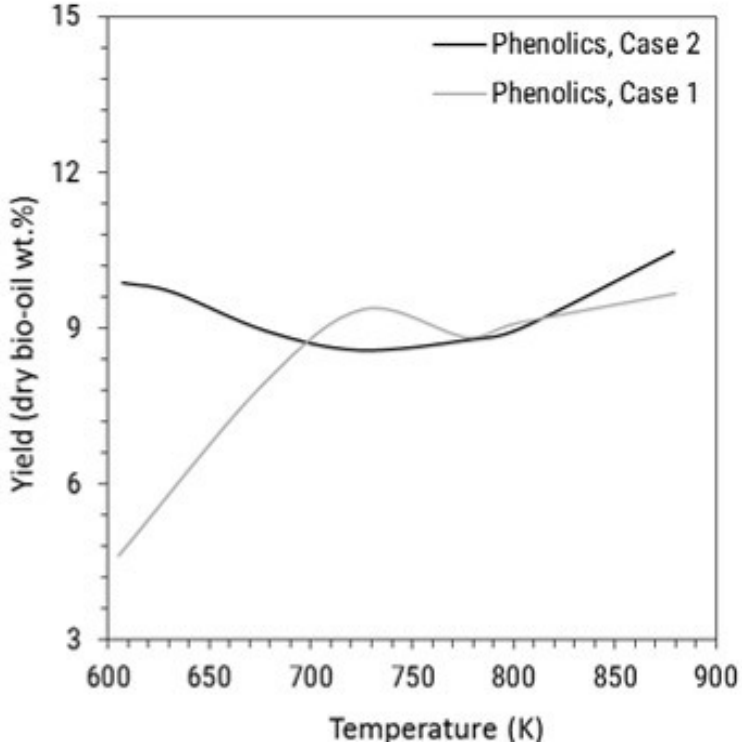

(b)

This figure is continued on the next page...

Figure 5.10

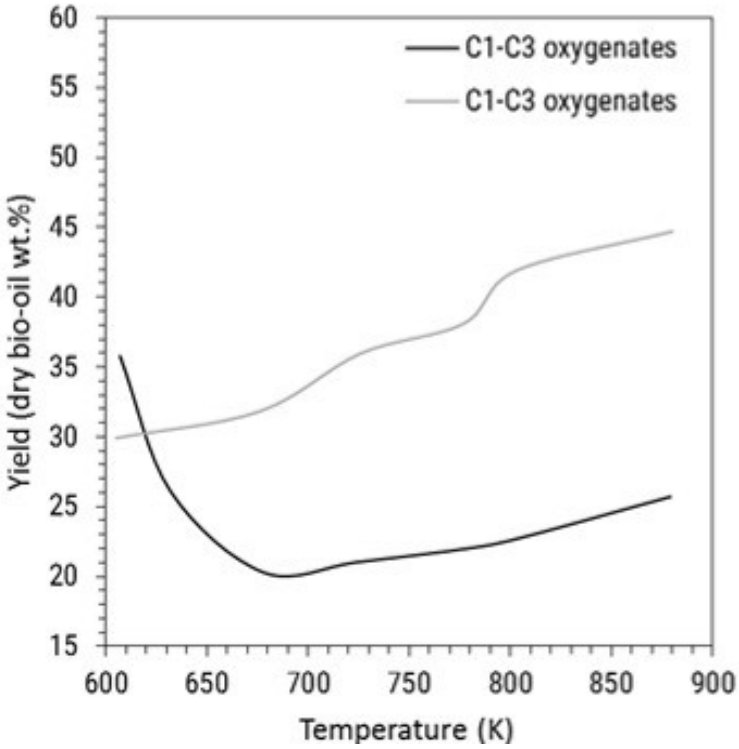

(c)

Figure 5.10: Lumped yields of liquid components for Case 1 and Case 2.

Table 5.2: Predicted yields of pyrolysis liquid components for Case 1 and Case 2 using BFB reaction engineering model. *The columns correspond to Case 2.

	Yield (dry biomass wt.%) at different reactor temperatures (K).													
	607*	605	632*	633	678*	676	724*	726	778*	777	804*	803	879*	880
Formaldehyde	1.32	0.90	1.62	1.62	2.03	2.15	2.17	2.75	2.32	2.92	2.49	3.14	3.09	3.16
Acetaldehyde	0.02	0.05	0.05	0.05	0.13	0.65	0.19	1.07	0.36	1.24	0.59	1.46	1.30	1.66
Glyoxal	1.05	0.63	1.03	1.03	1.17	1.00	1.14	1.26	1.17	1.34	1.18	1.39	1.53	1.26
Acrolein	0.05	0.00	0.04	0.04	0.05	0.01	0.05	0.04	0.05	0.13	0.06	0.06	0.17	0.22
Propanal	0.36	0.15	0.40	0.40	0.59	1.66	0.63	2.65	0.71	2.93	0.75	3.06	0.70	2.25
Hydroxy acetaldehyde	0.30	0.25	0.60	0.60	1.08	2.11	1.20	3.30	1.35	3.67	1.41	3.90	1.62	3.70
Acetol	2.24	1.32	2.18	2.18	2.45	1.93	2.35	2.33	2.20	2.29	1.88	2.03	0.46	0.44
Furfural	2.91	1.68	2.85	2.85	3.23	2.12	3.15	2.43	3.20	2.55	3.17	2.62	3.09	2.77
5-HMF	0.06	0.19	0.21	0.21	0.58	2.52	0.76	4.06	0.97	4.52	1.07	4.80	1.76	4.33
Methanol	2.09	0.08	2.13	2.13	2.39	0.78	2.33	1.47	2.37	1.89	2.36	2.57	2.84	2.80
Ethanol	0.25	0.14	0.29	0.29	0.32	0.27	0.31	0.29	0.31	0.29	0.30	0.29	0.34	0.28
Formic acid	0.23	0.14	0.22	0.22	0.23	0.25	0.21	0.32	0.21	0.32	0.22	0.33	0.56	0.39
Acetic acid	1.14	0.66	1.34	1.34	1.48	1.21	1.41	1.32	1.41	1.34	1.39	1.33	1.65	1.37
Propionic acid	0.01	0.00	0.01	0.01	0.01	0.00	0.02	0.00	0.03	0.00	0.02	0.00	0.01	0.00
Phenol	1.93	0.42	2.29	2.29	2.88	1.07	2.78	1.42	2.82	1.61	2.88	1.80	3.68	2.17
Cresol	0.01	0.00	0.01	0.01	0.01	0.00	0.01	0.00	0.00	0.00	0.00	0.00	0.03	0.01
Anisole	0.02	0.04	0.02	0.02	0.02	0.30	0.01	0.50	0.01	0.44	0.01	0.39	0.01	0.18
methyl Guaiacol	0.05	0.00	0.06	0.06	0.08	0.00	0.10	0.00	0.14	0.00	0.17	0.00	0.31	0.00
dimethoxy Phenol	0.02	0.00	0.02	0.02	0.02	0.00	0.01	0.00	0.01	0.00	0.01	0.00	0.01	0.04
Coumaryl alcohol	0.72	0.13	1.62	1.62	2.59	0.64	2.53	0.79	2.51	0.78	2.47	0.85	2.31	0.84
Synalpyl alcool	0.02	0.00	0.03	0.03	0.06	0.00	0.10	0.00	0.16	0.00	0.20	0.00	0.37	0.00
Sinapylaldehyde	0.11	0.16	0.11	0.11	0.10	1.36	0.07	2.24	0.05	1.97	0.04	1.80	0.03	1.23
KETM2	0.001	0.000	0.001	0.001	0.002	0.000	0.002	0.000	0.002	0.000	0.002	0.000	0.003	0.000
HMWL	0.002	0.000	0.002	0.002	0.003	0.000	0.003	0.000	0.003	0.000	0.003	0.000	0.002	0.000
Levoglucosan	5.11	1.52	16.19	16.19	32.44	11.60	31.24	11.61	30.31	9.79	29.36	8.17	27.02	4.71
Xylan	2.99	0.00	2.89	0.00	3.18	0.00	3.05	0.00	3.06	0.00	3.02	0.00	3.09	0.00
DAXP	2.99	6.92	2.89	5.77	3.18	8.73	3.05	10.03	3.06	10.48	3.02	10.66	3.09	9.56
Free fatty acid	0.68	0.01	0.65	0.65	0.72	0.19	0.68	0.62	0.68	1.83	0.68	0.65	0.80	0.67
Water	3.84	1.90	4.72	2.65	5.45	4.97	8.27	6.16	8.28	6.28	8.54	6.50	8.95	7.07

5.8 Summary

The present work describes a comprehensive mathematical model for simulating biomass pyrolysis in a bubbling fluidized bed reactor. A generalized framework of a dynamic model based on mixing cell approach and rigorous biomass pyrolysis kinetics was developed. The coupled model was used to understand the effect of primary pyrolysis reaction model on the pyrolysis product profiles over a wide range of operating temperatures. Considerable difference of product yield was observed for Ranzi model and DAEM-coupled Ranzi model (with correction factor) developed in previous chapter. The severe drawbacks observed for Ranzi model were, (a) pyrolysis reactions did not activate substantially at temperatures between 600 to 650 K, and (b) intermediate solid products remain unreacted. Both these issues were addressed by the DAEM-coupled Ranzi model. However, the model still requires further improvement to accurately predict sugar yield and gas composition.

The presented model is shown to reasonably predict bio-oil composition . The composition can then be used to design appropriate downstream unit operations to fractionally condense bio-oil into distinct chemical families, which is described in the next chapter.

Chapter 6

Fractional condensation of biomass pyrolysis vapors

6.1 Introduction

Lignocellulosic biomass components - cellulose, hemicellulose, and lignin undergo depolymerization followed by secondary reactions of volatile products that leads to the formation of bio-oil, which is a complex mixture of several hundred compounds [29-31]. The wide spectrum of chemical functionalities namely, carboxylic acid, aldehyde, ketone, furan, carbohydrate and phenol in bio-oil make it unstable. These chemical families undergo condensation reactions with one another to form polymerized byproducts during storage or when exposed to heat [36]. Handling and storage of bio-oil as a mixture is therefore, tedious. Stage-wise condensation strategies have been proposed (Chapter 2 section 2.5), but for maximizing recovery of bio-oil as well as isolating organic and aqueous fractions. However, the separation processes reported till date are unable to fractionate the chemical families from one another. Therefore, this paper uses Aspen Plus to simulate different configurations of multi-stage unit operations for condensing a mixture of model compounds, representing pyrolysis vapors, into fractions of individual chemical families. The condensation behavior of the model compounds is also analyzed by changing the operating conditions of condensation schemes and initial feed composition.

Design and operation of the condenser train, for accommodating variable nature

of bio-oil, to achieve the desirable fractionation of bio-oil is not a simple task. Prior knowledge of condensation behavior of different chemical families/ compounds is vital for the consistent and efficient operation of pyrolysis plant. The condensation behavior is goverend by the chemical functionalities present in bio-oil. As bio-oil is a mixture of several hundred compounds, it is not possible to consider all the chemical compounds for simulation studies. Therefore, a set of model compounds are used to represent bio-oil mixture. This chapter investigates the effect on operating conditions on condensation behavior of bio-oil model compounds.

Appropriate choice of model compounds is crucial to reduce the ambiguity in predicting the distribution of bio-oil chemical families into various fractions. Representing whole bio-oil using a set of model compounds reduces the computational efforts while simulating condensation. The set of model compounds should represent, as close as possible, all chemical families present in bio-oil to account for the interaction between different chemical families. Qualitative and quantitative GC-MS characterization of bio-oil from various biomass sources have been reported in several research articles [151, 220, 149, 221]. Model compounds are selected based on characterization of bio-oil fractionated using water and different organic solvents [48].

Stage-wise condensation of the bio-oil model compounds is simulated using AspenPlus process simulator for separating the chemical families. Model compounds and phase equilibrium model are selected based on validation of AspenPlus simulation using literature data for fractional condensation of pyrolysis vapors. Two condensation schemes are compared in terms of separation of chemical families under different operating conditions. The effect of feed composition and the ratio of condensible to non-condensible components on the predicted yield and separability of chemical families are also investigated. Figure 6.1 shows the approach to simulate and optimize fractional condensation of bio-oil.

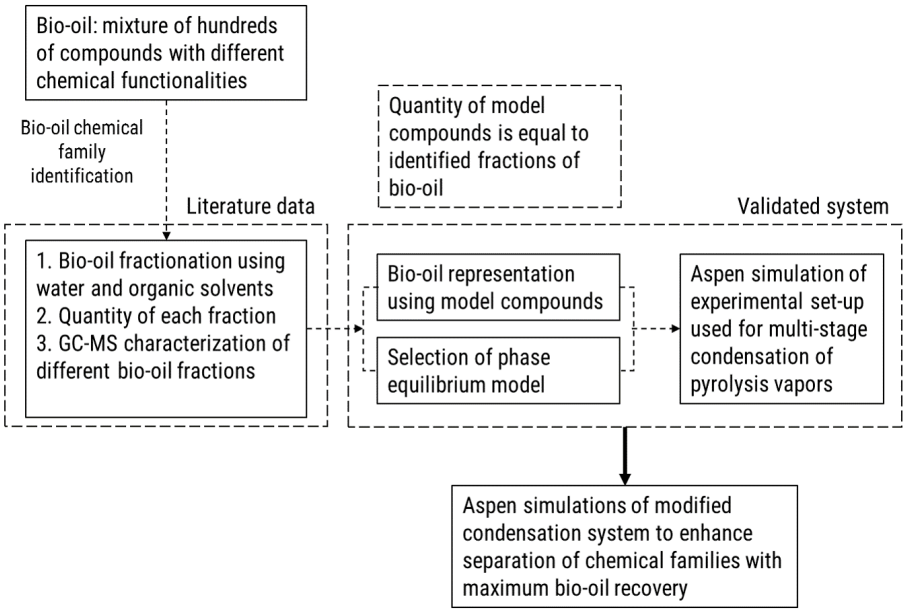

Figure 6.1: Approach to fractional condensation of bio-oil

6.2 Modeling fractional condensation

ASPENPlus was used to simulate steady state multistage condensation of pyrolysis vapors. The pyrolysis vapors were represented using 28 model compounds which represent different chemical families in bio-oil. Nitrogen was used to represent the non-condensible gas component in pyrolysis vapors. Thermodynamic model used to simulate the condensation schemes were validated using fractional condensation data available in the literature. After selection of appropriate thermodynamic model, two condensation schemes were simulated over a wide range of operating conditions. The schemes were compared based on fractionation of chemical families.

6.2.1 Multistage condensation

The multi-stage condensation system reported by Prof. Brown's group [18, 26] was simulated in AspenPlus process simulator. The experimental data for fractional condensation of pyrolysis vapors [26] was obtained using three shell and tube heat exchangers (STHE) and two ESP's as shown in Figure 6.2(a). The function of the ESP in the condenser train was to capture aerosols and did not serve as a condenser. Therefore, in the AspenPlus simulation environment, one STHE

followed by an ESP was assumed to be a single stage operation and simulated as a STHE only with no liquid entrainment(Figure 6.2(b)). The heat exchange surface area was adjusted to match the outlet temperature of each heat exchanger.

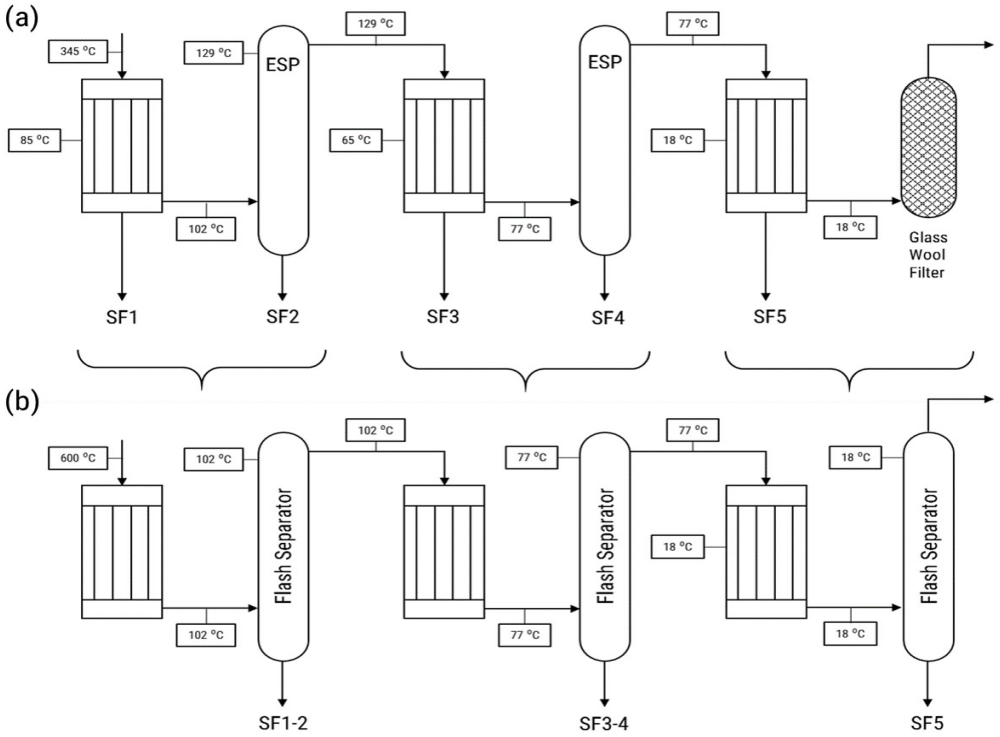

Figure 6.2: (a) Multi-stage condensation scheme in [26] (b) Modified scheme for validation of AspenPlus simulations

Bio-oil was represented using a set of twenty-eight model compounds. The model compounds represent different chemical families in bio-oil as shown in Figure 6.3. As ketones were not quantified in [26], model compounds representing the ketone family were selected using data available in [18]. Table 6.1 shows the concentration of model compounds based on the mass balance of various bio-oil fractions reported in [26]. Iso-eugenol and model compounds representing pyrolytic lignin (HMWL-1 and HMWL-2) were user-defined components. The structure and properties of model compounds representing high molecular weight lignin were taken from [222]. The bio-oil mass flow rate used in the simulations was 800 kg/hr.
The model compounds were grouped into chemical families as shown in Table 6.2. Sugars and water-insoluble fraction of lignin were grouped together because they have similar boiling points but can be easily separated from one other using water as an extraction solvent for sugars. Pyrolysis vapors comprise of carrier and

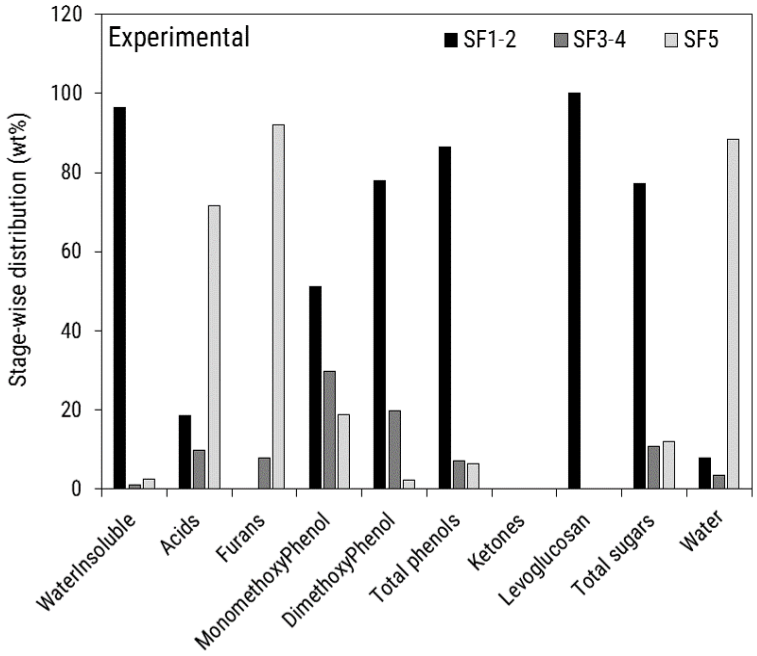

Figure 6.3: Quantitative distribution of fractions and chemical families in bio-oil obtained at 400°C in [26]

non-condensible gases along with bio-oil components. Nitrogen was the only NCG component considered for the simulations. The mass ratio of non-condensible gases (NCG) to that of condensible vapors was 2.87 as calculated from the experimental procedure used in [18]. Non-random two-liquid (NRTL) and UNIQUAC activity coefficient models were coupled with Nothnagel (NTH) equation of state to calculate equilibrium concentrations of liquid and vapor phase. Most of the binary interaction parameters for phase equilibrium model were predicted using the UNIFAC model as shown in Figure 6.4.

6.2.2 Pyrolysis vapor fractionation

Pyrolysis vapor fractional condensation into respective groups was also evaluated for two multi-stage condensation schemes under different operating conditions (Figure 6.5). The ratio of non-condensible gases to condensible vapors changes depending on the reactor type and geometry used for pyrolysis reactions. For instance, in a bubbling fluidized bed reactor [223] or conical spouted bed reactor [224] the mass ratio of NCG to condensible vapors can be as high as 3 while that for an auger reactor can be as low as 1 [225]. Operating conditions used for the

Table 6.1: Composition of representative model compounds of bio-oil for Aspen-Plus validation study and simulations. Bio-oil mass flow rate of

Components	MW	bp (°C)	Mass Concentration (wt% of bio-oil)	
Water	18.02	100	29.02	
Formic Acid	46.02	101	0.25	
Acetic Acid	60.05	118	8.09	Acids
Propionic acid	74.08	141	1.57	
Acetol	74.08	145	1.35	
Glyoxal	58.04	51	1.09	Ketones
Glycol aldehyde	60.05	131	1.09	
Gamma Butyrolactone	86.09	204	3.90	
Furfural	96.08	161	0.33	Furans
Furfuryl alcohol	98.10	171	0.33	
o-Cresol	108.14	191	1.78	
p-Cresol	108.14	202	1.78	Other phenols
2,4-Xylenol	122.16	210	2.64	
Guaiacol	124.14	205	1.62	
4-methyl Guaiacol	138.16	221	0.43	Monomethoxy phenol
iso-Eugenol	164.20	266	0.69	
Vanillin	152.15	285	0.35	
Syringol	154.16	261	1.87	Dimethoxyphenol
1,2-Benzenediol	110.10	245	0.93	
trans-3,5-dimethoxystilbene	240.30	375	4.13	Low molecular weight lignin (Water insolubles)
1,2-diphenyl ethane	182.26	284	6.99	
diBenzofuran	168.19	285	6.56	
High Molecular weight lignin-2	406.43	634	2.86	High Molecular weight lignin (Water insolubles)
High Molecular weight lignin-1	394.42	648	2.86	
Xylose	150.13		2.94	Total Water Soluble sugars
Levoglucosan	162.14		6.79	
Cellobiose	342.30		6.35	
Dehydroabietic acid	300.44		1.40	Acids/Extractive (Water insoluble)

Table 6.2: Classification of model compounds into groups

Chemical Family (CF)	Model Compounds
CF 1-1	High molecular weight lignin, Low molecular weight lignin, Dehydroabetic acid
CF 1-2	Water soluble sugars
CF 2	o-cresol, p-cresol, Guaiacol, γ-butyrolactone, 2,4-Xylenol, 4-methyl-Guaiacol, 1,2-Benzenediol, I-eugenol
CF 3	Acetol, Glyoxal, Glycolaldehyde, Furfural, Furfuryl alcohol
CF 4	Water, Formic acid, Acetic acid and Propionic acid

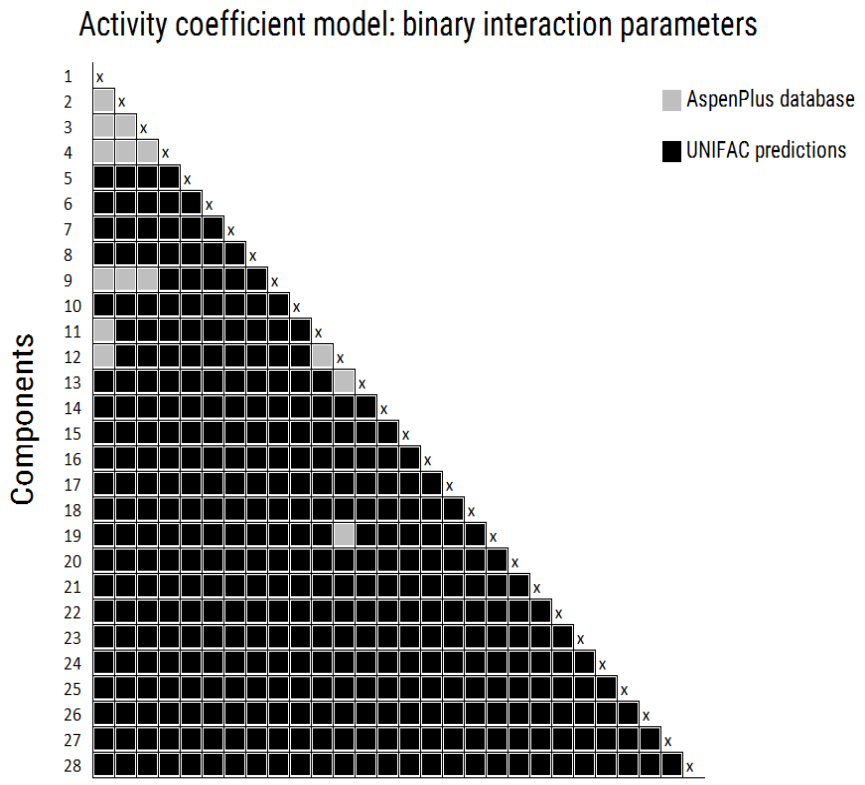

Figure 6.4: Experimental and predicted binary interaction parameters for set of model compounds used in this study. Serial numbers in this figure sequentially represent components in Table 6.1

simulation schemes are shown in Table 6.3. To compare the configurations for

Table 6.3: Operating conditions for multi-stage condensation schemes

	IDHE1-1 (°C)	IDHE1-2 (°C)	IDHE1-3 (°C)	IDHE1-4 (°C)			NCG:CV (wt:wt)
Scheme1	110 to 260	50 to 140	20 to 90	5 to 25			1.5,2,2.5, 2.87
	IDHE2-1 (°C)	DCHE water flow (kg/hr)	IDHE2-2 (°C)	DCHE water flow (kg/hr)	IDHE2-3 (°C)	IDHE2-4 (°C)	NCG:CV (wt:wt)
Scheme2	20 to 50	150 to 500	20 to 50	100 to 400	10 to 70	5	1.5,2,2.87

fractional condensation of pyrolysis vapors, a separation factor (SF) was defined as shown in Eq.6.1

$$SF_{k-j} = \frac{\sum_{i=1}^{m} M_{stage,j}^{i,k}}{\sum_{j=1}^{n}\sum_{i=1}^{m} M_{stage,j}^{i,k}} \tag{6.1}$$

where, i is a component in a k chemical family condensed in any of the stage j. Total number of components in any chemical family and total number of stages is denoted by n and m respectively. To achieve complete separation of chemical

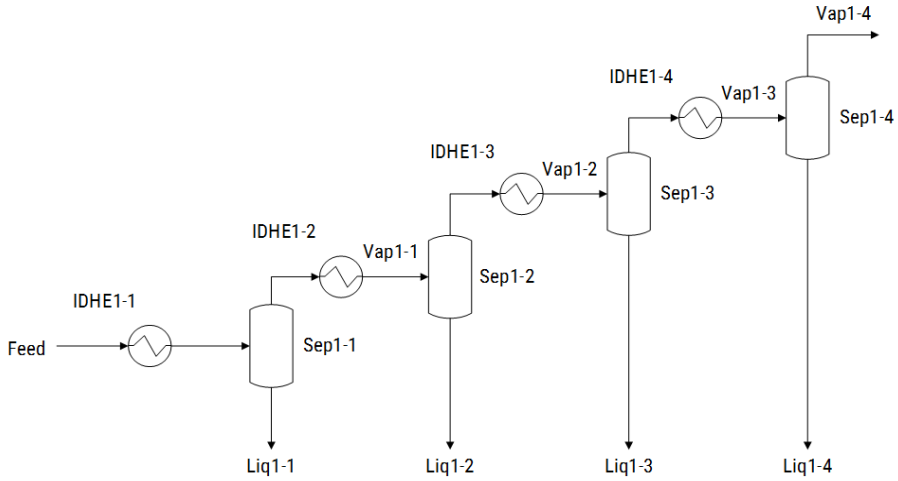

(a)

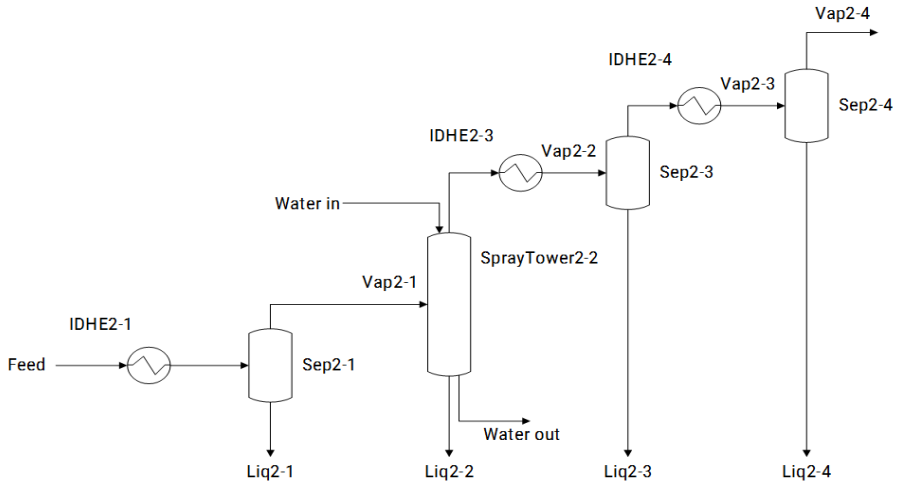

(b)

Figure 6.5: Condensation schemes for simulation of multi-stage condensation of bio-oil model compounds. IDHE stands for indirect contact heat exchanger. SEP stands for flash separators. Spray tower uses water as a direct contact heat exchange medium.

families, the separation factor for each chemical family should be unity.

6.3 Results and discussion

6.3.1 AspenPlus simulation validation

As evident from Figure 6.4 most of the binary interaction parameters for a pair of components are predicted using UNIFAC group contribution method. Thus, validation of simulation results is essential. One way to validate the simulation is

to compare the yield of each fraction shown in Figure 6.3 to that predicted using AspenPlus. Both the phase equilibrium models, NRTL-NTH and UNIQUAC-NTH, were in good agreement with the experimental data (Figure 6.6). The average absolute error for NRTL-NTH and UNIQUAC-NTH was 8.86 $\pm$ 11.05, and 9.90 $\pm$ 12.38 respectively. Chemical families like sugars and dimethoxy phenols are present in SF3-4 and SF5 because of liquid droplet entrainment. Partly, the mean error between model and experimental data could occur because carry over of liquid from upstream condensers was not considered in the simulation. While both the models exhibit good agreement with experiments, combination of UNIQUAC and NTH is used for further analysis as UNIQUAC can predict the liquid-liquid phase splitting. UNIQUAC determines the activity coefficient for two components based on their experimental vapor-liquid and liquid-liquid equilibrium data. However, for the compounds used in this study, experimental data for all possible pairs of components is not available in the AspenPlus database. Therefore, UNIFAC's group contribution method is used to determine the unknown binary interaction parameters. While UNIFAC's group contribution method is reliable, the model accuracy may be hampered due to large number and polar nature of the components used in this work [**?**]. Accurate prediction of bubble/dew points, and liquid/vapor phase concentrations of a component depends on the value of binary interaction parameter. Thus, a sensitivity analysis of experimental and predicted binary interaction parameters was carried out. The binary interaction parameters were varied within a range of $\pm$ 40% of actual value.

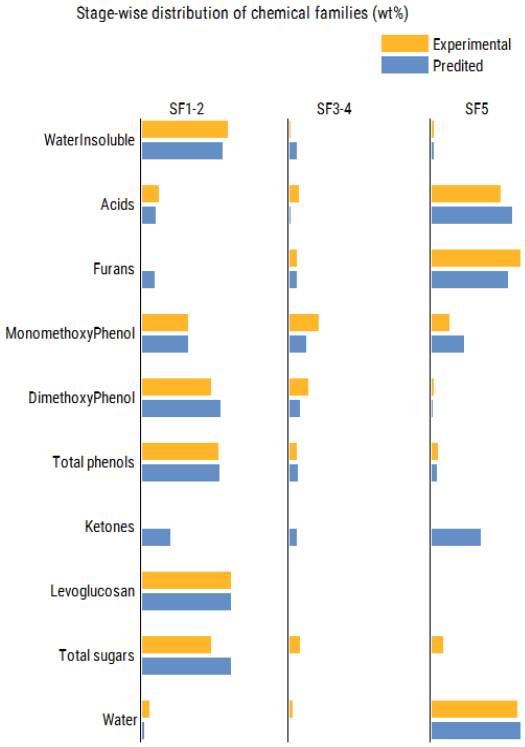

(a)

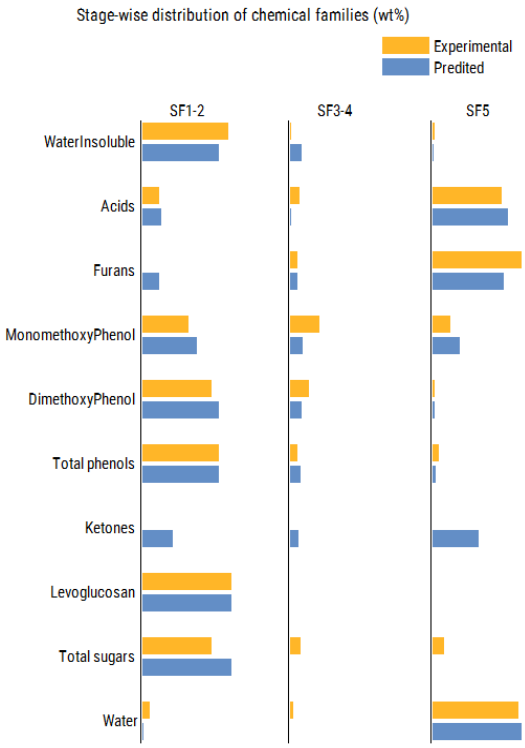

(b)

Figure 6.6: Comparison of experimental and predicted values of bio-oil fractions collected in SF1-2, SF3-4 and SF5 stages of condensation train using (a) NRTL-NTH and (b) UNIQUAC-NTH phase equilibrium models.

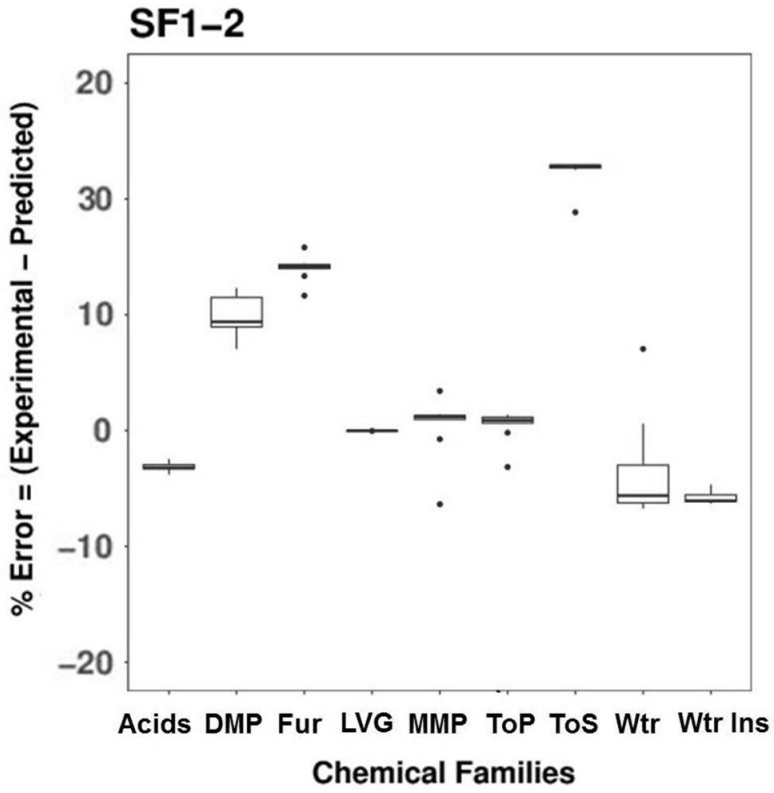

(a)

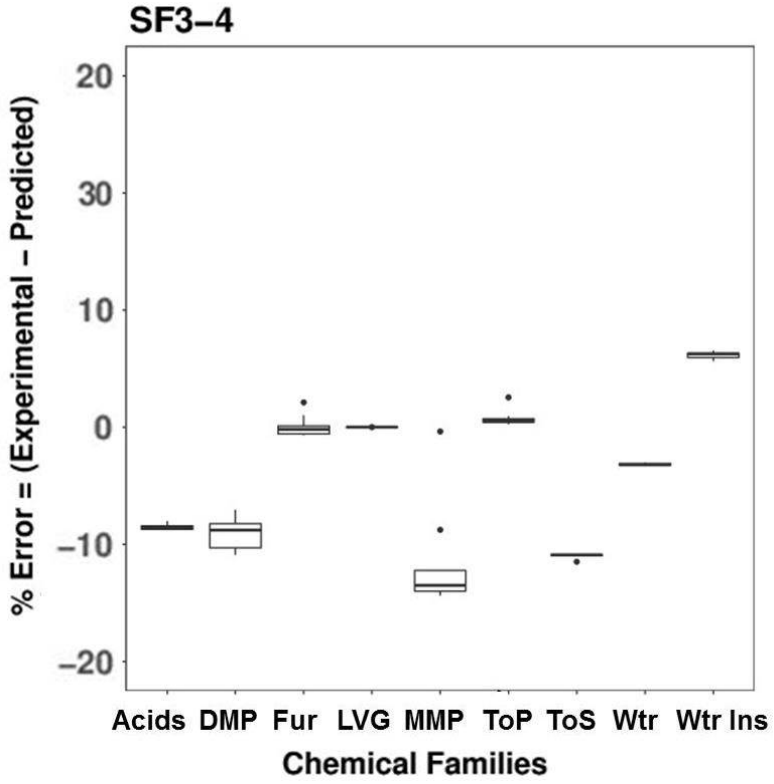

(b)

This figure is continued on the next page...

Figure 6.7

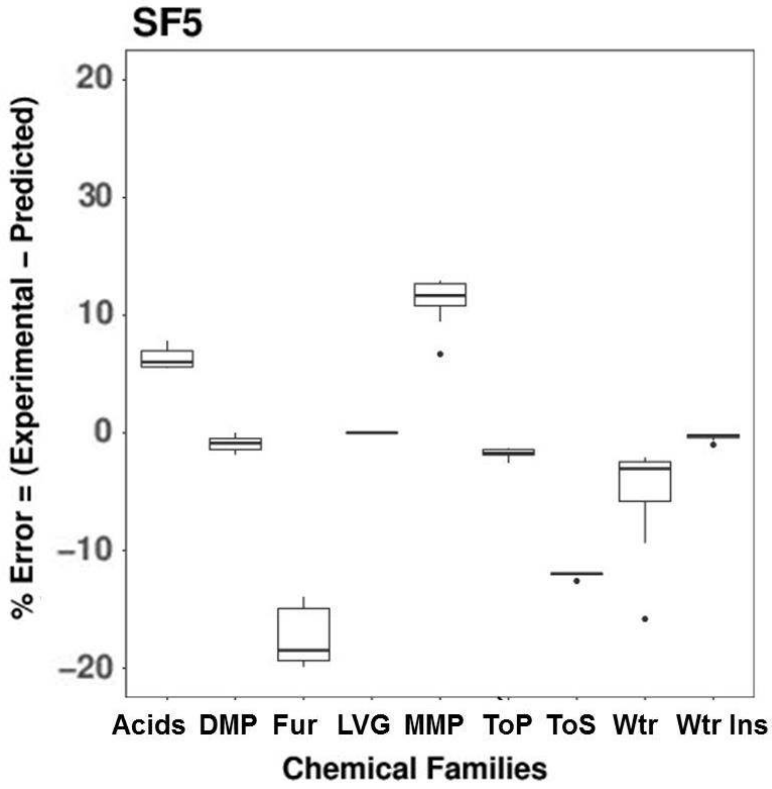

(c)

Figure 6.7: Error between experimental and predicted value when UNIQUAC parameters are varied within a range of $\pm 40\%$ of the parameter's original value. (Acids: Carboxylic acid, DMP: dimethoxyphenol, Fur: Furans, LVG: Levglucosan, MMP: monomethoxyphenol, ToP: total phenols, ToS: total sugars, Wtr: Water, Wtr Ins: Water insolubles)

Box plots in Figure 6.7 show that binary interaction parameter sensitivity depends on the liquid composition and chemical families under consideration. Prediction of dimethoxy and monomethoxy phenol concentration in any fraction is most sensitive as compared to other chemical families. However, though the binary interactions parameters were varied over $\pm$ 40%, the square root of mean squared error between experimental and predicted values is 8.68 $\pm$ 10.75. Therefore, the interaction parameters used for the set of bio-oil model components can be used to fairly predict the liquid phase concentrations of bio-oil model compounds.

The composition of bio-oil depends on biomass source and operating conditions of pyrolysis reactor. Therefore, the concentration of the chemical families was varied and percent change in their yield in each condenser with respect to the base case (composition in Table 6.1) was plotted in Figure 6.8. Except sugars, yields of all the other chemical families changed even if their respective concentration was

not altered. Thus, co-condensation of compounds occurs due to complex interaction between various bio-oil components. This can explain why certain compounds condense at temperatures above their boiling points. Further the average change in yield of any chemical family is linear with respect to its change in feed composition.

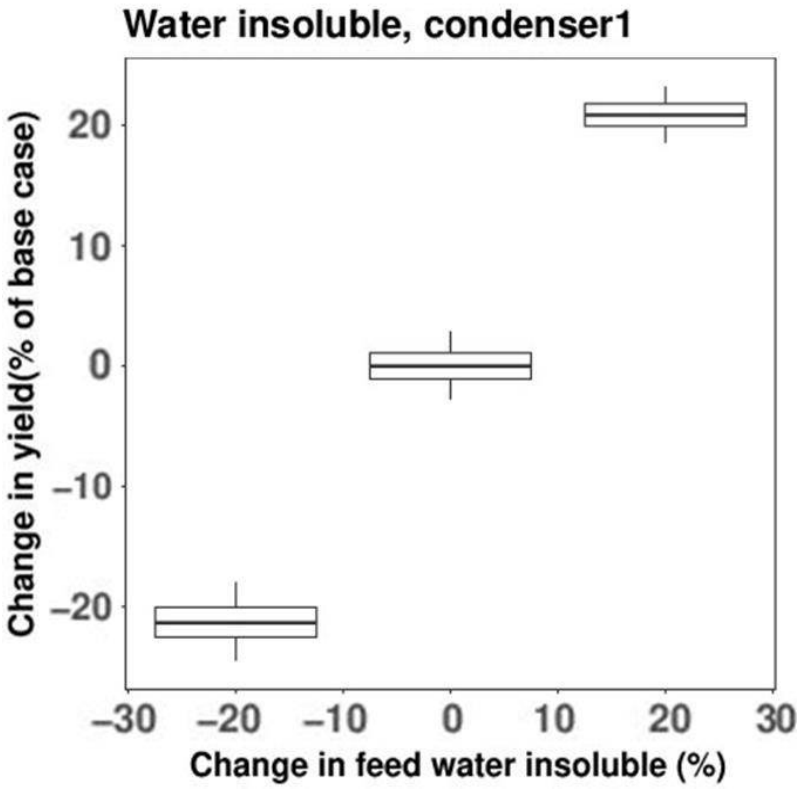

(a)

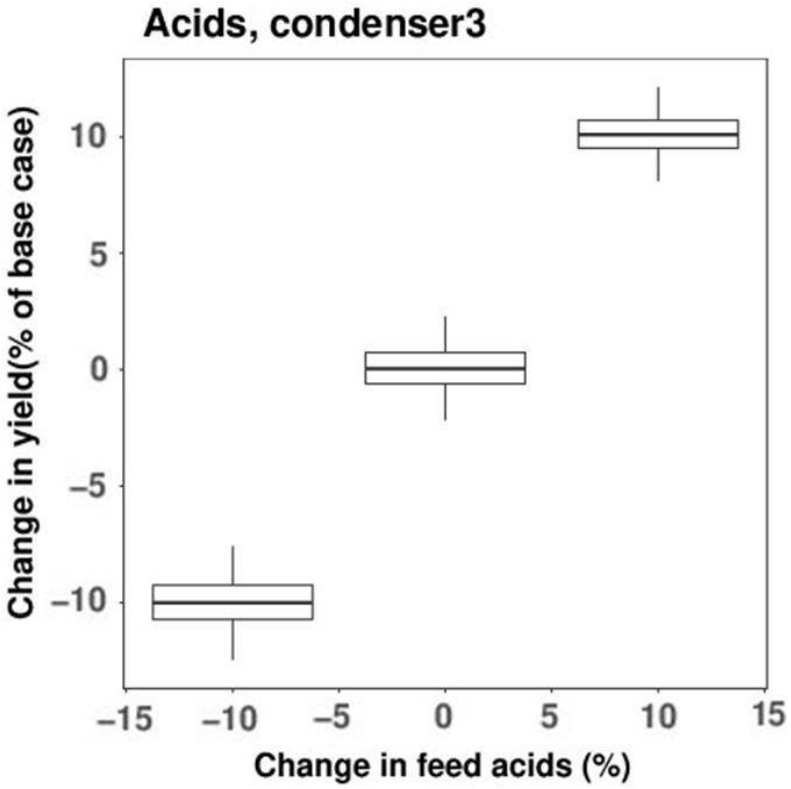

(b)

This figure is continued on the next page...

Figure 6.8

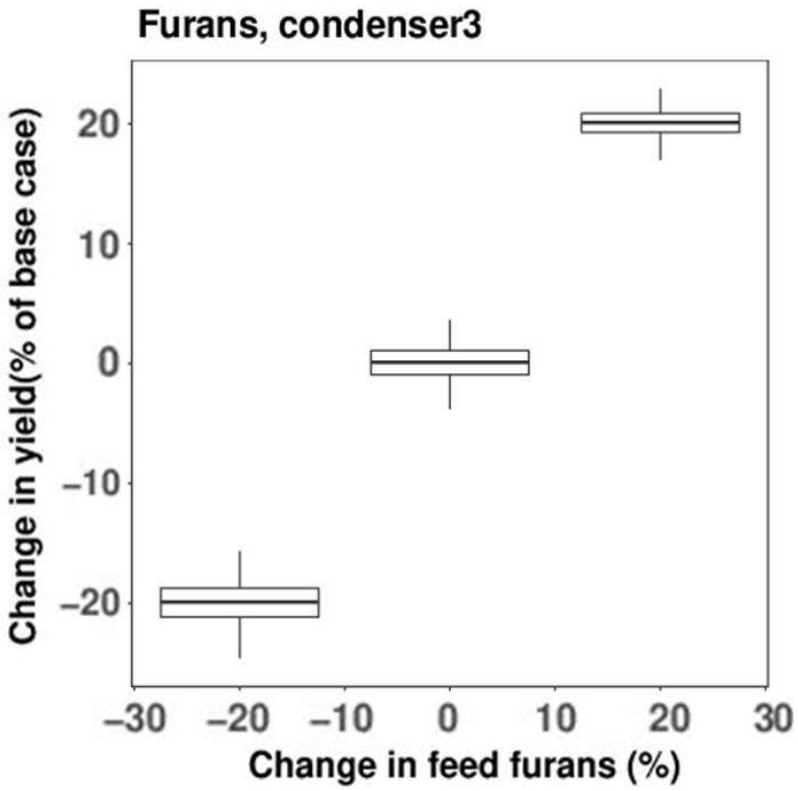

(c)

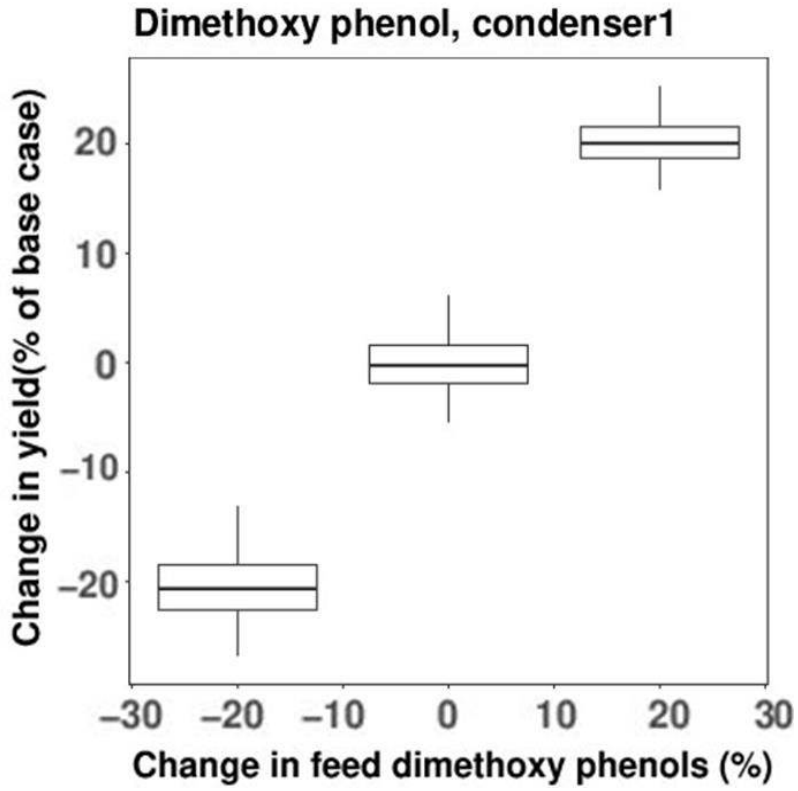

(d)

This figure is continued on the next page...

Figure 6.8

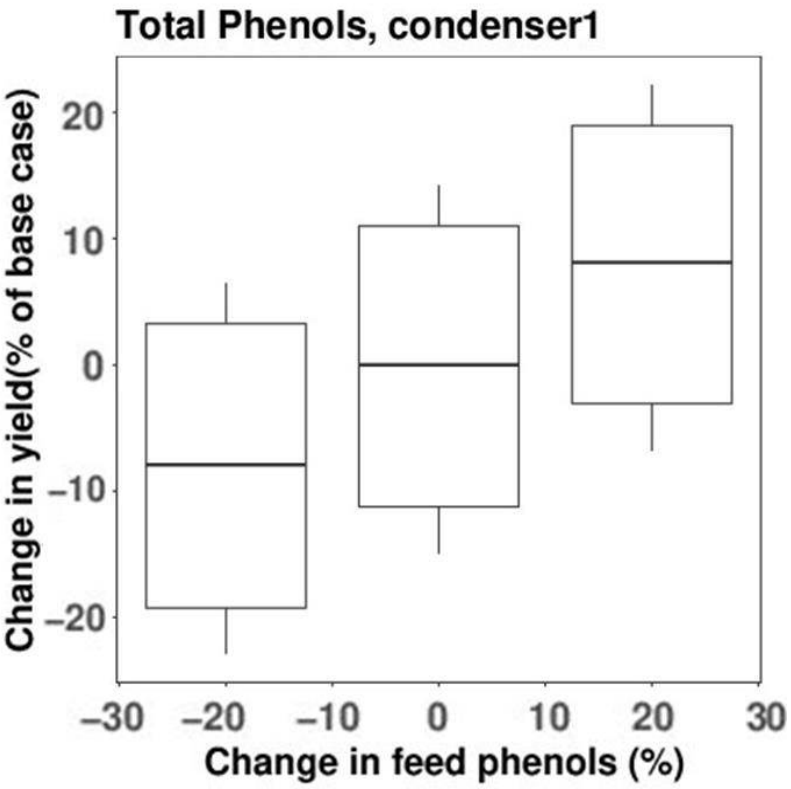

(e)

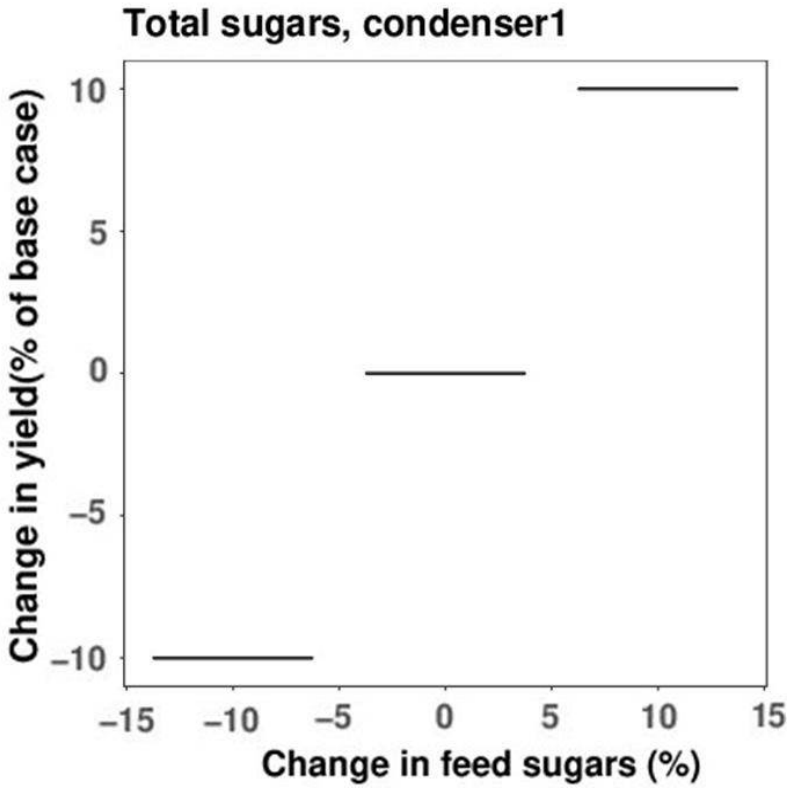

(f)

This figure is continued on the next page...

Figure 6.8

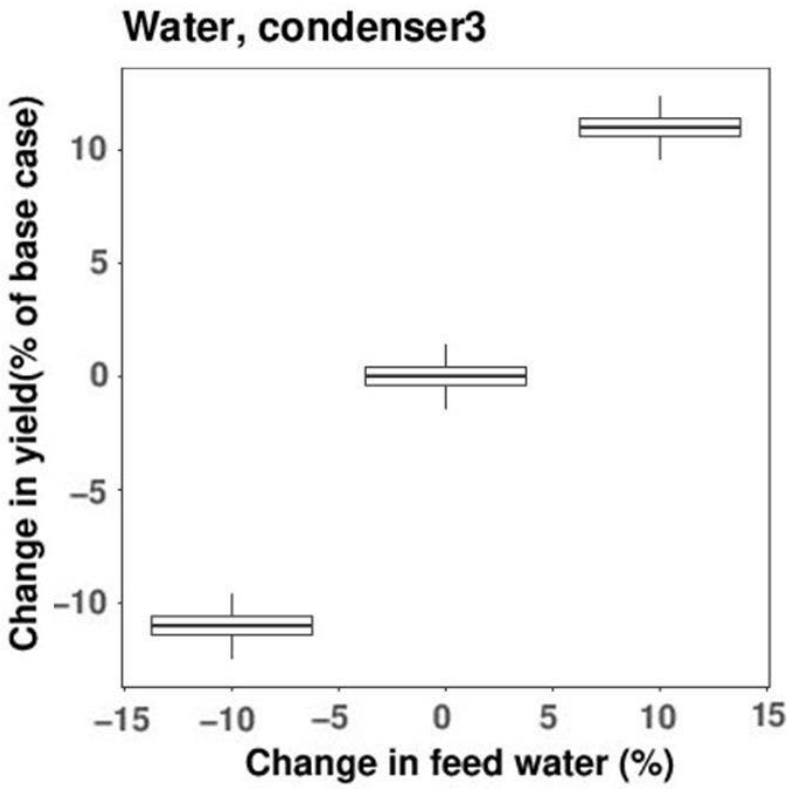

(g)

Figure 6.8: Sensitivity study of concentration of model compounds used to represent bio-oil.

6.3.2 Pyrolysis vapor fractionation

6.3.2.1 Fractional condensation of pyrolysis vapors: Scheme 1

A train of indirect contact heat exchangers is the most simple and widely used configuration for stage-wise condensation of pyrolysis vapors. The separation of chemical families is governed by the boiling point and mole fractions of components in the vapor mixture. The simulations predict that phase separation occurs at temperatures below 160°C, 70°C and 60°C for first, second and third stage respectively. For the third stage proportion of one of the phase (signified as Liq1-3-1) is very less and can be ignored. Figure 6.9 shows the degree of separation achieved between chemical families for the operating conditions shown in Table 6.3.

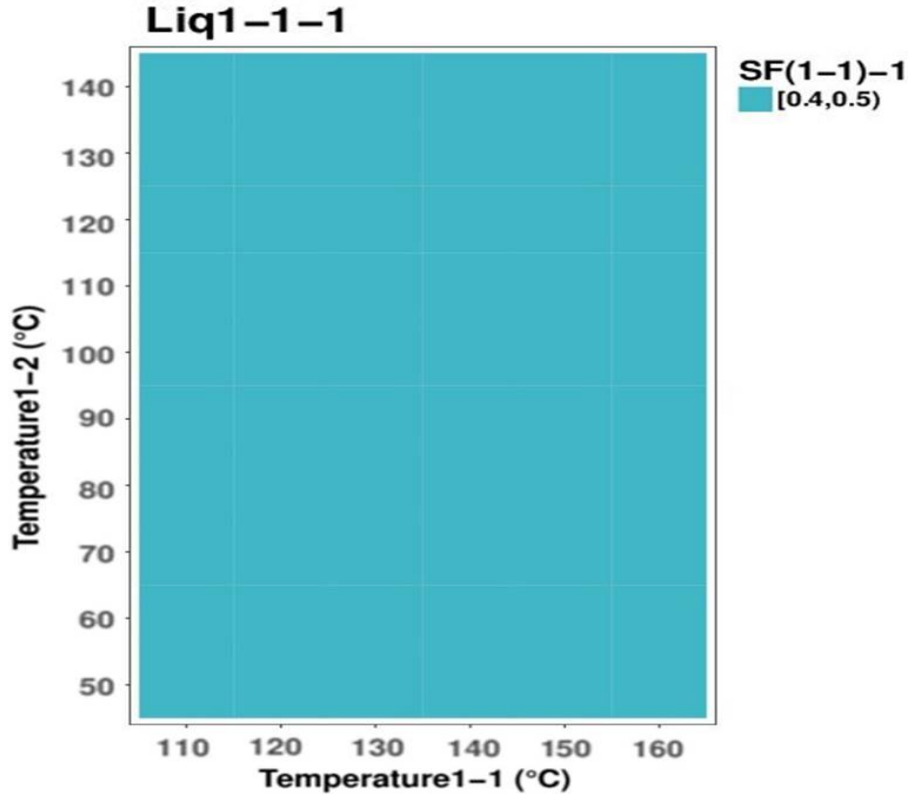

(a)

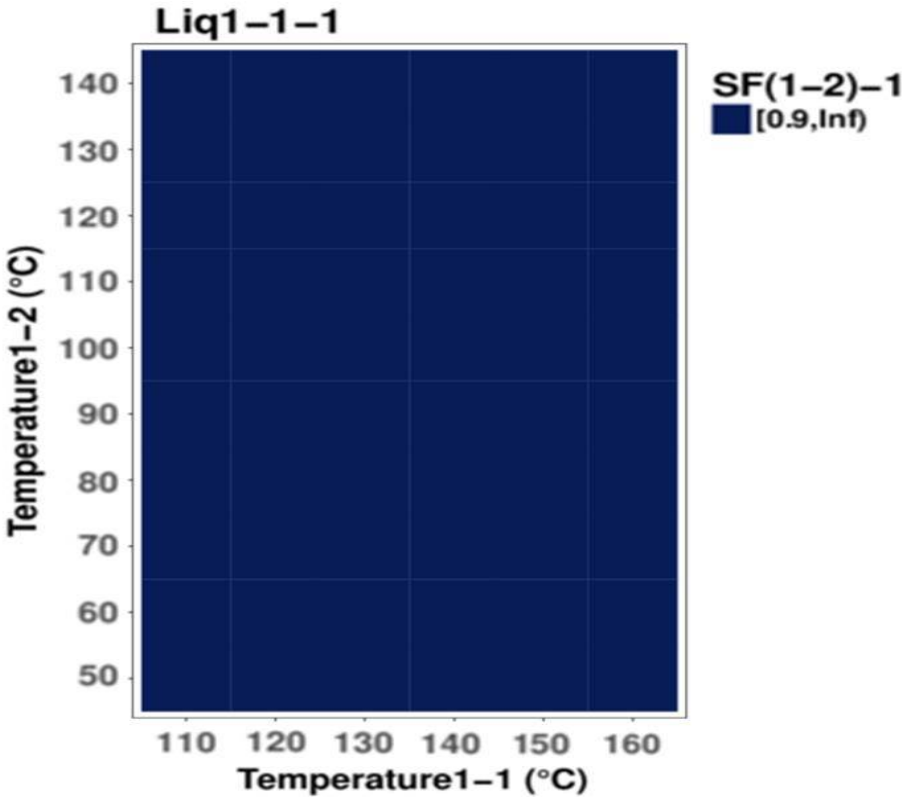

(b)

This figure is continued on the next page...

Figure 6.9

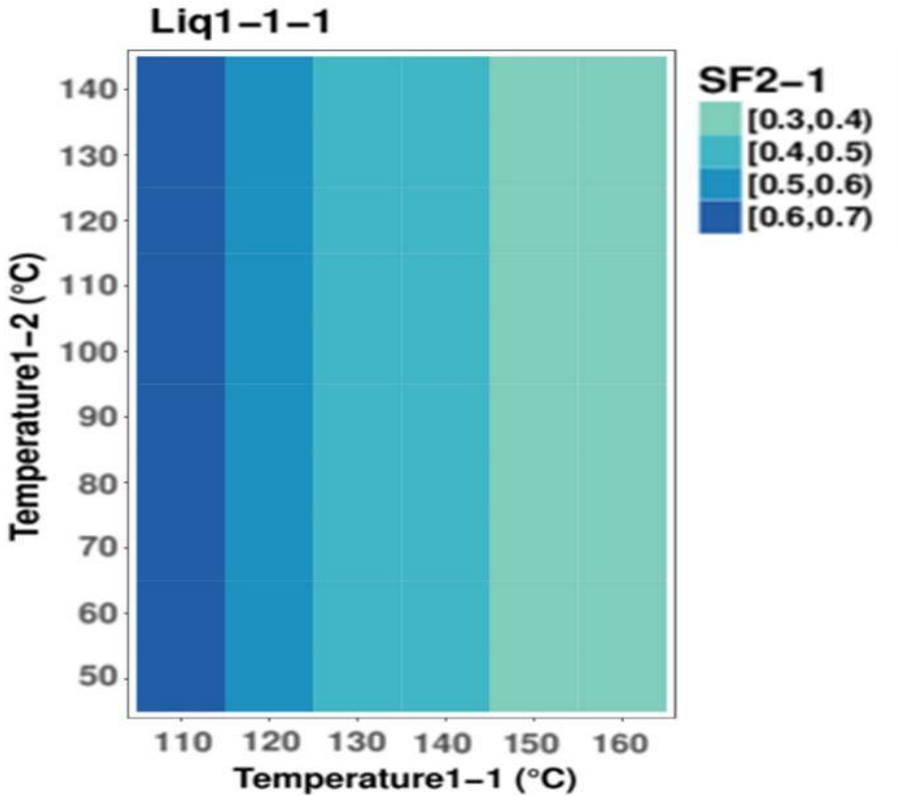

(c)

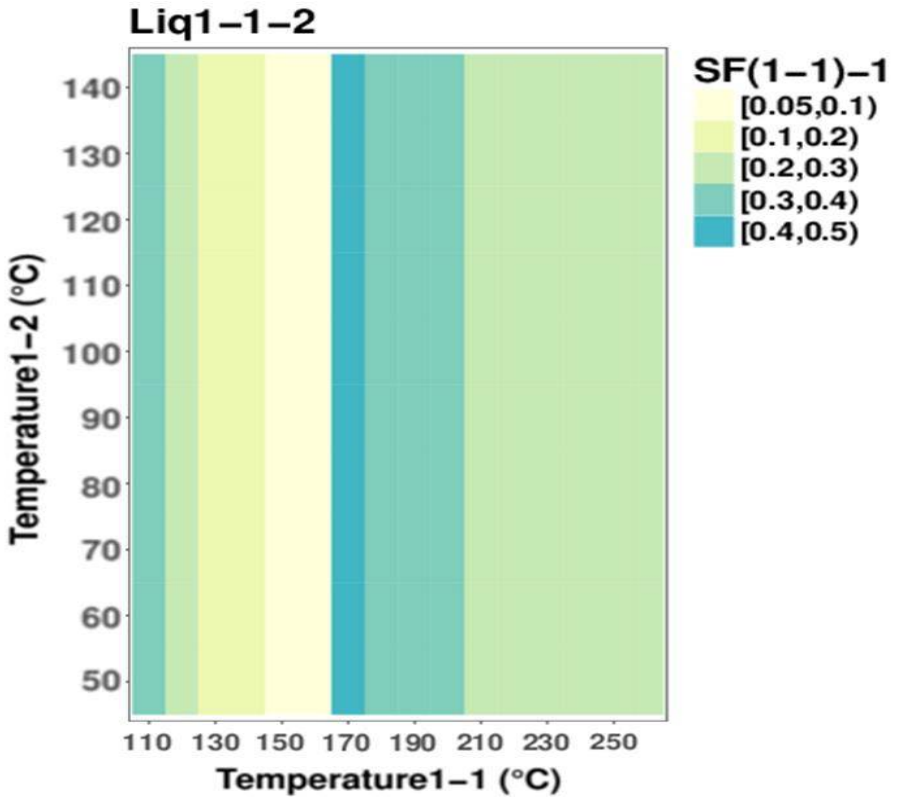

(d)

This figure is continued on the next page...

Figure 6.9

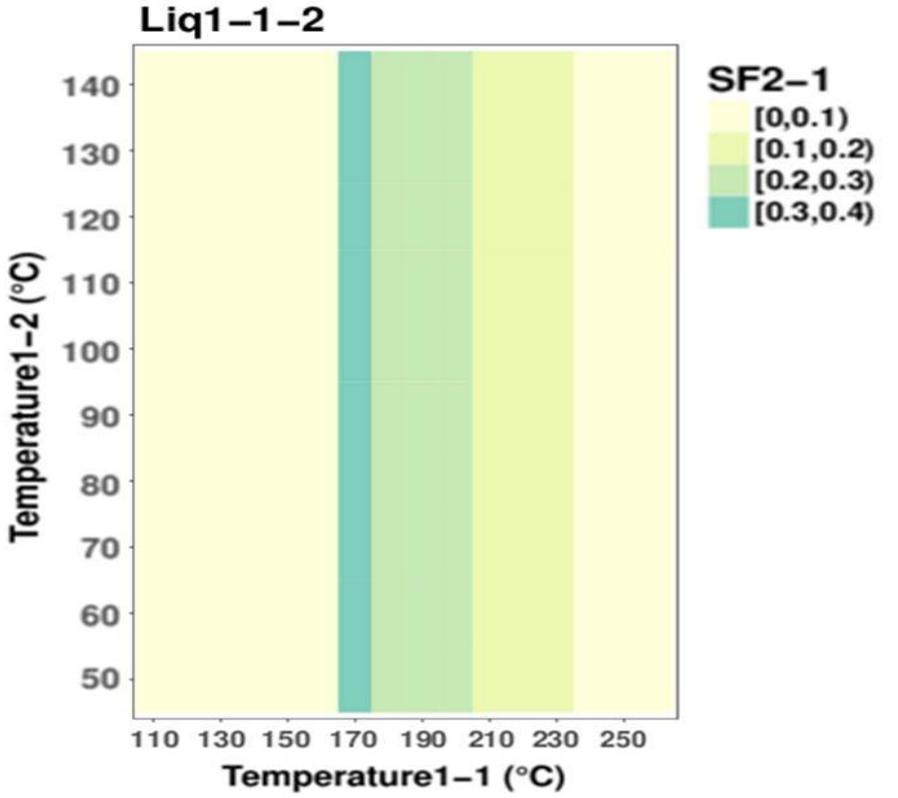

(e)

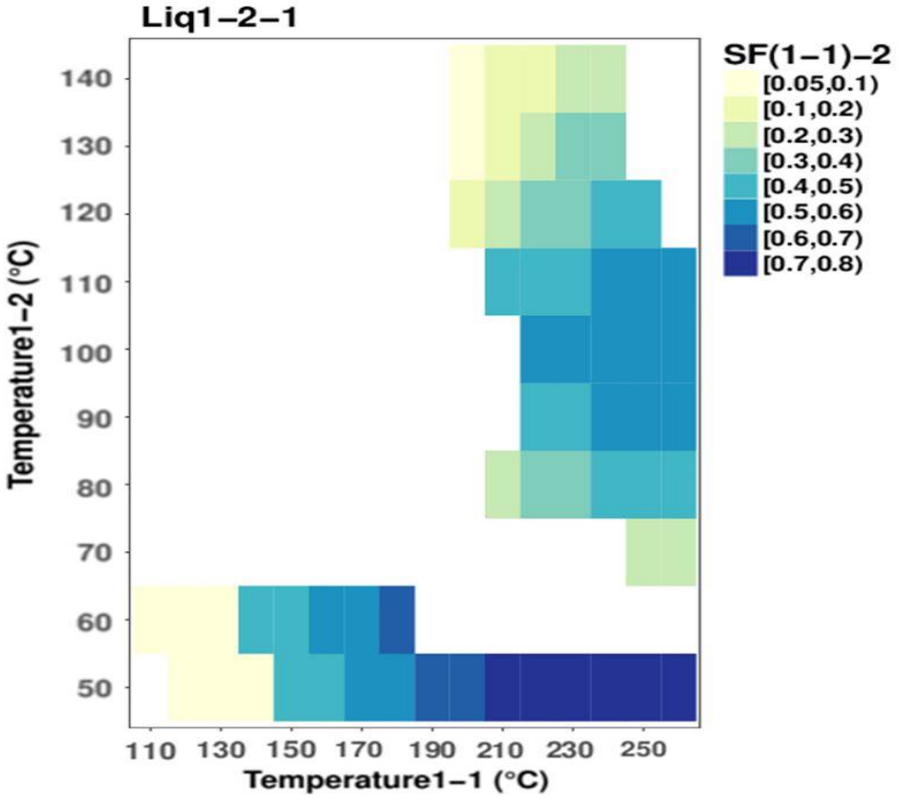

(f)

This figure is continued on the next page...

Figure 6.9

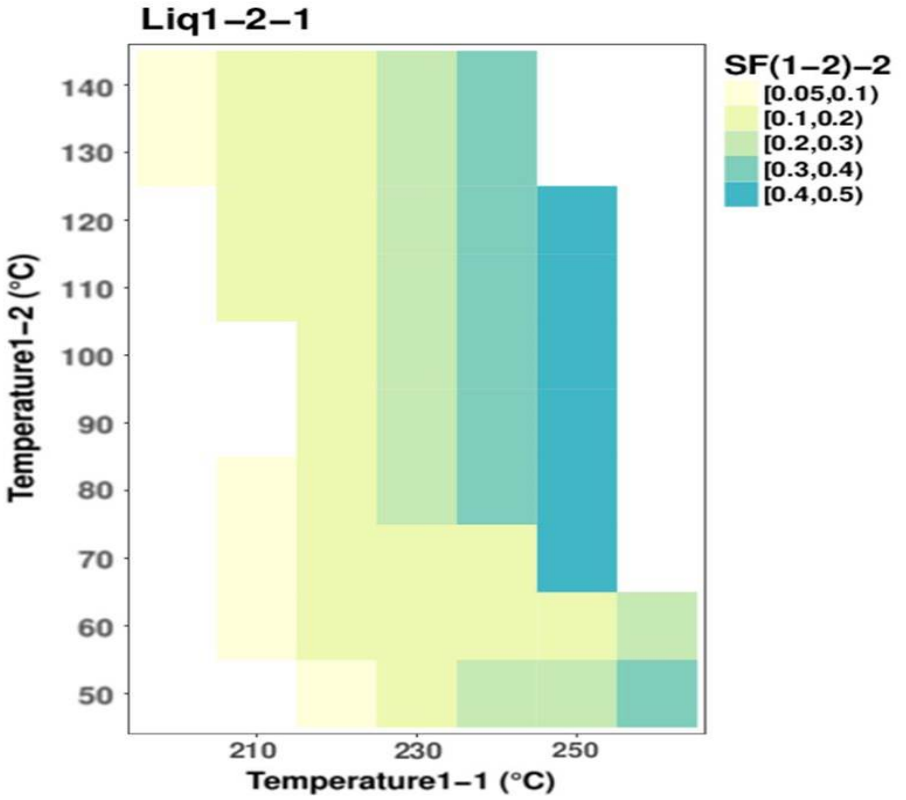

(g)

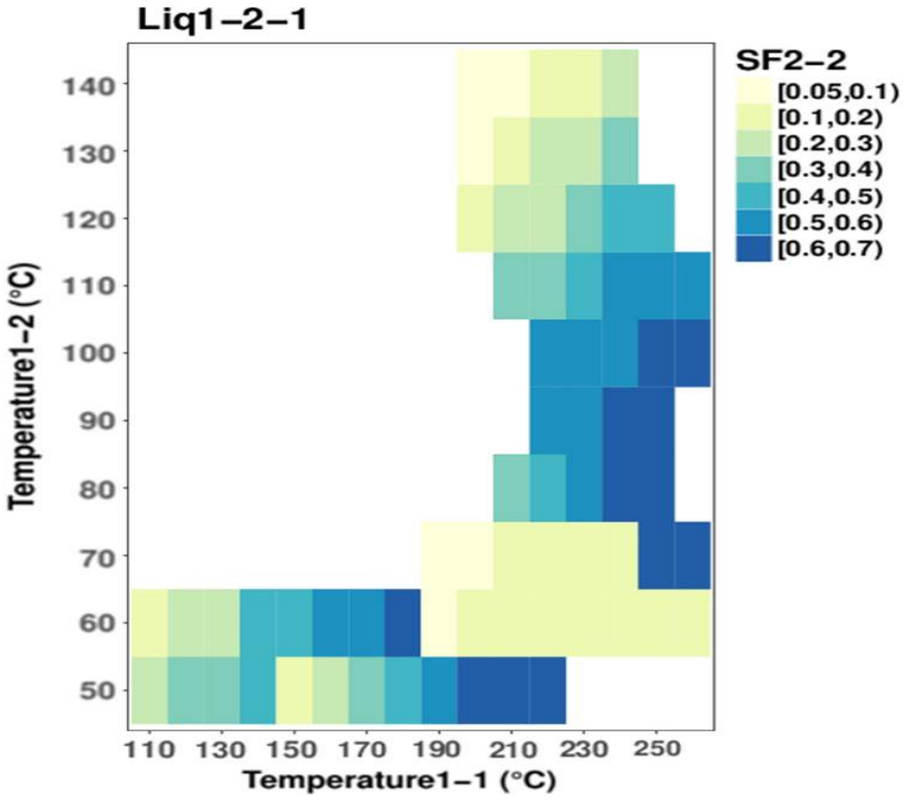

(h)

This figure is continued on the next page...

Figure 6.9

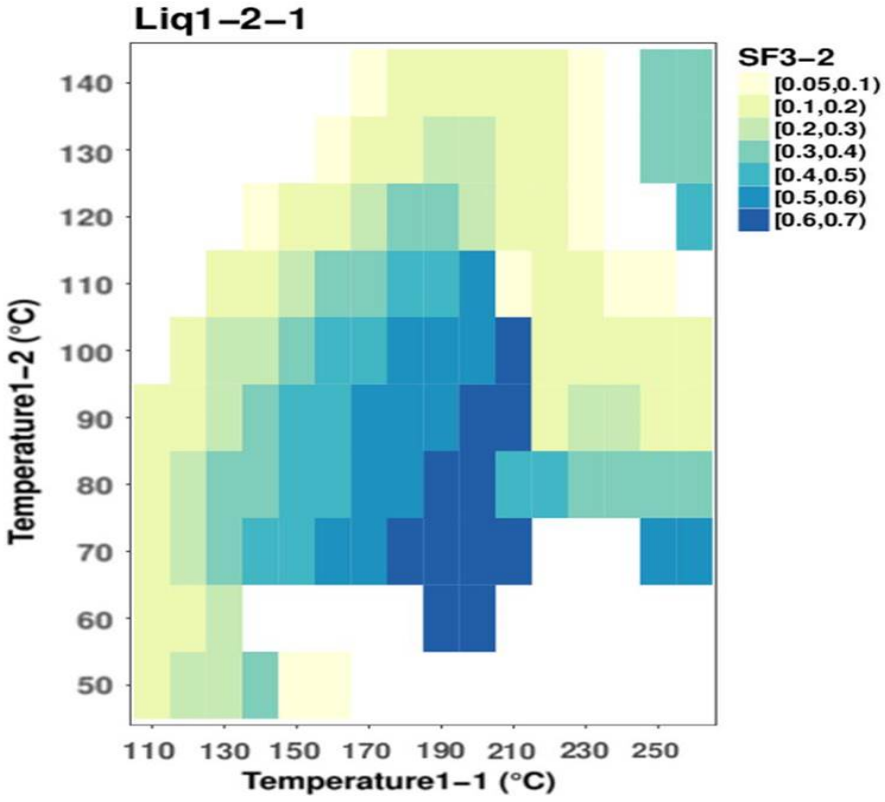

(i)

Figure 6.9: Separation factors of chemical families in different liquid streams obtained for scheme 1

Figure 6.9 illustrates the separation factor for liquid 1-2-1. Chemical families (CF) 1-1, 1-2 and 2 are condensed together in the first condenser. The separation factor $SF_{(1-2)-1}$ is close to 0.99 in the first stage below 200°C but $SF_{(1-1)-1}$ and SF_{2-1} is also 0.43 and 0.37 respectively. The phase separation does not result in any significant fractionation between CF1-1 and CF1-2, despite their chemically different nature. The absence of water, due to high condenser temperature, from Liq1-1-1 prevents the phase separation of CF1-1 from CF1-2. A temperature of 170 °C was optimized for stage one to maximize separation between CF1-1 and CF-2 as they have similar nature and can pose difficulty in downstream purification. At 170°C, values of $SF_{(1-1)-1}$ and $SF_{(1-2)-1}$ reached a maximum, while separation factors for all other chemical families were at minimum. The optimal temperature condition for stage 2 is 90°C, where remaining CF1-1 is recovered completely while CF3 and CF4 yields are minimized. The temperature of third and fourth condenser are optimized to 50 and -5°C respectively to maximize the separation between CF3 and CF4, and maximize the overall recovery of bio-oil.

Table 6.4: Liquid yield and purity of components for scheme 1 under optimized operating conditions for NCG: condensible ratio of 2.87

			Liquid Yield (Purity), wt.%			
Components	MW	bp (°C)	Cond 1	Cond 2	Cond 3	Cond 4
Water	18.02	100	0.15 (0.14)	2.88 (3.02)	71.38 (67.4)	23.07 (79.94)
Formic Acid	46.02	101	0.4 (0)	3.17 (0.03)	73.17 (0.59)	21.58 (0.64)
Acetic Acid	60.05	118	0.67 (0.17)	13.94 (4.07)	71.18 (18.73)	13.43 (12.97)
Propionic acid	74.08	141	0.98 (0.05)	20.61 (1.17)	64.57 (3.29)	13.01 (2.43)
Acetol	74.08	145	0.91 (0.04)	42.51 (2.07)	53 (2.32)	3.51 (0.57)
Glyoxal	58.04	51	0.07 (0)	0.82 (0.03)	6.92 (0.25)	9.35 (1.22)
Glycol aldehyde	60.05	131	1.15 (0.04)	61.78 (2.44)	36.2 (1.29)	0.86 (0.11)
Gamma Butyrolactone	86.09	204	3.34 (0.41)	73.71 (10.38)	20.1 (2.55)	2.67 (1.24)
Furfural	96.08	161	0.87 (0.01)	38.52 (0.46)	40.86 (0.44)	18.24 (0.72)
Furfuryl alcohol	98.10	171	1.02 (0.01)	57.53 (0.69)	38.24 (0.41)	3.15 (0.12)
o-Cresol	108.14	191	63.04 (3.58)	35.94 (2.32)	1.02 (0.06)	0 (0)
p-Cresol	108.14	202	70.83 (4.02)	27.68 (1.78)	1.47 (0.09)	0.02 (0)
2,4-Xylenol	122.16	210	61.31 (5.14)	37.5 (3.57)	1.19 (0.1)	0.01 (0)
Guaiacol	124.14	205	2.46 (0.13)	81.31 (4.76)	16.2 (0.86)	0.03 (0.01)
4-methyl Guaiacol	138.16	221	2.66 (0.04)	90.42 (1.41)	6.92 (0.1)	0.01 (0)
iso-Eugenol	164.20	266	9.26 (0.2)	90.14 (2.24)	0.59 (0.01)	0 (0)
Vanillin	152.15	285	25.41 (0.28)	74.45 (0.93)	0.14 (0)	0 (0)
Syringol	154.16	261	7.09 (0.42)	92 (6.23)	0.91 (0.06)	0 (0)
1,2-Benzenediol	110.10	245	36.61 (1.09)	61.66 (2.08)	1.73 (0.05)	0 (0)
trans-3,5-dimethoxystilbene	240.30	375	81.11 (10.66)	18.89 (2.82)	0 (0)	0 (0)
1,2-diphenyl ethane	182.26	284	2.49 (0.55)	92.71 (23.39)	4.51 (1.02)	0.02 (0.01)
diBenzofuran	168.19	285	11.3 (2.36)	86.88 (20.59)	1.8 (0.38)	0.01 (0.01)
High molecular weight lignin-2	406.43	634	100 (9.09)	0 (0)	0 (0)	0 (0)
High molecular weight lignin-1	394.42	648	100 (9.09)	0 (0)	0 (0)	0 (0)
Xylose	150.13		96.77 (9.05)	3.23 (0.34)	0 (0)	0 (0)
Levoglucosan	162.14		99.45 (21.47)	0.55 (0.13)	0 (0)	0 (0)
Cellobiose	342.30		100 (20.18)	0 (0)	0 (0)	0 (0)
Dehydroabietic acid	300.44		39.89 (1.78)	60.1 (3.05)	0.01 (0)	0 (0)

Table 6.4 shows yield and purity of each compound obtained under optimal operating conditions for scheme 1. Compounds like guaiacol, syringol and 1,2- diphenyl ethane that have mole fractions and boiling points similar to or greater than cresols and xylenol did not condense significantly in stage 1. When stage 1 condenser is simulated at 260°C, 14 wt.% (based on feed) of o- and p-cresol, and 10 wt.% of 2,4-xylenol condense despite condenser temperature being higher than their respective boiling points. Such a anomalous behavior is corroborated by GC-MS profile of fractionally condensed bio-oil reported in [19]. To analyze which compounds strongly interact with cresols and xylenol and cause them to condense at high temperature, the flow rate of each model component is equaled to zero one at a time, while keeping the flow rate of other components constant. For example, in one instance the water flow rate is equaled to zero and flow rate of all other components is calculated based on mass fractions from Table 6.1. The mass ratio of non-condensible to condensible components is maintained at 2.87 for each case and optimal temperature conditions are used for the condensers. As mole fraction in liquid or vapor phase is an actual measure of driving force for mass transfer, the ratio of volatility of a component under altered feed conditions to its volatility for the base case (where feed conditions are as stated in Table 6.1) is plotted as points in Figure 6.10. On the other hand the percent change in the mass yield of each component is shown as bar chart for an easier comprehension of co-condensation effect.

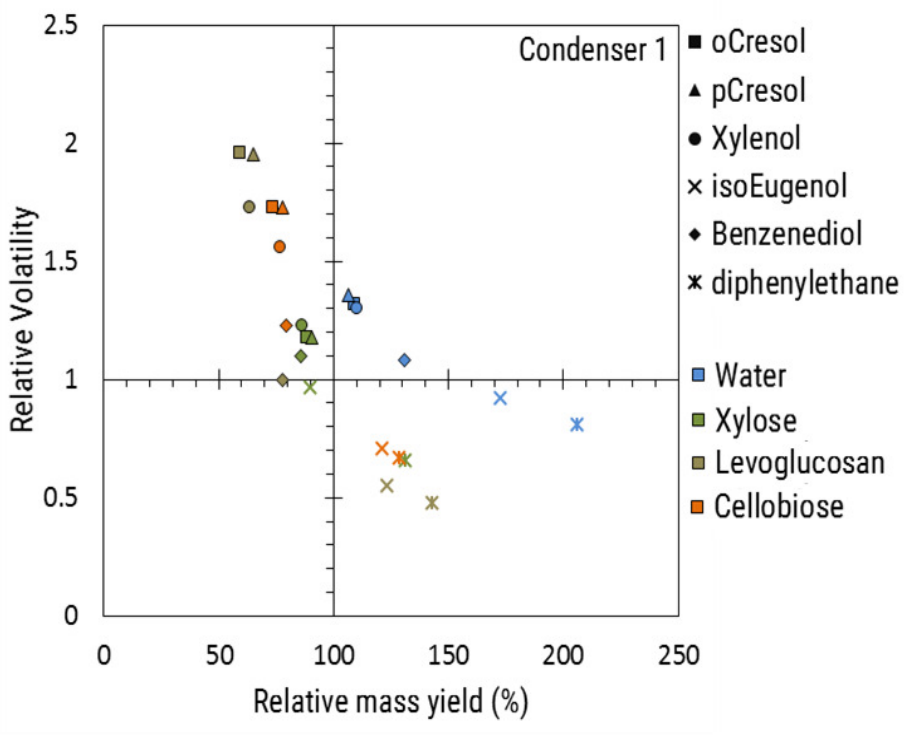

(a)

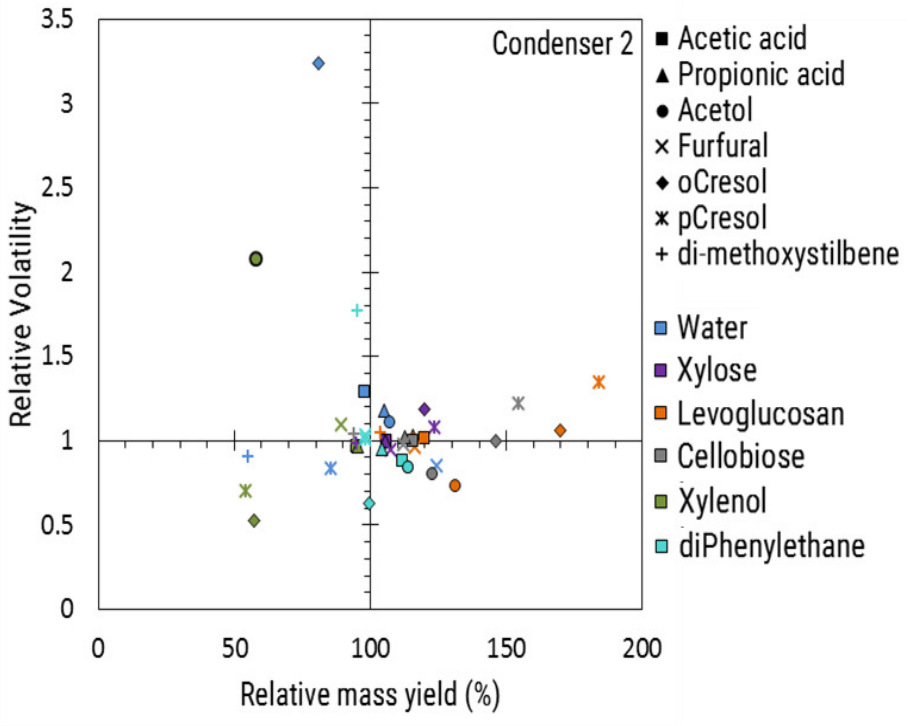

(b)

This figure is continued on the next page...

Figure 6.10

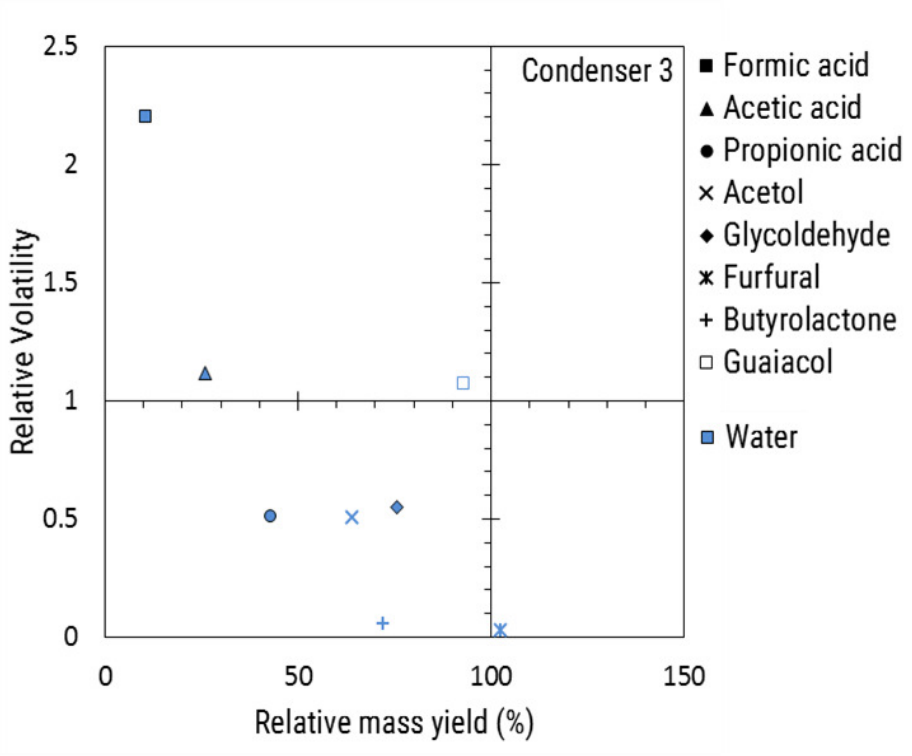

(c)

Figure 6.10: Relative volatility dependence of model components

Compounds that have significantly condensed at each stage are plotted in Figure 6.10. Effect of water on condensation is also tested because, following nitrogen, water has the highest mole fraction in the pyrolysis vapor stream and thus, profoundly affects the dew point of the vapor mixture. Condensation of the compounds represented by marker shape (group 1) is affected by absence of compounds indicated by color (group 2) in the figure legend. Though high and low molecular weight phenols are present in stage 1, they do not affect the condensation or co-condensation of other components significantly. The mass yield and volatility of cresols and xylenol in stage 1 is significantly affected by levoglucosan and cellobiose as compared to xylose and water (Figure 6.10 (a)). The yield of cresols and xylenol decreases to an average value of 69 ± 3 wt.% (on the basis of mass yield for base case) when levoglucosan and cellobiose are absent in the feed, since the bubble point of the mixture decreases in the absence of sugars. On the other hand relative volatility of benzenediol does not change but the yield decreases to 81 ± 4 wt.% in the absence of sugars and increases to 131 wt.% in the absence of water. Yield of iso-eugenol (mole fraction comparable to benzenediol)

and diphenylethane (mole fraction 10 times of benzenediol) increases in the absence of sugars. To generalize, points that lie in the second quadrant indicate that yield decreases as a result of decrease in the bubble point of the mixture as a consequence of absence of high boiling compounds. On the other hand, points in the fourth quadrant imply a weak interaction amongst group 1 and group 2 compounds.

For condenser 2, most of the points are clustered around the origin which show that, at operating condition of 70°C, the composition of the condensate is not considerably sensitive to feed composition. Points lying in the third quadrant, where relative volatility and yield both decrease, suggest the effect of upstream condenser. The points correspond to o- and p-cresol when xylenol is not present in the feed. The absence of xylenol causes an increase in the yield of cresols (122 wt.%) and a decrease in relative volatility (0.45). Similarly if any point lies in the first quadrant, the yield and relative volatility of corresponding group 1 compound(s) would have decreased and increased respectively under the influence of group 2 component. Similar behavior is observed for components condensing in stage 3.

Thus, to sum up, condensation of phenols is strongly affected by sugars in the first condenser. The effect of components on the each other's condensation becomes less prominent after the first stage because the operating temperatures are well below the boiling point of most of the components. The amount of inert/carrier gas used in the fast pyrolysis reaction depends on the reactor configuration. For example the amount of carrier gas used in a bubbling fluidized bed reactor is more as compared to that used in an auger reactor. Thus, the effect of amount of non-condensible gas on the operating conditions and bio-oil condensation is studied. As the NCG: condensible ratio decreases, higher condenser temperatures are required to achieve a similar extent of separation between chemical families. The optimal conditions of condensers, yield, and purity of chemical families are presented in Figure 6.11. Also, there is no significant difference between the yield of individual chemical compounds obtained under optimal operating conditions for each of the case in Figure 6.11.

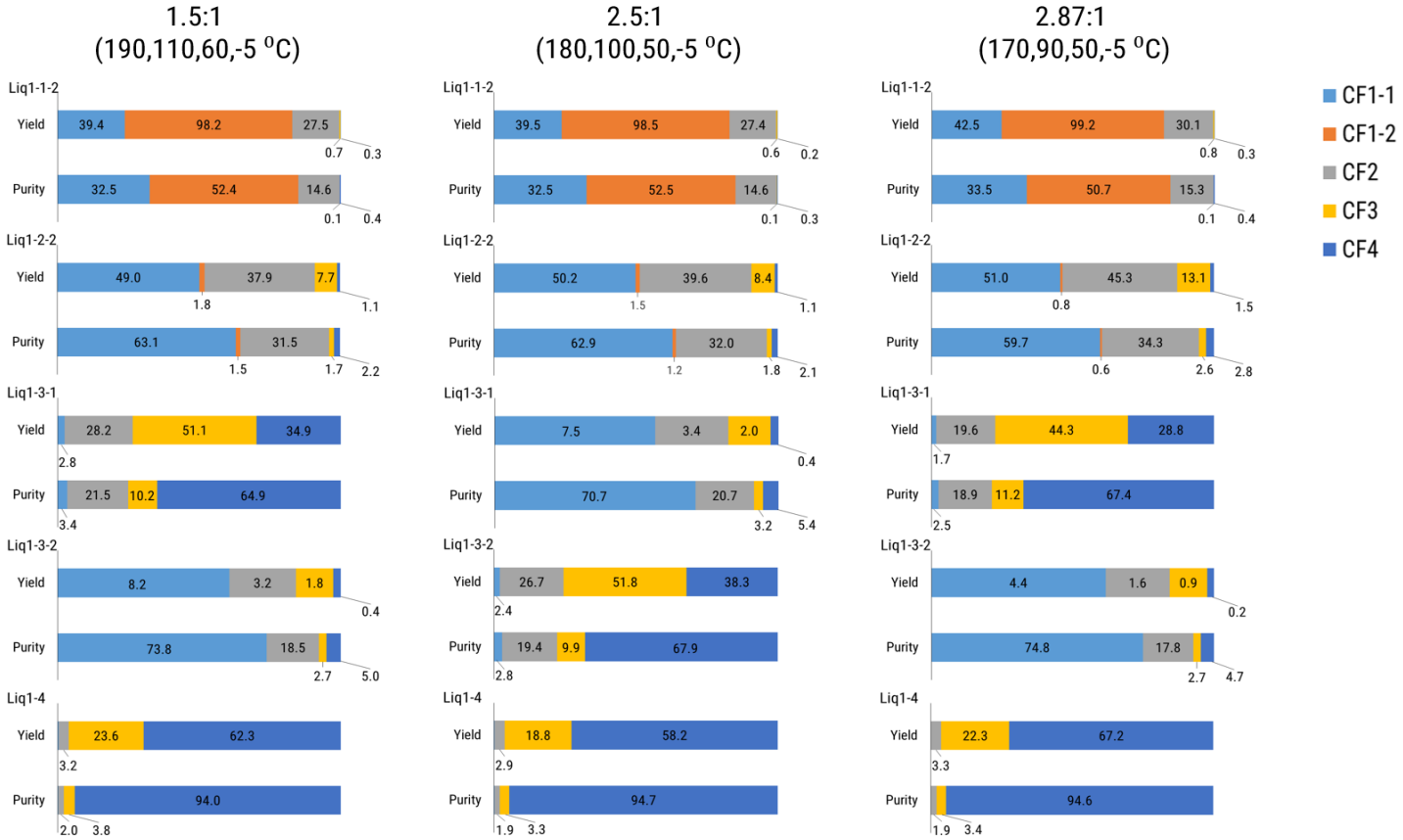

Figure 6.11: Scheme 1 yield and purity of chemical families under optimal operating conditions for different mass ratios of NCG: condensible components

On the other hand, when the operating conditions are kept constant and the NCG ratio is varied (Table 6.5), yields of components having boiling points less than 132°C (acetol) are affected significantly. The saturation temperature vs. saturation pressure curves are exponential in nature [18] and if the saturation pressure falls below a limit, a small change in saturation pressure, the saturation temperature decreases drastically. Therefore, the yield of water, acids and acetol decreases in condenser 3 for NCG: condensible ratio of 2.87. However, yield of compounds like cresols in the first condenser is not significantly different, again proving that there is a strong interaction between cresols and chemical family 1-1 and 1-2.

6.3.2.2 Fractional condensation of pyrolysis vapors: Scheme 2

Increase in the non-condensible gas content improves the separation ability between chemical families. However, increasing the non-condesible gas content would increase the cooling duty. Therefore, for scheme 2, indirect contact heat exchangers were replaced with spray towers using water as a cooling medium. The flow rate and temperature of cooling water was maintained so that water evaporated completely, cooling the pyrolysis vapors in the two spray towers. Evaporated water decreases the bubble point of the vapor exiting the spray towers. The vapor and liquid streams exiting the spray towers have different temperatures. The different liquid and vapor temperatures, along with the increase in mole fraction of water in the vapor phase improves the separation ability of the chemical families.

The conditions for scheme 2 were optimized using the separation factors of chemical families as done for scheme 1. Figure 6.12 shows the effect of NCG: condensible ratio on the separability of bio-oil components along with the optimal conditions for each case. The yield and purity of the chemical families represented in the figure is on water-free basis. Direct contact counter-current cooling in the tower resembled a stripping section of distillation column, where, downward moving liquid, formed at the top of the spray tower, was reheated by the pyrolysis gas traveling upwards. The reheating led to evaporation of some low boiling components and condensation of high boiling components from the vapor.

Table 6.5: Effect of NCG: Condensible mass ratio on yield of each bio-oil model component

	Scheme 1									
Component	Yield (wt.%) for NCG: Condensibles mass ratio 1.5					Yield (wt.%) for NCG: Condensibles mass ratio 2.87				
	Cond 1 (190°C)	Cond 2 (110°C)	Cond 3 (60°C)		Cond 4 (-5°C)	Cond 1 (190°C)	Cond 2 (110°C)	Cond 3 (60°C)		Cond 4 (-5°C)
Water	0.15	0.42	29.21	0.08	68.83	0.09	0.23	2.44	3.91	90.87
Formic Acid	0.43	0.71	33.06	0.22	64.73	0.25	0.37	3.48	2.30	91.95
Acetic Acid	0.64	2.77	52.07	1.05	43.05	0.37	1.53	13.46	5.65	77.88
Propionic acid	0.89	4.37	52.41	1.88	40.03	0.51	2.42	19.38	5.23	71.40
Acetol	0.83	8.25	71.51	0.86	18.49	0.45	4.18	44.95	8.69	41.57
Glyoxal	0.08	0.23	2.98	0.07	38.86	0.04	0.12	0.67	0.36	32.89
Glycol aldehyde	0.97	11.52	76.85	0.99	9.66	0.52	6.11	45.37	25.93	22.05
Gamma Butyrolactone	3.00	34.72	39.25	10.54	12.37	1.63	21.40	52.79	4.87	19.11
Furfural	0.82	9.12	37.22	6.73	45.51	0.44	4.74	35.56	5.35	53.07
Furfuryl alcohol	0.94	15.84	55.86	9.00	18.30	0.51	8.63	48.52	7.31	34.89
o-Cresol	58.71	17.06	24.23	0.00	0.00	52.42	14.63	1.32	31.63	0.00
p-Cresol	66.17	18.79	13.72	1.04	0.29	59.98	17.40	21.20	0.80	0.60
2,4-Xylenol	56.46	27.02	14.54	1.71	0.27	48.59	24.95	25.69	0.45	0.32
Guaiacol	2.26	27.42	68.04	1.17	1.11	1.24	15.68	62.98	13.03	7.07
4-methyl Guaiacol	2.24	47.57	48.17	1.60	0.41	1.16	30.97	57.89	7.54	2.43
iso-Eugenol	7.29	83.08	8.62	0.99	0.02	3.84	76.93	17.94	1.23	0.07
Vanillin	18.93	76.00	5.05	0.02	0.00	11.24	77.62	8.22	2.91	0.01
Syringol	5.47	76.64	17.74	0.14	0.01	2.90	64.46	24.62	7.91	0.10
1,2-Benzenediol	32.11	46.51	21.33	0.04	0.01	22.08	41.21	27.69	8.69	0.33
trans-3,5-dimethoxystilbene	70.02	29.97	0.00	0.01	0.00	53.65	46.29	0.05	0.00	0.00
1,2-diphenyl ethane	1.95	71.44	0.43	24.49	0.52	0.97	56.75	39.05	0.18	1.28
diBenzofuran	9.72	74.83	10.28	4.96	0.22	5.46	66.29	26.48	1.25	0.52
High molecular weight lignin-2	100.00	0.00	0.00	0.00	0.00	100.00	0.00	0.00	0.00	0.00
High molecular weight lignin-1	100.00	0.00	0.00	0.00	0.00	100.00	0.00	0.00	0.00	0.00
Xylose	93.19	6.81	0.00	0.00	0.00	87.38	12.61	0.00	0.01	0.00
Levoglucosan	98.58	1.42	0.00	0.00	0.00	97.19	2.81	0.00	0.00	0.00
Cellobiose	100.00	0.00	0.00	0.00	0.00	100.00	0.00	0.00	0.00	0.00
Dehydroabietic acid	27.85	71.95	0.00	0.19	0.00	15.79	83.72	0.49	0.00	0.00

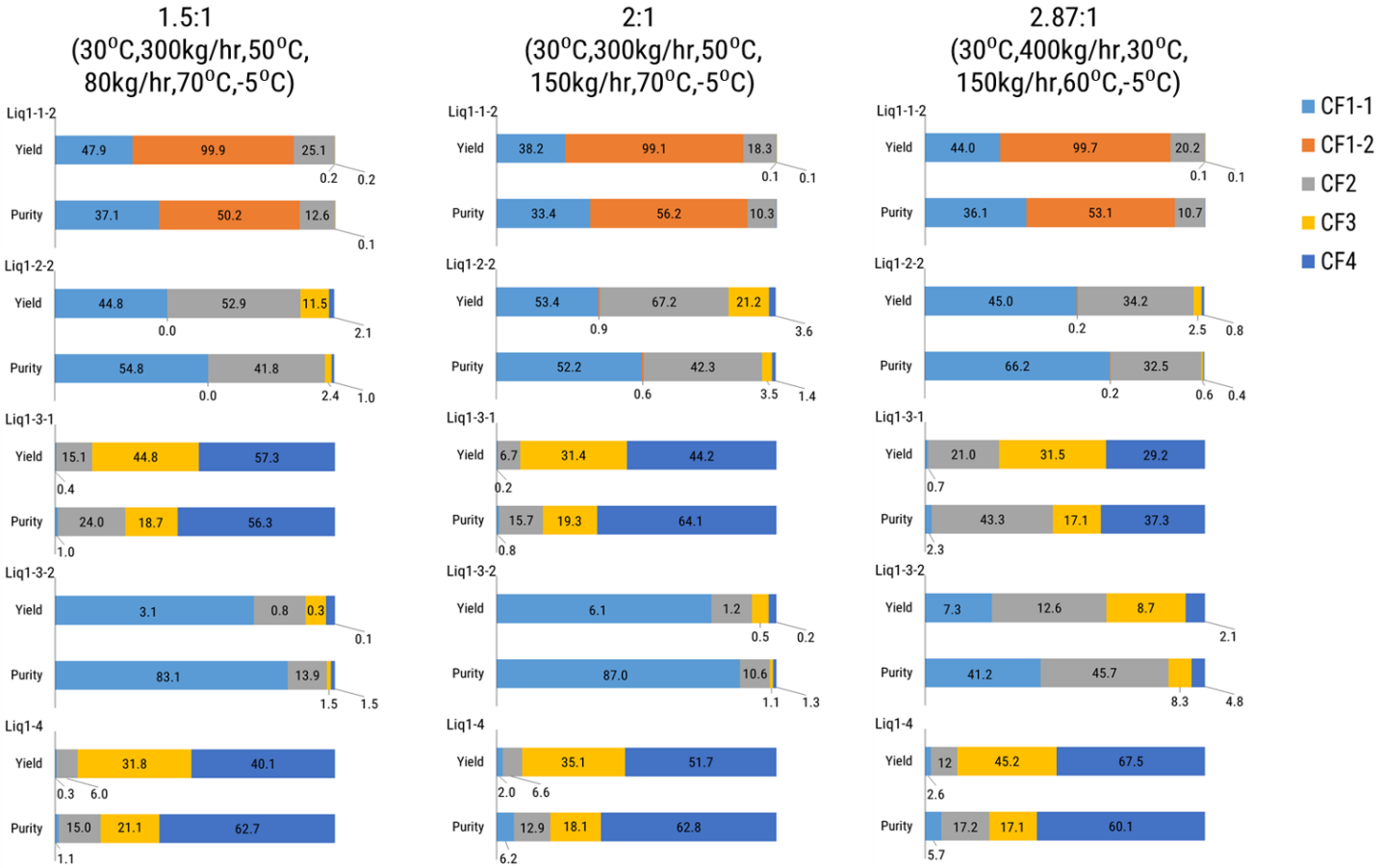

Figure 6.12: Scheme 2 yield and purity of chemical families under optimal operating conditions

For an NCG: condensible ratio of 2.87, the liquid stream from the first condenser exited at 250°C and the vapor stream at 144°C. The low temperature at the top of the tower was a result of water evaporation which caused condensation of chemical family 1-1 and 1-2 components. As the liquid descended along the column, it was stripped of chemical family 2 components (except alkyl phenols). For condenser 2, liquid stream exited at 96°C and vapor at 74°C. The liquid in second condenser was stripped of chemical family 3, which was present in significant quantities in condenser 2 for scheme 1. Figure 6.13 shows the distribution of chemical functionalities in different condensers for scheme 1 and scheme 2. Thus, the use of direct contact heat exchanger improves the separation amongst the chemical families as compared to indirect contact heat exchangers.

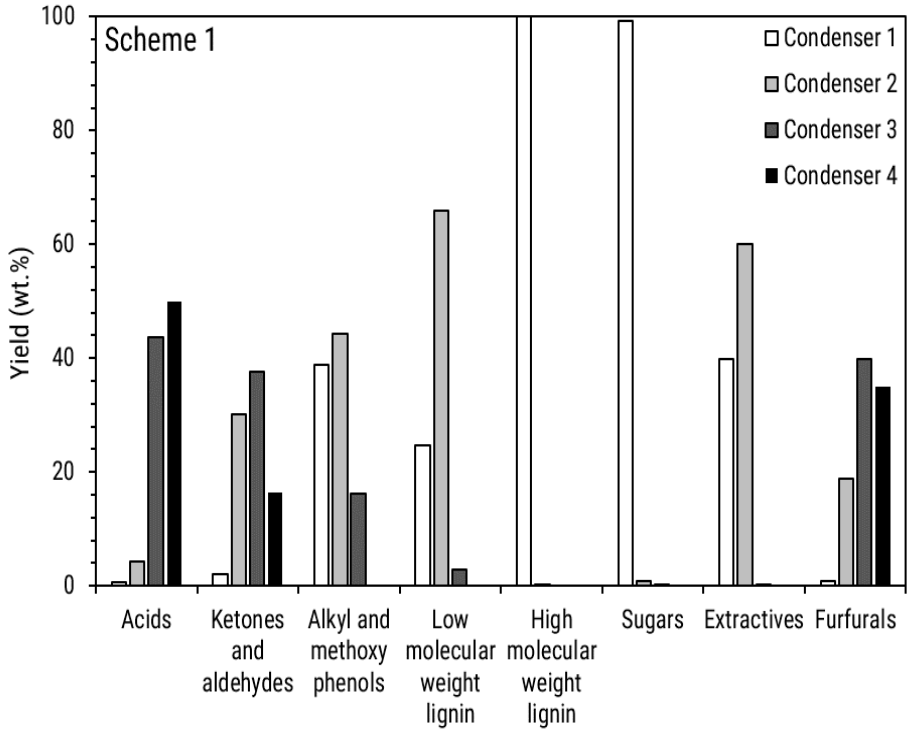

(a)

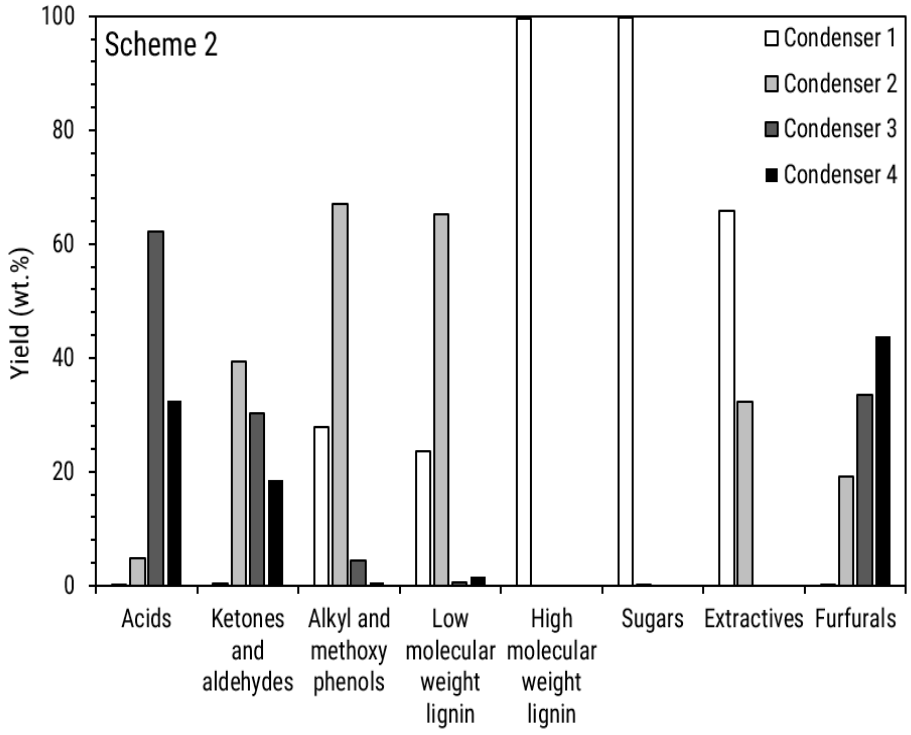

(b)

Figure 6.13: Comparison of scheme 1 and scheme 2 for chemical family yields in each condenser.

To test if cooling medium has any effect on the selective condensation of any component, water was replaced by toluene. Toluene flow rate and temperature were adjusted so that temperature of the liquid and vapor stream exiting the column were same when water was used as a cooling medium. Toluene did not have any effect on the selective condensation of any component in condenser 1. However, in condenser 2, the yield of propionic acid, butyrolactone, furfural, furfuryl alcohol and 1,2-diphenylethane increased approximately 2.2 ± 0.7 folds while that of acetol and glycoldehyde decreased by 0.6 ± 0.05 fold. Compared to pyrolysis oil components, significant amount of toluene was condensed in stage 2 which therefore, affected condensation selectivity of several compounds. Thus, in case of a direct contact heat exchanger, the liquid and vapor composition is affected by their respective exit temperatures. If the cooling medium condenses, it can affect the distribution of compounds in the vapor and liquid phase.

The energy required to condense 1 kg of bio-oil (on water free basis), using scheme 1, for NCG: condensible ratio of 2.87, 2.5 and 1.5 was 5.91, 5.59, and 4.65 MJ/kg-bio-oil respectively. Using scheme 2 the energy requirement for NCG: condensible ratio of 2.87, 2 and 1.5 was 5.93, 5.15, and 4.71 MJ/kg-bio-oil respectively. Energy required to cool the liquid to 25°C was also considered for calculation. The energy consumption increases linearly with respect to non-condensible gas content but there is no significant difference between energy requirement between two schemes. Though scheme 2 improves the separability between chemical families, but, the water content in the third and fourth stage increases, which can make recovery of acids and carbonyl compounds energy intensive.

Table 6.6: Liquid yield and purity of components for scheme 2 under optimized operating conditions for NCG: condensible ratio of 2.87

	Liquid Yield (Purity), wt.%				
Components	Cond 1	Cond 2	Cond 3		Cond 4
Formic Acid	0.09(0)	0.96(0.01)	54.09(1.45)	0.02(0)	44.25(2.08)
Acetic Acid	0.1(0.03)	4.5(1.54)	63.45(55.69)	0.18(0.75)	31.54(48.44)
Propionic acid	0.13(0.01)	6.84(0.45)	56.59(9.62)	0.41(0.34)	35.71(10.62)
Acetol	0.11(0)	28.37(1.62)	56.58(8.28)	0.08(0.06)	14.81(3.79)
Glyoxal	0.02(0)	0.31(0.01)	3.99(0.47)	0.01(0.01)	37.4(7.76)
Glycol aldehyde	0.12(0)	45.85(2.12)	48.04(5.7)	0.07(0.04)	5.91(1.23)
Gamma Butyrolactone	0.55(0.07)	52.42(8.65)	23.64(10.01)	4.92(10.12)	18.2(13.48)
Furfural	0.14(0)	12.75(0.18)	19.22(0.69)	2.28(0.4)	64.47(4.06)
Furfuryl alcohol	0.17(0)	25.68(0.36)	47.81(1.72)	3.32(0.58)	22.93(1.45)
o-Cresol	41.06(2.43)	58.9(4.45)	0.03(0.01)	0(0)	0(0)
p-Cresol	54.82(3.24)	39.3(2.97)	4.25(0.82)	0.49(0.46)	1.14(0.39)
2,4-Xylenol	48.63(4.25)	45.53(5.08)	3.92(1.12)	0.75(1.04)	1.16(0.58)
Guaiacol	0.49(0.03)	80.88(5.55)	17.59(3.1)	0.11(0.09)	0.93(0.29)
4-methyl Guaiacol	0.59(0.01)	93.17(1.7)	5.76(0.27)	0.15(0.03)	0.33(0.03)
iso-Eugenol	4.72(0.11)	95.08(2.76)	0.14(0.01)	0.02(0.01)	0(0)
Vanillin	9.07(0.1)	90.9(1.33)	0(0)	0(0)	0(0)
Syringol	1.76(0.11)	98.18(7.79)	0.05(0.01)	0(0)	0(0)
1,2-Benzenediol	11.77(0.36)	88.11(3.48)	0.11(0.01)	0(0)	0(0)
trans-3,5-dimethoxystilbene	94.82(12.98)	3.89(0.68)	0(0)	0(0)	0(0)
1,2-diphenyl ethane	0.58(0.13)	72.53(21.45)	0.01(0)	22.6(83.36)	4.26(5.65)
diBenzofuran	5.04(1.1)	92.59(25.72)	1.44(1.02)	0.78(2.69)	0.13(0.16)
High molecular weight lignin-2	99.16(9.39)	0(0)	0(0)	0(0)	0(0)
High molecular weight lignin-1	99.9(9.46)	0(0)	0(0)	0(0)	0(0)
Xylose	98.76(9.63)	1.19(0.15)	0(0)	0(0)	0(0)
Levoglucosan	99.93(22.48)	0.05(0.01)	0(0)	0(0)	0(0)
Cellobiose	100(21.02)	0(0)	0(0)	0(0)	0(0)
Dehydroabietic acid	65.83(3.06)	32.23(1.92)	0(0)	0.02(0.01)	0(0)

6.4 Summary

Biomass pyrolysis oil is a complex mixture of hundreds of chemical compounds, that pose a difficulty in simulating bio-oil separation processes. Therefore, bio-oil composition was represented using twenty-eight model compounds based on their abundance in bio-oil. The model compounds were classified into five chemical families. As the compounds are polar in nature it was important to test the accuracy of the phase equilibrium model used in simulations. Therefore, a literature reported multistage bio-oil collection system was simulated initially. The error between the experimental and predicted values for liquid phase composition of various chemical families in different liquid streams using NRTL-NTH and UNIQUAC-NTH phase equilibrium models was $8.86 \pm 11.05\%$ and $9.90 \pm 12.38\%$ respectively. Further, variation of binary interaction parameters within a range of $\pm 40\%$ did not have a significant effect on the prediction ability of liquid composition. Thus, UNIQUAC and NRTL activity coefficient models coupled with NTH equation of state can be used to design bio-oil fractionation or collection systems with a fair degree of accuracy.

To address the bio-oil stability issue, two different condensation schemes were simulated to separate constituent chemical families from one another. A train of four indirect contact heat exchangers was simulated over a wide range of operating conditions with an objective to separate the chemical families from one another. Such a simplified and widely used bio-oil recovery approach was found unsuitable for fractionation of chemical families. Therefore, first two heat exchangers were replaced by direct contact cooling towers, where water was used as the cooling medium. The direct contact heat exchangers were similar to the stripping section of a distillation column. This led to increase in the recovery of phenols in the first two condensers while acids, aldehydes, ketones and furfurals condensed in stage 3 and stage 4. Moreover, the energy requirement for both the schemes is the same. However, water content significantly increases in the liquid streams obtained from third and fourth stage, which can make recovery of organic components energy intensive. Also the modified condensation scheme could not effectively separate chemical family 3 and 4 from one another.

Chapter 7

Closure and future work

7.1 Closure

The present research focused on modeling and simulation of different biomass pyrolysis phenomena that occur over a wide range of length and time scales. Reaction kinetics and first principle bubbling fluidized bed reactor (BBR) models along with simulation strategies for pyrolysis vapor condensation were developed to understand various aspects of upstream and downstream operations in biomass pyrolysis process. Experiments were carried out to understand and model weight loss kinetics of biomass under a wide range of pyrolysis conditions.

Yield and composition of pyrolysis products exiting a BBR depend on rate of pyrolysis reaction which in turn depends on operating temperature, heat and mass transfer rates, and residence time of solid and vapor phases. Further, bio-oil stability depends on liquid collection system succeeding the pyrolysis reactor. To understand the multi-scale nature and complex interaction between different processes in biomass pyrolysis a multi-layered approach was adopted.

Based on experimental findings of present work a multi-reaction single step kinetics was developed using distributed activation energy (DAE) approach. Literature studies limit themselves to using a narrow range of heating rate and particle sizes to determine kinetic parameters. Therefore, a systematic study was performed to study the effect of heating rate and particle size on the rate of pyrolysis reaction. Further, the findings of these experiments along with other literature reports were used to develop a detailed lumped kinetic model using DAE approach. The

detailed lumped model is capable of predicting the composition of major bio-oil and gas components as against a lumped model which gives global vapor and solid yields. At reactor scale different hydrodynamic parameters affect the reactor's performance (gas, liquid, and solid yield and composition). Mixing characteristics of a reactor influence the gas-solid heat and mass transfer coefficients, which affect the selectivity of devolatilization and char forming reactions in biomass particle. Also, long gas residence time leads to secondary reactions reducing the liquid yield. An extensible 1-D BBR reactor model was developed to assess the performance of kinetics developed in the present study. The reactor model uses a rigorous secondary reaction mechanism to simulate gas the phase reactions of biomass pyrolysis. The reactor scale model gives global yields of gas, liquid, and solid products along with composition of liquid and gas products. Based on the major components of bio-oil, liquid collection schemes were simulated to fractionally condense bio-oil into distinct chemical families. The simulations were carried out over a wide range of operating conditions. Sensitivity analysis of feed composition was conducted to understand its effect on condensation behavior of different chemical families. Following paragraphs describe the outcomes of the present work in these three areas of biomass pyrolysis.

1. Experimental findings of biomass (Mallee wood and bark) pyrolysis

    (a) Studied the effect of heating rate on changes in morphology of biomass particle.

    (b) Increase in heating rate caused the biomass particle to soften and led to formation of bubbles on the particle surface.

    (c) The partial melting is attributed to increase in selectivity for deploymerization reactions over char forming reactions.

    (d) Morphological changes that occur beyond heating rate of 75°C/min, affect the rate of biomass volatilization.

    (e) The uneven shift in the mass loss profile of biomass is attributed to changes in the pores structure of biomass particle.

    (f) The study demonstrates that the choice of heating rate to determine biomass pyrolysis reaction kinetics is vital.

2. Kinetic modeling of biomass pyrolysis

   (a) Developed a multi-reaction single step and detailed lumped kinetic model based on the DAE approach.

   (b) For heating rates where softening or partial melting of biomass particle was dominant, an increase in the frequency factor was observed for the single step lumped model.

   (c) This finding led to incorporation of correction factor dependent on heating rate for the detailed lumped model.

   (d) The effect of qualitatively observed morphological changes were translated quantitatively in the reaction kinetics using the correction factor.

   (e) Coupling of detailed lumped kinetic model and DAE approach caused substantial improvement in prediction of biomass pyrolysis reaction rate.

   (f) DAE coupled detailed lumped model also incorporates prediction of additional monomeric lignin components.

Chapter 3 outlines the impact of heating rate and particle size on biomass morphology, pyrolysis kinetics, and highlights the importance of selection of experimental conditions on kinetic model parameters. The results show that extrapolation of TGA derived kinetics to large scale fast pyrolysis reactors is feasible if TGA experiments are carried out such that biomass particles (correctly representing length scale of pore structure) experiences similar conditions as those within the reactor. Compared to slow pyrolysis the reaction selectivity and physical changes in biomass particles are completely different under fast pyrolysis conditions. The plasticity elicited in biomass particles undergoing pyrolysis can be used as an indicator for increased selectivity of depolymerization and volatilization reactions over cross-linking/ char forming reactions. Moreover, partial melting or softening of biomass particle, observed under fast pyrolysis conditions, increases molecular mobility and also causes bubble formation, which results in open pore structure. Significant plasticity was induced in biomass particles at

heating rates of 200 and 250 °C/min. It implies that kinetic parameters derived using the mass loss data obtained at these heating rates could be extrapolated to fast pyrolysis. The DAEM is valid over a wide range of heating rates and it is also capable of quantifying the effect of molecular heterogeneity in solids and in-situ physical changes on pyrolysis reaction kinetics using a probabilistic distribution of activation energy.

Chapter 4 couples the DAE modeling strategy with literature reported detailed pyrolysis kinetics. The coupling extends the applicability of model to wide range of heating rates and takes into account the effect of biomass plasticity on reaction rates. As ash has a significant effect on biomass plasticity and reaction selectivity, the model parameters are derived for biomass with ash content < 1 and > 1 wt.%. The model additionally highlights that biomass undergoes considerable mass loss as its temperature rises to the reactor temperature. Thus, the consideration of mass loss in dynamic temperature is important to determine accurate kinetic parameters. This justifies the employment of TGA for determining the pyrolysis kinetic parameters.

3. Reaction engineering model of bubbling fluidized bed reactor for biomass pyrolysis

   (a) Developed an extensible reaction engineering model of bubbling fluidized bed reactor using a mixing cell framework.

   (b) The BBR model was used to simulate biomass pyrolysis using rigorous primary (developed in the present study) and secondary reaction kinetics.

   (c) The DAE coupled detailed lumped model performs better than the model reported in literature when global yields of gas, liquid, and solid products were compared.

Chapter 5 tests the primary reaction kinetic model developed in Chapter 4 and compares its performance with that reported in the literature at the reactor scale. The improved kinetic model performs better than the one in the literature at all, especially low, temperatures. Thus, considering pyrolysis behavior of biomass particles while they experience temperature rise

in the reactor is vital for determining kinetic model parameters. Also, the results show that consideration of DAEM to account for the effect of plasticity on reaction rate is vital for accurate prediction of yield and composition of pyrolysis liquid, gas, and solid. The reactor model, with certain modifications, can be used to design large scale pyrolysis reactors capable of handling different kinds of biomass.

4. Fractional condensation of biomass pyrolysis vapors

   (a) Simulated pyrolysis vapor condensation schemes over a wide range of operating conditions using representative model compounds.

   (b) A literature reported multistage bio-oil collection system was initially simulated to test the accuracy of the phase equilibrium model used in simulations. Predictions using UNIQUAC-NTH and NRTL-NTH models showed good agreement with the literature experiments.

   (c) The simulation strategy can be used to design collection systems for biomass pyrolysis vapors.

   (d) A train of standard indirect contact heat exchangers was found unsuitable for fractionation of chemical families.

   (e) Use of water spray towers instead of indirect contact heat exchangers resulted in effective separation of phenols from aldehydes and ketones (most reactive components of bio-oil) without substantial increment in the energy requirement.

   Chapter 6 proposes simulation strategy to design downstream unit operations for pyrolysis plants and a scheme to fractionally condense pyrolysis vapors into distinct chemical families. The simulation strategy can be extended to pyrolysis vapors of different composition and the condensation scheme can be designed accordingly.

Commercial success of biomass fast pyrolysis process is hindered by variable biomass composition, the complex nature of pyrolysis chemistry, and bio-oil instability. Accurate modeling of reaction kinetics and determination of parameters is vital for reactor design. The thesis reports models for reaction kinetics, reactor, and

condensation systems. These multi-scale models can be coupled to design fast pyrolysis plants that use completely different biomass varieties to get bio-oil.
This research has helped understand various complex phenomena, which span over a wide range of length and time scales, of biomass pyrolysis process. However, there still persist many issues.

7.2 Future work

The effect of heating rate on biomass pyrolysis needs further exploration. Only one biomass type was used in this study. Morphological changes in biomass particle not only depend on heating rate but also on the biomass composition - cellulose, hemicellulose, lignin, and ash content. It will be interesting to determine the range of heating rate where morphological changes become significant for different biomass species. This may serve as a guide to define a new, composition dependent, variable to account for the effect of morphological changes on pyrolysis reaction kinetics. The effect of various ash constituents on distribution of biomass pyrolysis products needs to be incorporated in the reaction kinetics. Further, the detailed lumped kinetic model needs to be validated using detailed bio-oil composition. Adding more reactions to the detailed kinetic model using results from molecular simulations of cellulose, hemicellulose, and lignin pyrolysis may improve the prediction ability of bio-oil components.
The reactor model has been applied to a small pilot scale reactor. To improve its predictability computational fluid dynamics (CFD) can be used to accurately estimate the velocity profiles and volume fractions of different phases in the reactor. As biomass reacts, its physical properties change and so does its mixing behavior. It will be interesting to develop new correlations for estimating the hydrodynamic parameters for biomass pyrolysis reactors by simulating several reactor geometries using Lagrangian approach. Further, the reactor model can be coupled with a single particle model to extend the range of biomass particle size the model can handle.
Fractional condensation of pyrolysis vapors into distinct chemical families has potential to add value to bio-oil. Bio-oil is a complex liquid with organic and aque-

ous phases, which undergo separation depending on the composition of bio-oil. Moreover, high molecular weight tar compounds form a large fraction of bio-oil whose structure is not defined accurately. Thermodynamics of phase equilibrium for bio-oil is complex. Accurate experimentation to study the condensation behavior of bio-oil model compounds in the presence of one another is essential. Rigorous experimental validation of simulations will thus, help establish a robust strategy for designing downstream operations for commercial pyrolysis plants.

Appendix A

A.1 Appendix: Chapter 3

A.1.1 Experimental data

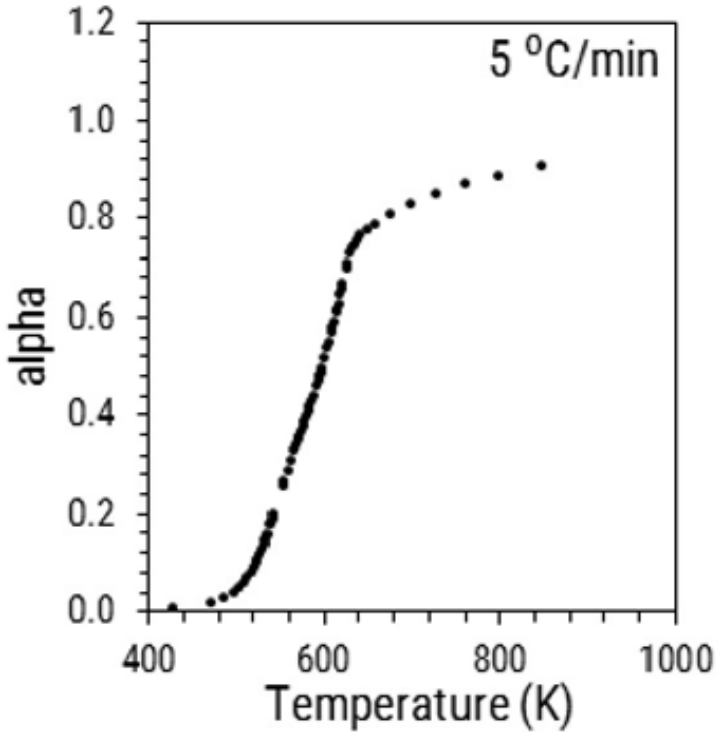

(a)

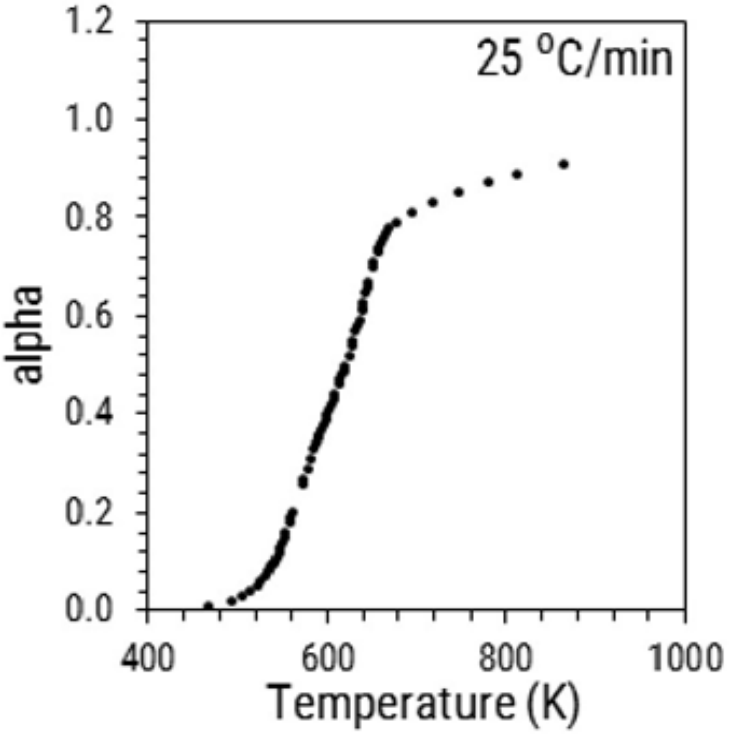

(b)

This figure is continued on the next page...

Figure A.1

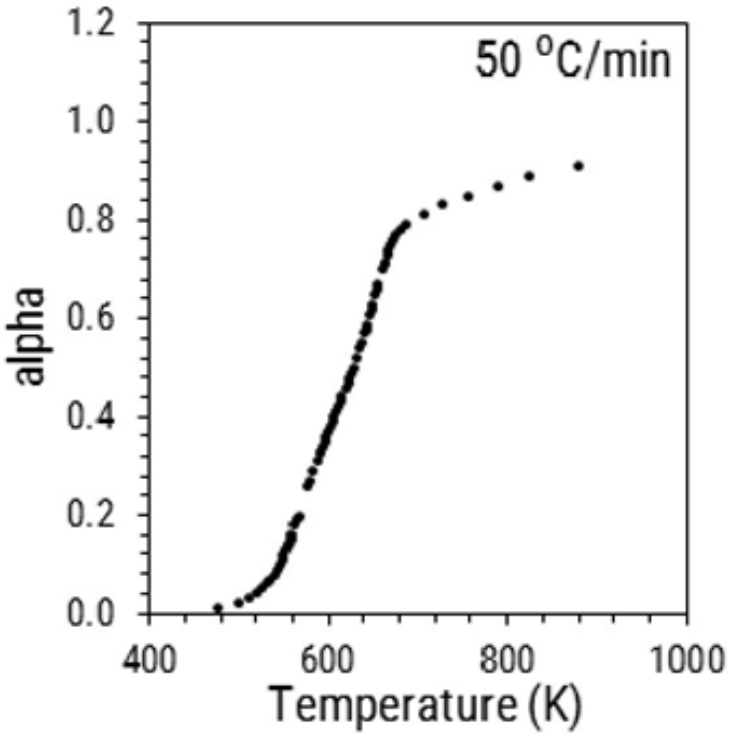

(a)

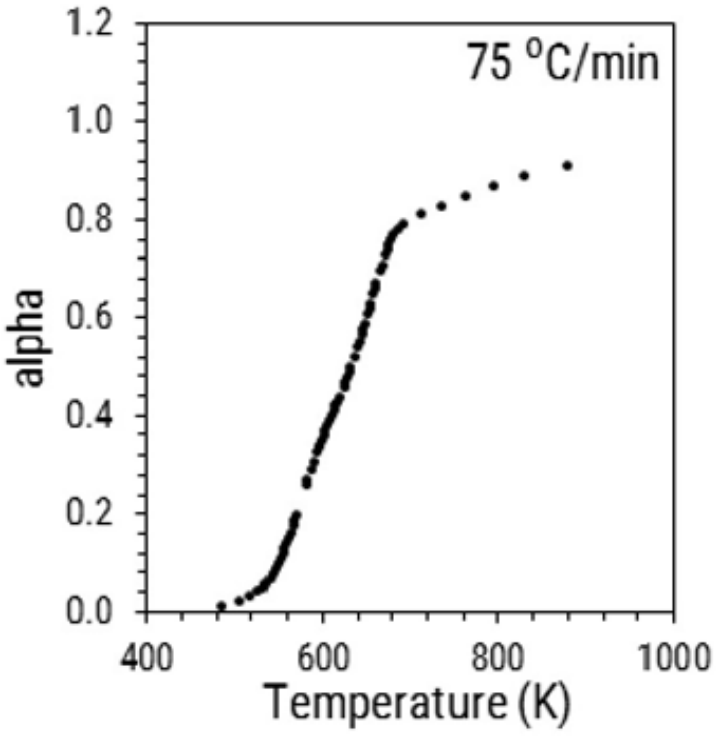

(b)

This figure is continued on the next page...

Figure A.1

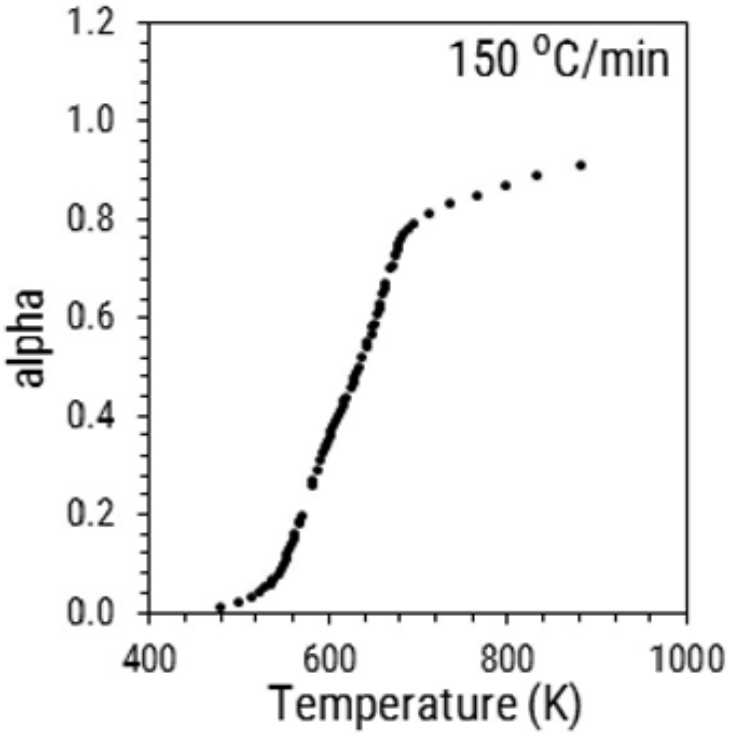

(c)

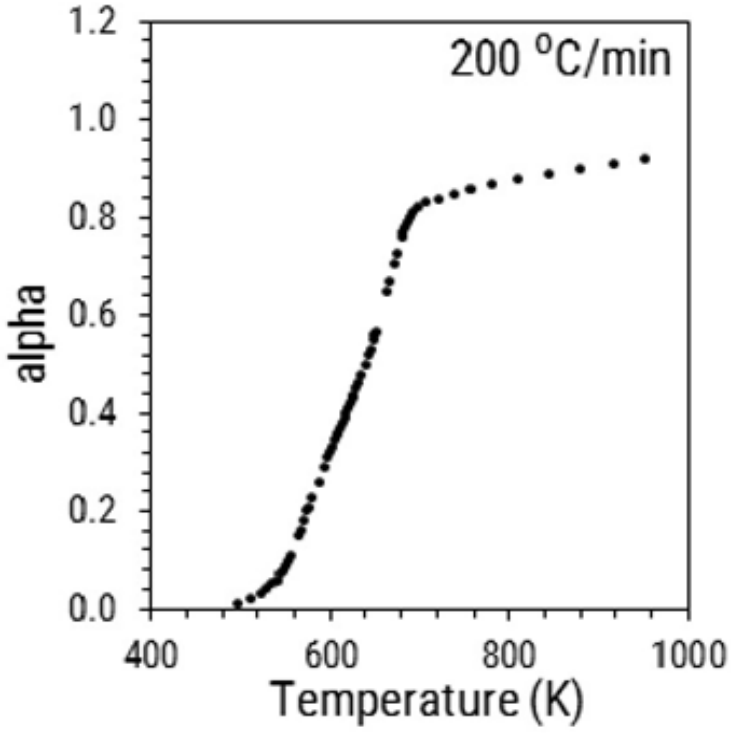

(d)

This figure is continued on the next page...

Figure A.1

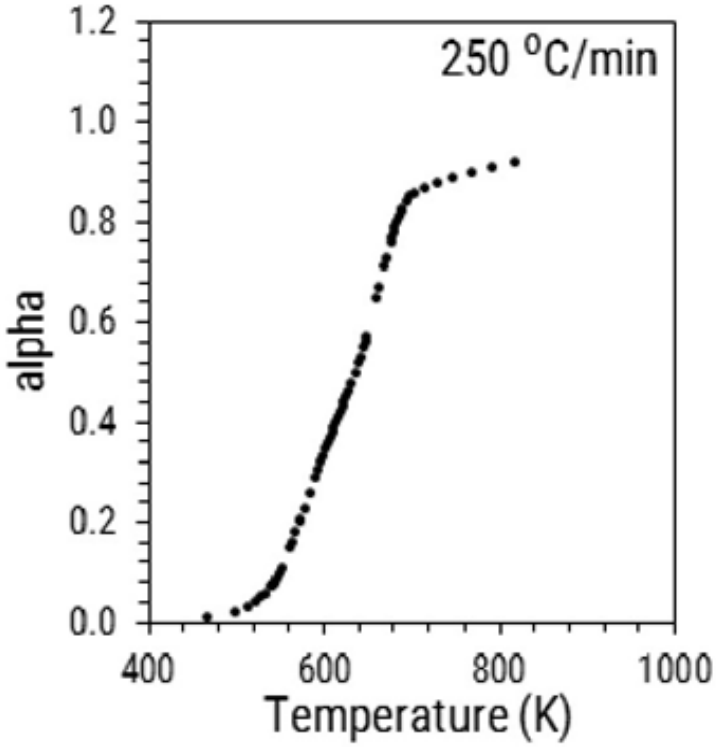

(e)

Figure A.1: Experimental values of α for biomass particle size less than 45 μm

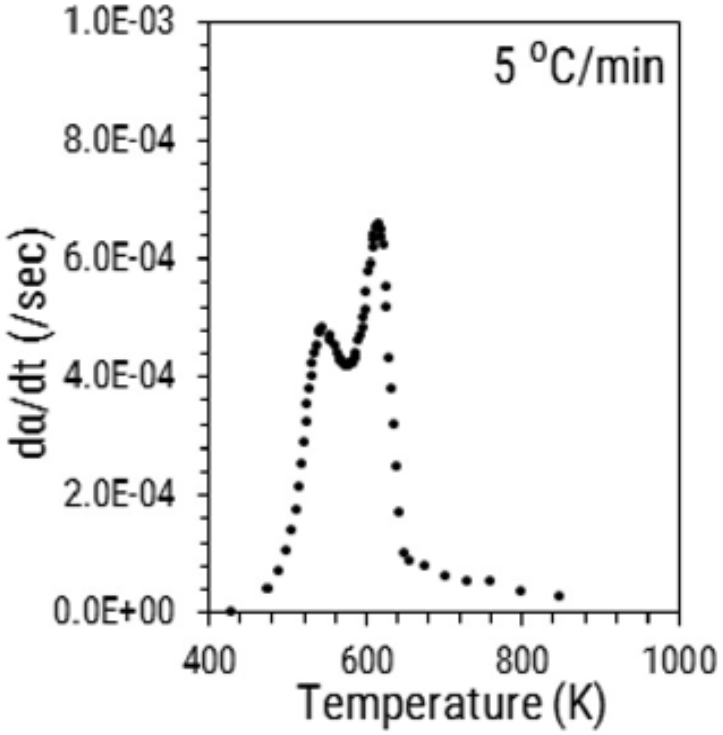

(f)

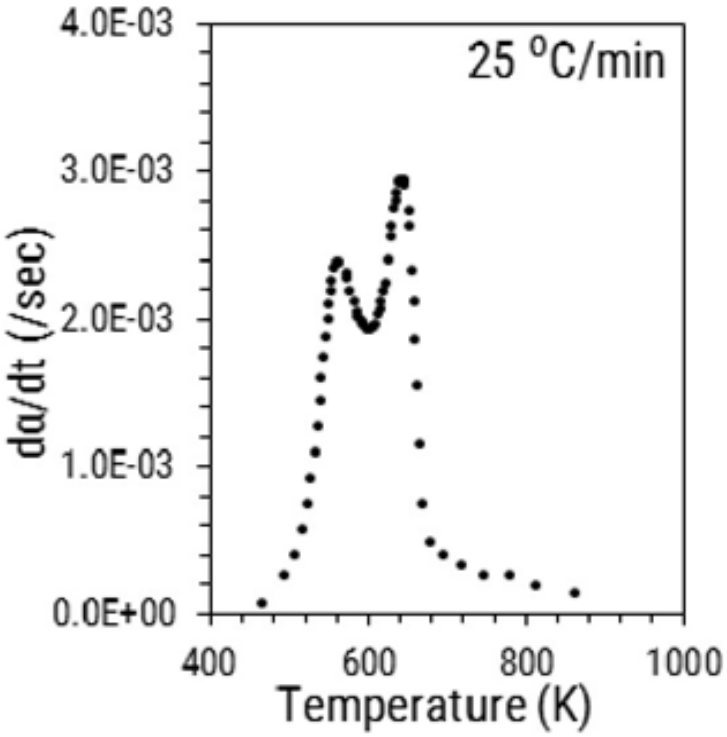

(g)

This figure is continued on the next page...

Figure A.2

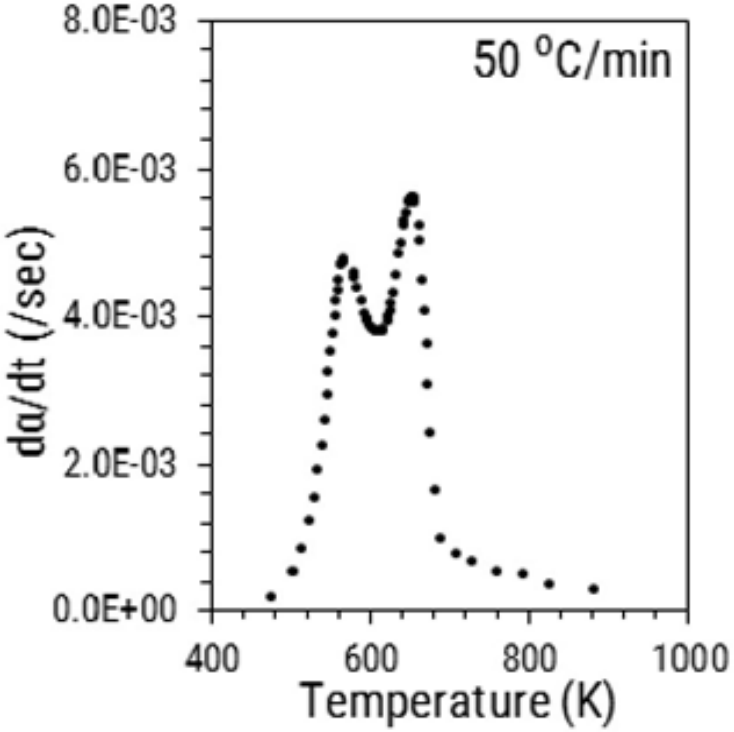

(a)

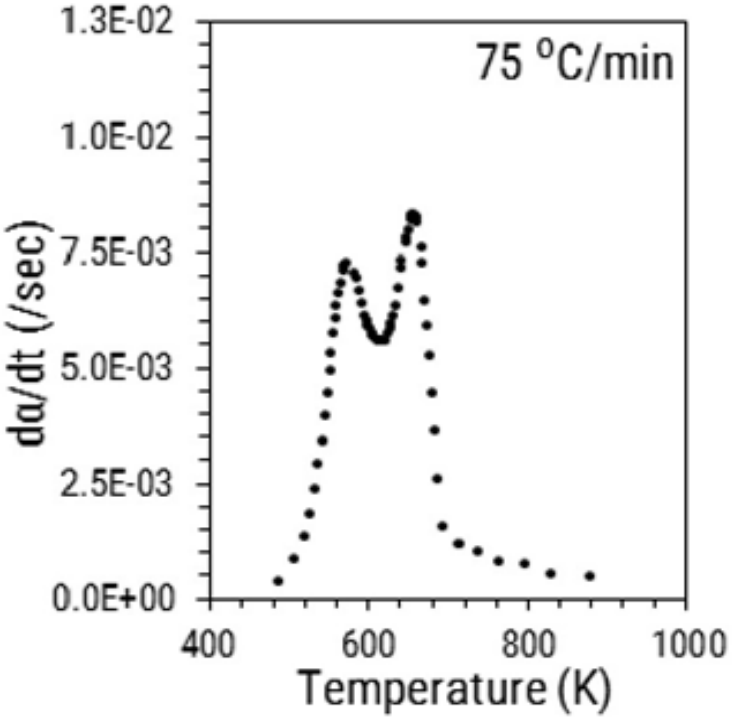

(b)

This figure is continued on the next page...

Figure A.2

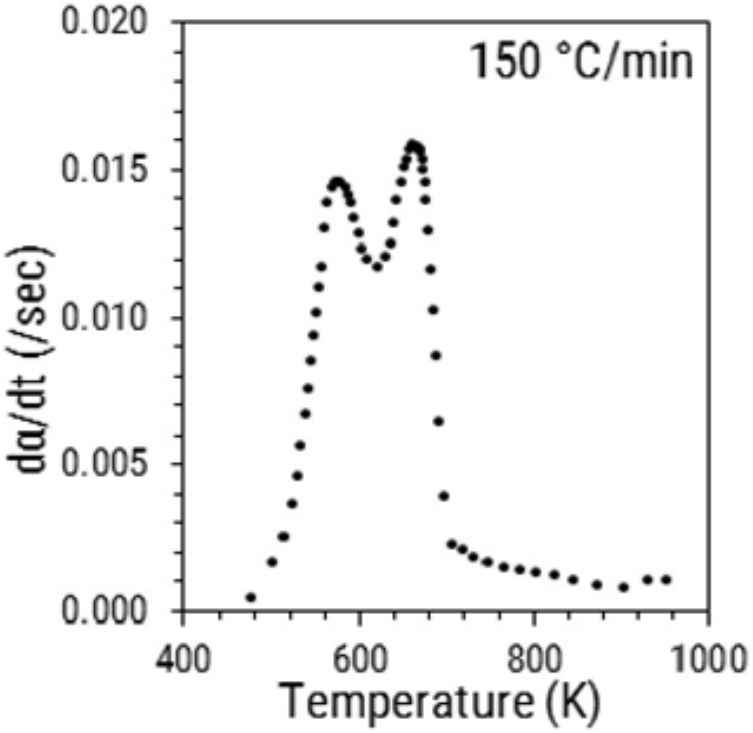

(c)

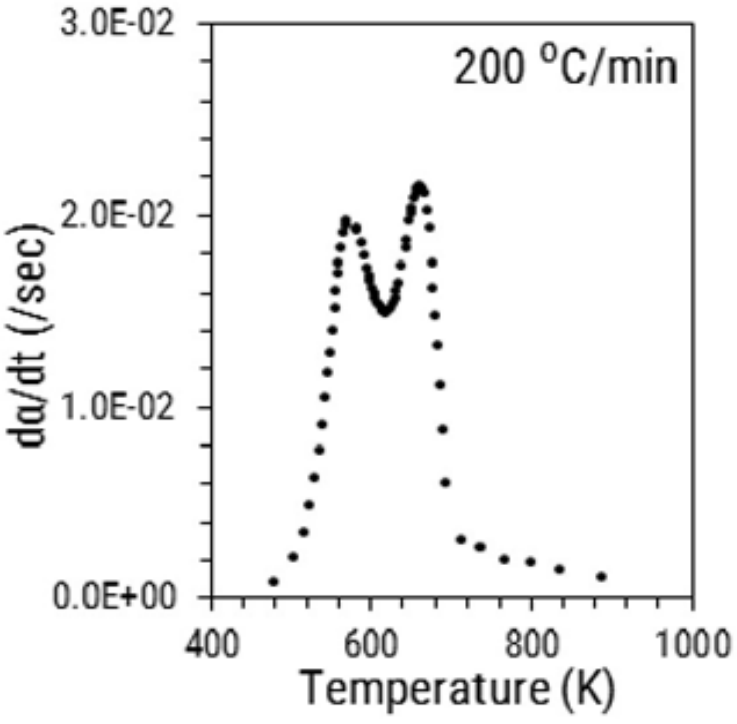

(d)

This figure is continued on the next page...

Figure A.2

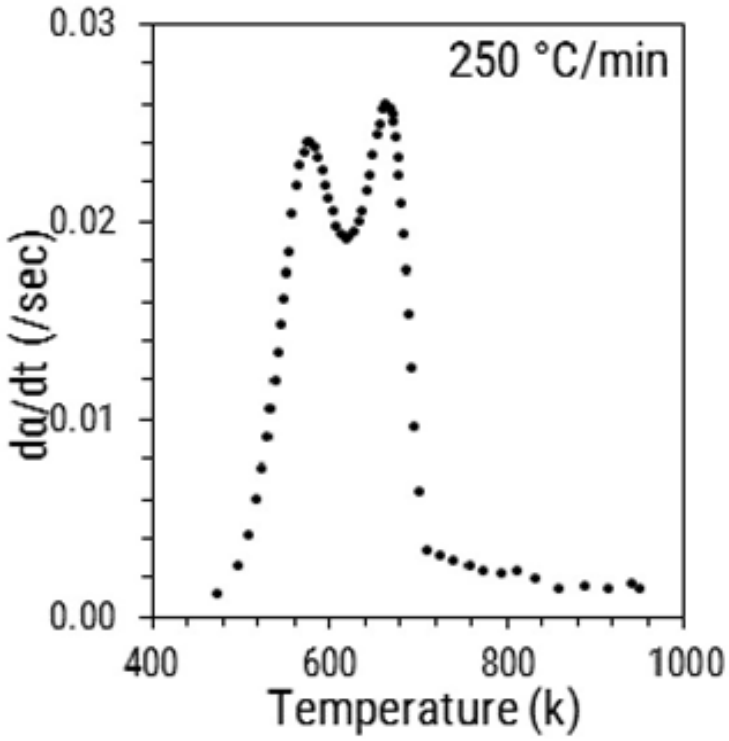

(e)

Figure A.2: Experimental values of dα/dt for biomass particle size less than 45 μm

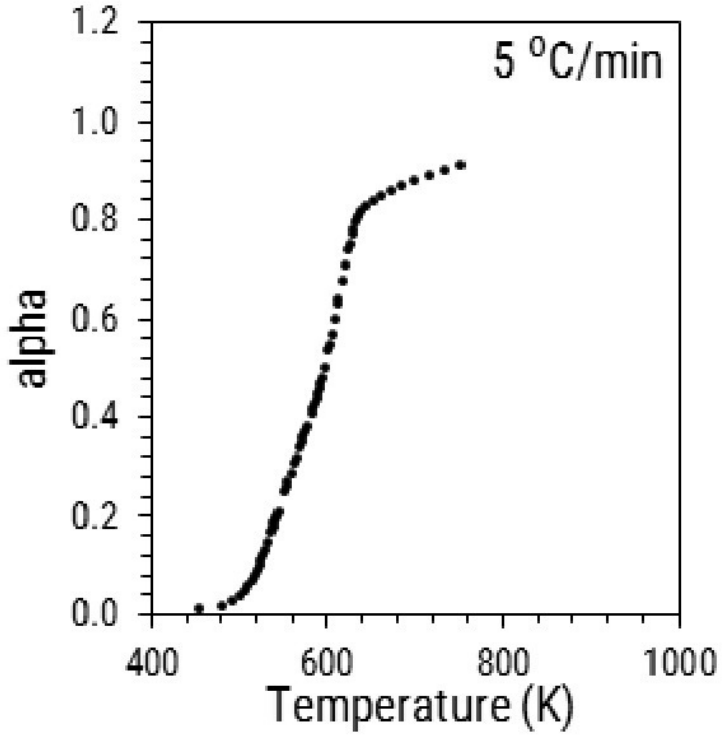

(f)

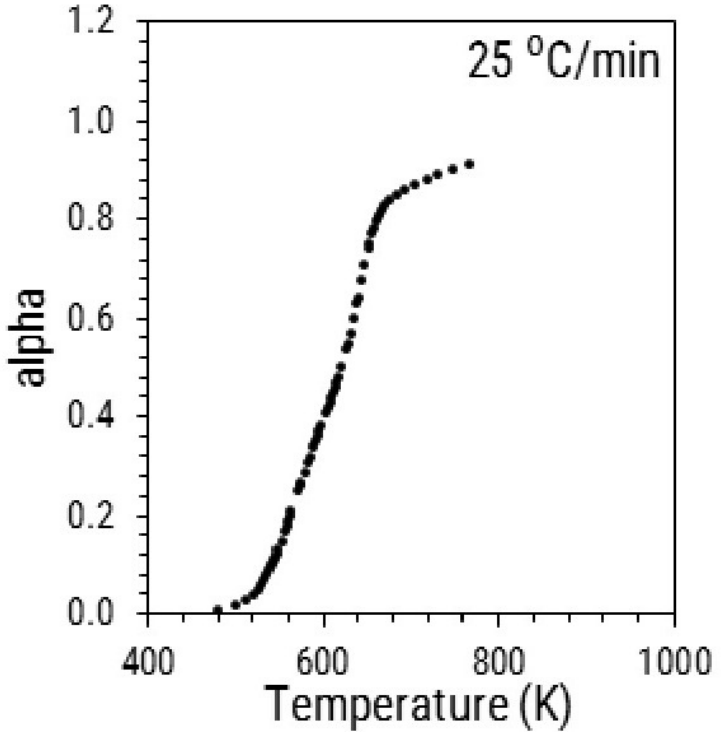

(g)

This figure is continued on the next page...

Figure A.3

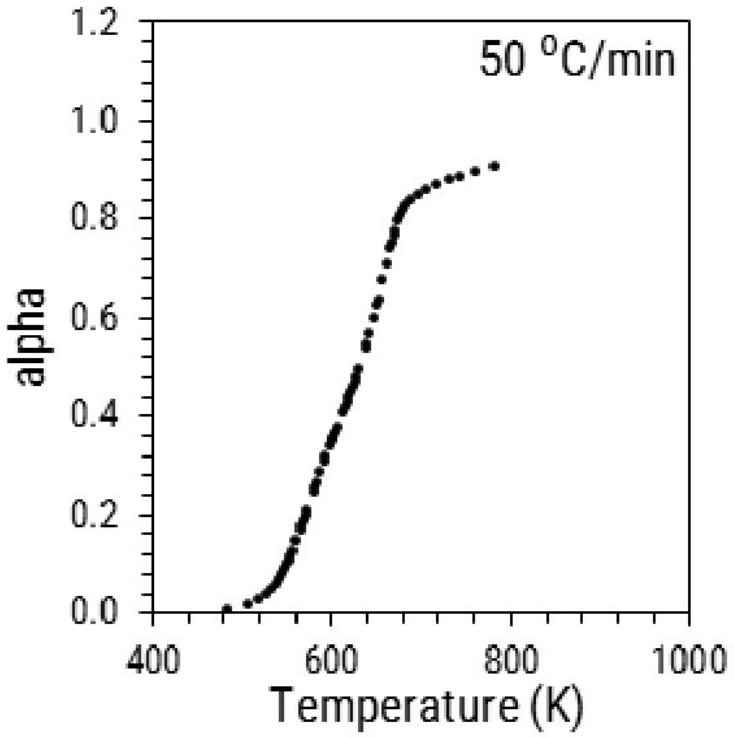

(a)

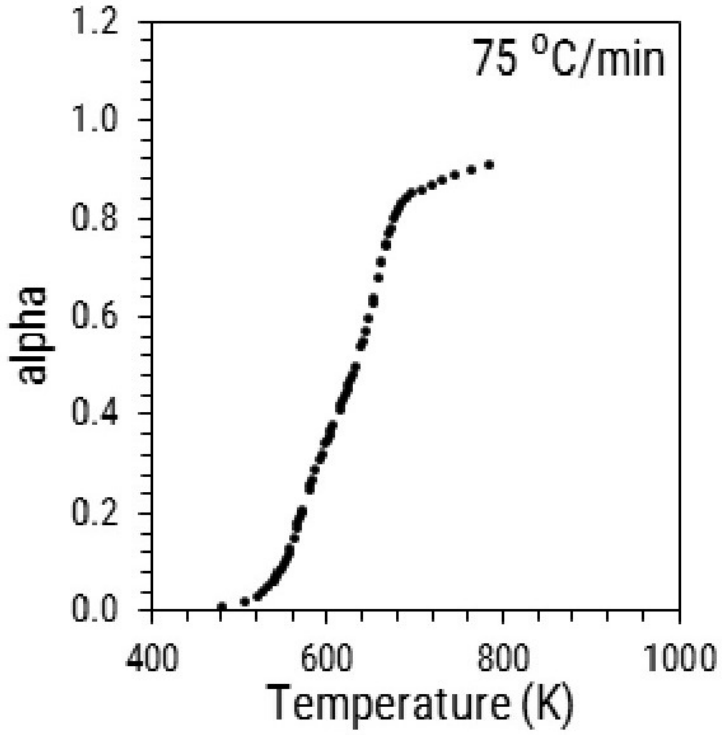

(b)

This figure is continued on the next page...

Figure A.3

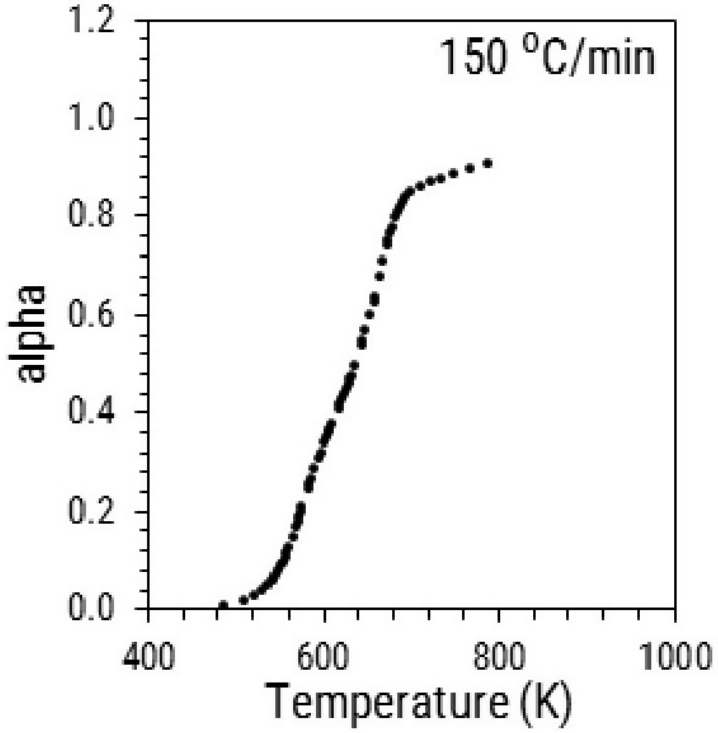

(c)

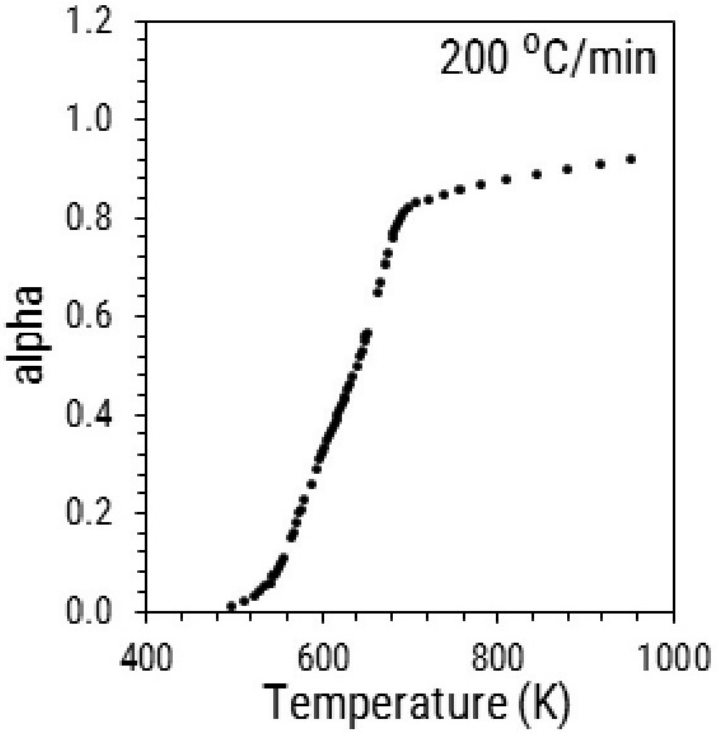

(d)

This figure is continued on the next page...

Figure A.3

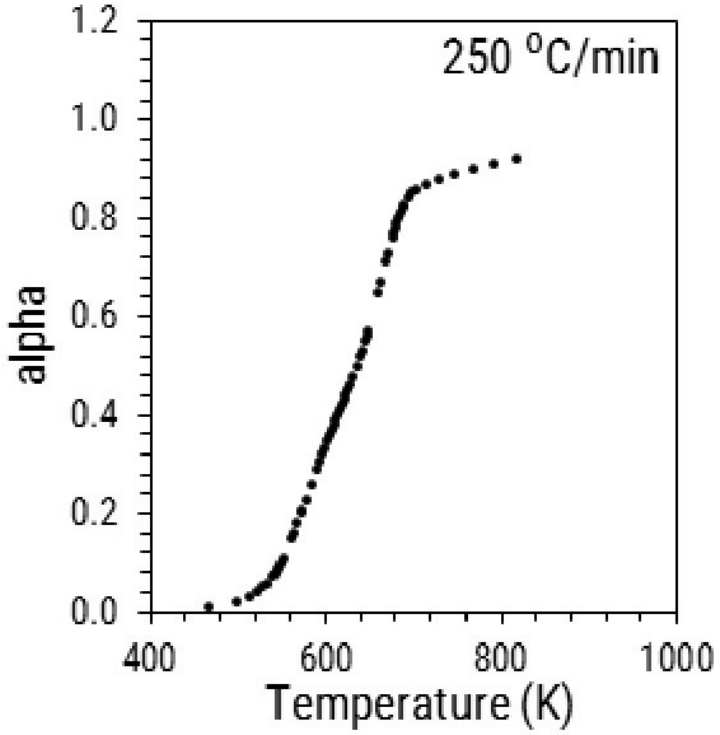

(e)

Figure A.3: Experimental values of α for biomass particle size between 75 to 106 μm

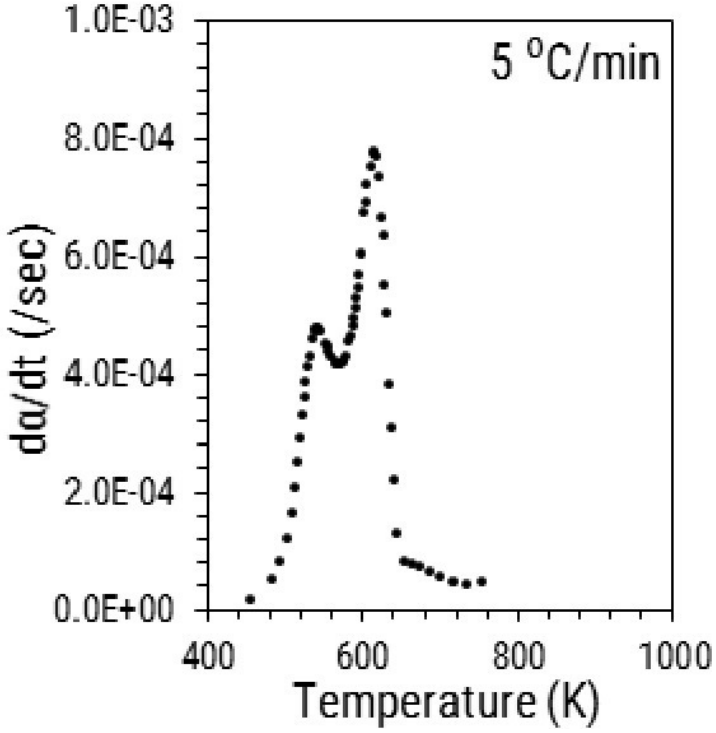

(f)

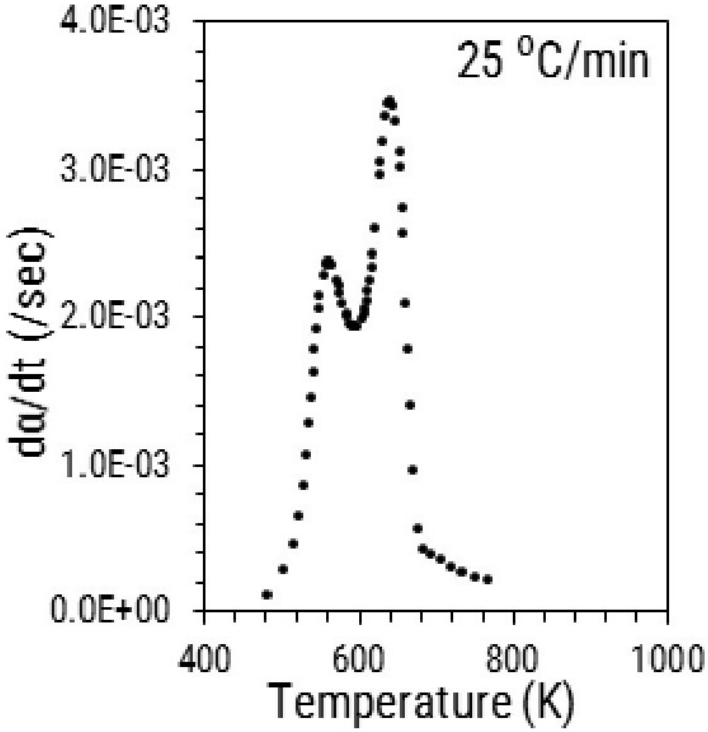

(g)

This figure is continued on the next page...

Figure A.4

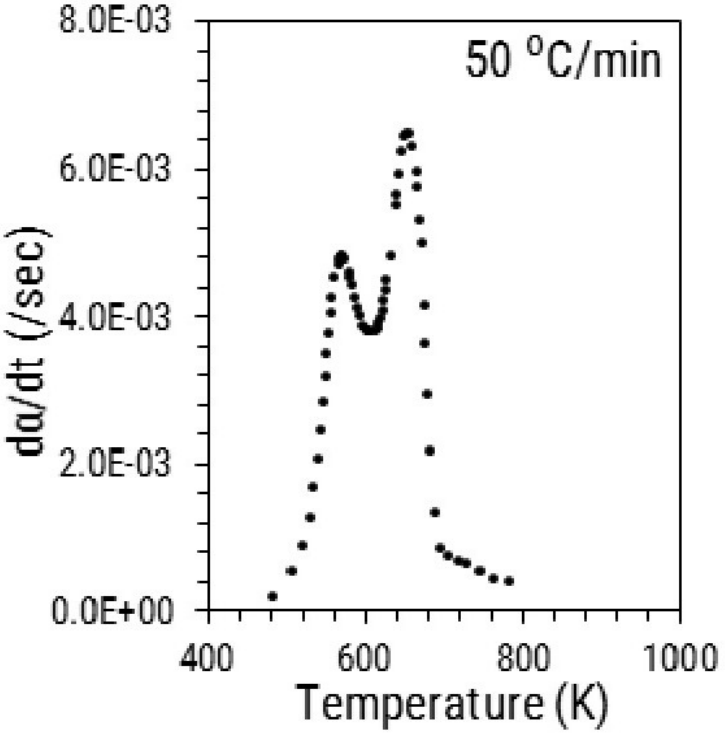

(a)

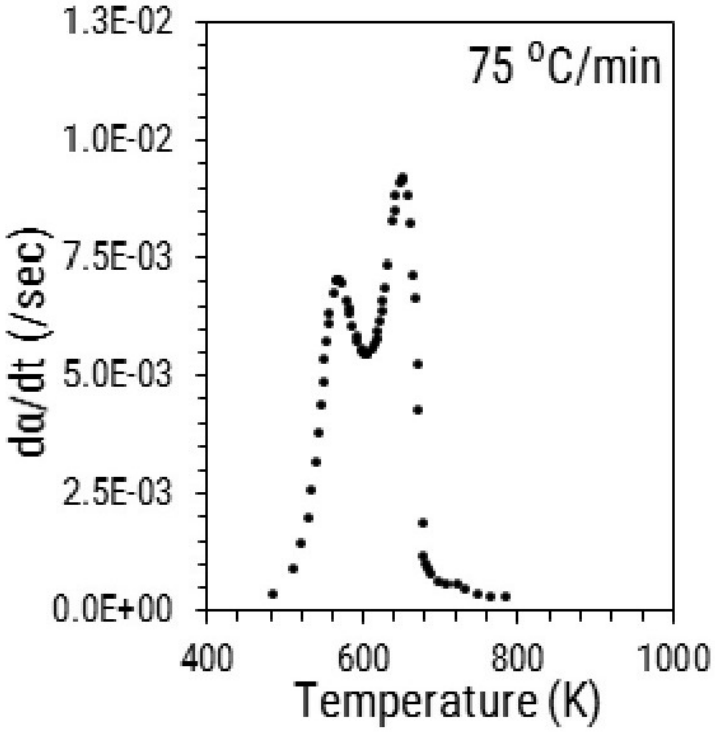

(b)

This figure is continued on the next page...

Figure A.4

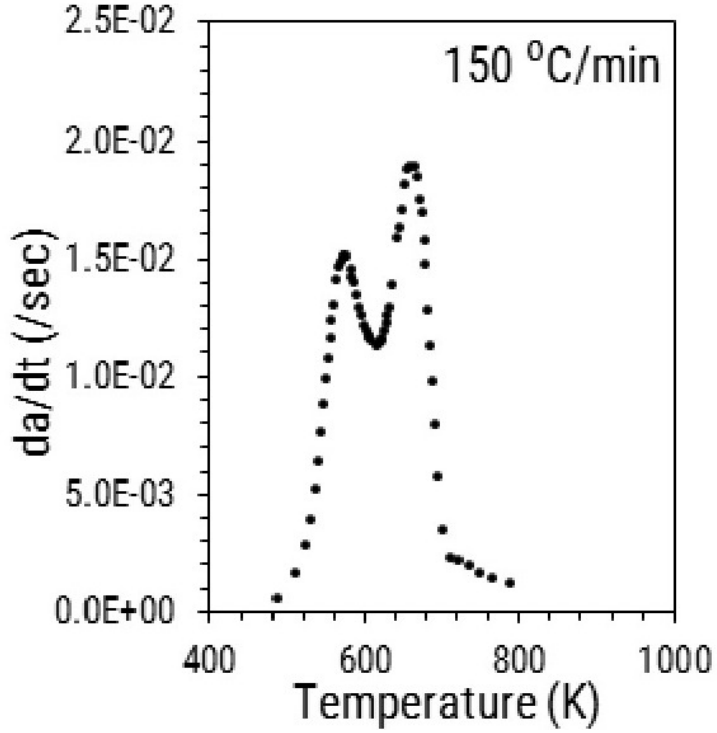

(c)

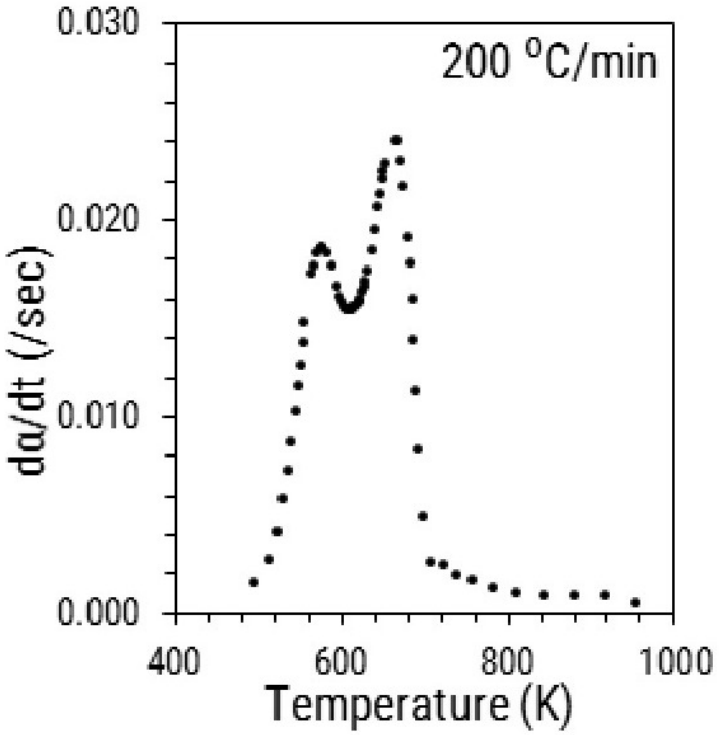

(d)

This figure is continued on the next page...

Figure A.4

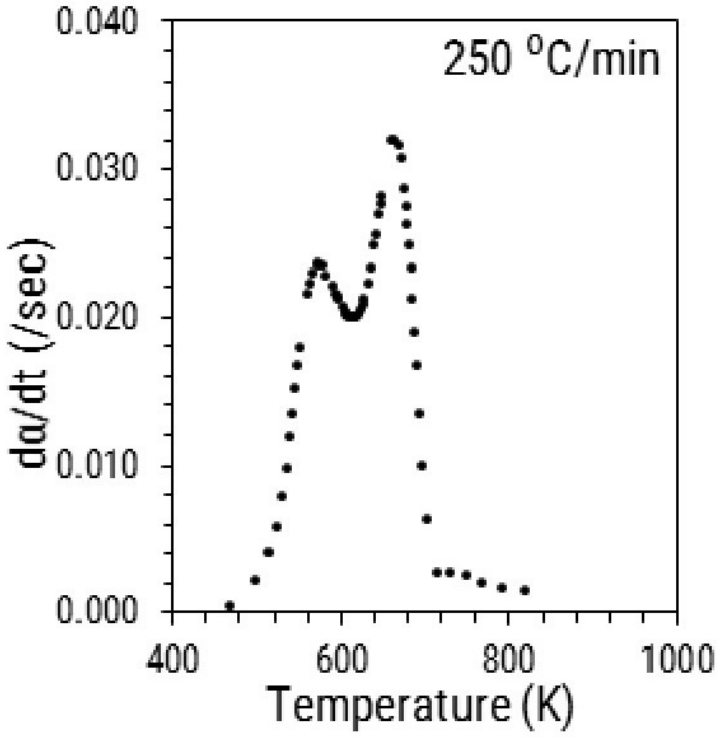

(e)

Figure A.4: Experimental values of dα/dt for biomass particle size between 75 to 106 μm

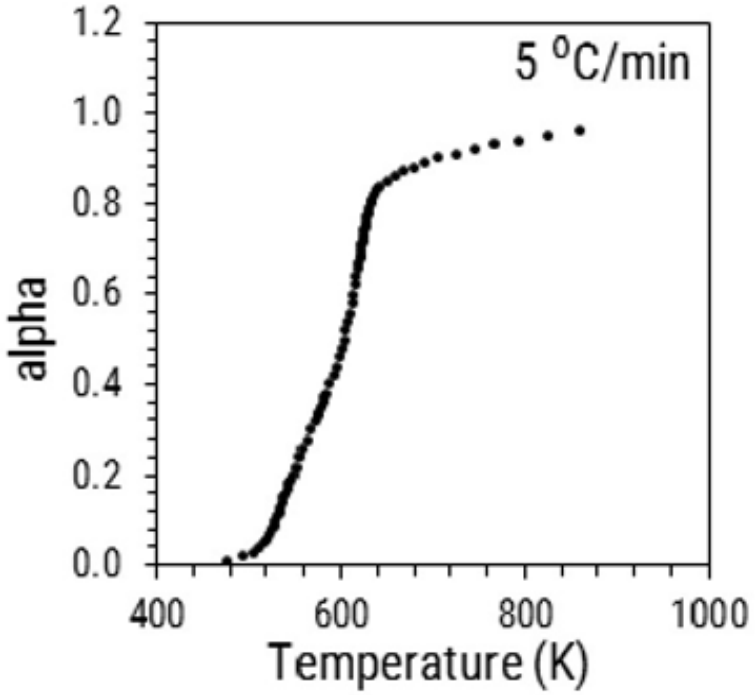

(f)

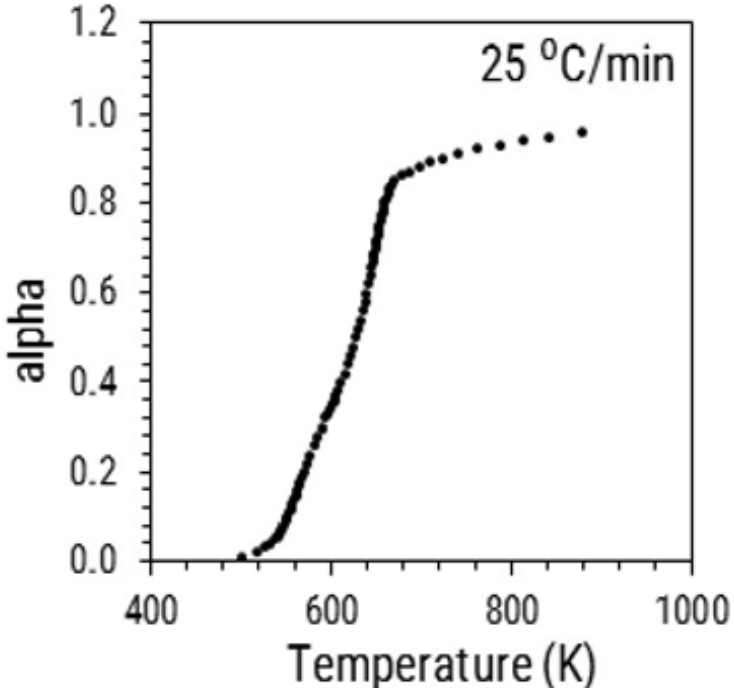

(g)

This figure is continued on the next page...

Figure A.5

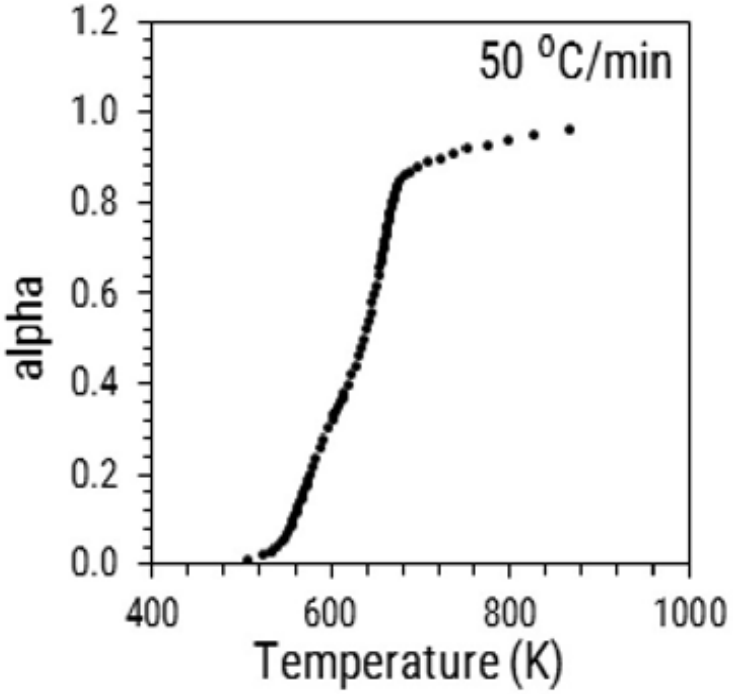

(a)

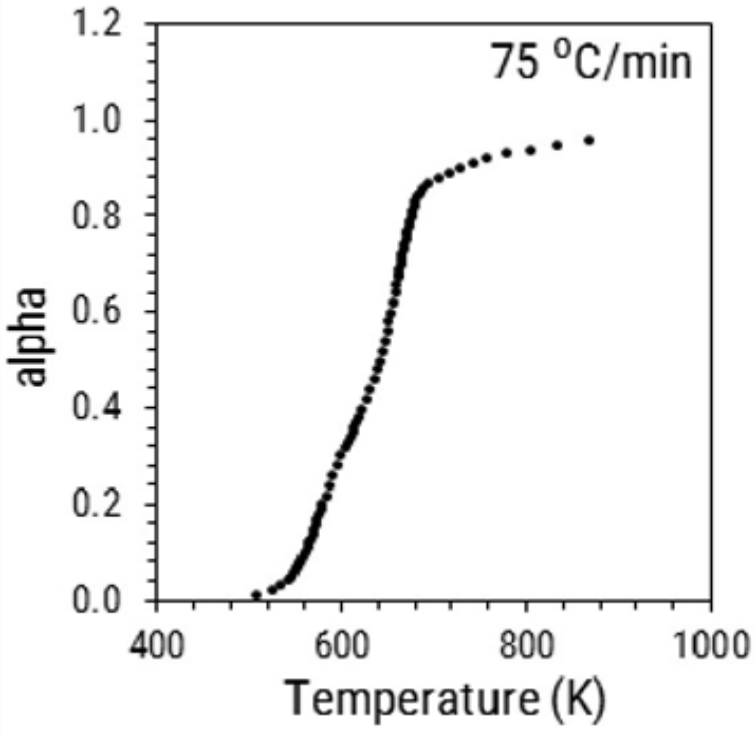

(b)

This figure is continued on the next page...

Figure A.5

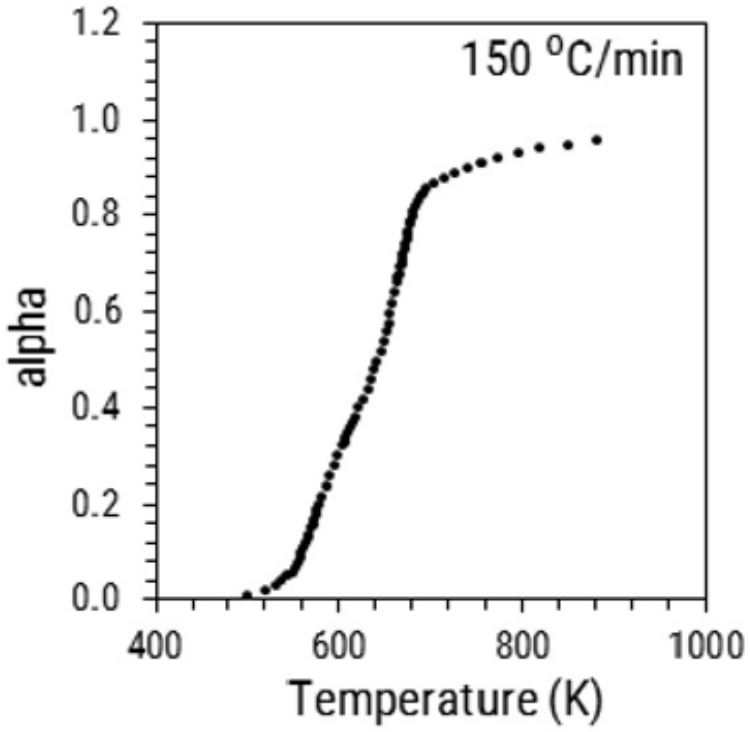

(c)

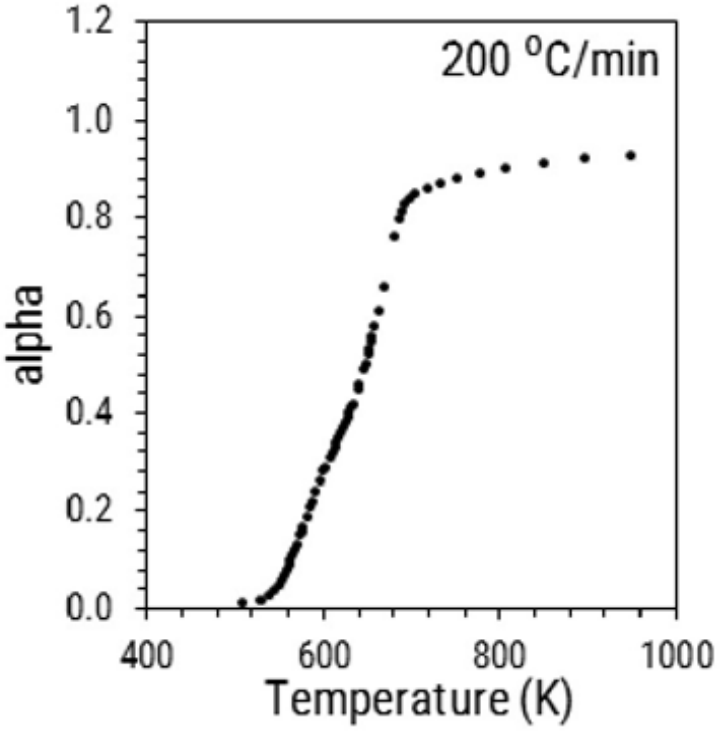

(d)

This figure is continued on the next page...

Figure A.5

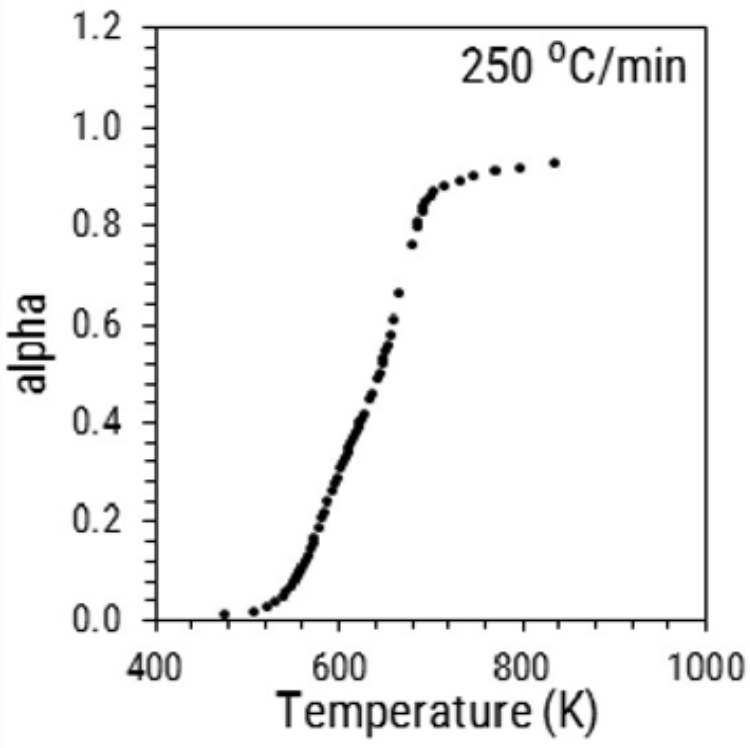

(e)

Figure A.5: Experimental values of α for biomass particle size between 300 to 425 μm

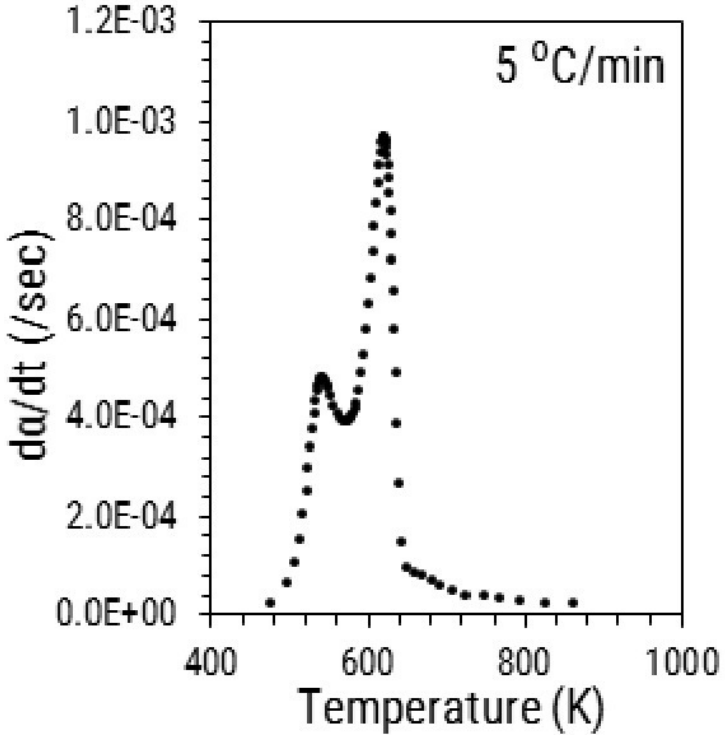

(f)

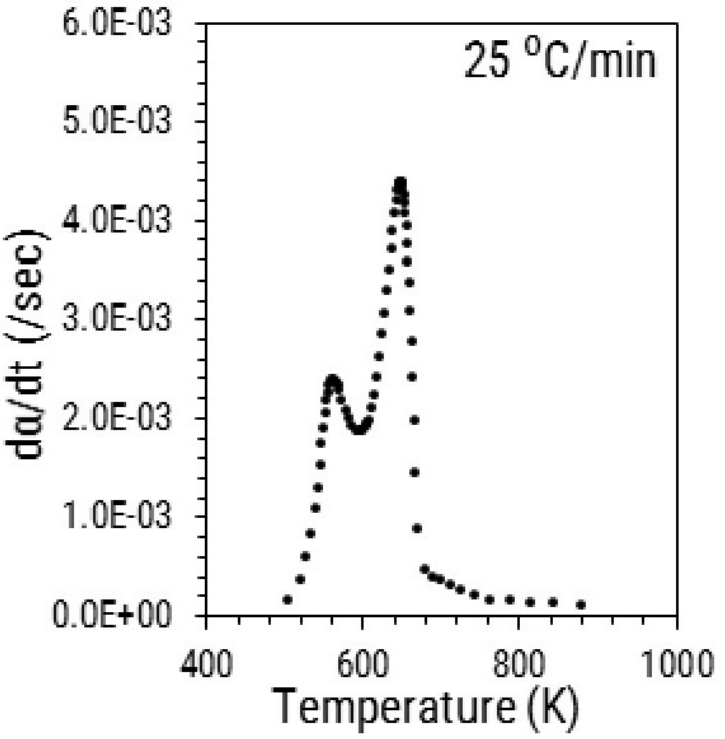

(g)

This figure is continued on the next page...

Figure A.6

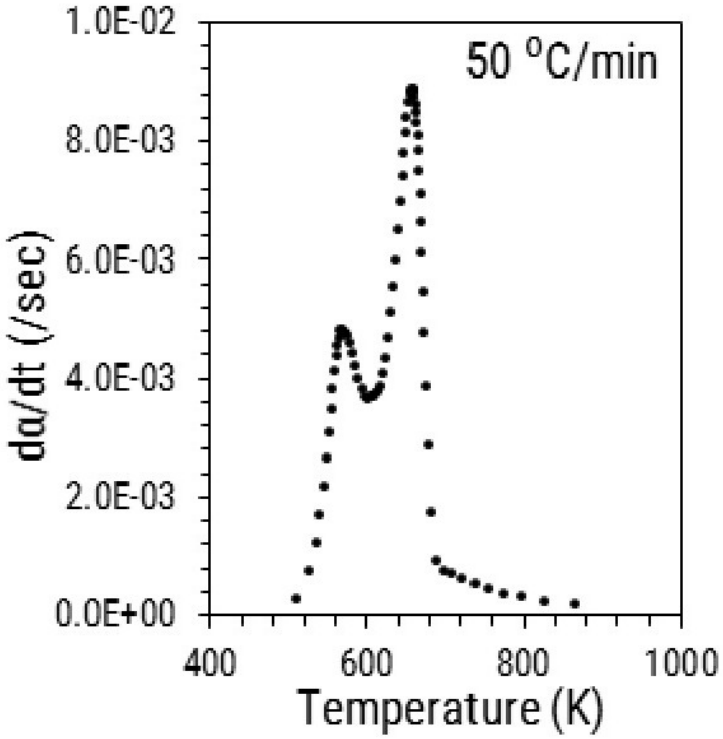

(a)

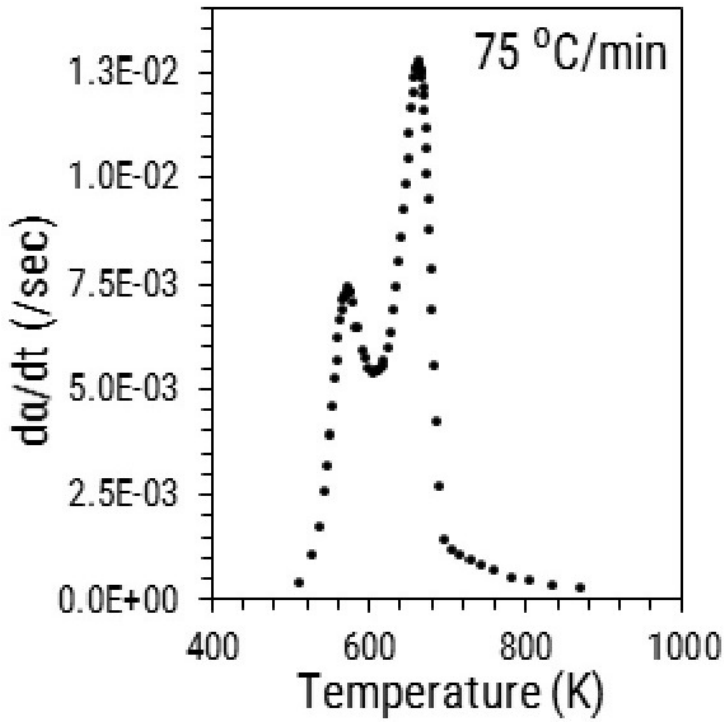

(b)

This figure is continued on the next page...

Figure A.6

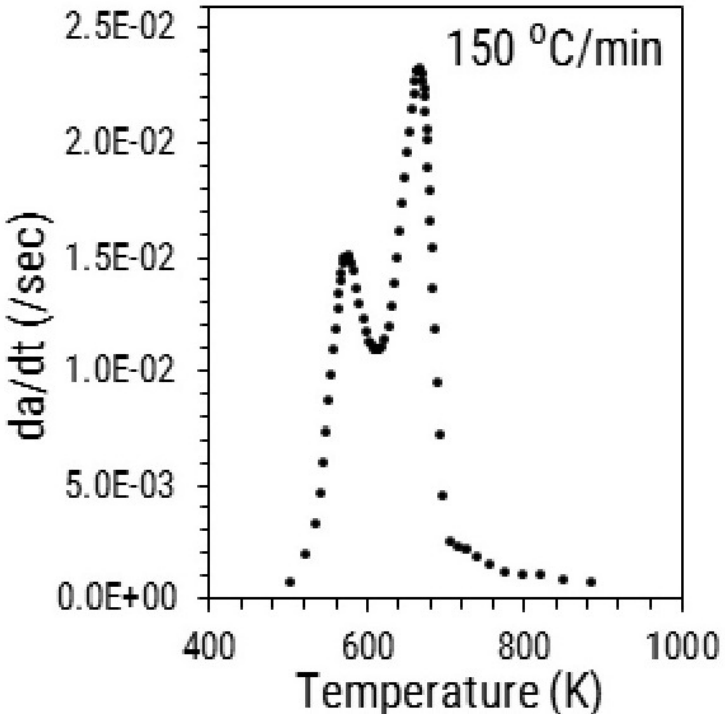

(c)

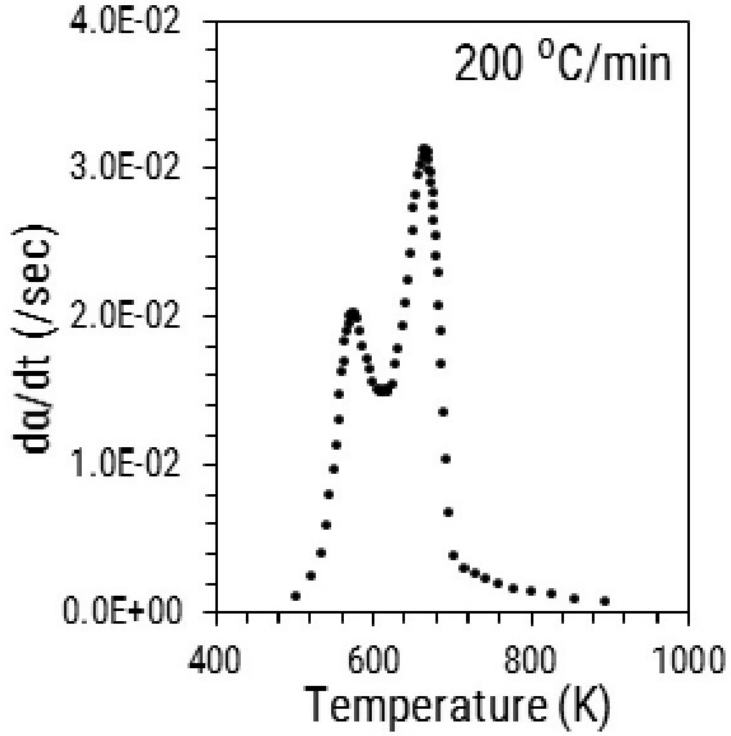

(d)

This figure is continued on the next page...

Figure A.6

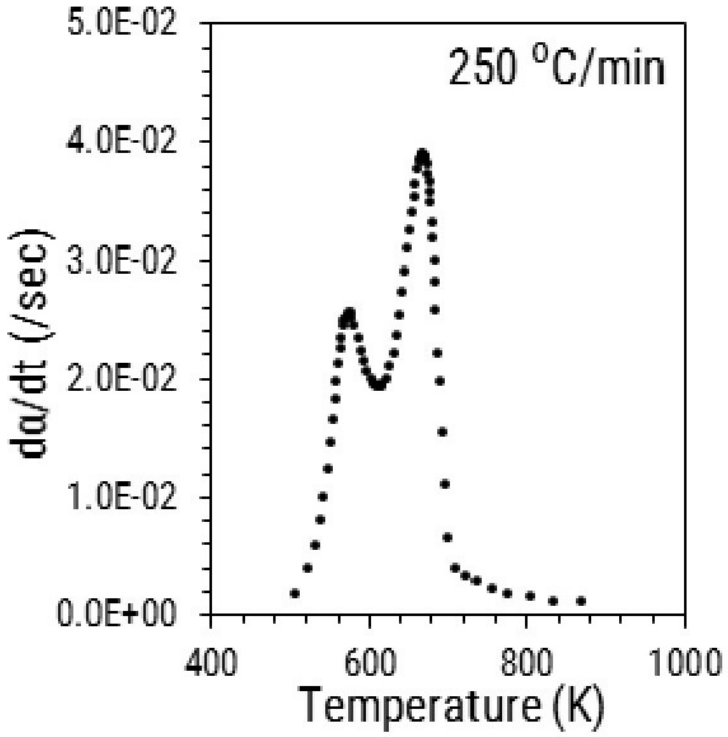

(e)

Figure A.6: Experimental values of dα/dt for biomass particle size between 300 to 425 μm

Appendix B

B.1 Appendix: Chapter 6

Table B.1: Yield and purity of bio-oil model components for scheme 1 for different NCG:condensible mass ratio.

	NCG:Condensible mass ratio 1.5 Liquid yield (purity), wt.%					NCG:Condensible mass ratio 2 Liquid yield (purity), wt.%				
Components	Cond 1	Cond 2	Cond 3		Cond 4	Cond 1	Cond 2	Cond 3		Cond 4
Formic Acid	0.15 (0.15)	0.42 (0.63)	29.21 (40.46)	0.08 (0.85)	68.83 (77.42)	0.13 (0.13)	0.41 (0.59)	0.09 (0.96)	32.81 (43.34)	64.39 (78.13)
Acetic Acid	0.43 (0)	0.71 (0.01)	33.06 (0.39)	0.22 (0.02)	64.73 (0.62)	0.35 (0)	0.63 (0.01)	0.21 (0.02)	35.44 (0.4)	61.9 (0.64)
Propionic acid	0.64 (0.17)	2.77 (1.17)	52.07 (20.1)	1.05 (3.08)	43.05 (13.49)	0.56 (0.15)	2.77 (1.13)	1.06 (3.29)	55.08 (20.27)	39.83 (13.47)
Acetol	0.89 (0.05)	4.37 (0.36)	52.41 (3.92)	1.88 (1.06)	40.03 (2.43)	0.79 (0.04)	4.45 (0.35)	1.94 (1.16)	55 (3.92)	37.12 (2.43)
Glyoxal	0.83 (0.04)	8.25 (0.58)	71.51 (4.6)	0.86 (0.42)	18.49 (0.97)	0.73 (0.03)	8.82 (0.6)	1.08 (0.56)	72.8 (4.47)	16.48 (0.93)
Glycolaldehyde	0.08 (0)	0.23 (0.01)	2.98 (0.16)	0.07 (0.03)	38.86 (1.65)	0.06 (0)	0.21 (0.01)	0.07 (0.03)	2.87 (0.14)	26.28 (1.2)

Table B.1 continued from previous page

	NCG:Condensible mass ratio 1.5 Liquid yield (purity), wt.%					NCG:Condensible mass ratio 2 Liquid yield (purity), wt.%				
Components	Cond 1	Cond 2	Cond 3		Cond 4	Cond 1	Cond 2	Cond 3		Cond 4
Gamma-Butyrolactone	0.97 (0.04)	11.52 (0.65)	76.85 (4.01)	0.99 (0.39)	9.66 (0.41)	0.88 (0.03)	13.22 (0.73)	1.22 (0.51)	77.13 (3.84)	7.53 (0.34)
Furfural	3 (0.39)	34.72 (7.04)	39.25 (7.31)	10.54 (14.87)	12.37 (1.87)	2.66 (0.34)	36.39 (7.17)	10.98 (16.37)	38.5 (6.83)	11.26 (1.84)
Furfurylalcohol	0.82 (0.01)	9.12 (0.16)	37.22 (0.59)	6.73 (0.81)	45.51 (0.59)	0.7 (0.01)	9.27 (0.16)	7.17 (0.91)	38.6 (0.58)	43.22 (0.6)
o-Cresol	0.94 (0.01)	15.84 (0.27)	55.86 (0.88)	9 (1.08)	18.3 (0.24)	0.82 (0.01)	16.85 (0.28)	9.12 (1.16)	57.3 (0.87)	15.81 (0.22)
p-Cresol	58.71 (3.48)	17.06 (1.58)	24.23 (2.06)	0 (0)	0 (0)	59.14 (3.5)	18.01 (1.62)	0 (0)	22.86 (1.86)	0 (0)
2,4-Xylenol	66.17 (3.92)	18.79 (1.74)	13.72 (1.17)	1.04 (0.67)	0.29 (0.02)	66.84 (3.96)	19.37 (1.75)	1.25 (0.85)	12.32 (1)	0.23 (0.02)

Table B.1 continued from previous page

	NCG:Condensible mass ratio 1.5 Liquid yield (purity), wt.%					NCG:Condensible mass ratio 2 Liquid yield (purity), wt.%				
Components	Cond 1	Cond 2	Cond 3		Cond 4	Cond 1	Cond 2	Cond 3		Cond 4
Guaiacol	56.46 (4.94)	27.02 (3.7)	14.54 (1.83)	1.71 (1.63)	0.27 (0.03)	56.68 (4.96)	28.12 (3.75)	2.06 (2.08)	12.95 (1.55)	0.19 (0.02)
4-methyl Guaiacol	2.26 (0.12)	27.42 (2.31)	68.04 (5.27)	1.17 (0.68)	1.11 (0.07)	1.98 (0.11)	29.73 (2.44)	1.22 (0.76)	66.32 (4.9)	0.75 (0.05)
iso-Eugenol	2.24 (0.03)	47.57 (1.07)	48.17 (0.99)	1.6 (0.25)	0.41 (0.01)	2.02 (0.03)	50.99 (1.11)	1.68 (0.28)	45.03 (0.88)	0.28 (0)
Vanillin	7.29 (0.17)	83.08 (2.96)	8.62 (0.28)	0.99 (0.25)	0.02 (0)	6.84 (0.16)	85.11 (2.95)	1.05 (0.28)	6.98 (0.22)	0.01 (0)
Syringol	18.93 (0.22)	76 (1.37)	5.05 (0.08)	0.02 (0)	0 (0)	19.02 (0.22)	77.18 (1.35)	0.02 (0)	3.78 (0.06)	0 (0)
1,2-Benzenediol	5.47 (0.34)	76.64 (7.46)	17.74 (1.59)	0.14 (0.09)	0.01 (0)	5.19 (0.32)	79.93 (7.57)	0.13 (0.09)	14.75 (1.26)	0 (0)

Table B.1 continued from previous page

	NCG:Condensible mass ratio 1.5 Liquid yield (purity), wt.%					NCG:Condensible mass ratio 2 Liquid yield (purity), wt.%				
Components	Cond 1	Cond 2	Cond 3		Cond 4	Cond 1	Cond 2	Cond 3		Cond 4
trans-3,5-dimethoxy stilbene	32.11 (1)	46.51 (2.26)	21.33 (0.95)	0.04 (0.01)	0.01 (0)	31.06 (0.96)	48.95 (2.31)	0.04 (0.01)	19.94 (0.85)	0.01 (0)
1,2-diphenylethane	70.02 (9.62)	29.97 (6.44)	0 (0)	0.01 (0.02)	0 (0)	71.95 (9.86)	28.04 (5.86)	0.01 (0.01)	0 (0)	0 (0)
diBenzofuran	1.95 (0.45)	71.44 (25.94)	0.43 (0.14)	24.49 (61.91)	0.52 (0.14)	1.8 (0.42)	74.69 (26.37)	22.05 (58.91)	0.28 (0.09)	0.22 (0.06)
High molecular weight lignin-2	9.72 (2.12)	74.83 (25.51)	10.28 (3.22)	4.96 (11.77)	0.22 (0.06)	8.89 (1.93)	77.33 (25.64)	4.66 (11.69)	8.96 (2.68)	0.16 (0.04)
High molecular weight lignin-1	100 (9.5)	0 (0)	0 (0)	0 (0)	0 (0)	100 (9.48)	0 (0)	0 (0)	0 (0)	0 (0)
Xylose	100 (9.5)	0 (0)	0 (0)	0 (0)	0 (0)	100 (9.48)	0 (0)	0 (0)	0 (0)	0 (0)

Table B.1 continued from previous page

	NCG:Condensible mass ratio 1.5 Liquid yield (purity), wt.%					NCG:Condensible mass ratio 2 Liquid yield (purity), wt.%				
Components	Cond 1	Cond 2		Cond 3	Cond 4	Cond 1	Cond 2		Cond 3	Cond 4
Levoglucosan	93.19	6.81	0	0	0	94.26	5.74	0	0	0
	(9.11)	(1.04)	(0)	(0)	(0)	(9.2)	(0.85)	(0)	(0)	(0)
Cellobiose	98.58	1.42	0	0	0	98.91	1.09	0	0	0
	(22.24)	(0.5)	(0)	(0)	(0)	(22.28)	(0.37)	(0)	(0)	(0)
Dehydroabietic acid	100	0	0	0	0	100	0	0	0	0
	(21.08)	(0)	(0)	(0)	(0)	(21.05)	(0)	(0)	(0)	(0)

Table B.2: Yield and purity of bio-oil model components for scheme 2 for different NCG:condensible mass ratio.

	NCG:Condensible mass ratio 1.5 Liquid yield (purity), wt.%					NCG:Condensible mass ratio 2 Liquid yield (purity), wt.%				
Components	Cond 1	Cond 2	Cond 3		Cond 4	Cond 1	Cond 2	Cond 3		Cond 4
Formic Acid	0.17 (0)	0.5 (0.01)	47.35 (1.16)	0.02 (0)	51.59 (2.01)	0.09 (0)	0.76 (0.01)	36.16 (1.31)	0.02 (0)	62.51 (1.9)
Acetic Acid	0.21 (0.05)	1.91 (0.76)	58.44 (46.93)	0.12 (1.03)	39.17 (50.03)	0.1 (0.03)	3.36 (1.07)	45.38 (53.81)	0.19 (0.9)	50.75 (50.37)
Propionic acid	0.26 (0.01)	3.1 (0.24)	52.92 (8.23)	0.26 (0.44)	43.25 (10.7)	0.12 (0.01)	5.37 (0.33)	39.15 (8.99)	0.42 (0.37)	54.65 (10.5)
Acetol	0.24 (0.01)	13.54 (0.9)	64.64 (8.65)	0.07 (0.1)	21.46 (4.57)	0.1 (0)	25.08 (1.33)	47.48 (9.38)	0.08 (0.06)	27.21 (4.5)
Glyoxal	0.04 (0)	0.2 (0.01)	3.62 (0.39)	0.01 (0.01)	52.73 (9.1)	0.02 (0)	0.27 (0.01)	2.19 (0.35)	0.01 (0.01)	53.03 (7.11)
Glycolaldehyde	0.28 (0.01)	20.15 (1.09)	67.62 (7.34)	0.08 (0.09)	11.86 (2.05)	0.12 (0)	39.96 (1.72)	45.91 (7.36)	0.08 (0.05)	13.93 (1.87)

Table B.2 continued from previous page

	NCG:Condensible mass ratio 1.5 Liquid yield (purity), wt.%					NCG:Condensible mass ratio 2 Liquid yield (purity), wt.%				
Components	Cond 1	Cond 2	Cond 3		Cond 4	Cond 1	Cond 2	Cond 3		Cond 4
Gamma-Butyrolactone	1.48	48.32	25.56	2.79	21.65	0.44	54.54	15.95	4.25	24.64
	(0.18)	(9.3)	(9.9)	(11.76)	(13.34)	(0.06)	(8.38)	(9.12)	(9.46)	(11.79)
Furfural	0.31	8.18	18.61	1.33	70.94	0.13	11.6	10.62	1.86	75.1
	(0)	(0.13)	(0.61)	(0.48)	(3.72)	(0)	(0.15)	(0.52)	(0.35)	(3.06)
Furfurylalcohol	0.38	14.65	51.4	2.15	31.34	0.15	22.53	35.54	3.54	38.16
	(0)	(0.24)	(1.69)	(0.77)	(1.64)	(0)	(0.29)	(1.73)	(0.67)	(1.55)
o-Cresol	46.04	34.88	19.03	0	0	39.59	59.56	0.84	0	0
	(2.57)	(3.07)	(3.37)	(0)	(0)	(2.49)	(4.19)	(0.22)	(0)	(0)
p-Cresol	59.98	31.54	6.62	0.33	1.46	51.98	43.62	2.81	0.3	1.27
	(3.35)	(2.78)	(1.17)	(0.64)	(0.41)	(3.27)	(3.07)	(0.74)	(0.31)	(0.28)
2,4-Xylenol	56.14	38.59	3.77	0.37	1.05	43.08	53.2	2.09	0.43	1.19
	(4.63)	(5.02)	(0.99)	(1.07)	(0.44)	(4.01)	(5.52)	(0.81)	(0.64)	(0.38)

Table B.2 continued from previous page

	NCG:Condensible mass ratio 1.5 Liquid yield (purity), wt.%					NCG:Condensible mass ratio 2 Liquid yield (purity), wt.%				
Components	Cond 1	Cond 2	Cond 3		Cond 4	Cond 1	Cond 2	Cond 3		Cond 4
Guaiacol	1.15 (0.06)	48.55 (3.89)	47.03 (7.58)	0.2 (0.34)	3.06 (0.78)	0.43 (0.02)	78.35 (5.01)	18.77 (4.47)	0.15 (0.14)	2.3 (0.46)
4-methyl Guaiacol	1.57 (0.02)	80.18 (1.71)	16.91 (0.72)	0.25 (0.12)	1.04 (0.07)	0.41 (0.01)	93.71 (1.59)	5.1 (0.32)	0.15 (0.04)	0.63 (0.03)
iso-Eugenol	15.86 (0.34)	83.24 (2.82)	0.22 (0.02)	0.01 (0.01)	0 (0)	2.08 (0.05)	97.81 (2.65)	0.09 (0.01)	0.01 (0)	0 (0)
Vanillin	30.43 (0.33)	69.11 (1.18)	0.02 (0)	0 (0)	0 (0)	4.46 (0.05)	95.54 (1.3)	0 (0)	0 (0)	0 (0)
Syringol	5.97 (0.35)	93.41 (8.64)	0.47 (0.09)	0 (0)	0 (0)	1.01 (0.07)	98.92 (7.3)	0.07 (0.02)	0 (0)	0 (0)
1,2-Benzenediol	25.33 (0.74)	72.38 (3.34)	2.16 (0.2)	0 (0)	0 (0)	9.34 (0.31)	90.39 (3.33)	0.27 (0.04)	0 (0)	0 (0)

Table B.2 continued from previous page

	NCG:Condensible mass ratio 1.5 Liquid yield (purity), wt.%					NCG:Condensible mass ratio 2 Liquid yield (purity), wt.%				
Components	Cond 1	Cond 2	Cond 3		Cond 4	Cond 1	Cond 2	Cond 3		Cond 4
trans-3,5-dimethoxy stilbene	99.52 (12.11)	0.48 (0.1)	0 (0)	0 (0)	0 (0)	79.57 (11.6)	20.43 (3.33)	0 (0)	0 (0)	0 (0)
1,2-diphenylethane	2.21 (0.48)	81.91 (28.26)	0.01 (0.01)	10.64 (80.22)	0.89 (0.98)	0.29 (0.07)	71.38 (19.65)	0.01 (0.01)	21.26 (84.74)	7.05 (6.05)
diBenzofuran	16.98 (3.48)	80.52 (26.08)	1.46 (0.95)	0.41 (2.92)	0.15 (0.16)	2.51 (0.58)	95.88 (24.79)	0.84 (0.81)	0.6 (2.25)	0.17 (0.14)
High molecular weight lignin-2	100 (8.55)	0 (0)	0 (0)	0 (0)	0 (0)	100 (10.08)	0 (0)	0 (0)	0 (0)	0 (0)
High molecular weight lignin-1	99.51 (8.89)	0 (0)	0 (0)	0 (0)	0 (0)	100 (10.08)	0 (0)	0 (0)	0 (0)	0 (0)
Xylose	99.6 (9.16)	0.16 (0.02)	0 (0)	0 (0)	0 (0)	95.46 (9.91)	4.54 (0.53)	0 (0)	0 (0)	0 (0)

Table B.2 continued from previous page

	NCG:Condensible mass ratio 1.5 Liquid yield (purity), wt.%				NCG:Condensible mass ratio 2 Liquid yield (purity), wt.%				
Components	Cond 1	Cond 2	Cond 3	Cond 4	Cond 1	Cond 2	Cond 3	Cond 4	
Levoglucosan	99.87	0.01	0	0	0	99.78	0.22	0	0	0
	(21.21)	(0)	(0)	(0)	(0)	(23.9)	(0.06)	(0)	(0)	(0)
Cellobiose	99.99	0	0	0	0	100	0	0	0	0
	(19.84)	(0)	(0)	(0)	(0)	(22.38)	(0)	(0)	(0)	(0)
Dehydroabietic acid	94.16	5.84	0	0	0	20.55	79.44	0	0	0
	(3.62)	(0.4)	(0)	(0)	(0)	(1.02)	(4.39)	(0)	(0)	(0)

References

[1] Fred Shafizadeh and Peter PS Chin. Thermal deterioration of wood. In ACS Symposium Series American Chemical Society, 1977.

[2] Colomba Di Blasi and Carmen Branca. Kinetics of primary product formation from wood pyrolysis. Industrial & engineering chemistry research, 40 (23):5547–5556, 2001.

[3] Fred Shafizadeh. Introduction to pyrolysis of biomass. Journal of Analytical and Applied Pyrolysis, 3(4):283–305, 1982.

[4] CA Koufopanos, N Papayannakos, G Maschio, and A Lucchesi. Modelling of the pyrolysis of biomass particles. studies on kinetics, thermal and heat transfer effects. The Canadian journal of chemical engineering, 69(4):907–915, 1991.

[5] Abhishek Sharma, Vishnu Pareek, Shaobin Wang, Zhezi Zhang, Hong Yang, and Dongke Zhang. A phenomenological model of the mechanisms of lignocellulosic biomass pyrolysis processes. Computers & Chemical Engineering, 60:231–241, 2014.

[6] A Broido and Maxine A Nelson. Char yield on pyrolysis of cellulose. Combustion and Flame, 24:263–268, 1975.

[7] Fred Shafizadeh and AGW Bradbury. Thermal degradation of cellulose in air and nitrogen at low temperatures. Journal of applied polymer science, 23 (5):1431–1442, 1979.

[8] Jan Piskorz, Desmond St AG Radlein, Donald S Scott, and Stefan Czernik. Pretreatment of wood and cellulose for production of sugars by fast pyrolysis. Journal of Analytical and Applied Pyrolysis, 16(2):127–142, 1989.

[9] JL Banyasz, San Li, J Lyons-Hart, and KH Shafer. Gas evolution and the mechanism of cellulose pyrolysis. Fuel, 80(12):1757–1763, 2001.

[10] Eliseo Ranzi, Paulo Eduardo Amaral Debiagi, and Alessio Frassoldati. Mathematical modeling of fast biomass pyrolysis and bio-oil formation. note i: Kinetic mechanism of biomass pyrolysis. ACS Sustainable Chemistry & Engineering, 5(4):2867–2881, 2017.

[11] Qingluan Xue, TJ Heindel, and RO Fox. A cfd model for biomass fast pyrolysis in fluidized-bed reactors. Chemical Engineering Science, 66(11):2440–2452, 2011.

[12] Thomas H Fletcher, Harland R Pond, Jarom Webster, Judson Wooters, and Larry L Baxter. Prediction of tar and light gas during pyrolysis of black liquor and biomass. Energy & Fuels, 26(6):3381–3387, 2012.

[13] Gavin M Wiggins, Peter N Ciesielski, and C Stuart Daw. Low-order modeling of internal heat transfer in biomass particle pyrolysis. Energy & Fuels, 30 (6):4960–4969, 2016.

[14] Eoin Butler, Ger Devlin, Dietrich Meier, and Kevin McDonnell. A review of recent laboratory research and commercial developments in fast pyrolysis and upgrading. Renewable and Sustainable Energy Reviews, 15(8):4171–4186, 2011.

[15] Greg Perkins, Thallada Bhaskar, and Muxina Konarova. Process development status of fast pyrolysis technologies for the manufacture of renewable transport fuels from biomass. Renewable and Sustainable Energy Reviews, 90:292–315, 2018.

[16] Shurong Wang, Yueling Gu, Qian Liu, Yan Yao, Zuogang Guo, Zhongyang Luo, and Kefa Cen. Separation of bio-oil by molecular distillation. Fuel Processing Technology, 90(5):738–745, 2009.

[17] Zuogang Guo, Shurong Wang, Yueling Gu, Guohui Xu, Xin Li, and Zhongyang Luo. Separation characteristics of biomass pyrolysis oil in molecular distillation. Separation and Purification Technology, 76(1):52–57, 2010.

[18] Anthony S Pollard, Marge R Rover, and Robert C Brown. Characterization of bio-oil recovered as stage fractions with unique chemical and physical properties. Journal of Analytical and Applied Pyrolysis, 93:129–138, 2012.

[19] Haiqing Sui, Haiping Yang, Jingai Shao, Xianhua Wang, Yunchao Li, and Hanping Chen. Fractional condensation of multicomponent vapors from pyrolysis of cotton stalk. Energy & Fuels, 28(8):5095–5102, 2014.

[20] Christian Lindfors, Eeva Kuoppala, Anja Oasmaa, Yrjo Solantausta, and Vesa Arpiainen. Fractionation of bio-oil. Energy & Fuels, 28(9):5785–5791, 2014.

[21] K Papadikis, S Gu, and AV Bridgwater. Cfd modelling of the fast pyrolysis of biomass in fluidised bed reactors. part b: Heat, momentum and mass transport in bubbling fluidised beds. Chemical Engineering Science, 64(5): 1036–1045, 2009.

[22] Daniel J McClelland, Ali Hussain Motagamwala, Yanding Li, Marjorie R Rover, Ashley M Wittrig, Chunping Wu, J Scott Buchanan, Robert C Brown, John Ralph, James A Dumesic, et al. Functionality and molecular weight distribution of red oak lignin before and after pyrolysis and hydrogenation. Green Chemistry, 19(5):1378–1389, 2017.

[23] Yanru Zhang, Yanqing Niu, Hao Zou, Yu Lei, Jiang Zheng, Huiyong Zhuang, and Shien Hui. Characteristics of biomass fast pyrolysis in a wire-mesh reactor. Fuel, 200:225–235, 2017.

[24] Jie Yu, Nigel Paterson, John Blamey, and Marcos Millan. Cellulose, xylan and lignin interactions during pyrolysis of lignocellulosic biomass. Fuel, 191:140–149, 2017.

[25] Roel Johannes Maria Westerhof. Refining fast pyrolysis of biomass. PhD thesis, University of Twente, Netherlands, 12 2011.

[26] Marjorie R Rover, Patrick A Johnston, Lysle E Whitmer, Ryan G Smith, and Robert C Brown. The effect of pyrolysis temperature on recovery of bio-oil as distinctive stage fractions. Journal of Analytical and Applied Pyrolysis, 105:262–268, 2014.

[27] R.L. Howard. Lignocellulose biotechnology: Bioconversion and cultivation of edible mushrooms. In Microbial Biotechnology in Horticulture, Vol. 3, pages 181–230. CRC Press, 2008.

[28] Pushkaraj Ramchandra Patwardhan. Understanding the product distribution from biomass fast pyrolysis. PhD thesis, 2010.

[29] Dinesh Mohan, Charles U Pittman, and Philip H Steele. Pyrolysis of wood/biomass for bio-oil: a critical review. Energy & fuels, 20(3):848–889, 2006.

[30] George W Huber, Sara Iborra, and Avelino Corma. Synthesis of transportation fuels from biomass: chemistry, catalysts, and engineering. Chemical reviews, 106(9):4044–4098, 2006.

[31] Tushar Vispute. Pyrolysis oils: characterization, stability analysis, and catalytic upgrading to fuels and chemicals, 2011.

[32] Abhishek Sharma, Vishnu Pareek, and Dongke Zhang. Biomass pyrolysisa review of modelling, process parameters and catalytic studies. Renewable and Sustainable Energy Reviews, 50:1081–1096, 2015.

[33] Eliseo Ranzi, Alberto Cuoci, Tiziano Faravelli, Alessio Frassoldati, Gabriele Migliavacca, Sauro Pierucci, and Samuele Sommariva. Chemical kinetics of biomass pyrolysis. Energy & Fuels, 22(6):4292–4300, 2008.

[34] Thomas J Haas, Mark R Nimlos, and Bryon S Donohoe. Real-time and post-reaction microscopic structural analysis of biomass undergoing pyrolysis. Energy & fuels, 23(7):3810–3817, 2009.

[35] Anthony Dufour, Bajil Ouartassi, Roda Bounaceur, and André Zoulalian. Modelling intra-particle phenomena of biomass pyrolysis. Chemical Engineering Research and Design, 89(10):2136–2146, 2011.

[36] Xun Hu, Yi Wang, Daniel Mourant, Richard Gunawan, Caroline Lievens, Weerawut Chaiwat, Mortaza Gholizadeh, Liping Wu, Xiang Li, and Chun-Zhu Li. Polymerization on heating up of bio-oil: A model compound study. AIChE Journal, 59(3):888–900, 2013.

[37] Ana Primo, Patricia Concepción, and Avelino Corma. Synergy between the metal nanoparticles and the support for the hydrogenation of functionalized carboxylic acids to diols on ru/tio 2. Chemical Communications, 47(12): 3613–3615, 2011.

[38] Wenqin Shen, Geoffrey A Tompsett, Karl D Hammond, Rong Xing, Fulya Dogan, Clare P Grey, W Curtis Conner Jr, Scott M Auerbach, and George W Huber. Liquid phase aldol condensation reactions with mgo–zro2 and shape-selective nitrogen-substituted nay. Applied Catalysis A: General, 392(1-2): 57–68, 2011.

[39] Huamin Wang, Jonathan Male, and Yong Wang. Recent advances in hydrotreating of pyrolysis bio-oil and its oxygen-containing model compounds. Acs Catalysis, 3(5):1047–1070, 2013.

[40] Huamin Wang, Suh-Jane Lee, Mariefel V Olarte, and Alan H Zacher. Bio-oil stabilization by hydrogenation over reduced metal catalysts at low temperatures. ACS Sustainable Chemistry & Engineering, 4(10):5533–5545, 2016.

[41] Xiujuan Guo, Shurong Wang, Zuogang Guo, Qian Liu, Zhongyang Luo, and Kefa Cen. Pyrolysis characteristics of bio-oil fractions separated by molecular distillation. Applied Energy, 87(9):2892–2898, 2010.

[42] Yaseen Elkasabi, Charles A Mullen, Michael A Jackson, and Akwasi A Boateng. Characterization of fast-pyrolysis bio-oil distillation residues and their potential applications. Journal of Analytical and Applied Pyrolysis, 114:179–186, 2015.

[43] Xiang Li, Richard Gunawan, Caroline Lievens, Yi Wang, Daniel Mourant, Shan Wang, Hongwei Wu, Manuel Garcia-Perez, and Chun-Zhu Li. Simultaneous catalytic esterification of carboxylic acids and acetalisation of aldehydes in a fast pyrolysis bio-oil from mallee biomass. Fuel, 90(7):2530–2537, 2011.

[44] Mingming Zhang and Hongwei Wu. Phase behavior and fuel properties of bio-oil/glycerol/methanol blends. Energy & Fuels, 28(7):4650–4656, 2014.

[45] Liang Zhu, Kai Li, Yiming Zhang, and Xifeng Zhu. Upgrading the storage properties of bio-oil by adding a compound additive. Energy & Fuels, 31(6): 6221–6227, 2017.

[46] Laibao Zhang, Yan Luo, Rangana Wijayapala, and Keisha B Walters. Alcohol stabilization of low water content pyrolysis oil during high temperature treatment. Energy & Fuels, 31(12):13666–13674, 2017.

[47] Daniel E Resasco and Steven P Crossley. Implementation of concepts derived from model compound studies in the separation and conversion of bio-oil to fuel. Catalysis Today, 257:185–199, 2015.

[48] Anja Oasmaa and Stefan Czernik. Fuel oil quality of biomass pyrolysis oils state of the art for the end users. Energy & Fuels, 13(4):914–921, 1999.

[49] Yu-Loong Loow, Ta Yeong Wu, Khang Aik Tan, Yung Shen Lim, Lee Fong Siow, Jamaliah Md. Jahim, Abdul Wahab Mohammad, and Wen Hui Teoh. Recent advances in the application of inorganic salt pretreatment for transforming lignocellulosic biomass into reducing sugars. Journal of agricultural and food chemistry, 63(38):8349–8363, 2015.

[50] Pratima Bajpai. Structure of lignocellulosic biomass. In Pretreatment of Lignocellulosic Biomass for Biofuel Production, pages 7–12. Springer, 2016.

[51] Tamilvendan Manavalan, Arulmani Manavalan, and Klaus Heese. Characterization of lignocellulolytic enzymes from white-rot fungi. Current microbiology, 70(4):485–498, 2015.

[52] Matthew S Mettler, Dionisios G Vlachos, and Paul J Dauenhauer. Top ten fundamental challenges of biomass pyrolysis for biofuels. Energy & Environmental Science, 5(7):7797–7809, 2012.

[53] Peter N Ciesielski, Michael F Crowley, Mark R Nimlos, Aric W Sanders, Gavin M Wiggins, Dave Robichaud, Bryon S Donohoe, and Thomas D Foust. Biomass particle models with realistic morphology and resolved microstructure for simulations of intraparticle transport phenomena. Energy & Fuels, 29(1):242–254, 2014.

[54] Sunil K Maity. Opportunities, recent trends and challenges of integrated biorefinery: Part i. Renewable and Sustainable Energy Reviews, 43:1427–1445, 2015.

[55] S N Naik, Vaibhav V Goud, Prasant K Rout, and Ajay K Dalai. Production of first and second generation biofuels: a comprehensive review. Renewable and sustainable energy reviews, 14(2):578–597, 2010.

[56] Robert P Anex, Andy Aden, Feroz Kabir Kazi, Joshua Fortman, Ryan M Swanson, Mark M Wright, Justinus A Satrio, Robert C Brown, Daren E Daugaard, Alex Platon, et al. Techno-economic comparison of biomass-to-transportation fuels via pyrolysis, gasification, and biochemical pathways. Fuel, 89:S29–S35, 2010.

[57] Haiping Yang, Rong Yan, Hanping Chen, Dong Ho Lee, and Chuguang Zheng. Characteristics of hemicellulose, cellulose and lignin pyrolysis. Fuel, 86(12): 1781–1788, 2007.

[58] Donald F Arseneau. Competitive reactions in the thermal decomposition of cellulose. Canadian Journal of Chemistry, 49(4):632–638, 1971.

[59] Ivan Milosavljevic, Vahur Oja, and Eric M Suuberg. Thermal effects in cellulose pyrolysis: relationship to char formation processes. Industrial & Engineering Chemistry Research, 35(3):653–662, 1996.

[60] Johannes Rath, MG Wolfinger, Gerhard Steiner, Gernot Krammer, Federica Barontini, and Valerio Cozzani. Heat of wood pyrolysis. Fuel, 82(1):81–91, 2003.

[61] Andres Anca-Couce. Reaction mechanisms and multi-scale modelling of lignocellulosic biomass pyrolysis. Progress in Energy and Combustion Science, 53:41–79, 2016.

[62] Pushkaraj R Patwardhan, Robert C Brown, and Brent H Shanks. Product distribution from the fast pyrolysis of hemicellulose. ChemSusChem, 4(5): 636–643, 2011.

[63] F Shafizadeh, GD McGinnis, and CW Philpot. Thermal degradation of xylan and related model compounds. Carbohydrate Research, 25(1):23–33, 1972.

[64] Yunyun Peng and Shubin Wu. The structural and thermal characteristics of wheat straw hemicellulose. Journal of Analytical and Applied Pyrolysis, 88(2):134–139, 2010.

[65] Shuai Zhou, Brennan Pecha, Michiel van Kuppevelt, Armando G McDonald, and Manuel Garcia-Perez. Slow and fast pyrolysis of douglas-fir lignin: Importance of liquid-intermediate formation on the distribution of products. biomass and bioenergy, 66:398–409, 2014.

[66] William S-L Mok and Michael J Antal Jr. Effects of pressure on biomass pyrolysis. ii. heats of reaction of cellulose pyrolysis. Thermochimica Acta, 68 (2-3):165–186, 1983.

[67] Colomba Di Blasi. Modeling chemical and physical processes of wood and biomass pyrolysis. Progress in Energy and Combustion Science, 34(1):47–90, 2008.

[68] Anthony V Bridgwater. Upgrading fast pyrolysis liquids. Thermochemical processing of biomass: conversion into fuels, chemicals and power, pages 157–199, 2011.

[69] Takashi Hosoya, Haruo Kawamoto, and Shiro Saka. Secondary reactions of lignin-derived primary tar components. Journal of Analytical and Applied Pyrolysis, 83(1):78–87, 2008.

[70] Takashi Hosoya, Haruo Kawamoto, and Shiro Saka. Pyrolysis gasification reactivities of primary tar and char fractions from cellulose and lignin as studied with a closed ampoule reactor. Journal of Analytical and Applied Pyrolysis, 83(1):71–77, 2008.

[71] Travis Fisher, Mohammad Hajaligol, Bruce Waymack, and Diane Kellogg. Pyrolysis behavior and kinetics of biomass derived materials. Journal of analytical and applied pyrolysis, 62(2):331–349, 2002.

[72] Jacques Lédé, Fabrice Blanchard, and Olivier Boutin. Radiant flash pyrolysis of cellulose pellets: products and mechanisms involved in transient and steady state conditions. Fuel, 81(10):1269–1279, 2002.

[73] Paul J Dauenhauer, Joshua L Colby, Christine M Balonek, Wieslaw J Suszynski, and Lanny D Schmidt. Reactive boiling of cellulose for integrated catalysis through an intermediate liquid. Green Chemistry, 11(10):1555–1561, 2009.

[74] Andrew R Teixeira, Kyle G Mooney, Jacob S Kruger, C Luke Williams, Wieslaw J Suszynski, Lanny D Schmidt, David P Schmidt, and Paul J Dauenhauer. Aerosol generation by reactive boiling ejection of molten cellulose. Energy & Environmental Science, 4(10):4306–4321, 2011.

[75] Mohd Asmadi, Haruo Kawamoto, and Shiro Saka. Gas-and solid/liquid-phase reactions during pyrolysis of softwood and hardwood lignins. Journal of analytical and applied pyrolysis, 92(2):417–425, 2011.

[76] Anthony Dufour, Miguel Castro-Díaz, Philippe Marchal, Nicolas Brosse, Roberto Olcese, Mohamed Bouroukba, and Colin Snape. In situ analysis of biomass pyrolysis by high temperature rheology in relations with 1h nmr. Energy & Fuels, 26(10):6432–6441, 2012.

[77] Andrew R Teixeira, Richard J Hermann, Jacob S Kruger, Wieslaw J Suszynski, Lanny D Schmidt, David P Schmidt, and Paul J Dauenhauer. Microexplosions in the upgrading of biomass-derived pyrolysis oils and the effects of simple fuel processing. ACS Sustainable Chemistry & Engineering, 1(3):341–348, 2013.

[78] Alan K Burnham, Xiaowei Zhou, and Linda J Broadbelt. Critical review of the global chemical kinetics of cellulose thermal decomposition. Energy & Fuels, 29(5):2906–2918, 2015.

[79] Ozlem Onay. Influence of pyrolysis temperature and heating rate on the production of bio-oil and char from safflower seed by pyrolysis, using a well-swept fixed-bed reactor. Fuel Processing Technology, 88(5):523–531, 2007.

[80] Colomba Di Blasi. Physico-chemical processes occurring inside a degrading two-dimensional anisotropic porous medium. International journal of heat and mass transfer, 41(24):4139–4150, 1998.

[81] Jorge Montoya, Brennan Pecha, Farid Chejne Janna, and Manuel Garcia-Perez. Micro-explosion of liquid intermediates during the fast pyrolysis of sucrose and organosolv lignin. Journal of Analytical and Applied Pyrolysis, 122:106–121, 2016.

[82] Jun Shen, Xiao-Shan Wang, Manuel Garcia-Perez, Daniel Mourant, Martin J Rhodes, and Chun-Zhu Li. Effects of particle size on the fast pyrolysis of oil mallee woody biomass. Fuel, 88(10):1810–1817, 2009.

[83] Roel Johannes Maria Westerhof, HS Nygard, Willibrordus Petrus Maria van Swaaij, Sascha RA Kersten, and Derk Willem Frederik Brilman. Effect of particle geometry and microstructure on fast pyrolysis of beech wood. Energy & fuels, 26(4):2274–2280, 2012.

[84] Eric M Suuberg, Ivan Milosavljevic, and Vahur Oja. Two-regime global kinetics of cellulose pyrolysis: the role of tar evaporation. In Symposium (International) on Combustion, volume 26, pages 1515–1521. Elsevier, 1996.

[85] CA Koufopanos, A Lucchesi, and G Maschio. Kinetic modelling of the pyrolysis of biomass and biomass components. The Canadian Journal of Chemical Engineering, 67(1):75–84, 1989.

[86] Theodore R Nunn, Jack B Howard, John P Longwell, and William A Peters. Product compositions and kinetics in the rapid pyrolysis of sweet gum hardwood. Industrial & Engineering Chemistry Process Design and Development, 24(3):836–844, 1985.

[87] MC Samolada and IA Vasalos. A kinetic approach to the flash pyrolysis of biomass in a fluidized bed reactor. Fuel, 70(7):883–889, 1991.

[88] BM Wagenaar, W Prins, and Willibrordus Petrus Maria van Swaaij. Flash pyrolysis kinetics of pine wood. Fuel processing technology, 36(1-3):291–298, 1993.

[89] Morten Gunnar Grønli, Gábor Várhegyi, and Colomba Di Blasi. Thermogravimetric analysis and devolatilization kinetics of wood. Industrial & Engineering Chemistry Research, 41(17):4201–4208, 2002.

[90] John E White, W James Catallo, and Benjamin L Legendre. Biomass pyrolysis kinetics: a comparative critical review with relevant agricultural residue case studies. Journal of analytical and applied pyrolysis, 91(1):1–33, 2011.

[91] Sadegh Papari and Kelly Hawboldt. A review on the pyrolysis of woody biomass to bio-oil: Focus on kinetic models. Renewable and Sustainable Energy Reviews, 52:1580–1595, 2015.

[92] T Faravelli, A Frassoldati, G Migliavacca, and E Ranzi. Detailed kinetic modeling of the thermal degradation of lignins. Biomass and Bioenergy, 34(3): 290–301, 2010.

[93] Andres Anca-Couce, Ramin Mehrabian, Robert Scharler, and Ingwald Obernberger. Kinetic scheme of biomass pyrolysis considering secondary charring reactions. Energy conversion and management, 87:687–696, 2014.

[94] Heather B Mayes and Linda J Broadbelt. Unraveling the reactions that unravel cellulose. The Journal of Physical Chemistry A, 116(26):7098–7106, 2012.

[95] R Vinu and Linda J Broadbelt. A mechanistic model of fast pyrolysis of glucose-based carbohydrates to predict bio-oil composition. Energy & Environmental Science, 5(12):9808–9826, 2012.

[96] James P Diebold. A unified, global model for the pyrolysis of cellulose. Biomass and Bioenergy, 7(1-6):75–85, 1994.

[97] Franz Thurner and Uzi Mann. Kinetic investigation of wood pyrolysis. Industrial & Engineering Chemistry Process Design and Development, 20 (3):482–488, 1981.

[98] BV Babu and AS Chaurasia. Modeling for pyrolysis of solid particle: kinetics and heat transfer effects. Energy conversion and Management, 44(14):2251–2275, 2003.

[99] Abhishek Sharma, Shaobin Wang, Vishnu Pareek, Hong Yang, and Dongke Zhang. Multi-fluid reactive modeling of fluidized bed pyrolysis process. Chemical Engineering Science, 123:311–321, 2015.

[100] Wai-Chun R Chan, Marcia Kelbon, and Barbara B Krieger. Modelling and experimental verification of physical and chemical processes during pyrolysis of a large biomass particle. Fuel, 64(11):1505–1513, 1985.

[101] Matteo Calonaci, Roberto Grana, Emma Barker Hemings, Giulia Bozzano, Mario Dente, and Eliseo Ranzi. Comprehensive kinetic modeling study of bio-oil formation from fast pyrolysis of biomass. Energy & Fuels, 24(10): 5727–5734, 2010.

[102] Eliseo Ranzi, Sauro Pierucci, Pier Carlo Aliprandi, and Silvano Stringa. Comprehensive and detailed kinetic model of a traveling grate combustor of biomass. Energy & Fuels, 25(9):4195–4205, 2011.

[103] Eliseo Ranzi, Michele Corbetta, Flavio Manenti, and Sauro Pierucci. Kinetic modeling of the thermal degradation and combustion of biomass. Chemical Engineering Science, 110:2–12, 2014.

[104] Alessio Frassoldati, G Migliavacca, T Crippa, F Velata, Tiziano Faravelli, and ELISEO Ranzi. Detailed kinetic modeling of thermal degradation of biomasses. In Proceeding of the 29th Meeting on Combustion, 2006.

[105] Alberto Cuoci, Tiziano Faravelli, Alessio Frassoldati, Silvia Granata, Gabriele Migliavacca, Eliseo Ranzi, and Samuele Sommariva. A general mathematical model of biomass devolatilization note 1. lumped kinetic models of cellulose, hemicellulose and lignin. In 30th Meeting of the Italian section of the Combustion Institute. Citeseer, 2007.

[106] Carmen Branca, Paola Giudicianni, and Colomba Di Blasi. Gc/ms characterization of liquids generated from low-temperature pyrolysis of wood. Industrial & Engineering Chemistry Research, 42(14):3190–3202, 2003.

[107] Xiaowei Zhou, Michael W Nolte, Heather B Mayes, Brent H Shanks, and Linda J Broadbelt. Experimental and mechanistic modeling of fast pyrolysis of neat glucose-based carbohydrates. 1. experiments and development of a detailed mechanistic model. Industrial & Engineering Chemistry Research, 53(34):13274–13289, 2014.

[108] Hyoe Hatakeyama and Tatsuko Hatakeyama. Lignin structure, properties, and applications. In Biopolymers, pages 1–63. Springer, 2009.

[109] Pooya Azadi, Oliver R Inderwildi, Ramin Farnood, and David A King. Liquid fuels, hydrogen and chemicals from lignin: A critical review. Renewable and Sustainable Energy Reviews, 21:506–523, 2013.

[110] W De Jong, A Pirone, and MA Wojtowicz. Pyrolysis of miscanthus giganteus and wood pellets: Tg-ftir analysis and reaction kinetics. Fuel, 82(9):1139–1147, 2003.

[111] Yonggang Chen, Sylvie Charpenay, Anker Jensen, Marek A Wójtowicz, and Michael A Serio. Modeling of biomass pyrolysis kinetics. In Symposium (international) on combustion, volume 27, pages 1327–1334. Elsevier, 1998.

[112] Stephen Niksa. Predicting the rapid devolatilization of diverse forms of biomass with bio-flashchain. Proceedings of the Combustion Institute, 28 (2):2727–2733, 2000.

[113] David M Grant, Ronald J Pugmire, Thomas H Fletcher, and Alan R Kerstein. Chemical model of coal devolatilization using percolation lattice statistics. Energy & Fuels, 3(2):175–186, 1989.

[114] Chandong Sheng and JLT Azevedo. Modeling biomass devolatilization using the chemical percolation devolatilization model for the main components. Proceedings of the Combustion Institute, 29(1):407–414, 2002.

[115] Aaron D Lewis and Thomas H Fletcher. Prediction of sawdust pyrolysis yields from a flat-flame burner using the cpd model. Energy & Fuels, 27 (2):942–953, 2013.

[116] P R Solomon, D G Hamblen, RM Carangelo, MA Serio, and GV Deshpande. General model of coal devolatilization. Energy & Fuels, 2(4):405–422, 1988.

[117] Vladimir Vand. A theory of the irreversible electrical resistance changes of metallic films evaporated in vacuum. Proceedings of the Physical Society, 55(3):222, 1943.

[118] Gábor Várhegyi, Balázs Bobály, Emma Jakab, and Honggang Chen. Thermogravimetric study of biomass pyrolysis kinetics. a distributed activation energy model with prediction tests. Energy & Fuels, 25(1):24–32, 2010.

[119] Shurong Wang, Haizhou Lin, Bin Ru, Gongxin Dai, Xiaoliu Wang, Gang Xiao, and Zhongyang Luo. Kinetic modeling of biomass components pyrolysis using a sequential and coupling method. Fuel, 185:763–771, 2016.

[120] Qingang Xiong, Jingchao Zhang, Fei Xu, Gavin Wiggins, and C Stuart Daw. Coupling daem and cfd for simulating biomass fast pyrolysis in fluidized beds. Journal of Analytical and Applied Pyrolysis, 117:176–181, 2016.

[121] Anthony Dufour, Miguel Castro-Diaz, Nicolas Brosse, Mohamed Bouroukba, and Colin Snape. The origin of molecular mobility during biomass pyrolysis as revealed by in situ 1h nmr spectroscopy. ChemSusChem, 5(7):1258–1265, 2012.

[122] Elly Hoekstra, Wim PM Van Swaaij, Sascha RA Kersten, and Kees JA Hogendoorn. Fast pyrolysis in a novel wire-mesh reactor: Decomposition of pine wood and model compounds. Chemical engineering journal, 187:172–184, 2012.

[123] Alex D Paulsen, Matthew S Mettler, and Paul J Dauenhauer. The role of sample dimension and temperature in cellulose pyrolysis. Energy & Fuels, 27 (4):2126–2134, 2013.

[124] Yu-Chuan Lin, Joungmo Cho, Geoffrey A Tompsett, Phillip R Westmoreland, and George W Huber. Kinetics and mechanism of cellulose pyrolysis. The Journal of Physical Chemistry C, 113(46):20097–20107, 2009.

[125] K Papadikis, S Gu, and Anthony V Bridgwater. Computational modelling of the impact of particle size to the heat transfer coefficient between biomass particles and a fluidised bed. Fuel Processing Technology, 91(1):68–79, 2010.

[126] Anthony V Bridgwater. Review of fast pyrolysis of biomass and product upgrading. Biomass and bioenergy, 38:68–94, 2012.

[127] AMC Janse, XA De Jong, W Prins, and Willibrordus Petrus Maria van Swaaij. Heat transfer coefficients in the rotating cone reactor. Powder technology, 106(3):168–175, 1999.

[128] G Muggen. Looking back at the first half year of commercial scale pyrolysis oil production at empyro. In tcbiomass2015 (4th International Conference on Thermochemical Conversion Science), 2015.

[129] RH Venderbosch and Wolter Prins. Fast pyrolysis technology development. Biofuels, bioproducts and biorefining, 4(2):178–208, 2010.

[130] George VC Peacocke. Ablative pyrolysis of biomass. PhD thesis, Aston University, 1994.

[131] JA Garcia-Nunez, MR Pelaez-Samaniego, ME Garcia-Perez, I Fonts, J Abrego, RJM Westerhof, and M Garcia-Perez. Historical developments of pyrolysis reactors: a review. Energy & fuels, 31(6):5751–5775, 2017.

[132] AV Bridgwater and DGB Boocock. Developments in Thermochemical Biomass Conversion: Volume 1, volume 2. Springer Science & Business Media, 2013.

[133] JN Brown and RC Brown. Process optimization of an auger pyrolyzer with heat carrier using response surface methodology. Bioresource technology, 103(1):405–414, 2012.

[134] Sonil Nanda, Javeed Mohammad, Sivamohan N Reddy, Janusz A Kozinski, and Ajay K Dalai. Pathways of lignocellulosic biomass conversion to renewable fuels. Biomass Conversion and Biorefinery, 4(2):157–191, 2014.

[135] RH Venderbosch. A critical view on catalytic pyrolysis of biomass. ChemSusChem, 8(8):1306–1316, 2015.

[136] D Vamvuka. Bio-oil, solid and gaseous biofuels from biomass pyrolysis processesan overview. International Journal of Energy Research, 35(10):835–862, 2011.

[137] LK Mok, RG Graham, BA Freel, MA Bergougnou, and RP Overend. Fast pyrolysis (ultrapyrolysis) of cellulose and wood components. Journal of Analytical and Applied Pyrolysis, 8:391–400, 1985.

[138] Anthony V Bridgwater. Pyrolysis of solid biomass: Basics, processes and products. Energy from Organic Materials (Biomass) A Volume in the Encyclopedia of Sustainability Science and Technology, Second Edition, pages 1221–1250, 2019.

[139] Dmitry Yu Murzin. Chemical engineering for renewables conversion, volume 42. Academic Press, 2012.

[140] A Oasmaa and E Kuoppala. Fast pyrolysis of forestry residue. 3. storage stability of liquid fuel. Energy & Fuels, 17(4):1075–1084, 2003.

[141] Anja Oasmaa, Yrjo Solantausta, Vesa Arpiainen, Eeva Kuoppala, and Kai Sipila. Fast pyrolysis bio-oils from wood and agricultural residues. Energy & Fuels, 24(2):1380–1388, 2009.

[142] James P Diebold. A review of the chemical and physical mechanisms of the storage stability of fast pyrolysis bio-oils. Technical report, National Renewable Energy Lab., Golden, CO (US), 1999.

[143] Anja Oasmaa, Eeva Kuoppala, and Yrjö Solantausta. Fast pyrolysis of forestry residue. 2. physicochemical composition of product liquid. Energy & fuels, 17(2):433–443, 2003.

[144] A Oasmaa and E Kuoppala. Fast pyrolysis of forestry residue. 3. storage stability of liquid fuel. Energy & Fuels, 17(4):1075–1084, 2003.

[145] Emiliano Fratini, Massimo Bonini, Anja Oasmaa, Yrjo Solantausta, José Teixeira, and Piero Baglioni. Sans analysis of the microstructural evolution during the aging of pyrolysis oils from biomass. Langmuir, 22(1):306–312, 2006.

[146] Jiajia Meng, Andrew Moore, David Tilotta, Stephen Kelley, and Sunkyu Park. Toward understanding of bio-oil aging: accelerated aging of bio-oil fractions. ACS Sustainable Chemistry & Engineering, 2(8):2011–2018, 2014.

[147] Anja Oasmaa, Isabel Fonts, Manuel Raul Pelaez-Samaniego, Martha Estrella Garcia-Perez, and Manuel Garcia-Perez. Pyrolysis oil multiphase behavior and phase stability: A review. Energy & Fuels, 30(8):6179–6200, 2016.

[148] Xun Hu, Caroline Lievens, Alfons Larcher, and Chun-Zhu Li. Reaction pathways of glucose during esterification: Effects of reaction parameters on the formation of humin type polymers. Bioresource technology, 102(21):10104–10113, 2011.

[149] Jon Alvarez, Gartzen Lopez, Maider Amutio, Javier Bilbao, and Martin Olazar. Bio-oil production from rice husk fast pyrolysis in a conical spouted bed reactor. Fuel, 128:162–169, 2014.

[150] Manuel Garcia-Perez, Shan Wang, Jun Shen, Martin Rhodes, Woo Jin Lee, and Chun-Zhu Li. Effects of temperature on the formation of lignin-derived oligomers during the fast pyrolysis of mallee woody biomass. Energy & Fuels, 22(3):2022–2032, 2008.

[151] Leonard Ingram, Dinesh Mohan, Mark Bricka, Philip Steele, David Strobel, David Crocker, Brian Mitchell, Javeed Mohammad, Kelly Cantrell, and Charles U Pittman Jr. Pyrolysis of wood and bark in an auger reactor: physical properties and chemical analysis of the produced bio-oils. Energy & Fuels, 22(1):614–625, 2007.

[152] Peter Mølgaard Mortensen, J-D Grunwaldt, Peter Arendt Jensen, KG Knudsen, and Anker Degn Jensen. A review of catalytic upgrading of bio-oil to engine fuels. Applied Catalysis A: General, 407(1-2):1–19, 2011.

[153] Yu-Hwa E Sheu, Rayford G Anthony, and Ed J Soltes. Kinetic studies of upgrading pine pyrolytic oil by hydrotreatment. Fuel processing technology, 19(1):31–50, 1988.

[154] A Gutierrez, RK Kaila, ML Honkela, R Slioor, and AOI Krause. Hydrodeoxygenation of guaiacol on noble metal catalysts. Catalysis Today, 147(3-4): 239–246, 2009.

[155] Edward Furimsky and Franklin E Massoth. Deactivation of hydroprocessing catalysts. Catalysis Today, 52(4):381–495, 1999.

[156] Roel JM Westerhof, D Wim F Brilman, Manuel Garcia-Perez, Zhouhong Wang, Stijn RG Oudenhoven, Wim PM van Swaaij, and Sascha RA Kersten. Fractional condensation of biomass pyrolysis vapors. Energy & fuels, 25(4): 1817–1829, 2011.

[157] Chih-Chiang Chang, Seng-Rung Wu, Chi-Cheng Lin, Hou-Peng Wan, and Hom-Ti Lee. Fast pyrolysis of biomass in pyrolysis gas: Fractionation of pyrolysis vapors using a spray of bio-oil. Energy & Fuels, 26(5):2962–2967, 2012.

[158] Tim Schulzke, Stefan Conrad, and Jan Westermeyer. Fractionation of flash pyrolysis condensates by staged condensation. Biomass and Bioenergy, 95: 287–295, 2016.

[159] Ann-Christine Johansson, Kristiina Iisa, Linda Sandström, Haoxi Ben, Heidi Pilath, Steve Deutch, Henrik Wiinikka, and Olov GW Öhrman. Fractional condensation of pyrolysis vapors produced from nordic feedstocks in cyclone pyrolysis. Journal of Analytical and Applied Pyrolysis, 123:244–254, 2017.

[160] Pyoungchung Kim, Samuel Weaver, and Nicole Labbé. Effect of sweeping gas flow rates on temperature-controlled multistage condensation of pyrolysis vapors in an auger intermediate pyrolysis system. Journal of analytical and applied pyrolysis, 118:325–334, 2016.

[161] Naoufel Jendoubi, François Broust, Jean-Michel Commandre, Guillain Mauviel, Michel Sardin, and Jacques Lede. Inorganics distribution in bio oils and char produced by biomass fast pyrolysis: The key role of aerosols. Journal of Analytical and Applied Pyrolysis, 92(1):59–67, 2011.

[162] Akhil Tumbalam Gooty, Dongbing Li, Cedric Briens, and Franco Berruti. Fractional condensation of bio-oil vapors produced from birch bark pyrolysis. Separation and Purification Technology, 124:81–88, 2014.

[163] Tianju Chen, Chunjian Deng, and Ronghou Liu. Effect of selective condensation on the characterization of bio-oil from pine sawdust fast pyrolysis using a fluidized-bed reactor. Energy & Fuels, 24(12):6616–6623, 2010.

[164] Paul T Williams and Serpil Besler. The influence of temperature and heating rate on the slow pyrolysis of biomass. Renewable energy, 7(3):233–250, 1996.

[165] Michael Jerry Antal and Morten Grønli. The art, science, and technology of charcoal production. Industrial & Engineering Chemistry Research, 42(8): 1619–1640, 2003.

[166] Colomba Di Blasi. Heat, momentum and mass transport through a shrinking biomass particle exposed to thermal radiation. Chemical engineering science, 51(7):1121–1132, 1996.

[167] Won Chan Park, Arvind Atreya, and Howard R Baum. Experimental and theoretical investigation of heat and mass transfer processes during wood pyrolysis. Combustion and Flame, 157(3):481–494, 2010.

[168] BV Babu and AS Chaurasia. Heat transfer and kinetics in the pyrolysis of shrinking biomass particle. Chemical Engineering Science, 59(10):1999–2012, 2004.

[169] Mathew J Hagge and Kenneth M Bryden. Modeling the impact of shrinkage on the pyrolysis of dry biomass. Chemical Engineering Science, 57(14):2811–2823, 2002.

[170] Addison Killean Stark. Multi-scale chemistry modeling of the thermochemical conversion of biomass in a fluidized bed gasifier. PhD thesis, Massachusetts Institute of Technology, 2015.

[171] AV Bridgwater, D Meier, and D Radlein. An overview of fast pyrolysis of biomass. Organic geochemistry, 30(12):1479–1493, 1999.

[172] Olivier Boutin, M Ferrer, and Jacques Lédé. Radiant flash pyrolysis of celluloseevidence for the formation of short life time intermediate liquid species. Journal of Analytical and Applied Pyrolysis, 47(1):13–31, 1998.

[173] Ramesh K Sharma, Jan B Wooten, Vicki L Baliga, Xuehao Lin, W Geoffrey Chan, and Mohammad R Hajaligol. Characterization of chars from pyrolysis of lignin. Fuel, 83(11):1469–1482, 2004.

[174] Pedro E Sánchez-Jiménez, Luis A Pérez-Maqueda, Antonio Perejón, and José M Criado. A new model for the kinetic analysis of thermal degradation of polymers driven by random scission. Polymer Degradation and Stability, 95(5):733–739, 2010.

[175] Sudhir V Golikeri and Dan Luss. Analysis of activation energy of grouped parallel reactions. AIChE Journal, 18(2):277–282, 1972.

[176] Sergey Vyazovkin. A unified approach to kinetic processing of nonisothermal data. International Journal of Chemical Kinetics, 28(2):95–101, 1996.

[177] Sergey Vyazovkin. Modification of the integral isoconversional method to account for variation in the activation energy. Journal of Computational Chemistry, 22(2):178–183, 2001.

[178] JH Flynn. A general differential technique for the determination of parameters for d (α)/dt= f (α) a exp (- e/rt) energy of activation, preexponential factor and order of reaction (when applicable). Journal of Thermal Analysis and Calorimetry, 37(2):293–305, 1991.

[179] Seyed Hadi Shahcheraghi, Gholam Reza Khayati, and Mohammad Ranjbar. An advanced reaction model determination methodology in solid-state kinetics based on arrhenius parameters variation. Journal of Thermal Analysis and Calorimetry, 126(2):981–993, 2016.

[180] Andrew K Galwey and Michael E Brown. A theoretical justification for the application of the arrhenius equation to kinetics of solid state reactions (mainly ionic crystals). In Proceedings of the Royal Society of London A: Mathematical, Physical and Engineering Sciences, volume 450, pages 501–512. The Royal Society, 1995.

[181] Andrew K Galwey and Michael E Brown. Application of the arrhenius equation to solid state kinetics: can this be justified? Thermochimica Acta, 386 (1):91–98, 2002.

[182] FH Constable. The mechanism of catalytic decomposition. Proceedings of the Royal Society of London. Series A, Containing Papers of a Mathematical and Physical Character, 108(746):355–378, 1925.

[183] Sergey Vyazovkin. On the phenomenon of variable activation energy for condensed phase reactions. New Journal of Chemistry, 24(11):913–917, 2000.

[184] Donald B Anthony and Jack B Howard. Coal devolatilization and hydrogastification. AIChE Journal, 22(4):625–656, 1976.

[185] José A Caballero and Juan A Conesa. Mathematical considerations for nonisothermal kinetics in thermal decomposition. Journal of analytical and applied pyrolysis, 73(1):85–100, 2005.

[186] Kongvui Yip, Fujun Tian, Jun-ichiro Hayashi, and Hongwei Wu. Effect of alkali and alkaline earth metallic species on biochar reactivity and syngas compositions during steam gasification. Energy & Fuels, 24(1):173–181, 2009.

[187] Hanisom Abdullah and Hongwei Wu. Biochar as a fuel: 1. properties and grindability of biochars produced from the pyrolysis of mallee wood under slow-heating conditions. Energy & Fuels, 23(8):4174–4181, 2009.

[188] Hanisom Abdullah, Kun Aussieanita Mediaswanti, and Hongwei Wu. Biochar as a fuel: 2. significant differences in fuel quality and ash properties of biochars from various biomass components of mallee trees. Energy & Fuels, 24(3):1972–1979, 2010.

[189] Karuppiah Raveendran, Anuradda Ganesh, and Kartic C Khilar. Influence of mineral matter on biomass pyrolysis characteristics. Fuel, 74(12):1812–1822, 1995.

[190] Daniel Mourant, Caroline Lievens, Richard Gunawan, Yi Wang, Xun Hu, Liping Wu, Syed Shatir A Syed-Hassan, and Chun-Zhu Li. Effects of temperature on the yields and properties of bio-oil from the fast pyrolysis of mallee bark. Fuel, 108:400–408, 2013.

[191] Mi-Kyung Bahng, Bryon S Donohoe, and Mark R Nimlos. Application of an fourier transform-infrared imaging tool for measuring temperature or reaction profiles in pyrolyzed wood. Energy & Fuels, 25(1):370–378, 2010.

[192] Ravi Narayan and Michael Jerry Antal. Thermal lag, fusion, and the compensation effect during biomass pyrolysis. Industrial & engineering chemistry research, 35(5):1711–1721, 1996.

[193] Michael E Brown and Andrew K Galwey. The significance of compensation effects appearing in data published in computational aspects of kinetic analysis: Ictac project, 2000. Thermochimica acta, 387(2):173–183, 2002.

[194] Anna Trubetskaya, Peter Glarborg, Peter Arendt Jensen, Anker Degn Jensen, and Alexander Shapiro. Fast pyrolysis of biomass at high temperatures. PhD thesis, 2016.

[195] Madhav Prasad Pandey and Chang Soo Kim. Lignin depolymerization and conversion: a review of thermochemical methods. Chemical Engineering & Technology, 34(1):29–41, 2011.

[196] Paulo Eduardo Amaral Debiagi, Chiara Pecchi, Giancarlo Gentile, Alessio Frassoldati, Alberto Cuoci, Tiziano Faravelli, and Eliseo Ranzi. Extractives extend the applicability of multistep kinetic scheme of biomass pyrolysis. Energy & Fuels, 29(10):6544–6555, 2015.

[197] Dekui Shen, Wei Jin, Jun Hu, Rui Xiao, and Kaihong Luo. An overview on fast pyrolysis of the main constituents in lignocellulosic biomass to valued-added chemicals: structures, pathways and interactions. Renewable and Sustainable Energy Reviews, 51:761–774, 2015.

[198] Marc Gaugler and Warren J Grigsby. Thermal degradation of condensed tannins from radiata pine bark. Journal of wood chemistry and technology, 29(4):305–321, 2009.

[199] Chunhua Luo, Warren Grigsby, Neil Edmonds, Allan Easteal, and Jafar Al-Hakkak. Synthesis, characterization, and thermal behaviors of tannin stearates prepared from quebracho and pine bark extracts. Journal of applied polymer science, 117(1):352–360, 2010.

[200] Houda Saad, Abdelouahed Khoukh, Naceur Ayed, Bertrand Charrier, and Fatima Charrier-El Bouhtoury. Characterization of tunisian aleppo pine tannins for a potential use in wood adhesive formulation. Industrial Crops and Products, 61:517–525, 2014.

[201] HF Meier, VR Wiggers, GR Zonta, DR Scharf, EL Simionatto, and L Ender. A kinetic model for thermal cracking of waste cooking oil based on chemical lumps. Fuel, 144:50–59, 2015.

[202] Stylianos D Stefanidis, Eleni Heracleous, Despina Th Patiaka, Konstantinos G Kalogiannis, Chrysoula M Michailof, and Angelos A Lappas. Optimization of bio-oil yields by demineralization of low quality biomass. Biomass and Bioenergy, 83:105–115, 2015.

[203] Anja Oasmaa, Tom Sundqvist, Eeva Kuoppala, Manuel Garcia-Perez, Yrjo Solantausta, Christian Lindfors, and Ville Paasikallio. Controlling the phase stability of biomass fast pyrolysis bio-oils. Energy & Fuels, 29(7):4373–4381, 2015.

[204] Fan Lin, Christopher L Waters, Richard G Mallinson, Lance L Lobban, and Laura E Bartley. Relationships between biomass composition and liquid products formed via pyrolysis. Frontiers in Energy Research, 3:45, 2015.

[205] Yonggang Chen. Modeling biomass pyrolysis kinetics and mechanisms. In Fuel and Energy Abstracts, volume 4, page 241, 1997.

[206] William F DeGroot and Fred Shafizadeh. The influence of exchangeable cations on the carbonization of biomass. Journal of analytical and applied pyrolysis, 6(3):217–232, 1984.

[207] Christoph Krumm, Jim Pfaendtner, and Paul J Dauenhauer. Millisecond pulsed films unify the mechanisms of cellulose fragmentation. Chemistry of Materials, 28(9):3108–3114, 2016.

[208] Saurabh Maduskar, Gregory G Facas, Costas Papageorgiou, C Luke Williams, and Paul J Dauenhauer. Five rules for measuring biomass pyrolysis rates: Pulse-heated analysis of solid reaction kinetics of lignocellulosic biomass. ACS Sustainable Chemistry & Engineering, 6(1):1387–1399, 2017.

[209] Juan Proano-Aviles, Jake K Lindstrom, Patrick A Johnston, and Robert C Brown. Heat and mass transfer effects in a furnace-based micropyrolyzer. Energy Technology, 5(1):189–195, 2017.

[210] Eliseo Ranzi, Paulo Eduardo Amaral Debiagi, and Alessio Frassoldati. Mathematical modeling of fast biomass pyrolysis and bio-oil formation. note ii: secondary gas-phase reactions and bio-oil formation. ACS Sustainable Chemistry & Engineering, 5(4):2882–2896, 2017.

[211] H Hatzantonis, H Yiannoulakis, A Yiagopoulos, and C Kiparissides. Recent developments in modeling gas-phase catalyzed olefin polymerization fluidized-bed reactors: The effect of bubble size variation on the reactor's performance. Chemical Engineering Science, 55(16):3237–3259, 2000.

[212] D Kunni and O Levenspiel. Fluidization engineering., edit, 1969.

[213] KB McAuley, JP Talbot, and TJ Harris. A comparison of two-phase and well-mixed models for fluidized-bed polyethylene reactors. Chemical Engineering Science, 49(13):2035–2045, 1994.

[214] Ju Yong Kim and Kyu Yong Choi. Polymer particle mixing and segregation in a gas phase olefin polymerization reactor. In AIChE Symposium Series, volume 95, pages 77–82. New York, NY: American Institute of Chemical Engineers, 1971-c2002., 1999.

[215] Johnny Matta. Biomass Fast Pyrolysis Fluidized Bed Reactor: Modelling and Experimental Validation. PhD thesis, Université d'Ottawa/University of Ottawa, 2016.

[216] WE Ranz, W R_ Marshall, et al. Evaporation from drops. Chem. Eng. Prog, 48(3):141–146, 1952.

[217] James R Welty, Charles E Wicks, Gregory Rorrer, and Robert E Wilson. Fundamentals of momentum, heat, and mass transfer. John Wiley & Sons, 2009.

[218] Cantera. Cantera matlab toolbox. URL https://cantera.org/#.

[219] M Brennan Pecha, Manuel Garcia-Perez, Thomas D Foust, and Peter N Ciesielski. Estimation of heat transfer coefficients for biomass particles by direct numerical simulation using microstructured particle models in the laminar regime. ACS Sustainable Chemistry & Engineering, 5(1):1046–1053, 2016.

[220] Charles U Pittman Jr, Dinesh Mohan, Anthonia Eseyin, Qi Li, Leonard Ingram, El-Barbary M Hassan, Brian Mitchell, Hua Guo, and Philip H Steele. Characterization of bio-oils produced from fast pyrolysis of corn stalks in an auger reactor. Energy & Fuels, 26(6):3816–3825, 2012.

[221] Maider Amutio, Gartzen Lopez, Jon Alvarez, Martin Olazar, and Javier Bilbao. Fast pyrolysis of eucalyptus waste in a conical spouted bed reactor. Bioresource technology, 194:225–232, 2015.

[222] Susanne B Jones, Pimphan A Meyer, Lesley J Snowden-Swan, Asanga B Padmaperuma, Eric Tan, Abhijit Dutta, Jacob Jacobson, and Kara Cafferty. Process design and economics for the conversion of lignocellulosic biomass to hydrocarbon fuels: fast pyrolysis and hydrotreating bio-oil pathway. Technical report, Pacific Northwest National Laboratory (PNNL), Richland, WA (US), 2013.

[223] Hyun Ju Park, Young-Kwon Park, and Joo Sik Kim. Influence of reaction conditions and the char separation system on the production of bio-oil from radiata pine sawdust by fast pyrolysis. Fuel Processing Technology, 89(8): 797–802, 2008.

[224] A Ruth Fernandez-Akarregi, Jon Makibar, Gartzen Lopez, Maider Amutio, and Martin Olazar. Design and operation of a conical spouted bed reactor pilot plant (25 kg/h) for biomass fast pyrolysis. Fuel processing technology, 112:48–56, 2013.

[225] Güray Yildiz, Marty Pronk, Marko Djokic, Kevin M van Geem, Frederik Ronsse, Ruben van Duren, and Wolter Prins. Validation of a new set-up for continuous catalytic fast pyrolysis of biomass coupled with vapour phase upgrading. Journal of analytical and applied pyrolysis, 103:343–351, 2013.